Development of HER2-targeted nanobodies for molecular optical imaging and therapy of breast cancer

Ontwikkeling van HER2-gerichte nanobodies voor moleculaire optische beeldvorming en therapie van borstkanker

(met een samenvatting in het Nederlands)

Proefschrift

ter verkrijging van de graad van doctor aan de Universiteit Utrecht op gezag van de rector magnificus, prof. dr. G.J. van der Zwaan, ingevolge het besluit van het college voor promoties in het openbaar te verdedigen op maandag 15 september 2014 des middags te 12.45 uur

door

Marta Magdalena Kijanka

geboren op 3 november 1985 te Wroclaw, Polen

Promotoren:	Prof. dr. A.S. Akhmanova
	Prof. dr. P.J. van Diest
Copromotoren:	Dr. P.M.P. van Bergen en Henegouwen
	Dr. S. Oliveira

The research presented in this thesis was partially performed within the framework of CTMM, the Center for Translational Molecular Medicine, project MAMMOTH (grant 030-201).

I am among those who think that science has great beauty.

A scientist in his laboratory is not only a technician:

he is also a child placed before natural phenomena which impress him like a fairy tale.

Maria Skłodowska-Curie

Development of HER2-targeted nanobodies for molecular optical imaging and therapy of breast cancer.

PhD thesis with a summary in Dutch

Department of Biology, Utrecht University, The Netherlands

ISBN: 978-90-393-5892-4

Printed by: **Proefschriftmaken.nl | Uitgeverij BOXPress**

Published by: **Uitgeverij BOXPress, 's-Hertogenbosch**

Design of the cover:

Anna Cieplińska

Design of the illustrations for chapters' title pages:

Magdalena Kijanka

Table of contents

Chapter 1

General Introduction

1

Breast cancer is the most prevalent cancer in women worldwide. It has been estimated that 1 in 8 women and 1 in 1,000 men will develop breast cancer during their lives. It is a complex disease represented by morphologically heterogeneous tumors, which differ in their biological features, behavior and response to therapy. Improved diagnostics and therapeutic strategies have resulted in the increase of the 5-year survival rates to nearly 90% since mid-1970s [1,2]. Nevertheless, despite this significant improvement, almost one third of all patients will still develop distant metastasis.

1.1 Morphological and molecular classification of breast cancer

To assess prognosis and plan the most appropriate therapy, breast cancer patients are categorized according to several factors such as histological features of the tumor, tumor size, hormone receptor status, HER2 receptor status, axillary lymph node status and patient age.

In situ breast carcinoma is confined to the original tissue compartment and does not penetrate the basement membrane and invade the surrounding tissue. It can be further categorized into ductal (DCIS) or lobular (LCIS) based on its histological appearance. Invasive breast carcinomas are divided into 8 main histological subtypes: infiltrating ductal, invasive lobular, ductal/lobular, mucinous, tubular, cribriform, medullary and micropapillary carcinomas. Infiltrating ductal carcinoma accounts for almost 80% of all invasive lesions. It can be graded (according to degree of tubular formation, nuclear atypia and mitotic rate) as well differentiated (grade 1), moderately differentiated (grade 2) or poorly differentiated (grade 3) which is strongly correlated to prognosis [3,4].

Molecular biomarkers have been introduced to improve the prediction of response to specific agents. Hormone receptor status (progesterone/estrogen receptors) is especially important for tailored endocrine therapy with aromatase inhibitors or tamoxifen [5,6]. HER2 receptor status is used to select patients eligible for HER2-targeted therapies with the use of anti-HER2 monoclonal antibody trastuzumab (also known as Herceptin®) [6].

On a molecular level, due to gene expression profiling studies, breast cancer can be divided into 3 main groups, namely: luminal, HER2-driven and basal like [3,7,8]. These groups do not only differ in gene expression pattern, but also in the prognosis and probability to develop distant metastasis. The most common breast cancer is the luminal type, which is the case for 70% of invasive breast cancers [7]. It is a hormone receptor positive subtype, which can be further distinguished into luminal A and luminal B subtypes, of which the luminal A subtype is characterized by higher expression of ER-related genes (such as LIV1 or CCND1) and lower expression of proliferative genes than the luminal B subtype, that may also be HER2 amplified/overexpressed. The luminal subtypes are associated with a relatively good prognosis (better for luminal A than B), however the response to the treatment (endocrine therapy, chemotherapy) may differ [7,8]. The HER2-driven subtype is characterized on one hand by high expression of HER2 receptor and other genes present

in the ERBB2 amplicon and low expression of ER and associated genes on the other. About 15% of all invasive breast cancers are of HER2-driven subtype, for which two main treatment options are most common: trastuzumab treatment and anthracycline-based chemotherapy. Nevertheless, the HER2-enriched subtype is associated with a poor prognosis, as the tumors are more likely to be high grade and lymph node-positive [7,8]. The basal-like cancers are characterized by lack of hormone receptors and associated genes expression as well as by low expression of HER2. This explains why they are often referred to as 'triple negative' (ER^-, PR^-, $HER2^-$). They do, however, strongly express the basal cytokeratines 5, 14 and 17 and proliferation-related genes. 15% of invasive breast cancers are described as basal-like. The prognosis for basal-like cancer is poor, partially due to few treatment options available (platinum based chemotherapy, PARP inhibitors) [7,8]. Integration of morphological and molecular classification of breast cancers may lead in the future to a better therapeutic decision making process.

1.2 Current guidelines for breast cancer: diagnosis and therapy

Clinical examination, including palpation of the breasts and locoregional lymph nodes, in combination with imaging, allow for breast cancer diagnosis, when confirmed by pathological assessment. Imaging can be done with the use of mammography and ultrasound, both of the breast and regional lymph nodes. In (young) women with dense breasts or when there is a history of breast cancer associated with BRCA mutations in the patient's family, an MRI is the preferred imaging modality. Before application of any treatment, pathological diagnosis must be performed based on a core needle biopsy. The removed tissue should be analyzed according to the **t**umor-**n**ode-**m**etastasis (TNM) staging system, but also subjected to immunohistochemical (IHC) evaluation of estrogen receptor (ER), progesterone receptor (PR) and HER2 receptor status. It is advised that in case of negative ER, PR or HER2 receptor status in the biopsy, the surgical specimen is retested for their expression (to account for tumor heterogeneity). Before choosing the appropriate treatment strategy several factors are taken into account such as: tumor size and location, grade, number of lesions, lymph node involvement, age and general health status of the patient. *In situ* and invasive breast cancer are treated by a combination of surgical-, chemical- and radiation based therapies. Surgery is the most common choice of local therapy, often in combination with radiotherapy. It is also often followed by an adjuvant therapy, such as hormonal (including selective estrogen receptor modulators e.g. tamoxifen or aromatase inhibitors) and/or chemotherapy (traditional chemotherapy, but also receptor specific immunotherapy e.g. trastuzumab).

1.3 HER receptor kinases: Human epidermal growth factor receptor 2

Human epidermal growth factor receptors family (HER family, also referred to as ErbB family)

consists of four members, namely epidermal growth factor receptor (EGFR, also referred to as HER1), HER2 (ErbB2), HER3 (ErbB3) and HER4 (ErbB4). These receptor tyrosine kinases play a key role in regulation of cell signaling pathways affecting cell proliferation and migration (both important for tumorigenesis), but also adhesion, differentiation and apoptosis. HER family members are located at the cell membrane and share a similar structure (Fig.1).

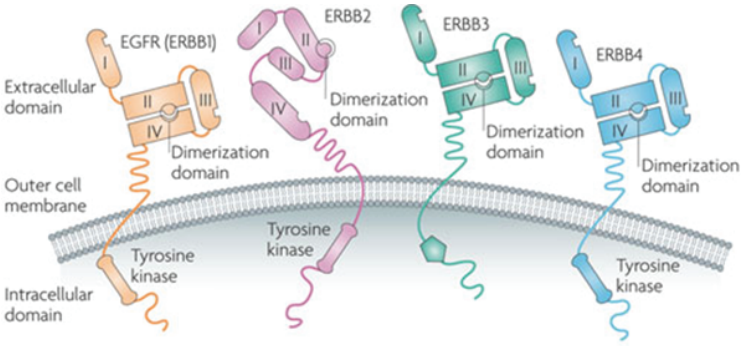

Fig. 1. Schematic representation of HER family members [9]. Used with permission of Nature Publishing Group.

All are composed of an extracellular domain, a single and lipophilic transmembrane part, and an intracellular tyrosine kinase domain. Two of the members are fully functional (EGFR, HER4), while there is no known ligand of HER2 and HER3 does not possess an active tyrosine kinase domain. The extracellular domain consists of four subdomains, of which two are leucine-rich (subdomains 1 and 3) and two are cysteine-rich (subdomain 2 and 4). Upon ligand binding, receptors undergo a reorganization in the extracellular part from a 'closed' to an 'open' conformation, which leads to exposure of the dimerization arm (present on subdomain 2), but also rearrangements in the transmembrane and intracellular domain (Fig.2).

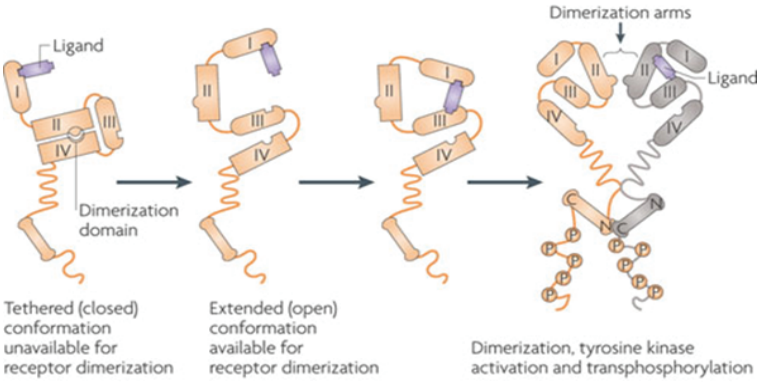

Fig. 2. Conceptualization of the receptor conformational change on ligand binding [9]. Used with permission of Nature Publishing Group.

HER2 is a unique family member as it is predominantly present on the membrane in an open conformation, which makes it a preferred dimerization partner for other HER family members. The HER2-HER3 heterodimers are regarded as the most oncogenic unit [9]. Homo- and heterodimerization of HER members results in kinase activation and phosphorylation of C-terminal tyrosine residues. These phosphorylated tyrosine residues serve as docking sites for various adaptor proteins, leading to activation of signaling cascades of both proliferative and anti-apoptotic pathways such as RAS/MAPK and PI3K and PLCγ signaling towards AKT activation.

HER2 receptor plays an important role during embryonic development and is later involved in the development and growth of breast. Its overexpression, however, has been described in various cancer types including breast, ovary, prostate, bladder, pancreas, and colon carcinomas. HER2 receptor overexpression is associated with a more aggressive disease, which has a greater likelihood of reoccurrence and a generally poor prognosis. Assessment of HER2 expression is a common practice for accurate diagnosis and subsequent selection of the treatment protocol for breast cancer patients. At the moment, there are several *ex vivo* approaches to assess HER2 expression levels, namely immunohistochemistry (IHC), *in situ* hybridization (using fluorescence (FISH) or silver (SISH) or DAB chromogen (CISH)), or PCR based techniques such as multiplex ligation-dependent probe amplification [10]. All these methods require a biopsy of the primary tumor, which does not necessarily reflect the HER2 status neither of the entire tumor nor in metastatic lesions, due to intra- and intertumoral heterogeneity of HER2 expression.

The importance of prognostic and predictive value of HER2 gene amplification in breast cancer has been known for more than 20 years, however the HER2 gene mutations independent of HER2 gene amplification resulting in increased cellular transformation and tumor formation have been identified only recently [11,12]. These somatic, activating mutations are mostly present in the tyrosine kinase domain (68%, exons 19-20) and the extracellular domain (20%, exon 8) [13]. Thirteen of these mutations were functionally characterized by Bose et al. using *in vitro* kinase assays, protein structure analysis, cell culture, and xenograft experiments [13]. All of these mutations were sensitive to the irreversible HER2/EGFR tyrosine kinase inhibitor neratinib, thus validating HER2 somatic mutations as drug targets for breast cancer treatment. The discovery of these mutations offers potential therapeutic opportunities as tumors considered to be HER2-negative based on current guidelines, which may still depend on HER2 signaling due to these HER2 gene mutations, may potentially benefit from HER2 targeting agents. Nevertheless, clinical trials are first needed to evaluate whether HER2-mutated tumors are indeed responsive to HER2-targeted drugs, and if so, which mutations are predictive of sensitivity to which agent.

1.4 Molecular imaging

At the moment there are several imaging modalities that are commonly used to detect and stage breast cancer, namely: X-ray mammography, **c**omputed **t**omography (CT), **u**ltra**s**onography (US), **m**agnetic **r**esonance **i**maging (MRI), **s**ingle **p**hoton **e**mission **c**omputed **t**omography (SPECT), **p**ositron **e**mission **t**omography (PET) and optical imaging. Each of these techniques comes with advantages and limitations. Mammography is, however, the most widely used technique to screen for breast cancer. The biggest limitation of this technique is its decreasing sensitivity with increasing breast density [14,15]. Also imaging of patients with implants or with surgical scars remains problematic. MRI, US and CT are the commonly used modalities providing anatomical information. They are fairly sensitive, especially MRI, but low specificity remains a serious problem. Therefore, to distinguish cancer cells from healthy tissues novel imaging modalities are required [16]. Radionuclide imaging techniques encompass SPECT and PET. These techniques provide physiological information. ^{18}F-fluoro-2-deoxy-D-glucose is a commonly used glucose analog (in more than 90% of all PET imaging procedures), approved by the U.S. **F**ood and **D**rug **A**dministration (FDA) [17]. It is preferentially taken up by cancer cells due to their enhanced glycolysis (Warburg effect). The disadvantage of ^{18}FDG-PET is its low specificity, as the glucose analog may also be taken up by non-malignant cells in the presence of inflammation [16].

Optical imaging is a novel emerging technology, which offers several advantages over traditional radiological imaging techniques. First of all, it does not require the ionizing radiation, which contributes to increased safety of both the operator and patient. Secondly, in contrast to e.g. MRI, it is highly sensitive. It is a non-invasive technique that can be used repeatedly for treatment monitoring purposes. Finally, it offers significant cost savings in comparison to conventional radiological technologies [18]. One of the biggest disadvantages of optical molecular imaging is the limited sensitivity due to restricted light penetration into the tissue, which prevents applications such as whole-body imaging. For this reason optical imaging is a technique suited for non-invasive detection of superficial tumors (e.g. breast cancer, head and neck tumors) or tumors accessible using an endoscope (e.g. lung cancer, tumors located in the gastrointestinal tract or abdominal cavity). The disadvantage of limited light penetration is, however, less of a problem in an invasive, intra-operative setting.

Optical imaging technique was first described in 1929 by Max Cutler, who observed that solid tumors appear as diffuse shadows upon transillumination of breast [19]. Limited specificity and sensitivity of this method allowed for detection of only large, highly vascular, malignant lesions at the time. However, since the time of Cutler's discovery a lot of progress in technology refinement and fluorescent contrast agents development has been achieved. Basically, the interaction of photons with tissue is described by three parameters, namely light absorption, light scattering, and fluorescence

emission [20]. The first two depend largely on the wavelength of the excitation source. Excitation with light of a wavelength lower than 700 nm results in shallow penetration depth (only a few millimeters), whereas excitation with light of a wavelength above 900 nm leads to decreased signal to background ratios due to absorption of water and hemoglobin. Near infrared optical imaging uses light of the near infrared range of the spectrum (NIR, 650-900 nm), in which light absorption by endogenous chromophores of a living tissue (melanin, water, lipids, oxy- and deoxyhemoglobin) is at the lowest, resulting in the deepest light penetration (up to several centimeters) [20-22]. Combining increased tissue penetration with low autofluorescence is essential for successful optical imaging and may be obtained with the use of NIR fluorophores. It is feasible to detect breast cancer in a non-invasive manner using the optical imaging approach [20].

One of the most promising clinical applications of NIR optical imaging is, however, providing surgical guidance during tumor resections in an intraoperative setting [23]. NIR fluorophores need to meet several criteria to ensure successful optical imaging. The key criteria include: excitation and emission maxima between 650 nm – 900 nm (NIR part of spectra), high fluorescence quantum yield, chemical stability, aqueous solubility, low or none non-specific binding, rapid clearance of the non-bound fluorophore, low toxicity, and finally easy production at low costs and stability during long-term storage [24]. Even though indocyanine green (ICG) does not meet all above mentioned criteria, to this date this it is the only clinically approved fluorescent contrast agent for NIR optical imaging [25,26]. The limitations of ICG include relatively weak fluorescence, limited chemical stability, pronounced aggregation tendency and strong interaction with serum proteins [25,27]. Much progress has been recently made on development of NIR fluorophores (including cyanine dyes, squaraine, phthalocyanines, porphyrin derivatives and borondipyrromethane analogues) improved in terms of their photo- and chemical stability as well as water solubility [24,27,28]. Two of these fluorophores, presenting excitation/emission maxima in the center of the optimal NIR imaging window, have attracted much attention, namely IRDye800CW developed by LI-COR and ZW800-1 synthetized by the group of John Frangioni [20,29-31]. Both of these promising molecules are being evaluated in clinical trials at the moment. The biggest disadvantage of clinically approved ICG in comparison to IRDye800CW or ZW800-1 is the lack of a reactive functional group that would allow its conjugation to a targeting moiety [26]. The most common functionalization of NIR fluorophores necessary for conjugation of the dye to a tumor targeting moiety include N-hydroxysuccinimide ester (NHS-ester) and maleimide [22].

Besides appropriate fluorophores, molecules that specifically bind tumor markers are needed for NIR molecular imaging to be successful in cancer detection. Increased understanding of cancer biology allowed selection of several biomarkers, the expression of which is associated with tumor development, such as epidermal growth factor receptor (EGFR), vascular endothelial growth factor (VEGF) and human epidermal growth factor receptor 2 (HER2) or hypoxia up-regulated cell

surface antigens (e.g. GLUT1 or CAIX) [32]. This knowledge prompted design and development of targeted pharmaceuticals. To improve the tumor specificity and provide high contrast imaging, at first monoclonal antibodies have been employed. To date, there are five monoclonal antibodies that have been approved by the FDA for diagnostic imaging, of which four are for cancer imaging [17]. All these compounds are at this point suitable for radioimmunodetection with SPECT when labeled with γ-emitting radionuclides (^{99m}Tc or ^{111}I). Antibodies targeting EGFR (Cetuximab®) and HER2 (Herceptin®) have been also recently evaluated in clinical studies for PET imaging [17,33,34]. Conventional full-size antibodies are known to have a long residence time in blood circulation, ranging from a few days to weeks. This results in optimal tumor-to-background ratios (T/B ratio) not earlier than at 2 to 4 days post injection (p.i.). Such long circulation makes antibodies suitable for therapy, but less so for rapid tumor imaging.

1.4.1 Camelid single domain antibodies as novel probes for optical molecular imaging

An ideal imaging probe for tumor detection should meet several criteria. First, it should be able to rapidly extravasate from the systemic circulation to the tumor site and penetrate it in a homogenous manner. Secondly, it should exert high affinity towards targets present, ideally, exclusively on the surface of cancer cells. Finally, it should be cleared from non-targeted tissues efficiently to provide high contrast between tumor and normal tissue shortly upon its administration.

Over the years, a lot of research was dedicated into finding the most optimal format of a tumor targeting moiety. To ensure that the optimal contrast is obtained shortly after injection of the tracer, the tendency to decrease the size of the targeting moiety was observed. The size of tested targeting moieties varied from conventional monoclonal antibodies (mAb; 150kDa), single-chain variable fragments (scFv; ~30 kDa) to as small as variable fragments (Fv; ~15 kDa), or affibodies (~7 kDa) [35-37]. Nevertheless, the advantage of the smaller size is in most cases counterbalanced by decreased stability resulting in aggregation (especially in case of scFv), lower affinity and/or difficulty in large scale production [38].

Heavy chain only antibodies (HcAbs, ~95 kDa) were discovered more than 20 years ago by Hamers-Casterman and co-workers. They are fully functional antibody structures found in *Camelidae* (bactrian camels, dromedaries, vicugnas, and llamas) and in cartilaginous fish (such as sharks, rays, and skates). Interestingly, the variable domain of HcAbs alone (i.e. VHH, also referred to as nanobody or single domain antibody) is a fully functional and the smallest naturally derived antigen-binding fragment.

Nanobodies, which are ten times smaller in molecular weight than conventional antibodies (15 kDa), are composed of 3 hypervariable regions (HV), surrounded by more conserved framework regions (FR), forming two β-sheets connected by loops and a conserved disulfide bond (between

Cys23 and Cys94) [39,40]. The hypervariable regions are located at the N-terminal end of the protein, forming a surface complementary to the surface of the epitope (CDR, complementarity-determining region). The largest differences in amino acid sequence homology between the variable domain of a heavy chain (VH) and a VHH are present in the framework 2 (FR2) and CDR regions. The highly conserved hydrophobic amino acids present in the FR2 of VH (Val47,Gly49, Leu50, Trp52) are replaced by smaller and/or more hydrophilic amino acids in the FR2 of VHH (mostly Phe47, Glu49, Arg50, Gly52) [39]. Replacement of these hydrophobic amino acids, which normally interact with the variable domain of a light chain (VL), results in higher solubility of nanobodies. Because HcAbs are completely devoid of light chains, the antigen is recognized by three (instead of six as in mAb) loops [39,40]. In order to provide large enough antigen-interacting surface, the loops are extended in comparison to loops present in VH domain of conventional Ab [39,40]. Small size, prolate shape (4 nm x 2.5 nm) and extended loops enable nanobodies to enter cavities present on the surface of the antigen. Nanobodies obtained from immune libraries display typically affinities in low nanomolar, or even picomolar, range. Several *in vitro* affinity maturation techniques, such as e.g. Ala-scanning based mutations, have been shown to improve the affinity constants even further [39]. High homology of VHH with human VH domains, stable behavior and rapid clearance from blood are likely to decrease immunogenicity of VHHs [39]. Several studies show that no immune response towards nanobodies was detected upon injection of VHH-containing constructs into mice or human [41-43]. Moreover, a strategy to further humanize VHHs has been recently described [44].

Recently, nanobodies have attracted much attention, as they fulfill all requirements for an ideal imaging probe [45]. They are stable and possess specificity towards their antigens; due to their small size, they rapidly distribute upon intravenous injection (iv), extravasate from the bloodstream and penetrate tumors in a homogenous manner; they bind tightly to their targets present on the surface of cancer cells; they are known to have low immunogenic potential therefore enabling repetitive injections e.g. for monitoring response to treatment; and finally the unbound nanobodies are cleared fast, allowing acquisition of images with acceptable T/B ratio at early time points after their administration (provided that the tumor is not in the proximity of kidneys or bladder) [39,40,46-48].

1.5 Targeted therapy for HER2-positive breast cancer

The development of targeted therapy was a major breakthrough in cancer treatment, which was at the time limited to surgery, chemo-, hormonal and radiation therapy. Due to the selective character of these anti-proliferative agents, only cancer cells are affected resulting in less severe side-effects. In 1998 trastuzumab (Herceptin®), the first mAb for use in women with HER2 positive metastatic breast cancer obtained the FDA approval [49]. Trastuzumab is a humanized mAb developed by

Genentech Inc (San Francisco, CA,USA) that binds to subdomain 4 of HER2 extracellular domain [50,51]. Clinical studies clearly showed that addition of trastuzumab to a standard chemotherapy has greatly improved the treatment outcome [49,51]. Even though it is routinely used in the clinic, its exact mode of action is not yet completely unraveled.

Several mechanisms have been, however, proposed. Firstly, trastuzumab, as a mAb is capable of attracting immune cells to HER2 overexpressing cells by a mechanism called **a**ntibody-**d**ependent **c**ellular **c**ytotoxicity (ADCC) [52,53]. The Fc portion of the mAb is recognized by Fcγ receptor present on immune effector cells, such as natural killer cells. Studies by Arnould et al. support this hypothesis. The group has shown an increased number of natural killer cells in tumor infiltrate of patients with locally advanced breast cancer that were treated with trastuzumab [54]. Secondly, trastuzumab may lead to inhibition of signal transduction pathways as preclinical data show that by binding to HER2 receptor it interferes with HER2 dimerization leading to suppression of Akt phosphorylation and inhibition of the PI3K/Akt signaling pathways. Furthermore, its binding leads to an increase of phosphatase and tensin homolog (PTEN) levels, which in turn suppresses the PI3K/Akt signaling pathways. As a result cell growth, proliferation and survival are potently decreased [51-53]. It has been also proposed that, due to steric hindrance, binding of trastuzumab inhibits proteolytic cleavage of the receptor and formation of free HER2 extracellular domain – p95-HER2 [52]. Presence of p95HER2 has been associated with a clinically more aggressive subset of HER2 positive breast cancers [52]. Finally, Klapper et al. proposed that trastuzumab leads to HER2 receptor internalization and subsequent degradation by recruiting the ubiquitin ligase c-Cbl to the Tyr_{1112} [55]. The exact mechanism of c-Cbl recruitment to the HER2 upon binding of the mAb as well as details of c-Cbl mediation of HER2 degradation remain unknown.

Trastuzumab has clearly paved the way for targeted therapy in breast cancer treatment. To date, there are four HER2-targeted therapeutics approved for treatment of metastatic breast cancer patients, namely trastuzumab, pertuzumab (since 2012), ado-trastuzumab emtansine (T-DM1) (since 2013) and a small molecule tyrosine kinase inhibitor – lapatinib (since 2007) [49,56-58]. Since 2006 trastuzumab has however been the only HER2-targeted agent approved by the FDA for the adjuvant treatment of patients with early-stage HER2-positive, node-positive breast cancer [49,59].

Despite the undebatable success of trastuzumab in improving the clinical outcome of HER2-positive breast cancer patients, 70% of them demonstrate acquired resistance to the trastuzumab treatment [52,60]. Moreover, less than 35% of patients initially respond to the treatment with mAb, which suggests existence of intrinsic (*de novo*) resistance. These facts highlight the urgent need for development of alternative HER2-targeted agents and therapeutic strategies.

The exact mechanism underlying trastuzumab resistance remains poorly understood. One of the possible mechanisms is truncation of the extracellular domain of the receptor, thereby inhibiting the binding of trastuzumab to the receptor. The p95-HER2 generated as a result of this

proteolysis possesses constitutive kinase activity [51,52]. The mechanism by which cancer cells induce receptor truncation in response to applied mAb treatment is still unclear. Another possibility is masking of the mAb epitope by overexpression of highly O-glycosylated mucin, MUC4, or up-regulation of the cleaved form of MUC1 [51,52]. The trastuzumab resistance may also be gained due to compensatory activation of parallel signaling pathways mediated by HER3 or insulin-like growth factor receptor 1 (IGF1R) or aberrant activation of downstream signaling cascades due to e.g. 'loss of function' deletions of PTEN or activating mutations of PI3KCA [51,52].

1.6 Aims and outline of the thesis

This thesis focuses on the development of high affinity, HER2-specific nanobodies. In **Part 1** of the thesis these nanobodies are employed for imaging purposes, whereas in **Part 2** their feasibility in nanobody-based therapeutic setting is evaluated.

In **Chapter 2** the selection procedure and preclinical *in vitro* and *in vivo* evaluation of chosen optical imaging probe candidates is described. In this part of the thesis we highlight the absolute necessity of nanobodies to display high affinity towards their targets to be successful imaging probes. The coupling of the NIR-fluorophore may have a detrimental effect on nanobody binding capacity. An example of this phenomenon is shown in this chapter together with a solution that allows overcoming affinity loss upon NIR-fluorophore conjugation. Furthermore, the potential of nanobodies as tools for image-guided surgery is introduced in this part of the thesis. Obtaining appropriate T/B ratios is essential for optical imaging. Based on successful rapid optical imaging with nanobodies described in Chapter 2 we have further evaluated if simultaneous injection of dual-specificity nanobodies would result in enhanced contrast between tumor and healthy tissue. Moreover, it has been hypothesized that such simultaneous injection of dual-specific nanobodies would allow non-invasive determination of tumor molecular status. These results are presented in **Chapter 3**, which describes the *in vivo* evaluation of dual-spectral combination of nanobodies targeting HER2 and CAIX in an orthotopic model. In **Chapter 4** development of nanobodies for optical imaging of canine HER2 is presented. Besides imaging at the *in vivo* level, nanobodies may have the potential to visualize HER2 receptor at the electron microscopy level. **Chapter 5** focuses on establishing a novel protocol for immune-electron microscopy using anti-HER2 nanobody as a tool for both staining on cryo-sections, but also in SEM and TEM.

Part 2 of this thesis focuses on the usage of nanobody-based therapeutics for cancer therapy. First, challenges of such nanomedicines are reviewed in **Chapter 6.** Nanobody-based therapeutics can be divided into three different platforms: (a) receptor antagonists that interfere with or block the activation of a certain signaling pathway; (b) a targeting moiety that transports effector domains, such as toxic peptides or drugs; and (c) targeting molecules on the surface of nanoparticles.

In **Chapter 7** we evaluate the performance of HER2 targeting nanobodies in platform (b). In this chapter we address the clinically relevant problem of overcoming trastuzumab resistance. We show that the photodynamic therapy (PDT) with anti-HER2 nanobodies conjugated to photosensitizers has the potential to eliminate HER2-overexpressing, trastuzumab-resistant breast cancer cells. **Chapter 8** describes the nanobody performance as nanoparticle targeting molecules. Here we use PLGA-nanoparticles encapsulating RNase and decorated on the surface with HER2-targeted nanobody. **Chapter 9** summarizes the obtained results and presents future perspectives on the nanobody-based optical imaging and therapy.

References

1. Berry DA, Cronin KA, Plevritis SK *et al.*: Effect of screening and adjuvant therapy on mortality from breast cancer. *N. Engl. J. Med.* 353(17), 1784-1792 (2005).

2. Siegel R, Naishadham D, Jemal A: Cancer statistics, 2012. *CA Cancer. J. Clin.* 62(1), 10-29 (2012).

3. Malhotra GK, Zhao X, Band H, Band V: Histological, molecular and functional subtypes of breast cancers. *Cancer. Biol. Ther.* 10(10), 955-960 (2010).

4. Corben AD: Pathology of invasive breast disease. *Surg. Clin. North Am.* 93(2), 363-392 (2013).

5. Rakha EA, Ellis IO: Modern classification of breast cancer: should we stick with morphology or convert to molecular profile characteristics. *Adv. Anat. Pathol.* 18(4), 255-267 (2011).

6. Rakha EA, Reis-Filho JS, Ellis IO: Combinatorial biomarker expression in breast cancer. *Breast Cancer Res. Treat.* 120(2), 293-308 (2010).

7. Schnitt SJ: Classification and prognosis of invasive breast cancer: from morphology to molecular taxonomy. *Mod. Pathol.* 23 Suppl 2, S60-4 (2010).

8. Brenton JD, Carey LA, Ahmed AA, Caldas C: Molecular classification and molecular forecasting of breast cancer: ready for clinical application? *J. Clin. Oncol.* 23(29), 7350-7360 (2005).

9. Baselga J, Swain SM: Novel anticancer targets: revisiting ERBB2 and discovering ERBB3. *Nat. Rev. Cancer.* 9(7), 463-475 (2009).

10. Moelans CB, de Weger RA, van Blokland MT *et al.*: HER-2/neu amplification testing in breast cancer by multiplex ligation-dependent probe amplification in comparison with immunohistochemistry and in situ hybridization. *Cell. Oncol.* 31(1), 1-10 (2009).

11. Bose R: A neu view of invasive lobular breast cancer. *Clin. Cancer Res.* 19(13), 3331-3333 (2013).

12. Ross JS, Wang K, Sheehan CE *et al.*: Relapsed classic E-cadherin (CDH1)-mutated invasive lobular breast cancer shows a high frequency of HER2 (ERBB2) gene mutations. *Clin. Cancer Res.* 19(10), 2668-2676 (2013).

13. Bose R, Kavuri SM, Searleman AC *et al.*: Activating HER2 mutations in HER2 gene amplification negative breast cancer. *Cancer. Discov.* 3(2), 224-237 (2013).

14. Herranz M, Ruibal A: Optical imaging in breast cancer diagnosis: the next evolution. *J. Oncol.* 2012, 863747 (2012).

15. Fowler AM: A molecular approach to breast imaging. *J. Nucl. Med.* 55(2), 177-180 (2014).

16. Belkic D, Belkic K: Molecular imaging in the framework of personalized cancer medicine. *Isr. Med. Assoc. J.* 15(11), 665-672 (2013).

17. van Dongen GA, Visser GW, Lub-de Hooge MN, de Vries EG, Perk LR: Immuno-PET: a navigator in monoclonal antibody development and applications. *Oncologist* 12(12), 1379-1389 (2007).

18. van de Ven S, Wiethoff A, Nielsen T *et al.*: A novel fluorescent imaging agent for diffuse optical tomography of the breast: first clinical experience in patients. *Mol. Imaging Biol.* 12(3), 343-348 (2010).

19. Cutler M: Transillumination as an aid in the

diagnosis of breast lesions. . *Surg Gynecol Obs.* 48, 721-728 (1929).

20. Kovar JL, Simpson MA, Schutz-Geschwender A, Olive DM: A systematic approach to the development of fluorescent contrast agents for optical imaging of mouse cancer models. *Anal. Biochem.* 367(1), 1-12 (2007).

21. Weissleder R: A clearer vision for in vivo imaging. *Nat. Biotechnol.* 19(4), 316-317 (2001).

22. Hadjipanayis CG, Jiang H, Roberts DW, Yang L: Current and future clinical applications for optical imaging of cancer: from intraoperative surgical guidance to cancer screening. *Semin. Oncol.* 38(1), 109-118 (2011).

23. van Dam GM, Themelis G, Crane LM *et al.*: Intraoperative tumor-specific fluorescence imaging in ovarian cancer by folate receptor-alpha targeting: first in-human results. *Nat. Med.* 17(10), 1315-1319 (2011).

24. Yi X, Wang F, Qin W, Yang X, Yuan J: Near-infrared fluorescent probes in cancer imaging and therapy: an emerging field. *Int. J. Nanomedicine* 9, 1347-1365 (2014).

25. Licha, K. & Resch-Genger, U.: Probes for optical imaging: new developments. . *Drug Discov. Today Technol.* 8, 87-94 (2011).

26. Sevick-Muraca EM: Translation of near-infrared fluorescence imaging technologies: emerging clinical applications. *Annu. Rev. Med.* 63, 217-231 (2012).

27. Escobedo JO, Rusin O, Lim S, Strongin RM: NIR dyes for bioimaging applications. *Curr. Opin. Chem. Biol.* 14(1), 64-70 (2010).

28. Luo S, Zhang E, Su Y, Cheng T, Shi C: A review of NIR dyes in cancer targeting and imaging. *Biomaterials* 32(29), 7127-7138 (2011).

29. Choi HS, Gibbs SL, Lee JH *et al.*: Targeted zwitterionic near-infrared fluorophores for improved optical imaging. *Nat. Biotechnol.* 31(2), 148-153 (2013).

30. Choi HS, Nasr K, Alyabyev S *et al.*: Synthesis and in vivo fate of zwitterionic near-infrared fluorophores. *Angew. Chem. Int. Ed Engl.* 50(28), 6258-6263 (2011).

31. Marshall MV, Draney D, Sevick-Muraca EM, Olive DM: Single-dose intravenous toxicity study of IRDye 800CW in Sprague-Dawley rats. *Mol. Imaging Biol.* 12(6), 583-594 (2010).

32. Vermeulen JF, van Brussel AS, van der Groep P *et al.*: Immunophenotyping invasive breast cancer: paving the road for molecular imaging. *BMC Cancer* 12, 240-2407-12-240 (2012).

33. van Dongen GA, Poot AJ, Vugts DJ: PET imaging with radiolabeled antibodies and tyrosine kinase inhibitors: immuno-PET and TKI-PET. *Tumour Biol.* 33(3), 607-615 (2012).

34. Gaykema SB, Brouwers AH, Lub-de Hooge MN *et al.*: 89Zr-bevacizumab PET imaging in primary breast cancer. *J. Nucl. Med.* 54(7), 1014-1018 (2013).

35. Zielinski R, Hassan M, Lyakhov I *et al.*: Affibody-DyLight conjugates for in vivo assessment of HER2 expression by near-infrared optical imaging. *PLoS One* 7(7), e41016 (2012).

36. Zdobnova TA, Stremovskiy OA, Lebedenko EN, Deyev SM: Self-assembling complexes of quantum dots and scFv antibodies for cancer cell targeting and imaging. *PLoS One* 7(10), e48248 (2012).

37. Kaur S, Venktaraman G, Jain M, Senapati S, Garg PK, Batra SK: Recent trends in antibody-based oncologic imaging. *Cancer Lett.* 315(2), 97-

111 (2012).

38. Bell A, Wang ZJ, Arbabi-Ghahroudi M *et al.*: Differential tumor-targeting abilities of three single-domain antibody formats. *Cancer Lett.* 289(1), 81-90 (2010).

39. Muyldermans S: Nanobodies: natural single-domain antibodies. *Annu. Rev. Biochem.* 82, 775-797 (2013).

40. Rahbarizadeh F, Ahmadvand D, Sharifzadeh Z: Nanobody; an old concept and new vehicle for immunotargeting. *Immunol. Invest.* 40(3), 299-338 (2011).

41. Cortez-Retamozo V, Backmann N, Senter PD *et al.*: Efficient cancer therapy with a nanobody-based conjugate. *Cancer Res.* 64(8), 2853-2857 (2004).

42. Baral TN, Magez S, Stijlemans B *et al.*: Experimental therapy of African trypanosomiasis with a nanobody-conjugated human trypanolytic factor. *Nat. Med.* 12(5), 580-584 (2006).

43. Coppieters K, Dreier T, Silence K *et al.*: Formatted anti-tumor necrosis factor alpha VHH proteins derived from camelids show superior potency and targeting to inflamed joints in a murine model of collagen-induced arthritis. *Arthritis Rheum.* 54(6), 1856-1866 (2006).

44. Vincke C, Loris R, Saerens D, Martinez-Rodriguez S, Muyldermans S, Conrath K: General strategy to humanize a camelid single-domain antibody and identification of a universal humanized nanobody scaffold. *J. Biol. Chem.* 284(5), 3273-3284 (2009).

45. Oliveira S, Heukers R, Sornkom J, Kok RJ, van Bergen En Henegouwen PM: Targeting tumors with nanobodies for cancer imaging and therapy. *J. Control. Release* 172(3), 607-617 (2013).

46. Kijanka M, Warnders FJ, El Khattabi M *et al.*: Rapid optical imaging of human breast tumour xenografts using anti-HER2 VHHs site-directly conjugated to IRDye 800CW for image-guided surgery. *Eur. J. Nucl. Med. Mol. Imaging* 40(11), 1718-1729 (2013).

47. Oliveira S, van Dongen GA, Stigter-van Walsum M *et al.*: Rapid visualization of human tumor xenografts through optical imaging with a near-infrared fluorescent anti-epidermal growth factor receptor nanobody. *Mol. Imaging* 11(1), 33-46 (2012).

48. Vaneycken I, D'huyvetter M, Hernot S *et al.*: Immuno-imaging using nanobodies. *Curr. Opin. Biotechnol.* 22(6), 877-881 (2011).

49. Figueroa-Magalhaes MC, Jelovac D, Connolly RM, Wolff AC: Treatment of HER2-positive breast cancer. *Breast* 23(2), 128-136 (2014).

50. Cho HS, Mason K, Ramyar KX *et al.*: Structure of the extracellular region of HER2 alone and in complex with the Herceptin Fab. *Nature* 421(6924), 756-760 (2003).

51. Vu T, Claret FX: Trastuzumab: updated mechanisms of action and resistance in breast cancer. *Front. Oncol.* 2, 62 (2012).

52. Wong AL, Lee SC: Mechanisms of Resistance to Trastuzumab and Novel Therapeutic Strategies in HER2-Positive Breast Cancer. *Int. J. Breast Cancer.* 2012, 415170 (2012).

53. Gajria D, Chandarlapaty S: HER2-amplified breast cancer: mechanisms of trastuzumab resistance and novel targeted therapies. *Expert Rev. Anticancer Ther.* 11(2), 263-275 (2011).

54. Arnould L, Gelly M, Penault-Llorca F *et al.*: Trastuzumab-based treatment of HER2-positive breast cancer: an antibody-dependent cellular

cytotoxicity mechanism? *Br. J. Cancer* 94(2), 259-267 (2006).

55. Klapper LN, Waterman H, Sela M, Yarden Y: Tumor-inhibitory antibodies to HER-2/ErbB-2 may act by recruiting c-Cbl and enhancing ubiquitination of HER-2. *Cancer Res.* 60(13), 3384-3388 (2000).

56. Olson E, Mullins D: When Standard Therapy Fails in Breast Cancer: Current and Future Options for HER2-Positive Disease. *J. Clin. Trials* 3, 1000129 (2013).

57. Malenfant SJ, Eckmann KR, Barnett CM: Pertuzumab: a new targeted therapy for HER2-positive metastatic breast cancer. *Pharmacotherapy* 34(1), 60-71 (2014).

58. Krop I, Winer EP: Trastuzumab emtansine: a novel antibody-drug conjugate for HER2-positive breast cancer. *Clin. Cancer Res.* 20(1), 15-20 (2014).

59. Baselga J, Perez EA, Pienkowski T, Bell R: Adjuvant trastuzumab: a milestone in the treatment of HER-2-positive early breast cancer. *Oncologist* 11 Suppl 1, 4-12 (2006).

60. Sahin O, Frohlich H, Lobke C *et al.*: Modeling ERBB receptor-regulated G1/S transition to find novel targets for de novo trastuzumab resistance. *BMC Syst. Biol.* 3, 1-0509-3-1 (2009).

Part 1

Chapter 2

Rapid optical imaging of human breast tumor xenografts using anti-HER2 VHHs site-directly conjugated to IRDye800CW for image-guided surgery

Marta M. Kijanka
Frank-Jan Warnders
Mohamed El Khattabi
Marjolijn N. Lub-de Hooge
Gooitzen M. van Dam
Vasilis Ntziachristos
Elisabeth G.E. de Vries
Sabrina Oliveira
Paul M.P. van Bergen en Henegouwen

Eur J Nucl Med Mol Imaging. 2013 Oct; 40 (11): 1718-29

Abstract

Introduction: Molecular optical imaging using monoclonal antibodies is slow providing for low tumor to back ground ratios. We used anti-HER2 VHHs conjugated to IRDye800CW to investigate their potential as probes for rapid optical molecular imaging of HER2-positive tumors by determining tumor accumulation and tumor to back ground levels.

Methods: Three anti-HER2 VHHs (11A4, 18C3, 22G12), were selected with phage display and produced in *E.coli*. Binding affinities of these probes to SKBR3 cells were determined before and after site-specific conjugation to IRDye800CW. To determine the potential of VHH-IR as imaging probes, serial optical imaging studies were carried out using human SKBR3 and human MDA-MB-231 xenograft breast cancer models. Performance of the anti-HER2 VHH-IR was compared to that of trastuzumab-IR and a non-HER2 specific VHH-IR. Image-guided surgery was performed during which SKBR3 tumor was removed under the guidance of the VHH-IR signal.

Results: Site-specific conjugation of IRDye800CW to three anti-HER2 VHHs preserved high apparent affinities of nanobodies (11A4: 1.9 ± 0.03 nM; 18C3: 14.3 ± 1.8 nM; and 22G12: 3.2 ± 0.5 nM). Based upon different criteria, such as binding, production yield and tumor accumulation, 11A4 was selected for further studies. Comparison of 11A4-IR with trastuzumab-IR showed ~20 times faster tumor accumulation of the anti-HER2 VHH, with a higher contrast between tumor and background tissue (11A4-IR: 2.5 ± 0.3, trastuzumab-IR: 1.4 ± 0.4; 4 hrs p.i.). 11A4-IR was demonstrated to be a useful tool in image-guided surgery.

Conclusion: VHH-IR led to a much faster tumor accumulation with higher tumor to background ratios as compared to trastuzumab-IR allowing the same-day imaging for clinical investigations as well as image-guided surgery.

Introduction

Breast cancer is the most frequent cancer in the European female population and 18-25% of all these cases have the HER2 gene amplified, resulting in HER2 receptors overexpression. Since HER2 is expressed only at very low levels in normal epithelial cells [1], it is considered a clinically relevant tumor marker. The human HER2 receptor is a 185 kDa transmembrane protein that, together with HER1 (EGFR), HER3 and HER4, belongs to the ErbB family of receptor tyrosine kinases. It is an auto-activated receptor, which is present on the cell membrane in an extended open conformation, enabling the continuous formation of homo- and heterodimers with other family members. As a result, signaling in tumors expressing HER2 is enhanced causing more aggressive disease, with greater likelihood of reoccurrence [2-3].

Assessment of HER2 expression is common practice for accurate diagnosis and subsequent selection of the treatment protocol for breast cancer patients. At the moment, there are two *ex vivo* tests to assess HER2 expression levels, e.g. immunohistochemistry (IHC) and fluorescence in situ hybridization (FISH). Both methods require a biopsy of the primary tumor, which does not necessarily reflect the HER2 status of the entire tumor nor in metastatic lesions, due to intra- and intertumoral heterogeneity of HER2 expression [4–7]. Conversely, non-invasive molecular imaging with PET imaging of HER2 can give information on HER2 expression levels of the entire tumor, its heterogeneity and also provide spatio-temporal information of the tumor within the breast at various stages of tumor progression [8]. Furthermore, molecular imaging can provide instant information on the response to applied treatment, e.g. trastuzumab, and possible reoccurrence of the tumor during follow-up [9–11]. Moreover, molecular imaging using optical imaging modalities allows for image-guided surgery, which can be of great help for the surgeon performing more radical tumor resections, but also for the detection of metastatic lesions in locoregional lymph nodes. Molecular imaging using a targeted tracer is usually performed with radioactive isotopes using SPECT, PET or Cerenkov luminescence imaging (CLI) [12-13]. More recently, optical imaging using non-radioactive fluorescent tracers is gaining more attention, because of recent advances in the technology (e.g. multispectral fluorescent imaging) and tracer development employed [14] and because it is more patient-friendly, lacks ionizing radiation and is cost-effective.

Advances in molecular imaging relate to novel improvements in technology simultaneously with the development of targeted probes which improve both specificity and sensitivity of imaging. This is usually done using antibodies or antibody fragments conjugated to fluorophores or isotopes. One of the disadvantages of antibodies is their long half-life in the bloodstream, which results in high background levels right after systemic administration and, consequently, in low tumor to background ratios. Moreover, conventional antibodies have a rather slow diffusion into the solid tumor, which may even prevent them from reaching and binding to the entire tumor mass [10, 11, 15]. For these

reasons more interest is now expressed in smaller tracers such as affibodies, designed ankyrin repeat proteins (DARPin's) and variable domain of the heavy chain of heavy-chain only antibodies that are found in animals from the *Camelidae*, indicated as VHH or nanobody.

VHHs are the smallest functional naturally derived antigen binding fragments of only 15 kDa. We have recently demonstrated that VHHs can be conjugated to near infrared fluorescent dyes and function as optical molecular imaging tracers [16]. Due to their small size, VHHs distribute and diffuse efficiently throughout solid tumors, and due to their high binding specificity and affinity (K_D < 10 nM) to their target antigens, high tumor uptake of VHHs has been observed. Importantly, their half-life in the blood stream is significantly shorter (1.5 hours) than full length antibodies (21 days for IgG1), allowing rapid clearance of the unbound fraction by the kidneys, leading to the visualization of tumors shortly after their administration [16–18]. Moreover, VHHs are stable and easily produced in large quantities using industrial grade and qualified bacteria, yeast or mammalian cells.

In this study we focused on selection and evaluation of anti-HER2 VHHs conjugated to the NIR fluorophore IRDye800CW (IR) as a probe for optical molecular imaging of breast cancer. *Llama glamas* were immunized with HER2-expressing MCF7 or BT474 cells and HER2-binding VHHs were selected by phage display. We demonstrate the specific and high affinity binding of these VHHs to HER2 *in vitro*. *In vivo*, visualization of human tumor xenografts was observed already 4 hrs after probe injection. This was found to be 20 times faster than the delineation of the tumors with the monoclonal antibody trastuzumab. Moreover, better contrast was obtained with the VHHs, which resulted in clear delineation and real-time imaging of the xenografts during image-guided surgery. The obtained results highlight the potential of anti HER2 VHHs as probes for optical molecular imaging of breast cancer and in particular image-guided surgery.

Materials and Methods

Cell lines

The human breast cancer cell lines SKBR3, BT474 and MDA-MB-231 were obtained from ATCC and maintained in DMEM (Gibco) with 7.5% (v/v) FBS, 100 IU/ml penicillin, 100 mg/ml streptomycin, and 2 mM L-glutamine. These cells were tested and authenticated by the provider.

Ethics statements

The animal experiments were approved by the Animal Ethical Committee board of Utrecht University (DEC#2010.III.03.038) and of the University Medical Center Groningen (DEC#6326A).

Immunization of llama and construction of VHH libraries

To induce a humoral immune response directed towards the cell surface proteins of human breast cancer cells, llamas were immunized with approximately 10^8 intact human MCF7 or BT474 cells. Each animal received four (BT474) or seven (MCF7) doses of subcutaneously administered cells. Pre-immune and immune sera were collected and tested by ELISA using HER2 ectodomain (ECD) [19]. Four days after the last immunization, blood was collected, and peripheral blood lymphocytes (PBLs) were purified by density gradient centrifugation on Ficoll-Paque™ PLUS gradients (GE Healthcare). Total RNA was extracted from these tissues and transcribed into cDNA using RT-PCR (Life Technologies). Purified cDNA was then used as template for creation of immune libraries, as described earlier [19].

Phage display selection of anti HER2 VHH fragments

To select VHHs binding human HER2 receptor, several phage display selections were performed. In our first approach, phages were panned on live BT474 cells in solution, followed by a second round on biotinylated with EZ-Link® NHS-Biotin (Thermo Scientific, Rockford, USA) HER2-ectodomain (HER2-ECD). Dynabeads® M-270 Streptavidin (Invitrogen Dynal AS, Oslo, Norway) were incubated with phages and biotinylated HER2-ECD for 1 h at RT, and after 10 washes with 0.05% Tween-20 in PBS and twice in PBS, bound phages were eluted with trypsin and used to infect *E.coli* TG1. In the second approach, anti-HER2 phages were selected on recombinant purified HER2-ECD captured on a Maxisorp plate (Nunc, Rochester, MN, USA). Coated wells were blocked with 4% milk powder in PBS for 1 h at RT. Phages preblocked with 4% milkpowder for 30 min at RT were panned for binding to immobilized HER2-ECD. After extensive washing with PBS/0.05% Tween-20, phages were eluted with trypsin (Sigma-Aldrich). In the second round, phages were panned for binding to subdomain 1 of HER2 ECD immobilized to maxisorp plate. The coding sequences of the obtained VHHs binding to the HER2 ectodomain were identified by performing sequence analysis.

Production of VHHs and conjugation of the Near-Infrared Fluorophore IRDye800CW

Anti-HER2 VHHs genes were re-cloned into expression vector pQVQ72, which enables site-directed conjugation of IRDyeCW800 (IR). Production of VHHs was induced with 0.1 mM IPTG, when DH5α bacteria reached log-phase. VHHs were purified from periplasmic fractions using HiTrap protein A HP columns (GE Healthcare). VHHs were treated with 20 mM TCEP in 50 mM Tris-HCL pH 8.5 for 15 min at RT, dialyzed with 0.4 mM EDTA in PBS and incubated with a threefold molar excess of IRDye800CW-maleimide O/N at 4^0C. After conjugation, free IR was

removed using sequentially two Zeba Spin Desalting columns (Thermo Fisher Scientific, Perbio Science Nederland B.V., Etten-Leur, Netherlands). The degree of IR conjugation was determined as described before [16]. IR-conjugated proteins were analyzed by 15% SDS-PAGE and gel permeation chromatography in a Waters Aliance system (Waters, Massachusetts) on Superdex 75 10/300GL column (GE Healthcare Europe GmbH, Munich, Germany).

Determination of apparent affinity of VHHs on HER2-ECD and SKBR3 cells

Maxisorp plates (Nunc, Rochester, MN, USA) were coated overnight at 4^0C with polyclonal rabbit anti human IgG antibody at dilution 1/500 (DakoCytomation, Glostrup, Denmark). After washing with PBS, the plate was incubated with 1 mg/ml of recombinant purified HER2 ectodomain in PBS for 2 hrs at RT, and then blocked with 4% milk powder in PBS for 1 h at RT. VHHs were added at decreasing concentrations and incubated for 2 hrs at RT on a shaker. After washing with PBS, the VHHs were detected with rabbit anti-VHH for 1 h at RT and donkey anti rabbit – HRP for 1 h at RT. To develop the reaction OPD was added, the reaction was stopped by 1M H_2SO_4 solution. For apparent affinity determination on SKBR3 cells, $2*10^4$ cells/well were seeded 1 day in advance. Cells were incubated at 4^0C for 1.5 h with a dilution series of VHHs in binding buffer (DMEM without phenol red, supplemented with 25 mM HEPES and 1% BSA, pH 7.2). After several washes cells were fixed with 4% formaldehyde (FA) for 30 min at RT and the fixative was blocked by 10 min incubation with 100 mM glycine in PBS. The detection of bound VHHs was performed as described above. In case of IR800CW conjugated VHHs, binding was determined directly after washing steps using Odyssey scanner.

Immunofluorescence

SKBR3, BT474 or MDA-MB-231cells, were grown on coverslips for 2 days. Cells were washed with CO_2-independent medium and incubated for 1.5 h at 4^0C with a 100 nM solution of VHH. Unbound VHHs were removed and cells were fixed with 4% FA. Bound VHH was detected with rabbit anti-VHH, followed by goat anti-rabbit Alexa 488 (Invitrogen, Breda, The Netherlands), and cell nuclei was stained with DAPI (Roche, Almere, The Netherlands). Images were acquired using wide field fluorescence microscopy.

In vivo studies

A detailed description of the *in vivo* studies can be found in supplementary information. Male nude BALBc mice (BALB/cOlaHSD-foxnu) were obtained from Harlan (Horst, the Netherlands). A

subcutaneous tumor was induced by inoculating $5*10^6$ of SKBR3 or MDA-MB-231 cells in Matrigel (BD Biosciences) at the right shoulder. Mice were anesthetized with isoflurane, and intravenously injected with either VHH-IR or trastuzumab-IR. *In vivo* fluorescence images were obtained with IVIS Spectrum (Caliper Life Sciences, Hopkinton, MA) and the data were analyzed using Living Image 3.2 software (Caliper Life Sciences). Regions of interest (ROI) were drawn around the tumor and in normal tissues (in the abdominal area, in such way that the signal derived from the kidneys or liver did not overlap the ROI). Values of average fluorescence radiance (photons/sec/cm^2/steradian) of these ROIs were used to calculate the tumor to background ratio (T/B). Biodistribution studies were performed as described by Oliveira et al. [16]. The location of fluorescently labeled VHH was visualized with the real-time intraoperative fluorescence imaging system (T3 platform, SurgOptix, Groningen, The Netherlands). Images were generated using a 673 nm CW laser diode (BWF2-673-0, 300 mW, B&W Tek, Newark, USA) for fluorochrome excitation. The collected image was divided into three channels: visible light towards the color camera (670 DCXXR, Chroma, Rockingham, Vermont, USA) and NIR light to the intrinsic and fluorescence channels. A band pass filter 716 ± 20 nm (Brightline HC 716/40, Semrock, USA) was used in the fluorescence channel and a laser cleanup filter was employed at the intrinsic channel (Laser Clean-up 676/10 Chroma, USA). The optical hardware was mounted on a modified arm and could extent over the operating table to gain a vertical or lateral view into the field of view. Images and videos were obtained during surgery in which HER2 positive tumors were removed under the guidance of the camera system.

Statistical analysis

Student's t-test with Mann-Whitney correction to evaluate the significance of differences between 2 groups and ANOVA to evaluate differences among 4 groups were performed using Prism 5. A p value ≤ 0.05 was considered significant.

Results

Affinity selection and characterization of anti-HER2 VHHs

To obtain anti-HER2 VHHs, llamas were immunized with either the human breast cancer cell line MCF7 (expresses a low amount of HER2) or BT474 (overexpresses HER2 due to gene amplification) [20]. The development of the immune response against HER2 was confirmed by the presence of anti-HER2 heavy chain only antibodies in serum, as evaluated on the HER2-ECD in an ELISA setup (Fig. 1A).

Two approaches were taken to select for VHHs that bind with high affinities to the human

HER2 receptor. In our first approach, phages from the MCF7 immune library were panned on live BT474 cells in solution, followed by panning on biotinylated HER2-ECD in solution. In the second approach phages from BT474 immune libraries were first selected on captured recombinant purified HER2 ectodomain, followed by panning on subdomain 1 of the HER2 ectodomain.

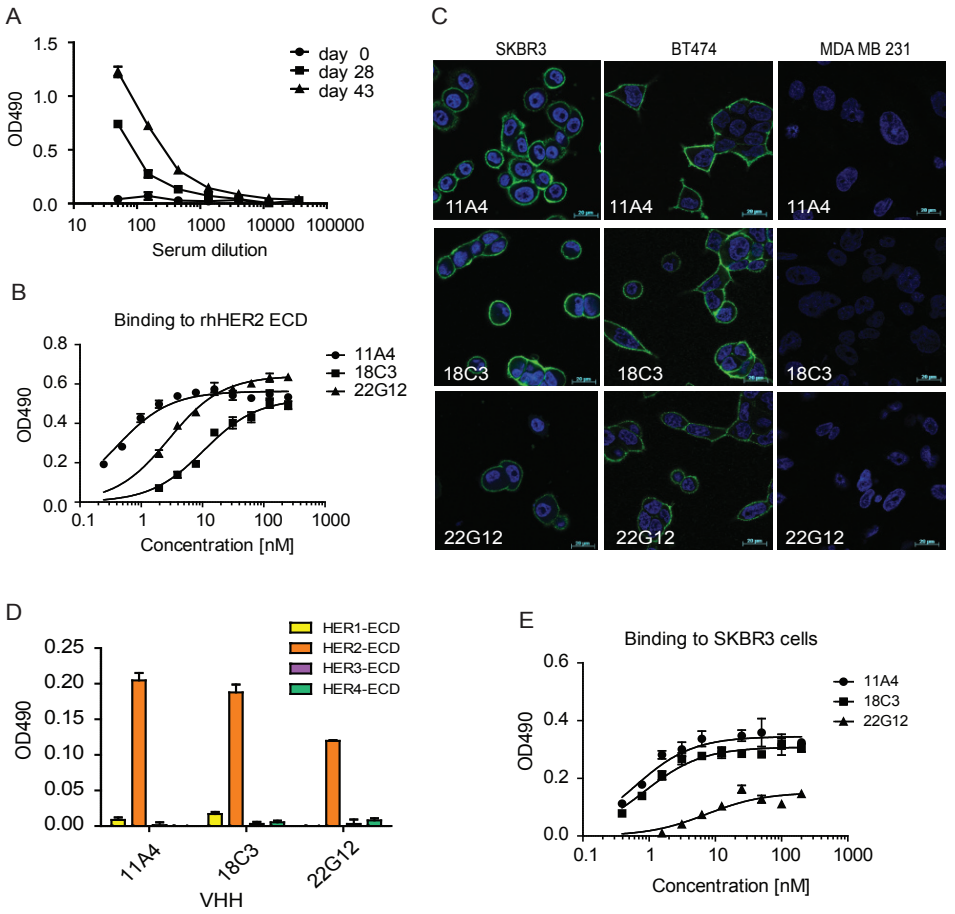

Fig. 1. Llamas heavy chain immune response against HER2. A. Immunization of *Llama glama* with HER2 overexpressing BT474 cells induces anti-HER2 humoral immune response. The reactivity of pre-immune (day 0) and immune (day 28 and 43) sera towards HER2-ECD was determined in ELISA on HER2 ECD. Results are plotted in duplicate ± SEM. B. Binding of three selected VHHs, 11A4, 18C3 and 22G12, was tested in dose response using immobilized HER2-ECD in ELISA. Bound VHHs were detected with an anti-VHH polyclonal antibody and a secondary anti-rabbit antibody coupled to HRP. The amount of bound HRP was developed using OPD and absorption at 490 nm. The graph shows absorbance (490nm) in triplicate ± SEM. C. HER2 positive (SKBR3 and BT474) or negative (MDA-MB-231) cells were incubated with the VHHs at 100 nM concentration, and imaged using confocal microscopy (scale bar = 20 μm). D. Selected anti-HER2 VHHs bind specifically to HER2-ECD. VHHs were incubated with ECDs of HER1-4. Triplicate data are expressed ± SEM. E, Binding of anti-HER2 VHHs to SKBR3 cells. Bound VHHs were detected through a primary antibody followed by an HRP-conjugated secondary antibody. The graph shows absorbance (490nm) in triplicate ± SEM with increasing concentrations of the purified VHH.

Together with 11A4, which was selected in the first approach, two other VHHs were selected for further research, namely: 18C3, obtained from the second approach, round one, and 22G12, obtained in the second round of the second approach. These three VHHs, i.e. 11A4, 18C3 and 22G12, bind specifically to HER2, as confirmed by ELISA assays on ectodomains of different ErbB receptors and immunofluorescence studies on live cells (Fig. 1B, Fig. 1SA). The highest affinity was obtained for 11A4, which was even below 1 nM (Fig. 1SA). All VHHs showed a clear membrane staining of both SKBR3 and BT474 cell lines while no labeling of the HER2 negative MDA-MB-231 cells was observed (Fig. 1C). Despite the high similarity in the amino acid sequence of the ECDs of HER1, HER2, HER3, and HER4, all three VHHs bound exclusively to the ectodomain of HER2, confirming their high specificity (Fig. 1D).

As the HER2-ECD may not mimic the receptor in its natural environment, we determined the apparent binding affinities of the selected VHHs to HER2 present on the surface of SKBR3 cells. Very high apparent affinities were obtained for VHH 11A4 and 18C3 (less than 1 nM) (Fig. 1E, Fig. 1SA). The differences in affinities of the VHHs in binding were to HER2-ECD and to cells indicate that binding of the VHHs is sensitive to HER2-ECD conformation. Moreover, the B_{max} of 22G12 was considerably lower than the B_{max} of 11A4 and 18C3, which may reflect differences in epitope access (Fig. 1S). In conclusion, employed selection strategy resulted in obtaining three VHHs that bind specifically and with high affinity to the ectodomain of the human HER2 in its natural surroundings.

Characterization of anti-HER2 VHHs conjugated to IRDye800CW

The three HER2 specific VHHs were subsequently evaluated for their potential use as probes for optical molecular imaging. In these experiments, the VHH R2, which recognizes copper-containing azo-dye RR6, was used as a negative control [16]. VHHs were randomly conjugated to the NHS-IRDye800CW (IRr) by coupling to the primary amines of the VHHs, i.e. N-terminal amino acid and lysine residues. Upon the IRr conjugation, a strong affinity drop was observed for all VHHs, especially for 11A4, which showed a 1000 fold reduction (Fig. 2, Fig 1SB). This particular case was most likely due to the presence of a lysine residue in the CDR3 region. The effect on the binding of the other two VHHs may reflect steric hindrance of the fluorophore during epitope binding. In order to avoid any effect of the fluorophore on the VHH binding capacity, all VHHs were provided with a C-terminal cystein, which was used to couple the VHH to maleimide-IRDye800CW (IR). The obtained IR conjugated VHHs are referred to as VHH-IR. The apparent affinity of the directionally coupled VHH-IR was higher than that of the randomly conjugated VHHs: 11A4-IR: 1.9 ± 0.3 nM, 18C3-IR: 14.3 ± 1.8 nM and 22G12-IR: 3.2 ± 0.5 nM (Fig. 1SB), and marginally affected when compared to the non-conjugated VHHs (Fig. 2A+B, Fig. 1SA+B). All standard quality controls

(SDS-PAGE and gel permeation chromatography) were within acceptable parameters (Fig. 2S). All VHH-IR preparations contained less than 5.5% of free IRDye800CW.

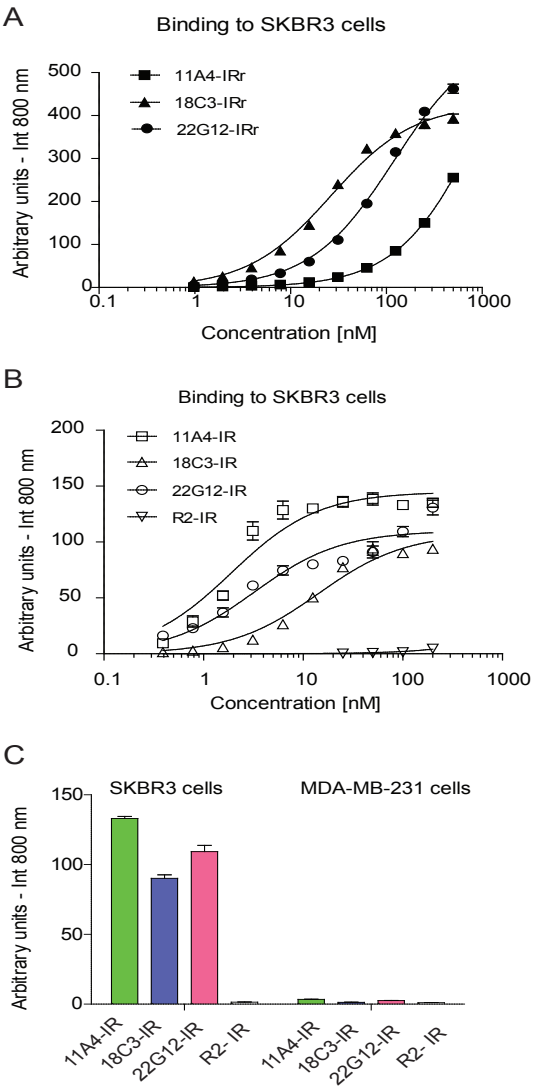

Fig. 2. High affinity of VHH can be preserved by site-directed conjugation of IRDye800CW. A. Reduced affinity after random labeling. SKBR3 cells were incubated with various concentrations of randomly labeled 11A4-IRr, 18C3-IRr and 22G12-IRr. Bound VHHs were directly detected with an Odyssey scanner. The graph shows fluorescence intensity at 800nm in triplicate ± SEM with increasing concentrations of the purified VHH. B. High affinity binding of site-directionally labeled VHHs. SKBR3 cells were incubated with various concentrations of site-directly labeled 11A4-IR, 18C3-IR, 22G12-IR and the negative control R2-IR. Bound VHHs were directly detected with an Odyssey scanner. The graph shows fluorescence intensity at 800 nm in triplicate ± SEM with increasing concentrations of the purified VHH. C. Specific binding of fluorescent VHHs to HER2. Site-directly labeled VHHs were incubated with HER2 positive SKBR3 cells and HER2 negative MDA-MB-231 cells. Bound VHHs were directly detected with an Odyssey scanner. The graph shows fluorescence intensity at 800nm in triplicate ± SEM.

HER2-targeted in vivo optical molecular imaging

To determine the potential of the IR-labeled anti-HER2 VHHs as probes for molecular optical imaging, mice bearing human tumor SKBR3 xenografts were injected with either 11A4-IR, 18C3-IR or 22G12-IR and imaged at different time points after injection (Fig 3). Already 1 h post injection (p.i.)

a clear accumulation of IR fluorescence was found at the tumor site in case of 11A4-IR and 22G12-IR. Surprisingly, no IR fluorescence was detected at the tumor area in mice injected with 18C3-IR (Fig. 3A). As expected, no IR fluorescence was detected in case of the negative control VHH R2-IR. Optimal imaging (i.e. the highest tumor uptake of the probe combined with the best contrast) was obtained at 4 hrs p.i, when the IR fluorescence of both 11A4-IR and 22G12-IR perfectly overlapped with the tumor area (Fig. 3B, red arrows).

In all animals, immediately after injection of the IR conjugated VHH, kidneys became clearly delineated (Fig. 3A+B, green arrows). The accumulation of IR fluorescence in the kidneys was expected due to low molecular weight of VHH (15 kDa).

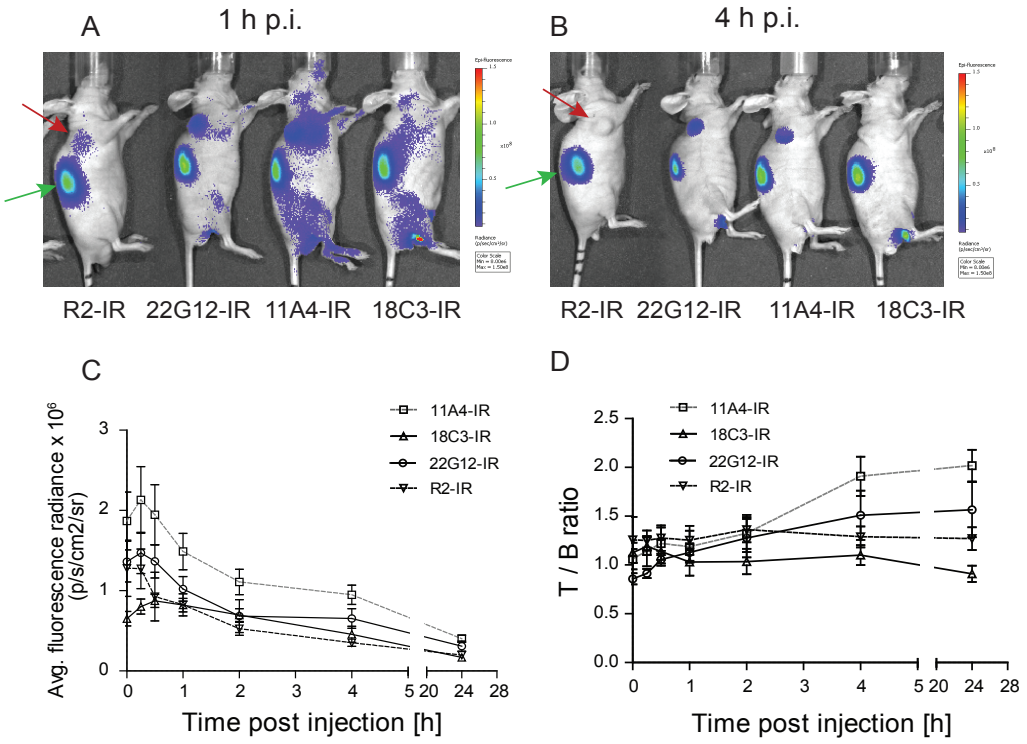

Fig. 3. *In vivo* optical molecular imaging. A. Imaging of mice 1 h p.i.. Male nude BALBc mice bearing SKBR3 human tumor xenografts at their shoulder were intravenously injected with 25 µg of site-directly labeled HER2 specific 11A4-IR, 18C3-IR or 22G12-IR and negative control VHH R2-IR, and imaged under anesthesia at 1 h p.i.. Tumors are indicated with red arrows and kidneys with green arrows. B. Images of mice at 4 hrs p.i. C. Average fluorescence radiance of tumors imaged by 11A4-IR (n=6), 18C3-IR (n=6) and 22G12-IR (n=6) and R2-IR (n=4). For all images obtained regions of interest (ROI) were drawn around the tumor areas and the corresponding values of fluorescence radiance (p/s/cm^2/sr) were plotted ± SEM. D. Tumor/background (T/B) ratio of tumors imaged with 11A4-IR (n=6), 18C3-IR (n=6) and 22G12-IR (n=6) and R2-IR (n=4). For all of the images obtained regions of interest (ROI) were drawn around the tumor areas and for normal tissue in the abdomen area and the corresponding values of fluorescence radiance (p/s/cm^2/sr) were used to calculate T/B ratios.

Fluorescence intensity was maximal shortly after injection and gradually decreased as a result of clearance of the unbound VHHs (Fig.3C). The T/B ratios of 11A4-IR and 22G12-IR increased over time, reaching after 24 hrs p.i. ratios of 2.0 ± 0.4 and 1.6 ± 0.7, respectively. The T/B ratios of approximately 1.0 in case of 18C3-IR remained constant over time, suggesting no specific accumulation of the probe at the tumor site. The same result was obtained for the negative control R2-IR, which is in agreement with the *in vitro* results (Fig. 2B), as well as our previous study [16]. Already 4 hrs p.i, the T/B ratio in animals injected with 11A4-IR was significantly higher than the T/B ratio in animals injected with control R2-IR (p=0.03). Based on both the *in vitro* data and optical molecular imaging data, 11A4-IR was selected as the most promising imaging agent among the tested VHHs. Further *in vivo* studies and biodistribution studies were carried out with this VHH-IR.

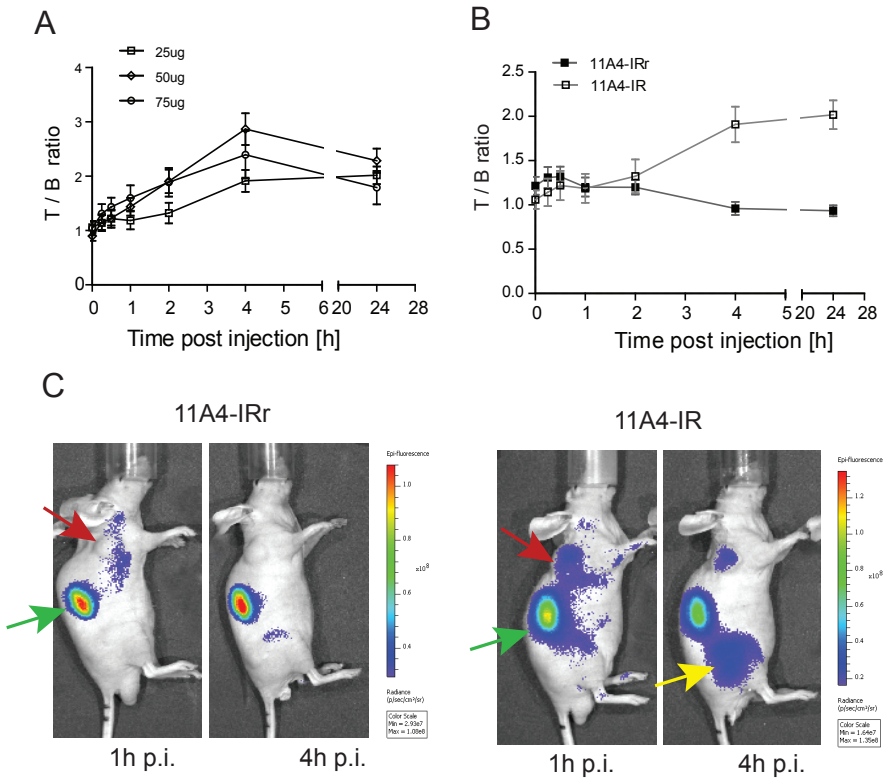

Fig. 4. High affinity of the probe is essential for successful imaging. A. Optimization of probe concentration. Male nude BALBc mice bearing SKBR3 human tumor xenografts at their shoulder were intravenously injected with 25, 50 or 75 µg of 11A4-IR and imaged under anesthesia at indicated points p.i. B. T/B ratios of randomly and or site directly labeled 11A4-IR; mice were injected with 50 µg of randomly (11A4-IRr) or site-directionally (11A4-IR) and imaged at indicated time intervals. Regions of interest (ROI) were drawn around the tumor and in normal tissue (the abdomen), and the corresponding values of fluorescence radiance were used to calculate tumor to background ratios (T/B ratio). The graph shows T/B ratio ± SEM (n=6). C. Images of mice were taken 1 h p.i. and 4 hrs p.i., tumors are indicated with red arrows and kidneys with green arrows, yellow arrow shows the bladder signal.

The initial dose of 25 μg of IR-labeled VHH was determined based on previous studies [16]. However, an increase to 50 μg turned out to be beneficial, as indicated by the higher T/B ratio obtained 4h p.i.: 1.9 ± 0.8 in the case of 25 μg compared to 2.9 ± 1.2 of 50μg ($p=0.03$) (Fig. 4A). Further increase of the dose to 75μg did not result in increased T/B ratios (T/B: 2.4 ± 1.0). On the basis of these results, 50 μg was considered as the optimal dose.

As a confirmation of our expectations, the affinity loss due to the random conjugation of the IR (Fig. 1S) would render 11A4-IRr unsuitable for optical molecular imaging. Accordingly, T/B ratios of the randomly conjugated 11A4 remained approximately 1 and no tumor delineation was observed (Fig. 4C). This clearly proved the advantage of the site-directed conjugation procedure for this particular VHH.

Comparison of HER2 targeting by 11A4-IR and trastuzumab-IR in HER2 positive and HER2 negative xenografts models

The performance of 11A4-IR as an optical imaging probe was compared to that of the conventional antibody trastuzumab. Trastuzumab was randomly conjugated to IRDye800CW and employed as previously described before [15]. HER2-binding specificity of both probes was evaluated *in vivo* using mice xenografted with either SKBR3 or MDA-MB-231 cells. Histochemical staining of the xenografts with an anti-HER2 antibody clearly evidenced the overexpression of HER2 in the SKBR3 xenograft and its absence in the MDA-MB-231 xenograft (Fig. 4S). The SKBR3 xenografts were rapidly delineated with the 11A4-IR probe; at 4 hrs p.i the xenografts were clearly visible (Fig. 5A). Remarkably, trastuzumab-IR reached a similar image and T/B ratio 72 hrs p.i. (Fig. 5B), which is a difference of approximately 20 times. Importantly, target specificity was also demonstrated *in vivo*. A clear difference in tumor accumulation between HER2 positive (SKBR3) and negative (MDA-MB-231) xenografts were observed for VHH-IR as 4 hrs p.i. the negative tumor was completely devoid of fluorescence from 11A4-IR. With trastuzumab-IR, even 72 hrs p.i. fluorescence was still present in the negative tumor. (Fig. 5A).

To determine the uptake of different probes in the tumor and in the main organs quantitatively, we analyzed the fluorescence signals in SKBR3 tumors and several organs *ex vivo* according to recently described method [21]. This method was specifically designed to determine the fluorescent signal quantitatively allowing determination of %ID/g of optical probes. Animals were sacrificed at the time points at which the best T/B ratios for 11A4-IR and trastuzumab-IR were obtained, which is 4 hrs p.i. for the VHH and 72 hrs p.i. for the mAb (Fig. 5A+B). The R2-IR VHH was included in this experiment as a negative control.

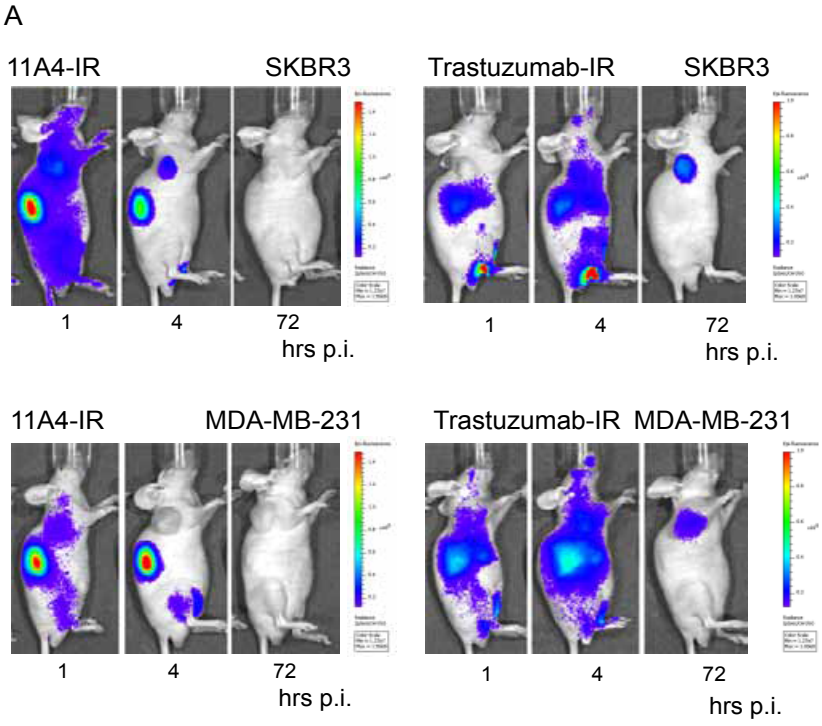
A
11A4-IR
SKBR3
Trastuzumab-IR
SKBR3
1
4
72
hrs p.i.
11A4-IR
MDA-MB-231
Trastuzumab-IR
MDA-MB-231

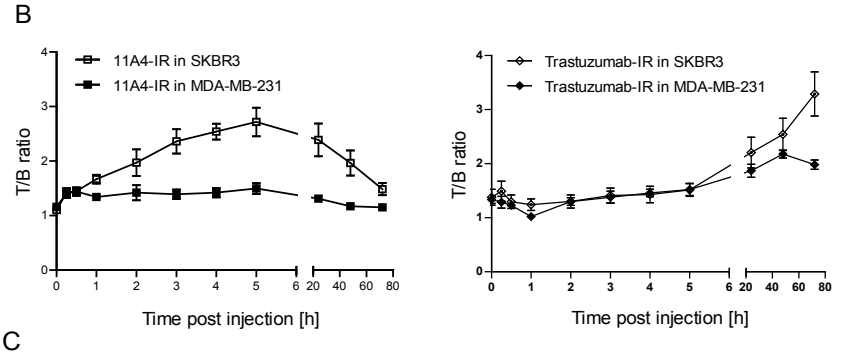
B
11A4-IR in SKBR3
11A4-IR in MDA-MB-231
T/B ratio
Time post injection [h]
Trastuzumab-IR in SKBR3
Trastuzumab-IR in MDA-MB-231

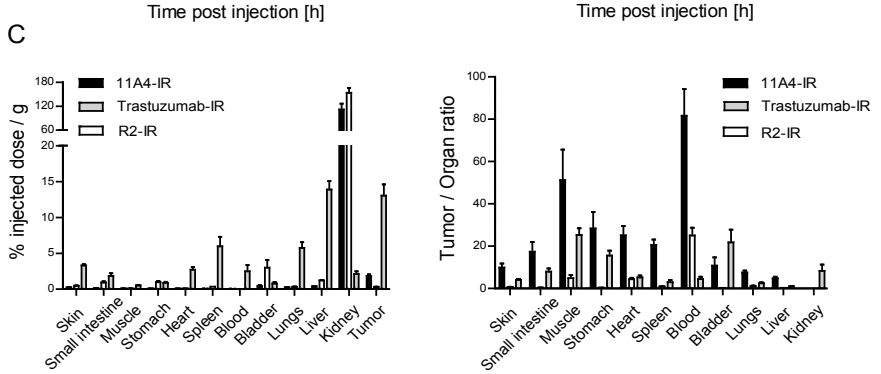
C
11A4-IR
Trastuzumab-IR
R2-IR
% injected dose / g
Tumor / Organ ratio
Skin
Small intestine
Muscle
Stomach
Heart
Spleen
Blood
Bladder
Lungs
Liver
Kidney
Tumor

Fig. 5. Comparison of optical imaging using site-directly labeled 11A4-IR and randomly labeled trastuzumab-IR. A. Tumor imaging. Representative pictures of male nude BALBc mice bearing HER2 positive SKBR3 human tumor xenografts (upper panel) and HER2 negative MDA-MB-231 human tumor xenografts (lower panel) at shoulders intravenously injected with 50 μg of site-directly labeled 11A4-IR or 100 μg randomly labeled trastuzumab-IR, imaged under anesthesia at different time points post injection (p.i). B. Tumor/Background ratio. T/B ratios were determined as described in legend to figure 4, for both11A4 and trastuzumab in HER2 positive (SKBR3) and negative (MDA-MB-231) tumors. C. Biodistribution study. At 4 hrs p.i. mice injected intravenously with 11A4-IR and at 72 hrs p.i. mice injected with trastuzumab-IR were sacrificed and their tumors and organs were collected for quantification of IR-conjugated proteins. Values are presented as percentage of injected dose per gram tissue/tumor ± SEM (n=5 for trastuzumab-IR and R2-IR group, n=7 for 11A4-IR group (left panel). From the values obtained for tumors and organs or tissues, ratios of tumor to organs were calculated and plotted ± SEM (n=5 for trastuzumab-IR and R2-IR group, n=7 for 11A4-IR group (right panel).

The data clearly shows that the biodistribution of the VHHs and trastuzumab differ significantly and are in agreement with previous studies [15-16] (Fig. 4S, 5C). In case of mice injected with VHH-IR (both 11A4-IR and R2-IR), a high percentage of injected dose was detected in kidneys, while in case of mice injected with trastuzumab-IR the largest percentage %ID/g was found in the liver (Fig. 5C).

Interestingly, 4 hrs p.i. only very low levels of VHH-IR were present in the blood. In contrast, at 72 hrs p.i. trastuzumab-IR was still detected in the blood pool (2.7 % ID/g) and in highly perfused organs, such as spleen and lungs, while VHH-IR levels were low in these organs. Importantly, tumor uptake of injected probes differed significantly: 1.8 ± 0.2 % ID/g of 11A4-IR was found at the tumor site 4 hrs p.i. and 13 ± 1.6 % ID/g of trastuzumab-IR 72 hrs p.i. As expected from the imaging data the negative control, R2-IR, did not accumulate at the tumor. The amount of R2-IR probe found at the tumor was similar to the amount present in the skin or lungs (about 0.3 % ID/g). The quantification of the IR-conjugated probes in the tumors and organs was used to determine the tumor to organ tissue ratios. Interestingly, in almost all cases the tumor-to-organ ratios were higher for 11A4-IR (except for bladder). A tumor-to-blood ratio of 11A4-IR was calculated to be ~82, whereas for trastuzumab-IR it was hardly 4.5, indicating that even though 11A4-IR accumulates at the tumor to a lower extent than trastuzumab-IR, a much better contrast was obtained. In conclusion, 11A4-IR outperformed trastuzumab-IR in respect to overall T/B ratios and time at which clear imaging of tumors was possible.

Image-guided surgery

With the results described above, 11A4-IR probe seemed to be suitable for complementary approaches, where good contrast between tumor and background tissues is essential, such as in surgical resection of a HER2 positive xenograft from a mouse, when guided by the fluorescence of the probe specifically accumulated at the tumor. Assisted by a clinical near-infrared multispectral fluorescence camera system, 11A4-IR probe accumulation in the tumor guided the surgical removal of a HER2 positive xenograft [15]. Both tumor and kidney were clearly visible through the skin, as

depicted by the fluorescence and overlaid images (Fig. 6).

The SKBR3 tumor was removed under the guidance of the real-time fluorescent images obtained by the camera system. In conclusion, contrast provided by the 11A4-IR probe was sufficient to allow the successful removal of the tumor by fluorescence image-guided surgery.

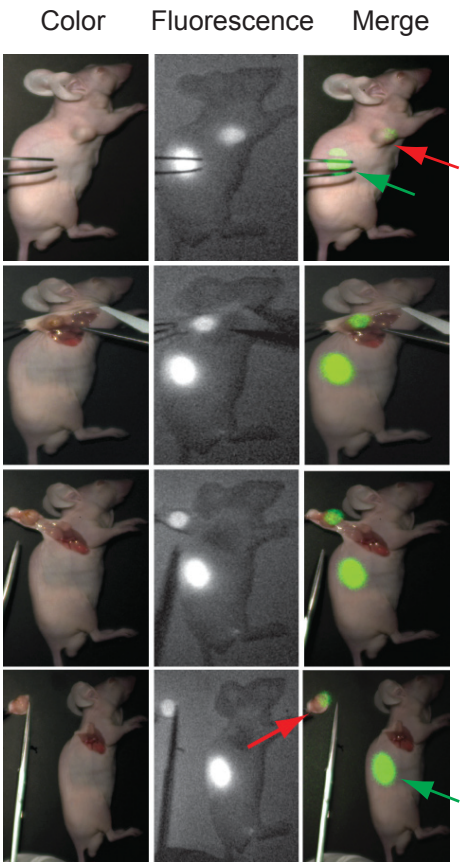

Fig. 6. NIR fluorescence image-guided surgery. Representative intraoperative images of SKBR3 tumor removal after intravenous injection of 50 μg 11A4-IR 4 hrs p.i.. Red arrows show the tumor, green arrows show the kidneys.

Discussion

Optical molecular imaging is an important and rapidly developing technology, which in due time could have a great impact on clinical management of various cancer patients with solid tumors. In this study, we preclinically evaluated three fluorescent VHHs as potential molecular optical imaging probes suitable for clinical translation. Important criteria for optical probes are rapid accumulation into the tumor resulting in high tumor to background ratio. This enables a clear visualization and delineation of the tumor. High contrast depends on two parameters: specific binding leading to accumulation of the probe in the tumor next to clearance of the unbound probe from surrounding

tissues and bloodstream, which decreases the background levels. Both parameters depend heavily on the molecular weight of the probe: a small probe of 15 kDa is expected to penetrate the tumor more rapidly than a conventional antibody with a molecular weight of 150 kDa. At the same time, clearance from the body of such small probes by the kidneys will be fast (molecular weight of VHH is below glomerular filtration threshold of 60 kDa), leading to short circulation and thus targeting times.

Therefore, probes like VHHs, require high affinities in order to accumulate sufficiently into the tumor [22]. Despite the small size of the VHH, these antibody fragments bind with high affinities to their target proteins [16, 23]. Selections performed in this study were specifically aimed at high affinity binders to HER2. The final lead compound 11A4 showed a binding affinity for HER2 on SKBR3 cells of < 2 nM. This VHH highlighted the tumor already 1 h p.i.. VHH 18C3-IR, which has a significantly lower affinity (13 nM), as compared to 11A4-IR and 22G12-IR, did not accumulate at the tumor at all. This observation may entirely depend on the low affinity of 18C3-IR, which is in good agreement with predictions made on basis of the Schmidt and Wittrup model [22].

A serious problem with the small-size VHH is the possible effect of the conjugation of the ~1 kDa fluorophore on binding affinity. Random conjugation, which involves fluorophore attachment to the primary amine groups, was reported previously by Oliveira et al. not to have detrimental effect on the affinity of anti-EGFR VHH [16]. However, there is a real chance of inactivation of VHHs displaying lysine residues in the CDR regions, which are involved in binding to the antigen, after conjugation to the fluorophore. The affinity of the anti-HER2 VHH 11A4 was strongly affected by the conjugation to NHS-IR, resulting in the inability to image the tumor (Fig 4.). To avoid affinity loss, site-directed conjugation using a maleimide group on the fluorophore reacting with a thiol group from an additional C-terminal cysteine was used. VHHs that were conjugated to maleimide-IRDye800CW showed a minor effect on the binding affinity. Nevertheless, the affinities of maleimide IR labeled VHHs tested *in vitro* on SKBR3 cells remained in the low nanomolar range. The efficiency of the coupling of maleimide to thiol was reproducibly 50%-70%, depending on the VHH. This is in agreement with studies from Mume et al. and Lee et al. who reported conjugation efficiency between 60% and 80% [24-25].

To the best of our knowledge, this is a first study in which a direct comparison is made between an anti-HER2 VHH-IR and the conventional anti-HER2 antibody, trastuzumab-IR. As could be expected due to the difference in molecular size, and based on our previous study [16], trastuzumab-IR required more time to accumulate at the tumor site. 11A4-IR allows clear visualization of the tumor already 4 hrs p.i., obtaining a similar T/B ratio as found with trastuzumab-IR after 72 hrs. 11A4-IR accumulated only in HER2 positive tumors, whereas trastuzumab-IR was also found in HER2 negative tumors. This non-specific accumulation can be explained by an enhanced permeability and retention effect (EPR) described earlier for conventional antibodies [26].

The biodistribution study was performed at the time point at which the highest T/B ratios were obtained based upon fluorescence images. The amount of 11A4-IR in the HER2 positive tumors 4 hrs p.i. was 6-fold higher than the amount of the negative control VHH R2-IR. Similar ratios between target receptor-specific and non-specific VHH-IR were observed by Oliveira et al. [16]. The amount of trastuzumab-IR 72 hrs p.i. was in agreement with the data reported in previous studies [27]. The %ID/g of 11A4-IR at the tumor was significantly lower than in case of trastuzumab-IR. Vaneycken et al. reported slightly higher %ID/g at the tumor of the ^{99m}Tc-VHH, with values ranging from 0.78 to 4.44% ID/g. This difference may be a result of different VHH, tumor xenograft model used (SKOV-3 instead of SKBR3), conjugation chemistry and time p.i (1.5 hrs instead of 4 hrs) [23]. Biodistribution studies showed that the tumor to blood ratios are much better for 11A4-IR, which is in agreement with the T/B ratios obtained from the fluorescence images. For imaging, the contrast between tumor and healthy tissue is more important than the absolute amount of probe that reaches the tumor. We therefore conclude that in imaging at early time points (< 5 hrs) the VHH-based probes outperform the conventional antibody-based ones. The application of this novel optical probe for molecular imaging was clearly demonstrated in image-guided surgery. For this technology, especially the rapid accumulation into the tumor and high T/B ratios are important. Using VHH as imaging tool, the probe would be administered intravenously to the patient a few hours prior to initiating surgery. This would ameliorate some of the aspects of using antibody injections 3 days prior to surgery from a logistical standpoint.

In contrast to the antibody-based probe, the anti-HER2 VHH was present to a high degree in the kidneys obviously due to its renal clearance. This may be of concern when the VHH is used for radioactive imaging modalities such as SPECT or PET. It has been suggested that retention of the probe in the kidneys is enhanced by the presence of a positively charged HIS-tag [28]. In this study, VHHs were used devoid of the HIS-tag, nevertheless biodistribution of 11A4-IR revealed that ~120% ID/g was present in the kidney. As described by Gainkam et al., renal retention of anti-HER2 VHH, ^{99m}Tc-7C12, was reduced by 45% upon co-injection of the probe with gelofusin and lysine, while the tumor uptake was increased [29]. It would be interesting to determine whether co-injection of 11A4-IR with gelofusin and/or lysine would result in lower renal retention and higher tumor uptake leading to even higher T/B ratios. High accumulation of probe in the kidneys may not be critical when imaging is not focused on kidneys or tissues in their proximity.

In conclusion, three high affinity anti HER2 VHHs were selected from a phage display library and coupled to maleimide-IRDye800CW. They were evaluated *in vitro* and *in vivo* and proved to be a valuable tool for the optical molecular imaging of HER2 positive breast cancer. When successfully translated into the clinic by executing animal toxicity studies according to FDA/EMA guidelines, followed by a phase I-III study according to GCP-guidelines for each specific oncological indication, this could render more precise and specific identification and classification of HER2-

positive tumors non-invasively, allow assessment of response to HER2 therapies in a patient-friendly and patient-tailored manner, and assist surgeons performing more radical tumor resections with improved cosmesis, thereby improving the management and welfare of breast cancer patients.

Supplementary information

Methods

Detailed description of in vivo studies set up

The goal of the first part of this experiment was to determine the lead compound from the 3 tested VHH-IR, namely 11A4-IR, 18C3-IR or 22G12-IR. 25 μg of tested VHH-IR was injected via the penile vein into mice inoculated with SKBR3 cells (for 11A4-IR, 18C3-IR and 22G12-IR n=6, for R2-IR n=4, dose was based on previous study [16]). Animals were then imaged immediately after injection, 15 min p.i., 30 min p.i., 1 h p.i., 2 hrs p.i., 4 hrs p.i. and 24 hrs p.i. Based on *in vivo* and *in vitro* data 11A4-IR was chosen as a lead compound. This VHH exclusively was then further evaluated *in vivo*. To compare *in vivo* performance of 11A4 conjugated with IRDye800CW site-specifically (11A4-IR) with 11A4 conjugated to the dye randomly (11A4-IRr), mice bearing SKBR3 tumors were injected intravenously with 25 μg 11A4-IRr (n=6) and imaged as described above. Results obtained for these animals were compared with results obtained in part one of the *in vivo* study for animals injected with 25 μg 11A4-IR.

In the second part of *in vivo* study the optimal dose of lead compound was determined. Mice bearing SKBR3 tumors were injected via penile vein with 25 μg (n=6), 50 μg (n=6) or 75 μg (n=5) of 11A4-IR and imaged at the same time points p.i. as in first part of *in vivo* study.

The goal of the third part was to compare performance of 11A4-IR as an optical imaging probe with trastuzumab-IR both in HER2 positive and HER2 negative tumor models. For this purpose mice inoculated with either HER2 positive cells (SKBR3) or HER2 negative cells (MDA-MB-231) were injected via penile vein with either 50 μg of 11A4-IR (n=6, based on results from second part of this *in vivo* study) or 100 μg trastuzumab-IR (n=6, dose of monoclonal antibody was based on previous study [15]). Animals were imaged immediately after injection, 15 min p.i., 30 min p.i., 1 h p.i., 2 hrs p.i., 3 hrs p.i., 4 hrs p.i., 5 hrs p.i., 24 hrs p.i., 48 hrs p.i. and 72 hrs p.i..

Biodistribution study was performed as described earlier [16, 21]. Briefly, mice bearing SKBR3 tumors were injected via penile vein with 50 μg 11A4-IR (n=7), 50 μg R2-IR (n=5) or 100 μg trastuzumab-IR (n=5). Mice were sacrificed by heart puncture under anaesthesia. Animals injected with VHH-IR were sacrificed 4 hrs p.i., whereas animals injected with trastuzumab-IR 72 hrs p.i.. Organs were then collected; their weight was determined and they were snap frozen until further

analysis.

To determine fluorescence signals quantitatively according to the method of Oliveira et al. [21], organs/tissues and tumors were lysed with a Tissue Lyser II system (Qiagen, Venlo, The Netherlands) using pre-cooled Eppendorf holders, 5-mm stainless steel beads, and RIPA buffer (50 mM Tris–HCl pH 7.4, 150 mM NaCl, 1 mM EDTA, 1% Triton X-100, 0.1% SDS) supplemented with a complete EDTA-free mini tablet protease inhibitor cocktail (Roche Applied Science, Penzberg, Germany). For detection of the fluorescence present in the lysates, a series of 1:2 step dilutions of homogenates were prepared in 96-well plates using RIPA buffer to determine the range in which fluorescence signal is linearly dependent on IR-probe concentration. As a reference, a dilution series of the injected probe was prepared in the same way. The intensity of the IR fluorescence was detected by an Odyssey scanner at 800 nm. Using GraphPad Prism 5 programme (GraphPad Software Inc., La Jolla, California, USA), the concentration of IR probes detected in homogenates of organs/tissues or tumors was extrapolated from the calibration curves made with the reference probe. Knowing the concentration of IR probe in the homogenate as well as the homogenates' volume and weight of collected organs and tumors prior to homogenization the percentage of injected dose per gram of tissue (%ID/g) were calculated.

To prove the imaging potential of VHH-IR in an intraoperative setting mice bearing SKBR3 tumors (n=2) were injected intravenously with 50 μg of 11A4-IR. 4 hrs p.i. the fluorescent signal of the probe was used to guide the tumor resection. Organs of these mice were then removed and included in the biodistribution study.

Results

A

Probe	Rh HER2 ECD		SKBR3	
	Affinity (nM)	B_{max}	Affinity (nM)	B_{max}
11A4	0.40 ± 0.04	0.56 ± 0.01	0.50 ± 0.09	0.38 ± 0.01
18C3	10.5 ± 1.25	0.52 ± 0.01	0.50 ± 0.10	0.34 ± 0.01
22G12	2.80 ± 0.23	0.64 ± 0.01	6.9 ± 1.54	0.18 ± 0.01

B

Probe	Random conjugation		Site-directed conjugation	
	Affinity (nM)	B_{max}	Affinity (nM)	B_{max}
11A4	1030 ± 69.4	780.2 ± 38.5	1.9 ± 0.3	144.9 ± 4.4
18C3	26.3 ± 1.5	426.6 ± 6.4	14.3 ± 1.8	107.8 ± 3.8
22G12	119.3 ± 5.4	587.4 ± 10.1	3.2 ± 0.5	110.1 ± 4.0

Fig.1S. Apparent affinities of anti-HER2 VHHs. A. HER2-ECD or attached SKBR3 cells were incubated with increasing concentrations of indicated anti-HER2 VHHs. Apparent affinity (K_D) and maximal binding (Bmax) was determined as described in Materials and Methods. B. Apparent affinity determination upon dye conjugation determined using SKBR3 cells.

A

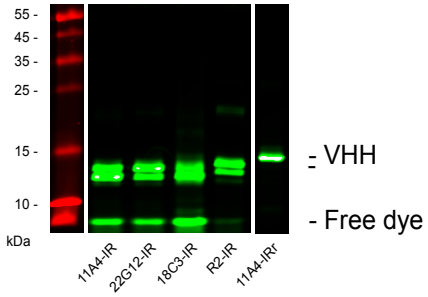

B

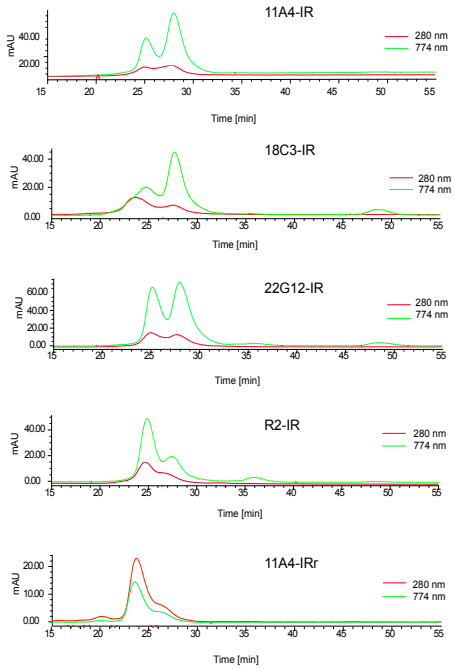

C

Probe	Retention time (min)	Area protein	Area free dye	% free dye	IR/Protein
11A4-IR	25.1	2548385	0	0	0.7
18C3-IR	23.6	9516216	540056	5.4	0.6
22G12-IR	25.1	18588121	539387	2.8	0.7
R2-IR	24.7	3249873	0	0	0.5
11A4-IRr	23.7	236224268	0	0	0.9

Fig.2S. VHH-IR characterization. A. SDS-PAGE of IR-conjugated proteins. Samples of purified IR-conjugated proteins were size separated by SDS-PAGE and imaged using an Odyssey: green corresponds to the IR signal, and in red the molecular weight marker. For each protein 2 bands were found, of which the high molecular weight protein corresponds with the expected size of the IR conjugated VHHs (13 kDa). The second band with a lower molecular weight protein was due to the loss of the epitope tag during the production procedure (except for 11A4-IRr). As this modification did not affect the binding properties of the probe, we decided to continue with these proteins. B. Gel Permeation Chromatography of IR-conjugated proteins. Samples of site-specifically labeled 11A4-IR, 18C3-IR, 22G12-IR and R2-IR, and randomly labeled 11A4-IRr were analyzed by gel permeation chromatography, absorbance was recorded at 280 nm (protein) and 774 nm (IR) wavelength. Overlap of retention times was observed of peaks detected at 280nm and 774nm, which confirms the conjugation of IR to the protein. C. IR/Protein ratios of IR-conjugated proteins. Quantitative assessment of the peaks shown in B, IR/Protein ratios have been determined as described in Materials and Methods.

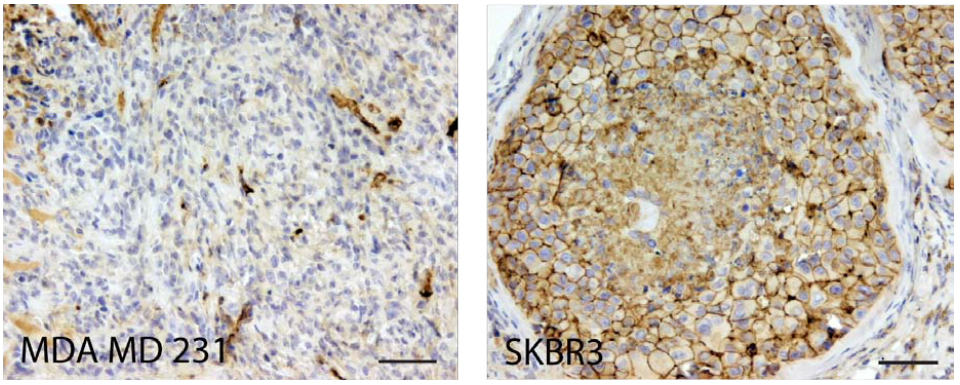

Fig.3S. Immunohistochemical staining of HER2 receptor in MDA-MB-231 and SKBR3 tumor sections. Xenografts were removed from mice, fixed and processes for immunohistochemistry as described in Materials and Methods. Note the absence of staining in the HER2 negative xenografts consisting of MDA-MB-231 cells and the clear staining of SKBR3 cells.

A

Organ	Herceptin-IR		11A4-IR		R2-IR	
	Average	SD	Average	SD	Average	SD
Skin	3.31	0.33	0.24	0.17	0.46	0.11
Colon	0.69	0.34	0.14	0.073	0.29	0.10
Small intestine	1.84	0.83	0.12	0.04	0.93	0.34
Muscle	0.52	0.08	0.07	0.08	0.09	0.05
Stomach	0.88	0.28	0.08	0.03	0.97	0.37
Heart	2.69	0.80	0.07	0.02	0.07	0.008
Bone	1.54	1.07	ND	ND	0.02	0.05
Tumor	13.04	3.51	1.84	0.55	0.31	0.09
Brain	0.38	0.22	ND	ND	ND	ND
Spleen	5.98	2.93	0.09	0.01	0.34	0.01
Pancreas	1.32	0.61	0.06	0.04	0.10	0.06
Blood	2.47	1.96	0.02	0.006	0.01	0.004
Bladder	0.78	0.49	0.41	0.41	2.98	2.44
Lungs	5.76	1.72	0.25	0.07	0.31	0.11
Liver	13.87	2.64	0.40	0.07	1.21	0.19
Kidney	2.11	0.85	111.75	38.65	153.47	26.65

B

Tumor / Organ	Herceptin-IR		11A4-IR		R2-IR	
	Average	SD	Average	SD	Average	SD
Skin	4.00	1.25	9.90	4.97	0.69	0.19
Small intestine	7.97	3.40	17.36	12.25	0.37	0.20
Muscle	25.32	7.03	51.21	38.21	4.90	3.30
Stomach	15.52	5.25	28.33	20.58	0.34	0.14
Heart	5.18	2.01	25.13	11.72	4.38	1.46
Spleen	2.94	2.20	20.52	6.82	0.92	0.28
Blood	4.47	2.18	81.64	33.13	25.03	8.17
Bladder	21.76	13.48	10.79	10.26	0.20	0.16
Lungs	2.45	1.02	7.58	2.30	1.09	0.58
Liver	0.98	0.41	4.78	1.93	0.26	0.06
Kidney	8.27	6.67	0.02	0.02	0.002	0.0005

Fig.4S. Biodistribution study of IR-conjugated proteins. A. Table shows percentage of injected dose per gram of organ or tumor ± SEM (%ID/g)(n=5 for trastuzumab-IR and R2-IR group, n=7 for 11A4-IR group). B. Table below shows tumor to organ ratios (n=5 for trastuzumab-IR and R2-IR group, n=7 for 11A4-IR group).

Acknowledgements

We would like to thank Mies Steenbergen, Anton Terwisscha van Scheltinga and Titia Lamberts for technical support. We thank prof. dr. Paul van Diest and prof. dr. Willem Mali for interesting discussions. We thank QVQ BV for providing pQVQ72 vector.

This research was supported by the Center for Translational Molecular Medicine (MAMMOTH project).

References

1. Capala J, Bouchelouche K: Molecular imaging of HER2-positive breast cancer: a step toward an individualized 'image and treat' strategy. *Curr. Opin. Oncol.* 22(6), 559-566 (2010).

2. Ross JS, Fletcher JA: The HER-2/neu oncogene in breast cancer: prognostic factor, predictive factor, and target for therapy. *Stem Cells* 16(6), 413-428 (1998).

3. Andreopoulou E, Hortobagyi GN: Prognostic factors in metastatic breast cancer: successes and challenges toward individualized therapy. *J. Clin. Oncol.* 26(22), 3660-3662 (2008).

4. Allison M: The HER2 testing conundrum. *Nat. Biotechnol.* 28(2), 117-119 (2010).

5. Moelans CB, de Weger RA, Van der Wall E, van Diest PJ: Current technologies for HER2 testing in breast cancer. *Crit. Rev. Oncol. Hematol.* 80(3), 380-392 (2011).

6. Cottu PH, Asselah J, Lae M *et al.*: Intratumoral heterogeneity of HER2/neu expression and its consequences for the management of advanced breast cancer. *Ann. Oncol.* 19(3), 595-597 (2008).

7. Wu JM, Halushka MK, Argani P: Intratumoral heterogeneity of HER-2 gene amplification and protein overexpression in breast cancer. *Hum. Pathol.* 41(6), 914-917 (2010).

8. Lindstrom LS, Karlsson E, Wilking UM *et al.*: Clinically used breast cancer markers such as estrogen receptor, progesterone receptor, and human epidermal growth factor receptor 2 are unstable throughout tumor progression. *J. Clin. Oncol.* 30(21), 2601-2608 (2012).

9. Sevick-Muraca EM: Translation of near-infrared fluorescence imaging technologies: emerging clinical applications. *Annu. Rev. Med.* 63, 217-231 (2012).

10. Kovar JL, Simpson MA, Schutz-Geschwender A, Olive DM: A systematic approach to the development of fluorescent contrast agents for optical imaging of mouse cancer models. *Anal. Biochem.* 367(1), 1-12 (2007).

11. Massoud TF, Gambhir SS: Molecular imaging in living subjects: seeing fundamental biological processes in a new light. *Genes Dev.* 17(5), 545-580 (2003).

12. Baum RP, Prasad V, Muller D *et al.*: Molecular imaging of HER2-expressing malignant tumors in breast cancer patients using synthetic 111In- or 68Ga-labeled affibody molecules. *J. Nucl. Med.* 51(6), 892-897 (2010).

13. Holland JP, Normand G, Ruggiero A, Lewis JS, Grimm J: Intraoperative imaging of positron emission tomographic radiotracers using Cerenkov luminescence emissions. *Mol. Imaging* 10(3), 177-86, 1-3 (2011).

14. van Dam GM, Themelis G, Crane LM *et al.*: Intraoperative tumor-specific fluorescence imaging in ovarian cancer by folate receptor-alpha targeting: first in-human results. *Nat. Med.* 17(10), 1315-1319 (2011).

15. Terwisscha van Scheltinga AG, van Dam GM, Nagengast WB *et al.*: Intraoperative near-infrared fluorescence tumor imaging with vascular endothelial growth factor and human epidermal growth factor receptor 2 targeting antibodies. *J. Nucl. Med.* 52(11), 1778-1785

(2011).

16. Oliveira S, van Dongen GA, Stigter-van Walsum M *et al.*: Rapid visualization of human tumor xenografts through optical imaging with a near-infrared fluorescent anti-epidermal growth factor receptor nanobody. *Mol. Imaging* 11(1), 33-46 (2012).

17. Huang L, Gainkam LO, Caveliers V *et al.*: SPECT imaging with 99mTc-labeled EGFR-specific nanobody for in vivo monitoring of EGFR expression. *Mol. Imaging Biol.* 10(3), 167-175 (2008).

18. Mould DR, Sweeney KR: The pharmacokinetics and pharmacodynamics of monoclonal antibodies--mechanistic modeling applied to drug development. *Curr. Opin. Drug Discov. Devel.* 10(1), 84-96 (2007).

19. Roovers RC, Laeremans T, Huang L *et al.*: Efficient inhibition of EGFR signaling and of tumour growth by antagonistic anti-EFGR Nanobodies. *Cancer Immunol. Immunother.* 56(3), 303-317 (2007).

20. Belsches-Jablonski AP, Biscardi JS, Peavy DR, Tice DA, Romney DA, Parsons SJ: Src family kinases and HER2 interactions in human breast cancer cell growth and survival. *Oncogene* 20(12), 1465-1475 (2001).

21. Oliveira S, Cohen R, Walsum MS *et al.*: A novel method to quantify IRDye800CW fluorescent antibody probes ex vivo in tissue distribution studies. *EJNMMI Res.* 2(1), 50-219X-2-50 (2012).

22. Schmidt MM, Wittrup KD: A modeling analysis of the effects of molecular size and binding affinity on tumor targeting. *Mol. Cancer. Ther.* 8(10), 2861-2871 (2009).

23. Vaneycken I, Devoogdt N, Van Gassen N *et al.*: Preclinical screening of anti-HER2 nanobodies for molecular imaging of breast cancer. *FASEB J.* 25(7), 2433-2446 (2011).

24. Mume E, Orlova A, Larsson B *et al.*: Evaluation of ((4-hydroxyphenyl)ethyl) maleimide for site-specific radiobromination of anti-HER2 affibody. *Bioconjug. Chem.* 16(6), 1547-1555 (2005).

25. Lee SB, Hassan M, Fisher R *et al.*: Affibody molecules for in vivo characterization of HER2-positive tumors by near-infrared imaging. *Clin. Cancer Res.* 14(12), 3840-3849 (2008).

26. Lammers T, Kiessling F, Hennink WE, Storm G: Drug targeting to tumors: principles, pitfalls and (pre-) clinical progress. *J. Control. Release* 161(2), 175-187 (2012).

27. Abbas N, Bruland OS, Brevik EM, Dahle J: Preclinical evaluation of 227Th-labeled and 177Lu-labeled trastuzumab in mice with HER-2-positive ovarian cancer xenografts. *Nucl. Med. Commun.* 33(8), 838-847 (2012).

28. Behr TM, Goldenberg DM, Becker W: Reducing the renal uptake of radiolabeled antibody fragments and peptides for diagnosis and therapy: present status, future prospects and limitations. *Eur. J. Nucl. Med.* 25(2), 201-212 (1998).

29. Gainkam LO, Caveliers V, Devoogdt N *et al.*: Localization, mechanism and reduction of renal retention of technetium-99m labeled epidermal growth factor receptor-specific nanobody in mice. *Contrast Media Mol. Imaging* 6(2), 85-92 (2011).

Chapter 3

Dual-probe optical imaging of breast cancer with a combination of VHHs targeting CAIX and HER2

Marta M. Kijanka [*]
Aram S.A. van Brussel [*]
Elsken van der Wall
Willem P.T.M. Mali
Paul J. van Diest
Paul M.P. van Bergen en Henegouwen
Sabrina Oliveira

[*]*equal contribution*

Submitted

Abstract

Introduction: Optical molecular imaging is an emerging novel technology with applications in diagnosis of breast cancer and assistance in image-guided surgery. A high tumor-to-background (T/B) ratio is crucial for successful imaging, which strongly depends on tumor-specific probes that rapidly accumulate in the tumor, while non-bound probes are rapidly cleared. We have investigated whether the use of combinations of probes with different target specificities allows dual spectral imaging resulting in higher T/B ratios and improved tumor analysis.

Methods: In this feasibility study we performed optical molecular imaging using an orthotopic breast cancer model mimicking ductal carcinoma *in situ*. A combination of CAIX- and HER2-specific VHHs was conjugated either to the same fluorophore to evaluate T/B ratios or to different fluorophores to analyze the expression of CAIX and HER2 simultaneously through dual-fluorescence detection. These experiments were performed non-invasively *in vivo*, in an intraoperative setting, and *ex vivo* on tumor sections and immunohistochemistry (IHC). For these purposes VHHs were conjugated to IRDye800CW, IRDye680RD or IRDye700DX.

Results: Application of the CAIX- and HER2- specific VHH combination resulted in an increase of the T/B ratio as compared to T/B ratios obtained from each of these single VHHs together with an irrelevant VHH. Injection of the dual tumor marker specific VHH combination enabled detection of small metastases in the lung. Furthermore, dual spectral imaging enabled the assessment of the expression status of both CAIX and HER2 *in vivo* in an intraoperative setting, as well as on tumor sections, as confirmed by IHC.

Conclusion: Dual-probe optical molecular imaging with the combination of two tumor specific VHHs improved T/B ratios. Dual-spectral optical imaging allowed simultaneous determination of the expression status of CAIX and HER2 in MCF10DCIS xenografts. These results establish feasibility of the use of VHH 'cocktails' for multispectral molecular imaging. This approach will potentially allow further improvements in early tumor detection, delineation of tumor margins during image-guided surgery, non-invasive molecular assessment of target expression status of tumors and metastases, and also direct tumor characterization by pathologists.

Introduction

Molecular imaging of cell surface markers has become an increasingly important technology for the imaging of cancer, which may be used for diagnosis, assessment of therapy response and for delineation of the tumor during surgical resection. Optical molecular imaging has recently attracted much attention, because the employed probes are non-radioactive and recent camera systems enable high resolution imaging. One of the limitations of optical molecular imaging is the limited sensitivity due to restricted light penetration into the tissue, which prevents applications such as whole-body imaging. Optical imaging is, however, perfectly suited for non-invasive detection of superficial tumors (e.g. breast cancer, head and neck tumors) or tumors accessible using an endoscope (e.g. lung cancer, tumors located in the gastrointestinal tract or abdominal cavity). Implementation of optical molecular imaging into clinical practice will enable non-invasive detection of cancer, monitoring of therapy response, and allow image guided surgery for radical tumor resections and their neighboring precursors with minimal removal of surrounding normal tissue. Moreover, optical molecular imaging would likely be highly suitable for *ex vivo* analysis of biopsies.

The basis of optical imaging lies in the detection of light emitted from fluorophore, making it a cost-effective, non-radioactive imaging modality for detection of cancer, both in the screening and intra-operative setting. Recent advances in optical imaging probes are focused on the development of near-infrared (NIR) fluorophores. Fluorophores emitting light in the NIR range of the spectrum (e.g. 700 nm and 800 nm) allow deeper tissue penetration by light than the standard UV fluorophores. These advantages are a result of lower light absorption by blood and other tissue components, as well as of minimal tissue auto-fluorescence in this range of the spectrum [1-3].

Besides an imaging system able to detect the light emitted by the NIR fluorophore, optical molecular imaging requires high tumor specificity, which can be obtained by employing fluorescent probes targeting tumor-specific markers that are ideally (over)expressed strictly in cancerous, but not in normal tissues. Several biomarkers, the (over)expression of which is associated with cancer development have been identified. Among these are the human epidermal growth factor receptor 2 (HER2) and the hypoxia marker carbonic anhydrase IX (CAIX) [4,5]. Various targeting moieties have been employed to facilitate tumor targeting, such as affibodies, peptides, conventional monoclonal antibodies, or antibody fragments. Previously, we reported optical molecular imaging using the variable domains of the heavy chain from heavy-chain antibodies (VHH, also referred to as nanobodies) conjugated to the near infra-red fluorophore IRDye800CW in breast cancer xenograft mouse models [6,7]. Nanobodies, which are the smallest, naturally derived, functional antigen binding fragments of only 15 kDa, proved to be very promising tumor targeting agents. The size ten times smaller in molecular weight than conventional monoclonal antibodies (mAbs), and the preservation of high affinity and specificity enables nanobodies to efficiently penetrate throughout the tumor

mass and be retained at the tumor. Due to the rapid accumulation of these nanobodies into the tumor, its visualization is already possible 2-4 hrs post injection (p.i.). In contrast, mAbs may require more than 48 hrs to accumulate at the tumor and provide comparable contrast.

Sufficient signal (described as contrast or tumor to background ratio, i.e. T/B ratio) and a clear delineation of the tumor are essential for successful and accurate tumor detection through imaging. In this respect, nanobodies are an optimal targeting moiety for molecular imaging, as they distribute rapidly upon administration and are rapidly cleared from the body (half time of 1-2 hrs) [7,8]. We hypothesized that the combination of two tumor specific probes would increase the T/B ratio and thus facilitate tumor detection. Moreover, by using dual-spectral imaging, information may be obtained about expression levels of different tumor markers within the same tumor, which could accelerate tumor characterization.

In this study we investigated whether a combination of two optical probes for breast cancer imaging that specifically recognize two independent cancer markers could improve tumor detection by optical imaging. For this, we have employed the VHH B9 targeting CAIX, which localizes to peri-necrotic regions of tumors (Brussel et al., submitted manuscript), and the VHH 11A4 targeting HER2, which is known to have a more homogenous distribution throughout the tumor tissue [6]. Both VHHs were conjugated to the same fluorophore, IRDye800CW, and the T/B ratios were compared in a breast cancer tumor model with the T/B ratios obtained after co-injection of either of the VHHs together with an irrelevant VHH R2. In addition, B9 and 11A4 were conjugated to different NIR fluorophores to investigate whether this approach could be used to detect the expression status of CAIX and HER2 *in vivo*. This combination of VHHs was also evaluated *ex vivo* in a surgical context and for the detection of lung metastases through dual-spectral optical imaging. Finally, immunohistochemistry was performed to validate fluorescent 11A4 and B9 probe localization through dual-spectral optical imaging of tumor sections.

Materials and Methods

Cell lines and cell culture conditions

MCF10DCIS.com (further referred to as MCF10DCIS) cells (Asterand, Detroit, MI, USA), mimicking ductal carcinoma *in situ* (DCIS) of breast, were cultured according to the supplier's guidelines in DMEM/F12 supplemented with 10% (v/v) FCS, 100 IU/ml penicillin, 100 μg/ml streptomycin and 2 mM L-glutamine at 37°C in a humidified atmosphere containing 5% CO_2. Generation of luciferase overexpressing MCF10DCIS cells has been described before [9].

VHH production and purification

The anti-HER2 VHH, 11A4, and the anti-CAIX VHH, B9, were produced as described before [6]. Briefly, VHH genes were re-cloned into the pQVQ72 expression vector (kindly provided by QVQ BV), which enables site-directed conjugation of IRDye680RD-maleimide and IRDye800CW-maleimide (LI-COR Biosciences, Lincoln, Nebraska, USA). Production of VHH was induced by addition of 1 mM isopropyl-beta-D-thiogalactopyranoside (IPTG) when bacteria reached log-phase. Irrelevant VHH, R2, was produced as described previously [8]. HER2- and CAIX-specific VHHs were purified from the periplasmic fraction by protein A affinity chromatography using a HiTrap protein A HP column (GE Healthcare, Zeist, The Netherlands) on the ÄKTAxpress system (GE Healthcare, Zeist, The Netherlands). Irrelevant VHH was purified using immobilized metal affinity chromatography (IMAC; Talon; Takara Bio Europe/Clontech, Saint-Germain-en-Laye, France).

Conjugation of the near infra-red fluorophores

Conjugation of the fluorophores was performed as described before [6]. Briefly, VHHs were treated with 20 mM TCEP in 50 mM Tris-HCL pH8.5 for 15 min at room temperature (RT), then buffer was replaced to 0.4 mM EDTA in phosphate buffered saline (PBS, Lonza, Basel, Switzerland) using a size exclusion chromatography resin in Pierce ZebaTM Desalting Spin Columns (Thermo Fisher Scientific, Landsmeer, The Netherlands) and incubated with a threefold molar excess of near infrared (NIR) fluorophore at 4^0C for 16 hrs. 11A4 was either conjugated to IRDye680RD-maleimide (further referred to as 11A4-680) or to IRDye800CW-maleimide (further referred to as 11A4-800), while B9 was conjugated exclusively to IRDye800CW-maleimide (further referred to as B9-800). The irrelevant VHH, R2, was randomly conjugated to N-hydroxysuccinimidine (NHS) esters of either IRDye800CW or IRDye700DX (further referred to as R2-800 and R2-700, respectively) in twofold molar excess of NIR fluorophore to protein for 2 hrs at room temperature. All fluorophores were purchased at LI-COR Biosciences (Lincoln, Nebraska, USA). After conjugation, the unconjugated fluorophores were removed using sequentially two (in case of IRDye800CW) or three (in case of IRDye680RD or IRDye700DX) Pierce ZebaTM Desalting Spin Columns (Thermo Fisher Scientific, Landsmeer, The Netherlands). The degree of conjugation was determined according to the instructions given by the provider for each of the fluorophores.

Ethics statements

All animal experiments were approved by the Utrecht University Animal Experimental Committee (DEC-Utrecht no. 2012.III.02.015).

In vivo studies

The mouse model used in this study was based on a previously described model [10]. Briefly, SCID/Beige female mice (6 weeks old) were purchased from Harlan Laboratories. Animals were housed in standard perspex cages with free access to food and water. To reduce food-induced fluorescence in the intestinal tract, animals received chlorophyll free diet two weeks prior to imaging (Harlan Laboratories, The Netherlands). In order to eliminate autofluorescence by the fur, mice were completely shaved and treated with Veet cream (local pharmacy) to remove remaining hair. Forty thousand MCF10DCIS cells were inoculated in the 4th mammary glands at both sides of mice. After tumor formation (approximately 8-9 weeks after inoculation of cells), mice carrying xenografts with diameters of approximately 0.5 cm were subjected to imaging.

In the first part of the study, where the advantage of using two probes instead of one was tested with respect to obtaining higher tumor-to-background ratios (T/B ratios), mice were divided into 3 groups. Each group was injected intravenously with one of the following combinations of VHHs (50 μg of each VHH-IR, thus 100 μg in total): 11A4-800 and B9-800 (n=7), 11A4-800 and R2-800 (n=7) or B9-800 and R2-800 (n=7). After the injections, mice were imaged with the Pearl Impulse Small Animal Imaging System (LI-COR) at the following time points: 30 min, 1 h, 2 hrs, 3 hrs, 4 hrs, 5 hrs, 6 hrs, 24 hrs and 48 hrs post injection (p.i.). Regions of interest (ROI) were drawn in the tumor and normal tissue areas. T/B ratios were calculated by dividing the mean intensity of tumor ROI by the mean intensity of background ROI (drawn in normal tissue area) determined with Pearl Impulse Software (v.2.0, LI-COR Biosciences).

In the second part of the study, mice were divided into 3 groups and then injected intravenously with combinations of VHHs conjugated to different NIR fluorophores to study whether the expression status of HER2 and CAIX could be detected simultaneously *in vivo* (50 μg of each VHH-IR, thus 100 μg in total): 11A4-680 and B9-800 (n=8), 11A4-800 and R2-700 (n=8) or B9-800 and R2-700 (n=7). After the injections, mice were imaged as described above. Fluorescence intensities of IRDye680RD and IRDye700DX were detected in the 700 nm channel, whereas fluorescence intensity of IRDye800CW was detected in the 800 nm channel. T/B ratios were calculated as described above.

In the third part of the study, the potential of VHH-IR to detect lung metastasis was evaluated. For the development of the lung metastasis model 1x10^5 MCF10DCIS cells were injected intravenously through the tail vein. Having confirmed the presence of lung metastasis in a non-invasive manner by bioluminescence imaging (Photon Imager, Biospace Labs, Paris, France), mice were injected intravenously with the combination of 50 μg 11A4-680 and 50 μg B9-800 (n=3). As controls, one mouse was injected with 50 μg R2-800 and 50μg R2-700 (n=1) and a healthy mouse with 50 μg 11A4-680 and 50 μg B9-800 (n=1). Mice were sacrificed 5 hrs p.i. by cervical dislocation

and lung metastases were imaged with the Pearl Impulse Small Animal Imaging System (LI-COR) upon surgical removal of lungs.

Imaging of fluorescent sections and immunohistochemistry

Mice injected with the combination of VHHs-IR labeled with either IRDye800CW, IRDye680RD or IRDye700DX were sacrificed 5 hrs p.i. and their tumors were collected. These were first imaged (i.e. *ex vivo*) and, immediately after, fixed in neutral buffered formalin, routinely processed to paraffin blocks and stored in the dark until further processing. Four μm thick sections were scanned using the Odyssey imaging system at the highest (21 μm) resolution and quality. IHC for detection of CAIX and HER2 combined with a hematoxylin and eosin (H&E) staining were performed as described before [11]. Slides were scanned with the Scanscope XT 120 scanner (Aperio, Vista, CA, USA).

Statistics

Statistical analysis was performed using GraphPad Prism (version 5.02). Comparisons of T/B ratios were analyzed using a Mann-Whitney test. P-values of ≤ 0.05 were considered to be statistically significant.

Results

Preparation of anti-HER2 and anti-CAIX VHHs conjugated to NIR-fluorophores

In order to investigate whether a combination of two fluorescent VHHs specifically recognizing two separate and validated breast cancer biomarkers could: a) improve tumor detection through optical imaging with an increase in T/B ratio, and/or b) facilitate tumor characterization and observation of different areas of the tumor, we used the anti-HER2 VHH, 11A4, and the anti-CAIX VHH, B9 [6]. As described previously an additional cysteine at the C-terminal end of the VHH was added to both 11A4 and B9 proteins for site-directed conjugation. In this study, 11A4 was site-specifically conjugated to either maleimide IRDye800CW or IRDye680RD (named 11A4-800 and 11A4-680, respectively), whereas B9 was conjugated to IRDye800CW only (named B9-800). In all *in vivo* experiments we have included an irrelevant VHH, R2, as a control, randomly conjugated to either IRDye800CW or IRDye700DX (referred to as R2-800 and R2-700, respectively). After the purification, the amount of free dye remaining in the sample was determined using SDS-PAGE (Fig. 1S). Conjugates containing less than 5% of free dye were considered suitable for use in the *in vivo* study. The degree of conjugation of each of the fluorophores to each VHH was 0.5, which is in

agreement with previously reported data [6].

In vivo single-spectrum imaging using a combination of VHH-IRDye800CW

To investigate whether targeting of the tumor with two tumor specific VHHs conjugated to the same fluorophore results in an increased contrast, we injected intravenously seven mice bearing two MCF10DCIS breast cancer xenografts in the 4th mammary glands with either 11A4-800 & B9-800 or the controls 11A4-800 & R2-800 or B9-800 & R2-800. The imaging was performed up to 48 hrs post injection (p.i.). Already 3 hrs p.i., a clear accumulation of the fluorescent probes was seen in the tumors for each of the three probe combinations (Fig. 1A, red arrows). IR fluorescence was also found at the bladder, which is expected due to the rapid renal clearance of VHH-IR. Accumulation of the IR fluorescence at the kidneys was not visible, because mice were imaged ventrally. Over time, the background fluorescence decreased as a result of rapid clearance of the probes, which led to an increase in contrast expressed as T/B ratios (Fig. 1B). After combining T/B ratios obtained at all time points, an overall significant difference in T/B ratio increase was found between the group injected with 11A4-800 & B9-800 and the control groups injected with either 11A4-800 & R2-800 (22% increase in T/B ratio), or the B9-800 & R2-800 cocktail (51% increase in T/B ratio) (Fig.1B). The average values of the T/B ratios for all groups were determined and a significant increase was observed between the tumor specific VHH combination group and the control groups. Interestingly, we also observed a significant difference between the two control groups. It indicated that the signal obtained with the anti-HER2 VHH was higher than that obtained with the anti-CAIX VHH, which may most likely be attributed to differences in expression levels of these two tumor markers within the same tumor.

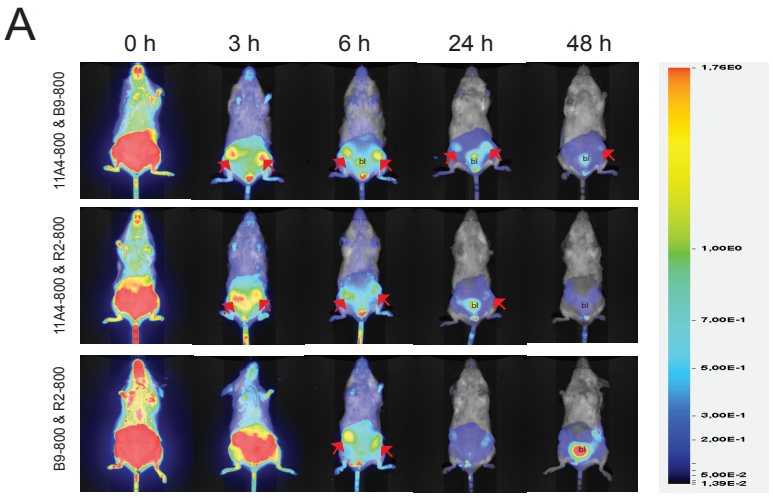

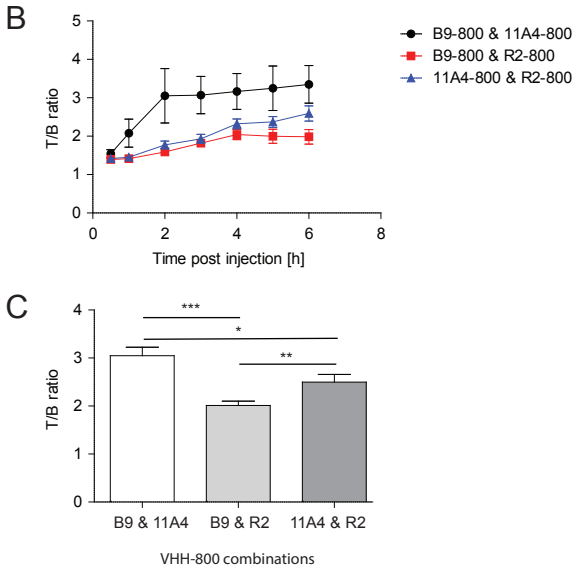

Fig.1. Use of a combination of two tumor-specific VHHs for optical imaging results in higher T/B ratios. A. Optical imaging of mice xenografted with MCF10DCIS cells in time upon injection of dual specific combination 11A4-800 & B9-800 (upper pannel), and control combinations, namely 11A4-800 & R2-800 (middle pannel) or B9-800 & R2-800 (bottom pannel). Arrows point to tumors, 'bl' depicts bladder. B. T/B ratios in time (n=7 per group). Graph represents mean ± SEM. These were calculated from ROIs drawn around each tumor and non-tumor area C. Comparison of overall T/B ratios obtained at all time points for animals injected with B9-800 & 11A4-800, and controls: B9-800 & R2-800 or 11A4-800 & R2-800 (* p=0.0199; ** p=0.0035; *** p=<0.0001).

In vivo dual-spectral imaging using VHH-IRDye800 and VHH-IRDye680

To determine whether two independent VHHs conjugated to two different NIR fluorophores have the potential to determine the expression levels of two relevant breast cancer markers *in vivo*, mice were injected intravenously with B9-800 & 11A4-680, or with B9-800 & R2-700 and 11A4-680 & R2-700 as controls. As expected, tumor xenografts were visible already 2 hrs p.i., however, the background fluorescence was also high at that time point (Fig. 2A-C) probably due to incomplete clearance of non-bound fluorescent VHHs. Clear delineation of the tumors was possible 4 hrs p.i.. The irrelevant VHH, R2-700, was also found at the tumor site, but this occurred to a lesser extent as compared to the tumor specific VHH-IR (Fig.3B and C). Both 11A4-800 and B9-800 specifically accumulated at the tumor when co-injected with irrelevant VHH, (Fig. 2 and Fig. 3A).

Fluorescence intensities were determined for each individual tumor (2 tumors per mouse of 7 mice in total) and a non-tumor tissue in the leg area in such a way that the signal was not affected by the signal of the tumor or bladder. The T/B ratios were calculated and plotted in time, revealing that the maximal T/B ratios were obtained already 2 hrs p.i. (Fig. 3). The T/B ratios of the irrelevant

VHH-IR, R2-700, were close to 1 (the average T/B ratio was equal 1.56 ± 0.41) and showed no increase in time, suggesting no specific accumulation of the irrelevant VHH at the tumor.

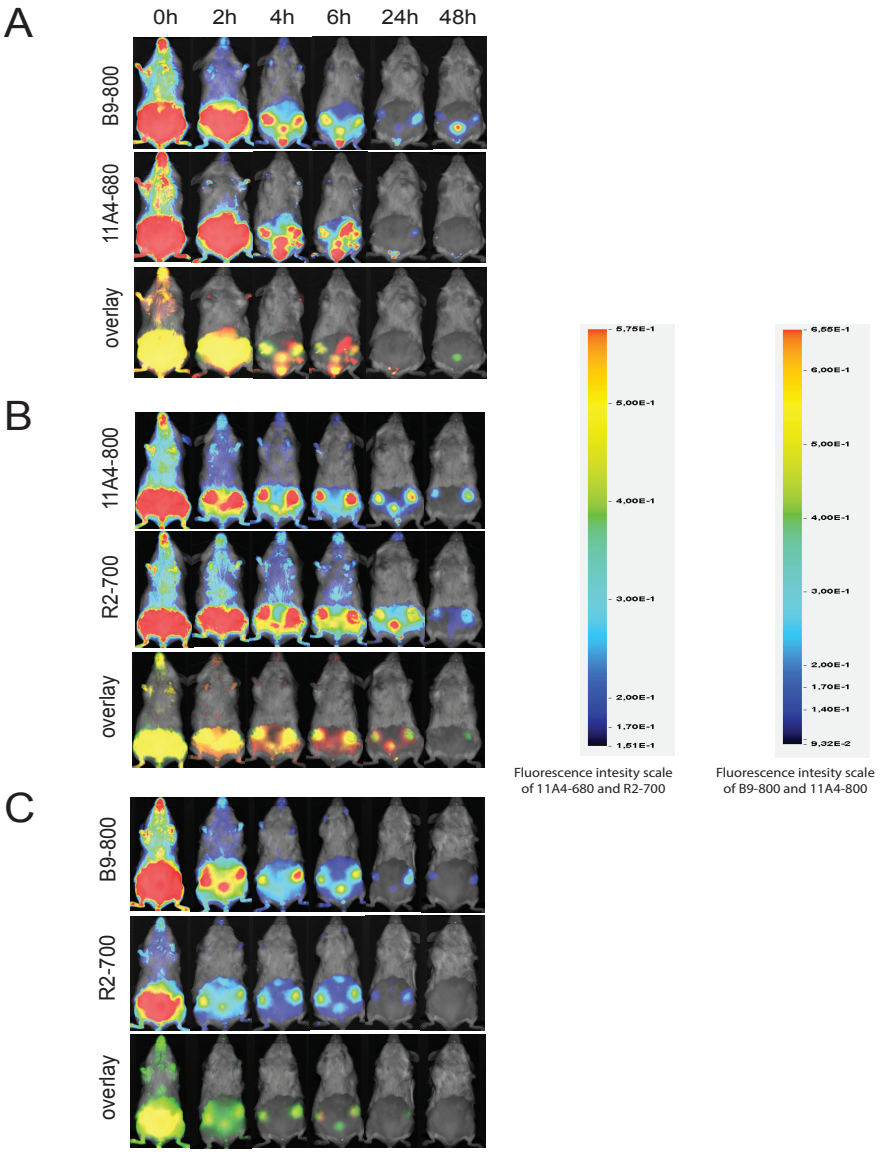

Fig.2. Dual spectral molecular imaging using tumor specific VHHs allows for simultaneous expression status determination of two different tumor markers, namely CAIX (targeted by B9 VHH) and HER2 (targeted by 11A4). Irrelevant R2-700 VHH was used as a negative control. Mice xenografted with MCF10DCIS cells were imaged in time upon injection of: (A)control combination consisting of 11A4-800 & R2-700, (B) control combination consisting of B9-800 & R2-700, and (C) tumor specific combination consisting of 11A4-680 & B9-800. The observed yellow color present in the overlays in each of the bottom panels originates from the overlay of green and red signals.

To enable sufficient removal of non-bound VHH-IR and therefore decrease of background intensity levels, 6 hrs p.i. was selected as an optimal imaging time point. A significant difference between the 11A4-680 and B9-800 T/B ratios was obtained 6 hrs p.i. (Fig. 3A); significant differences were also observed between 11A4-800 and the irrelevant VHH, R2-700 (Fig. 3B). The difference between B9-800 and the irrelevant VHH, R2-700 at 6 hrs p.i. was of borderline significance (Fig. 3C; p=0.0582).

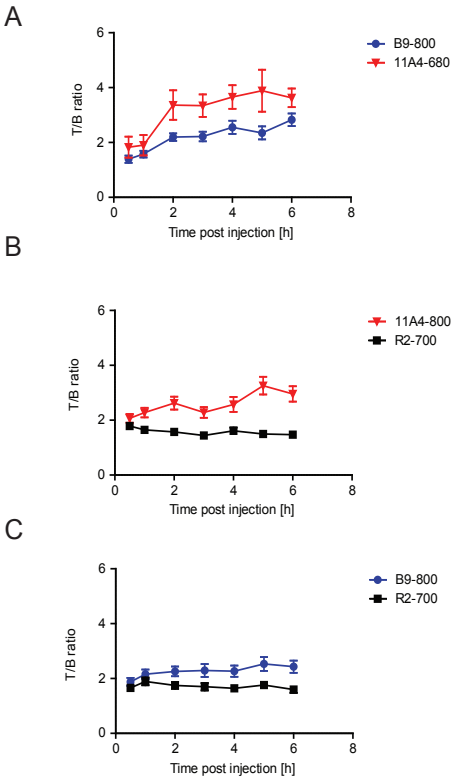

Fig.3. Rapid increase of T/B ratio in the first 6h p.i. allows fast imaging upon injection of (A) B9-800 & 11A4-680 (n=8), (B) 11A4-800 & R2-700 (n=8) and (C) B9-800 & R2-700 (n=7). T/B ratios were obtained from analysis of images as represented in Fig. 2 for each tumor individually, by drawing ROIs around tumors and normal tissues. Graphs represent mean ± SEM.

Dual-spectral imaging in the surgical setting

To investigate the possible application of dual-spectral imaging in a surgical setting, a number of mice bearing MCF10DCIS xenografts were injected with the indicated fluorescent VHH combinations, 5 hrs p.i. mice were sacrificed, the skin was removed thereby uncovering the xenografts and optical imaging was performed (Fig. 4A).

The following VHH combinations were injected: B9-800 & 11A4-680, B9-800 & R2-700,

and 11A4-800 & R2-700. As expected, a clear accumulation of IR fluorescence was found at the tumor site. The T/B ratios obtained after imaging tumors in this invasive manner were approximately 2 fold higher than those obtained in the non-invasive imaging set-up (Fig. 3) at the same time point p.i.. No differences in T/B ratios were observed in case of the control R2-700 analyzed in an *in vivo* or *ex vivo* setting. In contrast, the T/B ratios of tumor marker specific VHH-IR were approximately 2 fold higher than those of irrelevant control VHH (Fig.4B and C). T/B ratios of 11A4-680 were almost two fold higher (73% increase in T/B ratio) that T/B ratios determined upon injection of B9-800 (Fig. 4D).

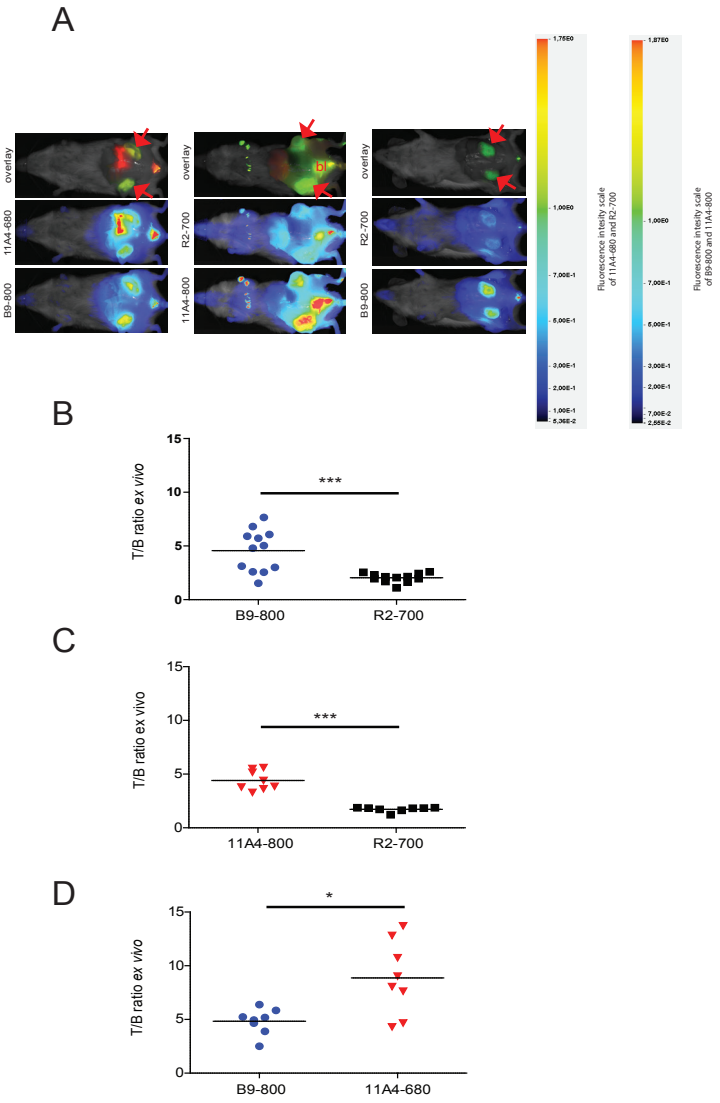

Fig.4. Dual-spectral imaging with two tumor specific VHHs allows simultaneous tumor molecular status determination in an invasive, intraoperative setting. A. Five hours p.i. of 11A4-680 & B9-800 (left), 11A4-800 & R2-700 (middle) or B9-800 & R2-700 (right) mice were sacrificed and their skin removed to mimic image-guided surgery setting. B-D. T/B ratios were calculated for tumors imaged in the intraoperative setting. Bars represent the mean, n=4 mice in groups 11A4-800 & R2-700 (*** p=0.0002) and B9-800 & 11A4-680 (* p=0.0281), n=6 mice in group B9-800 & R2-700 (*** p=0.0006).

We have observed that the T/B ratios differed by a factor of two in case of 11A4-680 and 11A4-800. This can be explained by a difference in background fluorescence levels (Fig. 2S), which were significantly higher in case of 11A4-800 (726 ± 138 vs 395 ± 120). The reason for increased background fluorescence levels in case of tracer conjugated to IRDye800CW is not clear, however, we are currently further exploring this observation.

Dual-spectral imaging of lung metastases in a surgical setting

MCF10DCIS cells are known to have the capacity to metastasize into the lungs. In this part of the study the B9-800 & 11A4-680 was evaluated for its potential to detect metastasis in a surgical setting. This would provide valuable information on their tumor marker expression status and its molecular resemblance to the primary tumor. For this experiment, mice were first injected with MCF10DCIS cells through the tail vein and the development of lung metastases was followed in time by bioluminescence imaging (BLI). When metastases of 1-2 mm were detected through BLI, mice were injected with the B9-800 & 11A4-680 combination. As controls, one mouse with developed lung metastases was injected with R2-800 & R2-700 irrelevant VHH combination and a healthy mouse without metastases was injected with B9-800 & 11A4-680 combination. Five hours p.i. all mice were sacrificed and their chest wall was removed in order to facilitate the imaging of the lungs. No IR fluorescence was found in the healthy lung controls, thus confirming the tumor marker specificity of the B9-800 and 11A4-680. Hardly any fluorescence accumulated at the lung bearing metastasis when mouse was injected with the irrelevant VHHs combination, while clear fluorescence was found upon injection of the B9-800 & 11A4-680 combination (Fig. 5).

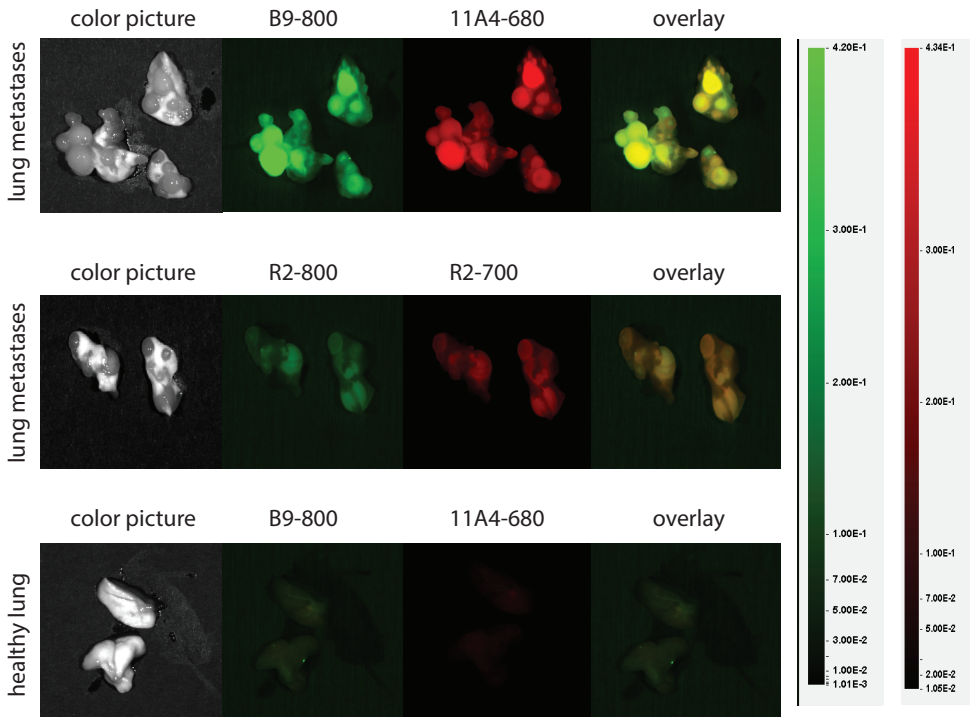

Fig.5. Invasive optical molecular imaging with two tumor specific VHHs allows detection of lung metastasis in an intra-operative setting. A. Detection of lung metastasis 5 hrs p.i. of B9-800 & 11A4-680 combination. Yellow color in the overlay panel corresponds to overlay of green (B9-800) and red (11A4-680) colors. B. Injection of a control irrelevant VHH combination R2-800 & R2-700 did not result in lung metastasis detection.

Dual-spectral imaging of tumor sections and immunohistochemical validation

To investigate the possibility of the *ex vivo* assessment of the molecular status of the tumor by employing the 11A4-680 & B9-800 combination, dual-spectral imaging of tumor sections was conducted and compared to conventional hematoxylin and eosin (H&E) staining. Tumors were fixed, embedded in paraffin and sections were imaged using the Odyssey imaging scanner (Fig 6). The HER2-targeted probe, 11A4-680, was observed to be homogenously distributed throughout the tumor section, while the CAIX-targeted one, B9-800, was only confined to the peri-necrotic areas of the tumor (Fig. 6A, * showing necrotic areas). Tumor sections obtained from mice that were injected with control combinations, B9-800 & R2-700, and 11A4-800 & R2-700, only presented IR fluorescence signal in the 800 nm channel. The distribution pattern of B9-800 and 11A4-800 from these control combinations was similar to the one observed earlier for 11A4-680 & B9-800 combination (Fig. 6B and 6C, respectively). These results confirm specific uptake of both HER2- and CAIX-targeted VHHs. In parallel, IHC analysis of the tumor section confirmed HER2 expression

of the tumors by a 2+ HER2 DAKO score for expression which was homogenously distributed throughout the tumor section, while CAIX expression was confined to the peri-necrotic tumor areas (Fig. 6D). These results validate the specificity of these VHHs for dual-spectrum imaging on tumor tissue sections.

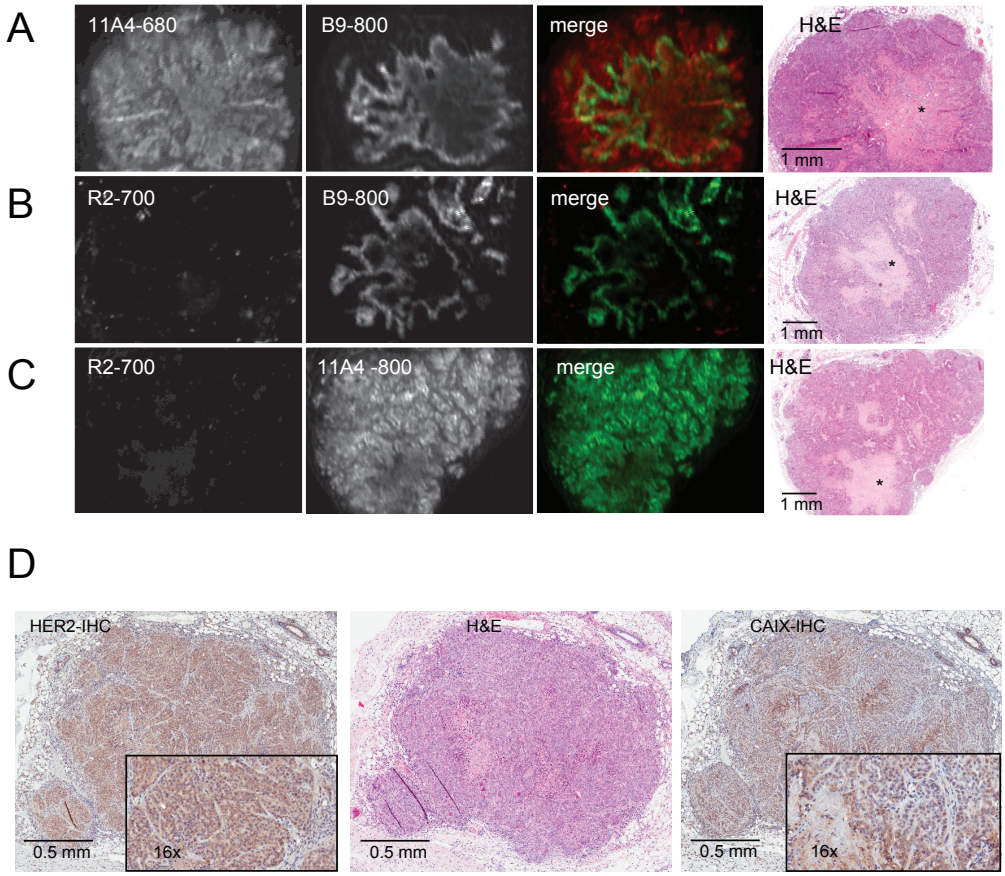

Fig.6. Dual-spectral fluorescence molecular pathology allows simultaneous determination of HER2 and CAIX expression status. A. Distribution of 11A4-680 (red) and B9-800 (green) VHHs in MCF10DCIC xenografts sections obtained 5h p.i.. H&E staining shows central necrosis (*). B. Perinecrotic distribution of B9-800 VHH and no binding of irrelevant VHH, R2-700. C. Homogenous distribution of 11A4-800 and no binding of irrelevant VHH, R2-700. D. IHC on sections of tumor xenografts confirms expression of HER2 (2+) and CAIX.

Discussion

Despite many efforts made over the years to facilitate early breast cancer detection, improvements are still eagerly awaited. At the moment there are six imaging modalities commonly used to detect and stage cancer, namely: X-ray, computed tomography (CT), magnetic resonance imaging (MRI), single-photon emission tomography (SPECT), positron emission tomography (PET), ultrasound (US) and optical imaging. Each of these techniques comes with advantages, but also limitations. Recent advances in targeted probe development stimulated further improvements of PET, SPECT and more recently also of optical imaging. Although the advantages of optical imaging are clear, the sensitivity of this technique is still a problem. When successful, optical imaging would provide a very good temporal and spatial resolution, without exposure to ionizing radiation. The limited penetration depth of the optical signal reduces the application of optical imaging to the analysis of local (whole-body scans remain impossible at this stage) and superficial tumors, such as head-and-neck or breast tumors, and tumors that are reachable by endoscopy or during surgery. In addition, as we have recently shown, optical imaging could also contribute to the analysis of expression of different tumor markers *ex vivo*, an approach indicated as molecular fluorescence pathology [9].

For such applications, further improvement of the sensitivity of optical imaging is essential. We have previously demonstrated that VHHs provide better T/B ratios than conventional antibodies at earlier time points p.i. [6,7]. As a result of their small size, VHHs accumulate more rapidly in the tumor and the non-bound fraction is more rapidly cleared. In the present study we hypothesized that the injection of two VHHs differing in their specificity and conjugated to the same fluorophore would result in an improved T/B ratio. The employed VHH combination consisted of a VHH binding to HER2 and a VHH binding to CAIX. The performance of this combination was evaluated in an orthotopic tumor model mimicking DCIS. Crucial for these studies is the similar conjugation efficiency of the fluorophore to the two VHHs. This would allow quantification of the imaging based on the fluorescence intensity. To avoid any detrimental effects of fluorophore conjugation on the binding capacity of the VHH, we performed the conjugation using maleimide-modified fluorophores that bind directly to the C-terminal cysteine at the VHH. Our data nicely show that the injection of two tumor-specific VHH-800 resulted in a higher T/B ratio than the injection of a single tumor specific VHH-800 combined with an irrelevant VHH-800. This resulted in a clear tumor delineation at early time points p.i.. Interestingly, significant differences in T/B ratios were also obtained between the control groups, indicating that HER2-targeted VHH injections result in a higher T/B ratio than imaging with CAIX-targeted VHH. This result may be explained by the differences in expression of the targeted molecules. Immunohistochemical analysis of HER2 expression showed that it is homogenously distributed throughout the tumors in contrast to CAIX, the expression of which was limited to the peri-necrotic region [12]. This result suggests that the application of more than two

tumor marker specific VHHs would overcome intratumoral heterogeneity and improve T/B ratios even further. The small size of the VHHs allows for simultaneous binding of different VHHs to neighboring molecules, most likely without steric hindrance. In addition, non-competitive VHHs targeting the same tumor marker could be combined as simultaneous binding of different VHHs to the same target molecule would likely lead to even better T/B ratios and consequently to an improved tumor detection.

Current diagnostic gold standard in biomarkers' expression assessment rely exclusively on *ex vivo* methods, such as immunohistochemistry (IHC) and gene amplification based fluorescent in situ hybridization (FISH). To obtain tissue for these assessments, a biopsy is required. This invasive procedure may have side effects, such as bleeding, and it is difficult to take many biopsies or repeat the procedure for monitoring the treatment response [13]. Furthermore, taking biopsies from metastases to assess receptor profiles is now common, but is an even greater burden to the patient as many sites are not easily accessible [14]. Due to these limitations, non-invasive alternatives are eagerly awaited. Our data demonstrate that *in vivo* dual-spectral imaging of two independent tumor markers, namely CAIX and HER2, is feasible. An important implication of this result is that it enables the simultaneous determination of the expression status of two tumor markers, both in a non-invasive manner *in vivo*, as well as *ex vivo*. To our knowledge, this is the first study in which VHHs were used in a dual-spectral imaging setting. Further histological processing of the labeled tumors also showed that the imaging of these two markers is possible on tissue sections, allowing molecular fluorescence pathology as recently described [9].

The idea of imaging with a combination of probes has been earlier investigated by Barrett et al. with the use of monoclonal antibodies targeting EGFR and HER2 conjugated to NIR fluorescent dyes such as Rhodamine green, Cy5.5 or Cy7 [15]. The tumor delineation was possible only 24 hrs p.i. of the mAb combination. Koyama et al. presented a study, in which optical imaging was performed with three different mAb, namely cetuximab (anti-EGFR), trastuzumab (anti-HER2) and daclizumab (anti-IL-2Rα), conjugated to three different fluorophores. Also in their study, optimal T/B ratios were obtained only 24 hrs p.i. [16]. Similar results were obtained by Sano et al. [17]. Xie et al. compared four different NIRF probes in a subcutaneous xenograft mouse model 24 hrs p.i. to bioluminescent and IHC data concluding that optical molecular imaging is a feasible approach to enable the detection of different tumor features simultaneously [18]. In all these studies, optimal imaging conditions were obtained not earlier than 24 hrs p.i.. Our data show that VHHs offer sufficient target specificity enabling dual-spectral imaging. The greatest advantage of VHHs, however, is that they provide optimal contrast for tumor detection already 2-4 hrs after injection.

Important for image-guided surgery is the clear delineation of the tumor and determination of the margins. After removal of the skin from the 4th mammary glands, higher T/B ratios were obtained as compared to T/B ratios obtained in a non-invasive imaging setting. These observations

highlight the potential of dual or even multi-spectral imaging in the surgical setting, allowing for complete tumor visualization in order to enable radical tumor resections. However, at wavelengths shorter than 800 nm more autofluorescence can be expected. It is essential that development of probes suitable for dual or even multi-spectral imaging is followed by improvement in imaging systems that would provide accurate separation of each signal.

Breast cancer is a clinically heterogeneous disease, which develops distant metastasis in 10-15% of breast cancer patients during 3 years post detection of the primary tumor [19]. Based on autopsy data, the most common sites for metastatic spread are bone, lung and liver [19-21]. With the dual spectral analysis of a MCF10DCIS lung metastasis model we could detect small metastases in the millimeter range. We expect that the simultaneous targeting of several different tumor markers might further improve the detection of small metastases, which would have a great importance in the surgical setting. Metastases may differ in expression of tumor markers compared to the primary tumor [14], therefore this approach would increase the probability of detecting the metastases and in addition provide the information of which tumor markers are predominant. In such setting, a general 'cocktail' of different tumor markers – the most frequently present markers in all breast cancers - could be sufficient to detect most, if not all, of the breast cancers. The use of different fluorophores in such 'cocktail' would provide further information on molecular heterogeneity of the tumors. In relation to this, we recently performed a study to determine which tumor markers would be sufficient to image most of breast cancer. The combination of HER2, CAIX, GLUT1, EGFR, IGF1-R, and MET could detect 45.5% of tumors, including basal/triple negative and HER2-driven ductal cancer [11]. Addition of markers with a 2-fold tumor to normal tissue ratio could increase detection rate to 98%.

Furthermore, multispectral optical imaging is a step forward towards implementation of the concept of molecular fluorescence pathology in the clinic as a cost-effective, time-efficient and sensitive alternative to conventional IHC. Due to their small size combined with high specificity and affinity, nanobodies are able to penetrate tumors much better than conventional antibodies [7]. Direct immunofluorescence of the near infra-red dyes coupled to nanobodies already present in the tumor tissue would require no further costly lab processing. This molecular fluorescent pathology would, however, strongly depend on the imaging target and probably be restricted to cell surface markers that are accessible to nanobodies.

In conclusion, we showed successful dual-probe and dual-spectral optical molecular imaging of CAIX and HER2 positive DCIS xenografts *in vivo*, in the surgical setting, as well as *ex vivo* on tumor sections. Simultaneous determination of expression status of multiple, clinically relevant tumor markers will lead to a better detection of the primary tumor and its metastases, providing optimal tumor delineation during surgery under image-guidance. Furthermore, this approach would provide a more rapid assessment of tumor marker expression in the pathological setting. Altogether,

this would significantly improve the current management of patients from early diagnosis of breast cancer and surgical procedures to treatment decision making and monitoring of treatment response.

Supplementary information

Results

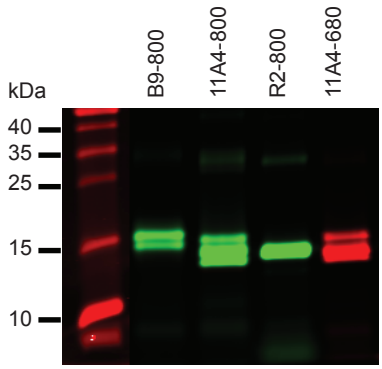

Fig.1S. SDS-PAGE analysis of IR-conjugated VHHs.

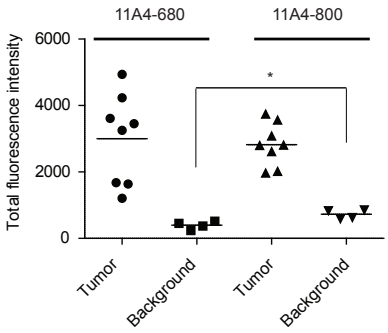

Fig.2S. Total fluorescence intensity of 11A4-800 and 11A4-680 at the tumor and in the background area obtained 5 hrs p.i. during the *ex vivo* tumor imaging . A significant difference between background fluorescence levels of 11A4-680 and 11A4-800 was detected (* p=0.0286).

Financial disclosure of authors

This research was supported by the Center for Translational Molecular Medicine (MAMMOTH project).

References

1. Kovar JL, Simpson MA, Schutz-Geschwender A, Olive DM: A systematic approach to the development of fluorescent contrast agents for optical imaging of mouse cancer models. *Anal. Biochem.* 367(1), 1-12 (2007).

2. Sevick-Muraca EM: Translation of near-infrared fluorescence imaging technologies: emerging clinical applications. *Annu. Rev. Med.* 63, 217-231 (2012).

3. Weissleder R: A clearer vision for in vivo imaging. *Nat. Biotechnol.* 19(4), 316-317 (2001).

4. Pinheiro C, Sousa B, Albergaria A *et al.*: GLUT1 and CAIX expression profiles in breast cancer correlate with adverse prognostic factors and MCT1 overexpression. *Histol. Histopathol.* 26(10), 1279-1286 (2011).

5. Ward C, Langdon SP, Mullen P *et al.*: New strategies for targeting the hypoxic tumour microenvironment in breast cancer. *Cancer Treat. Rev.* 39(2), 171-179 (2013).

6. Kijanka M, Warnders FJ, El Khattabi M *et al.*: Rapid optical imaging of human breast tumour xenografts using anti-HER2 VHHs site-directly conjugated to IRDye 800CW for image-guided surgery. *Eur. J. Nucl. Med. Mol. Imaging* 40(11), 1718-1729 (2013).

7. Oliveira S, van Dongen GA, Stigter-van Walsum M *et al.*: Rapid visualization of human tumor xenografts through optical imaging with a near-infrared fluorescent anti-epidermal growth factor receptor nanobody. *Mol. Imaging* 11(1), 33-46 (2012).

8. Huang L, Gainkam LO, Caveliers V *et al.*: SPECT imaging with 99mTc-labeled EGFR-specific nanobody for in vivo monitoring of EGFR expression. *Mol. Imaging Biol.* 10(3), 167-175 (2008).

9. van Brussel AS, Adams A, Vermeulen JF *et al.*: Molecular imaging with a fluorescent antibody targeting carbonic anhydrase IX can successfully detect hypoxic ductal carcinoma in situ of the breast. *Breast Cancer Res. Treat.* 140(2), 263-272 (2013).

10. Behbod F, Kittrell FS, LaMarca H *et al.*: An intraductal human-in-mouse transplantation model mimics the subtypes of ductal carcinoma in situ. *Breast Cancer Res.* 11(5), R66 (2009).

11. Vermeulen JF, van Brussel AS, van der Groep P *et al.*: Immunophenotyping invasive breast cancer: paving the road for molecular imaging. *BMC Cancer* 12, 240-2407-12-240 (2012).

12. Wykoff CC, Beasley N, Watson PH *et al.*: Expression of the hypoxia-inducible and tumor-associated carbonic anhydrases in ductal carcinoma in situ of the breast. *Am. J. Pathol.* 158(3), 1011-1019 (2001).

13. Shetty MK, Breast and Gynecological Cancers. An integrated Approach for Screening and Early Diagnosis in Developing Countries. , Springer New York, 2013,.

14. Hoefnagel LD, van de Vijver MJ, van Slooten HJ *et al.*: Receptor conversion in distant breast cancer metastases. *Breast Cancer Res.* 12(5), R75 (2010).

15. Barrett T, Koyama Y, Hama Y *et al.*: In vivo diagnosis of epidermal growth factor receptor expression using molecular imaging with a cocktail of optically labeled monoclonal antibodies. *Clin. Cancer Res.* 13(22 Pt 1), 6639-6648 (2007).

16. Koyama Y, Barrett T, Hama Y, Ravizzini G, Choyke PL, Kobayashi H: In vivo molecular imaging to diagnose and subtype tumors through receptor-targeted optically labeled monoclonal antibodies. *Neoplasia* 9(12), 1021-1029 (2007).
17. Sano K, Mitsunaga M, Nakajima T, Choyke PL, Kobayashi H: In vivo breast cancer characterization imaging using two monoclonal antibodies activatably labeled with near infrared fluorophores. *Breast Cancer Res.* 14(2), R61 (2012).
18. Xie BW, Mol IM, Keereweer S *et al.*: Dual-wavelength imaging of tumor progression by activatable and targeting near-infrared fluorescent probes in a bioluminescent breast cancer model. *PLoS One* 7(2), e31875 (2012).
19. Weigelt B, Peterse JL, van 't Veer LJ: Breast cancer metastasis: markers and models. *Nat. Rev. Cancer.* 5(8), 591-602 (2005).
20. Minn AJ, Gupta GP, Siegel PM *et al.*: Genes that mediate breast cancer metastasis to lung. *Nature* 436(7050), 518-524 (2005).
21. Pagani O, Senkus E, Wood W *et al.*: International guidelines for management of metastatic breast cancer: can metastatic breast cancer be cured? *J. Natl. Cancer Inst.* 102(7), 456-463 (2010).

Chapter 4

Development of canine HER2 targeted nanobodies for optical imaging

Marta M. Kijanka
Carlo Zimarino
Purvi Jain
Sofia Doulkeridou
Sabrina Oliveira
Peter J.M. Rottier
Monique H. Verheije
Paul M.P. Bergen en Henegouwen

Manuscript in preparation

Abstract

Introduction: Options for diagnosis and treatment of canine mammary tumors (CMT) are currently limited. Mammary tumors from dogs express validated human prognostic and predictive markers such as HER2. Here we present the development of canine HER2-targeted nanobodies to enable optical imaging of CMT.

Methods: To obtain phage display library containing binders specific to CMT biomarkers, such as HER2, we immunized two llama's with HMPOS cells. This library was used to select HER2 targeted nanobodies by employing specific elution with the HER2-targeted monoclonal antibody trastuzumab. After production in *E.coli* and their purification, the binding affinities of these nanobodies to the canine mammary carcinoma P114 cells were determined and their potential optical imaging probes was evaluated after conjugation to the near infra-red fluorophore IRDye800CW in a small pilot study. Two different xenografts models were used, namely canine mammary carcinoma P114 model and canine osteosarcoma MCKOS model. The performance of these nanobodies-IR was compared to that of a negative control nanobody-IR, referred to as R2-IR.

Results: Random conjugation of IRDye800CW to two non-competing nanobodies preserved their low nanomolar affinities as determined using P114 cells. Regions of interest drawn in tumor and healthy tissue areas were used to calculate tumor-to-background ratios. No significant differences were found between *in vivo* determined tumor-to-background ratios of neither negative control nanobody R2-IR and single selected nanobody-IR, nor negative control nanobody R2-IR and a combination of two selected nanobodies-IR. However, *ex vivo*, a clear difference was found between the tumor-to-background ratios of the R2-IR and a combination of two selected nanobody-IR injected simultaneously.

Conclusion: We selected nanobodies that bind with high affinity to HER2 positive canine mammary tumor cells and successfully conjugated them to IRDye800CW for optical imaging. The highest nanobody-IR accumulation at the tumor was obtained with the nanobody-IR combination. These results stimulate further research to confirm the specificity of selected nanobodies and to further optimize molecular optical imaging in dogs.

Introduction

Canine mammary gland carcinoma is the second most frequent cancer in female dogs after skin tumors [1,2]. These tumors share several similarities with human mammary tumors, however, their incidence rate among bitches is three times higher than among women [1,2]. Canine mammary tumors (CMT) occur very rarely in male dogs. Almost half of CMT is malignant and capable to metastasize to the lungs, which is the most common site of distant metastasis [1].

Several genes overexpressed in human breast cancer are also overexpressed in the canine counterpart [2,3]. One of them is the HER2 receptor, which is found to be overexpressed in about 17% of CMT [4], similar to the frequency of overexpression in human breast cancer patients. However, there is discussion on the significance of HER2 overexpression in CMT, because no HER2 gene amplification was found by chromogenic in situ hybridization (CISH)) studies [5,6]. The study by Singer et al. shows that the homology between the canine and human HER2 receptor amino acid sequence is very high, reaching 92% [7]. Furthermore, these authors show that the epitope recognized by human HER2 targeted monoclonal antibody, trastuzumab, is highly conserved, differing by only one amino acid. The proline residue at position 557 of human HER2 is replaced by a serine residue in the canine counterpart [7]. Although with a lower affinity, trastuzumab binds to cHER2.

Based on the fact that tumors of pet dogs and human share many characteristics, the concept of 'comparative oncology' has been introduced [2,7]. The aim of this concept is to fasten the development of novel anti-cancer therapeutics for both human and veterinarian medicine [7]. At the moment, the availability of therapeutics for veterinary use is limited, as surgery and to some extent chemotherapy involving cyclophosphamide, 5-fluorouracil, and doxorubicin, are the most common approaches.

Currently, no specific antibodies targeting canine breast tumor markers for either molecular imaging or targeted therapy have been developed. We have recently demonstrated the successful employment of antibody fragments for rapid molecular imaging using HER2 as a target. These antibody fragments have been derived from heavy chain antibodies (HcAb) of members of the Camelidae family, and are referred to as nanobodies. Even though they are ten times smaller than conventional antibodies they retain the specificity and high affinity towards targets against which they are raised [8,9]. Nanobodies have been preclinically evaluated as promising imaging agents for PET and molecular optical imaging [10-13], but also as targeting moieties for toxic payload delivery [14-17].

The current study was aimed at the development of nanobodies targeting canine HER2. Phage display selections were performed using a dog library obtained by immunization of two Llama glamas with HER2 positive HMPOS cells. We demonstrate the specific and high affinity binding of these nanobodies to canine cells *in vitro*. Furthermore, we present evaluation of these nanobody near-

infrared fluorophore (nanobody-IR) conjugates *in vivo* in two canine tumor xenograft models.

Materials and Methods

Cell lines and culture conditions

Highly Metastasizing POS cells (HMPOS) were maintained in RPMI 1640 medium (Gibco) with 7.5 % (v/v) fetal bovine serum (FBS), 100 IU/ml penicillin, 100 mg/ml streptomycin and 2 mM L-glutamine. Madin-Darby Canine Kidney Epithelial Cells (MDCK cells), D-17, MCKOS and SKOS canine osteosarcoma cell lines were maintained in DMEM medium (Gibco) supplemented as described above. The canine mammary carcinoma cell lines Sh1b and P114 were maintained in DMEM/F12 supplemented as described above with an addition of 10 μg/ml gentamicin sulfate. The human breast cancer cell lines, SKBR3 and MDA-MB-231, were maintained as MDCK, D-17 and MCKOS cell lines. All cells were cultured at 37^0C in a humidified atmosphere of 5% CO_2. P114 and Sh1b cells were a kind gift of Dr. Gerard Rutteman (Department of Clinic Science and Companion Animals, University of Utrecht, The Netherlands) and HMPOS, MCKOS and SKKOS cells of prof. Jolle Kirpensteijn (Department of Clinical Sciences of Companion Animals, Faculty of Veterinary Medicine, Utrecht University). MDCK, D-17, SKBR3 and MDA-MB-231 cells were obtained from the American Type Culture Collection (ATCC).

Llama immunization and phage display library construction

To induce a humoral immune response directed towards the cell surface proteins of canine HMPOS cells, two llamas were immunized with 10^7 canine HMPOS cells in incomplete Freund's Adjuvant. Each animal received with one week interval six doses of subcutaneously administered cells. At the end of immunization process, blood was collected, and peripheral blood lymphocytes (PBLs) were purified from which total RNA was obtained. This RNA was transcribed into cDNA using RT-PCR (Life Technologies), which was used as a template to generate immune libraries, as described earlier [18].

Phage display selection of canine HER2 targeted nanobodies

To select nanobodies binding canine HER2 receptor, several phage display selections employing P114 and Sh1b cells were performed. In our first approach, phages were panned on Sh1b cells in the first round and P114 cells in the second round. In the second approach, two sequential pannings on P114 cells were performed. After intense washing with 0.05% Tween-20 in PBS, specific phages

were eluted with trypsin (1 mg/ml, 30 min at RT) after first rounds and with monoclonal antibody, trastuzumab, after second rounds (1 mg/ml, 3 hrs at RT). The coding sequences of the obtained nanobodies binding to the canine cells were identified by performing sequence analysis (Macrogen Inc., Amsterdam, The Netherlands).

Production of nanobodies and conjugation of the near-infrared fluorophore IRDye800CW

Genes of selected nanobodies were re-cloned into expression vector containing an EPEA tag downstream the nanobody, which enables nanobody purification. Production of nanobodies was induced with 0.1 mM Isopropyl β-D-1-thiogalactopyranoside (IPTG), when SHuffle® T7 *E. coli* bacteria reached log-phase. Nanobodies were purified from periplasmic fractions using Capture Select C-tag affinity matrix (Life Technologies, Bleiswijk, The Netherlands). Nanobodies were conjugated to IRDye800CW-NHS (LI-COR Biosciences, Lincoln, Nebraska, USA) in a random manner using a four-fold molar excess of the infra-red dye (IR) as described earlier [13]. After conjugation, free IR was removed using sequentially two Zeba Spin Desalting columns (Thermo Fisher Scientific, Perbio Science Nederland B.V., Etten-Leur, The Netherlands). The degree of IR conjugation was determined as described before [13]. IR-conjugated proteins were analyzed by 15% SDS-PAGE.

Determination of apparent affinity of nanobodies and nanobodies-IR on a panel of canine cells

Two days in advance 20.000 P114 cells were seeded in a 96-well plate. On the day of the assay cells were incubated with a two-fold dilution series of nanobody for 2 hrs at 4^0C. After removal of the non-bound nanobody in subsequent washing steps, cells were fixed with 4% paraformaldehyde (PFA) for 30 min at RT, incubated with 100 mM glycine for 10 min at RT and blocked with 2% milk powder in PBS (MPBS). The bound nanobodies were detected with rabbit anti VHH protein G purified serum (home-made, 1:1000, 1 h at RT) and goat anti rabbit – IR800 (Li-COR Biosciences, 1:1000, 1 h at RT). The fluorescent signal was detected using Odyssey scanner. For determination of apparent affinity of nanobodies-IR a panel of several canine cells was employed (namely P114, Sh1b, MCKOS, MDCK, D17, SKOS). Cells were seeded and incubated with a dilution series of nanobodies-IR as described above. The IR fluorescent signal of membrane bound nanobodies-IR was detected at Odyssey scanner (Li-COR Biosciences) after washing off the non-bound nanobodies-IR (800Int4).

Competition assay

Two days in advance 20.000 P114 cells were seeded in a 96-well plate. On the day of the assay cells were incubated for 2 hrs at 4^0C with either 10 nM solution of canine specific nanobody-IR, or

10 nM solution of canine specific nanobody-IR and a 100 fold excess of non-conjugated canine specific nanobody or trastuzumab. The IR fluorescent signal of membrane bound nanobodies-IR was detected at Odyssey scanner after washing off the non-bound nanobodies-IR (800Int4). Data are presented as mean ± SD (n=3).

Ethics statements

The animal experiments were approved by the Animal Ethical Committee board of Utrecht University (DEC# 2013.II.10.070).

Pilot in vivo study

Female nude BALBc mice were obtained from Harlan Laboratories (Horst, The Netherlands). Subcutaneous tumors were induced by inoculating $2x10^6$ of P114 or MCKOS cells at the left hind leg. To reduce food-induced fluorescence in the intestinal tract, animals received chlorophyll free diet prior to imaging (Harlan Laboratories, Horst, The Netherlands). After tumor formation, mice carrying xenografts of approximately 100 mm^3 were subjected to imaging. Mice were anesthetized with isoflurane and intravenously injected with either canine cell specific nanobody-IR (50 μg, n=3 in case of P114 model, n=1 in case of MCKOS model), a combination of two canine cell specific nanobodies-IR (100 μg, n=4 in case of P114 model) or a control nanobody-IR (50 μg, n=2 in case of P114 model). *In vivo* fluorescence images were obtained with Pearl Impulse Small Animal Imaging System (LI-COR) at the following time points: 30min, 1 h, 2 hrs, 3 hrs, 4 hrs, 5 hrs, 6 hrs and 24 hrs post injection (p.i.). Mice were sacrificed by cervical dislocation under anesthesia, their tumors with surrounding healthy tissue excised and imaged *ex vivo*. The data were analyzed using Pearl Impulse Software (v.2.0, LI-COR Biosciences). Regions of interest (ROI) were drawn around the tumor and in normal tissues. Tumor to background ratios (T/B ratios) were calculated by dividing mean intensity of tumor ROI by the mean intensity of background ROI (drawn in normal tissue area).

Histology

Tumor tissue were collected and fixed in 4% formalin and subsequently dehydrated in series of alcohol. Next, they were embedded in paraffin and sectioned to 4 μm sections using a rotary microtome, after which sections were stained with hematoxylin and eosin (H&E) as described before [19].

Results

Phage display selection and characterization of canine specific nanobodies

To obtain canine HER2 targeted nanobodies, llamas were immunized with canine osteosarcoma HMPOS cells. Expression of HER2 by these cells was confirmed in a binding assay employing trastuzumab. Several selection rounds were performed on canine mammary cancer cells. As a second step, specific elution was performed using trastuzumab, an anti-human HER2 antibody with cross-reactivity for cHER2 (Fig.1 A) [7]. This approach resulted in the elution of phages, which were further tested for binding to the cHER2 expressing canine mammary carcinoma cells P114 and Sh1b by both phage ELISA and ELISA using periplasm fractions obtained from nanobody expressing *E. coli*. Clones binding to canine, but not to human HER2 negative MDA-MB-231 cells, were further re-cloned into a bacterial production vector, produced, purified and further characterized. The binding affinity of selected nanobodies, 11B12 and 15C4, was determined on P114 cells and was in nanomolar range (15.6 ± 2.6 and 10.9 ± 1.0, nM respectively) (Fig.1 B).

A

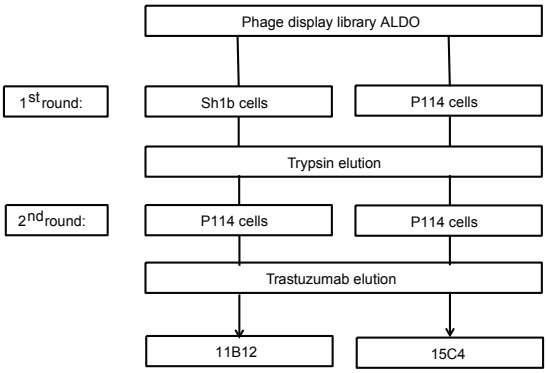

Fig.1. Selection of canine HER2-specific nanobodies. A. Selection protocol designed to obtain canine HER2 specific nanobodies. B. P114 cells were incubated with various concentrations of purified 11B12 and 15C4. Bound nanobodies were directly detected upon incubation with rabbit-anti-nanobody serum and goat-anti-rabbit-IRDye800 using Odyssey scanner. The graph shows fluorescence intensity at 800nm in triplicate ± SEM with increasing concentrations of the purified nanobody.

B

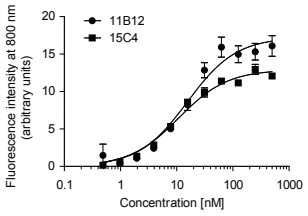

Characterization of anti-HER2 VHHs conjugated to IRDye800CW

As no lysines are present in the CDR regions of the two selected nanobodies, we conjugated the selected nanobodies in a random manner to the IRDye800CW fluorophore using an NHS ester. The obtained dye to protein ratio was 0.95 for both canine specific nanobodies and 1.15 in case of the R2-IR nanobody, which was used as a negative control in the *in vivo* part of the study. The amount of free dye present in the samples was lower than 10% as determined by SDS-PAGE (Fig. 2A). Upon random conjugation of the nanobodies with IRDye800CW-NHS, their apparent affinity decreased two fold in case of 11B12-IR (33.8 ± 4.4 nM) and remained in the same range in the case of 15C4-IR (14.6 ± 1.3 nM) when tested on P114 cells (Fig. 2 B and C). To determine whether the two selected nanobodies are binding to the same or overlapping epitopes we performed a competition assay. In this assay one of the nanobodies was incubated with an excess of the other one and no competition for binding was observed (Fig. 2D). This indicates that 11B12 and 15C4 recognize different, non-overlapping epitopes.

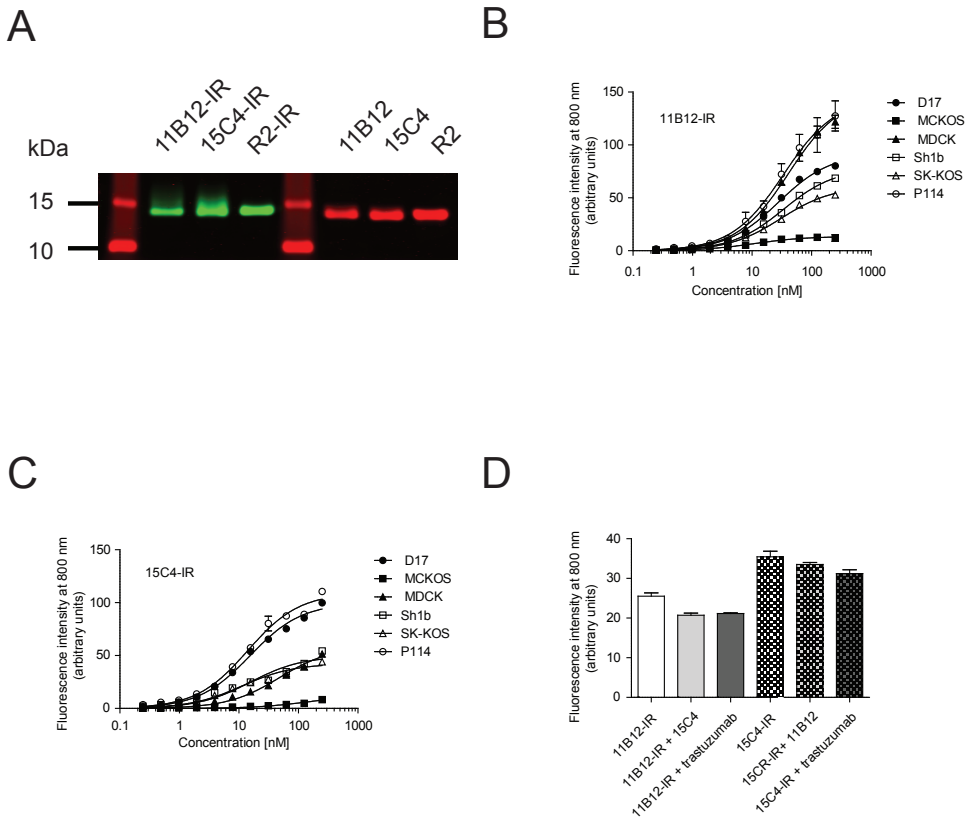

Fig.2. Selected nanobodies bind to canine cell lines with high affinity. A. SDS-PAGE of produces nanobodies prior to and after IRDye800CW-NHS conjugation. A panel of canine cells was incubated with various concentrations of 11B12-IR (B) or 15C4-IR (C). Bound nanobodies were directly detected using Odyssey scanner. The graph shows fluorescence intensity at 800 nm as mean ± SD (n=2) with increasing concentrations of the nanobody-IR. D. 10 nM of canine specific nanobody was incubated on P114 cells either alone, or with a 100 fold excess of non-conjugated canine specific nanobody or trastuzumab. After 2 hrs of incubation at 4^0C, the fluorescent signal of bound nanobody was detected using Odyssey scanner. The graph shows mean ± SD (n=3).

To confirm the specificity of the selected nanobodies for HER2, we performed a competition study using P114 cells. These cells were incubated with nanobody-IR in the presence of a 100 fold excess of trastuzumab (Fig. 2D). No decrease of the bound nanobody-IR signal was detected, suggesting that at current the binding specificity for HER2 is not yet confirmed. We also tested the binding of the two nanobodies to HER2-overexpressing human cells; surprisingly no binding to SKBR3 cells was detected (data not shown). More experiments are therefore needed to obtain confirmation of the binding specificity of these nanobodies.

Furthermore, we analyzed binding of these two nanobodies to a panel of selected canine cells. The highest maximal binding (B_{max}) was obtained with P114 cells and the lowest with MCKOS cells, which was similar for both 11B12-IR and 15C4-IR. However, differences in B_{max} were obtained with MDCK and SKKOS cells, where the incubation of the cells with 11B12-IR resulted in almost a two-fold higher B_{max} in comparison to incubation with 15C4-IR (146.5 ± 3.5 vs 75.8 ± 3.2 and 60.7 ± 1.1 vs 39.7 ± 1.4, respectively).

Nanobody-based in vivo optical molecular imaging

To evaluate the potential of the selected canine-specific nanobodies-IR as optical imaging probes, we performed a pilot study, where we used a small number of nude mice. The mice were injected at their hind legs with either high HER2 expressing P114 cells or with low HER2 expressing MCKOS cells. After formation of xenografts (Fig.S1), we injected intravenously the nanobody-IR constructs 11B12-IR, and 15C4-IR. As application of a combination of the two non-overlapping nanobodies conjugated to the same fluorophore has been shown previously to result in an increased fluorescent signal (chapter 3), besides the negative control (R2-IR nanobody), these mice were also injected with a combination of 11B12-IR and 15C4-IR. The injected mice were imaged at different time points post injection (p.i.) (Fig. 3A). Regions of interest (ROI) were drawn around the tumor and healthy tissue in proximity to the tumor, and total fluorescence of these ROI was used to calculate tumor to background ratios (T/B ratios). For both xenograft models, no clear IR fluorescence accumulation *in vivo* was found at the tumor site in case of the injected single nanobody-IR, but also not in case of two nanobodies-IR combination. Plotting T/B ratios over time confirms absence of nanobody-IR accumulation at the tumor (Fig. 3B).

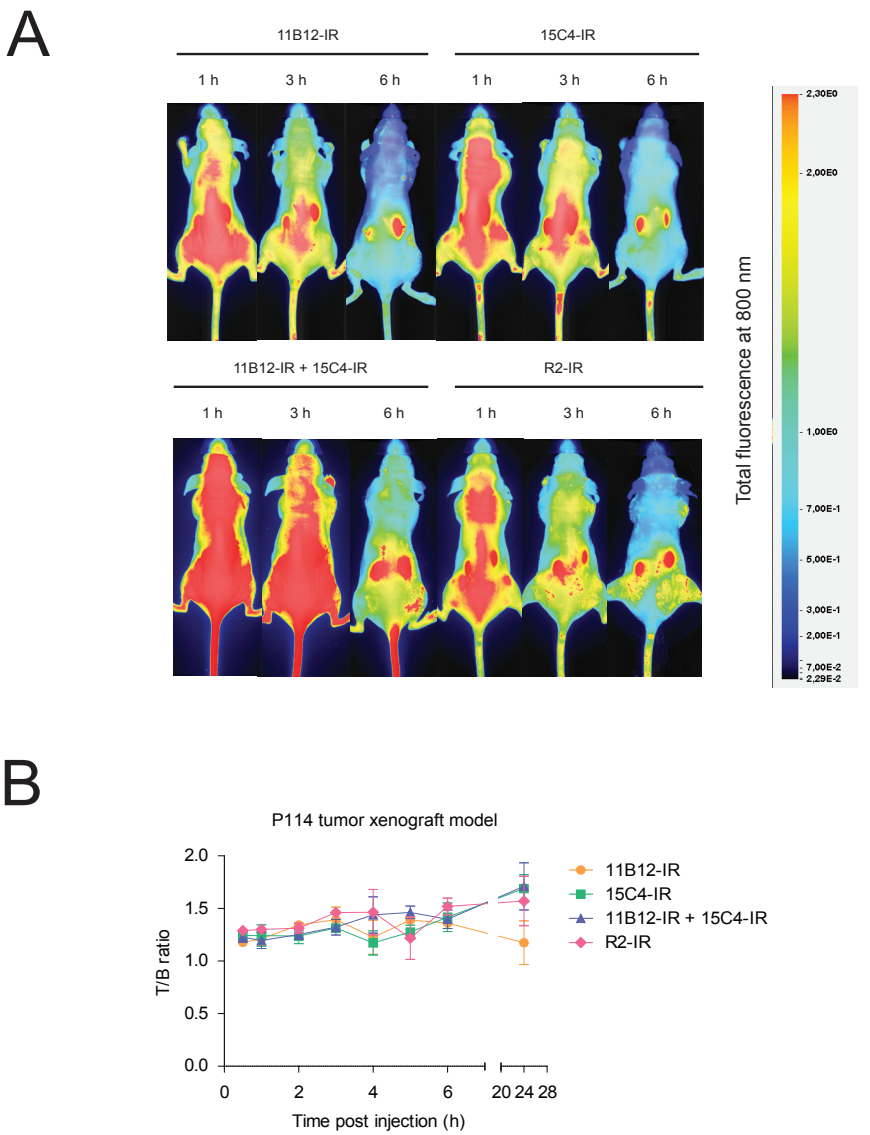

Fig.3. *In vivo* optical molecular imaging. Female nude BALB/c mice bearing P114 canine tumor xenografts at their hind leg were intravenously injected with 50 µg of randomly labeled 11B12-IR, 15C4-IR or a combination of both (100 µg in total) and a negative control nanobody R2-IR, and imaged under anesthesia up to 24 hrs p.i.. A. *In vivo* molecular optical imaging of P114 tumors. B. Mean ± SEM of tumor/background (T/B) ratio of P114 tumors imaged with 11B12-IR (n=3), 15C4-IR (n=3) and a combination of both nanobodies-IR (n=4) and R2-IR (n=2) were plotted.

We subsequently analyzed tumor accumulation *ex vivo*, in which the skin was removed from the tumor, resulting in an image-guided surgery model. After animals were sacrificed 24 hrs p.i., their

tumors were removed with a part of surrounding healthy tissue and imaged *ex vivo*. Importantly, clear fluorescent signal was observed at the tumor in case of the mice bearing P114 xenografts injected with 15C4-IR and a combination of both nanobodies-IR (Fig. 4A, red arrows point to the tumor). No fluorescence accumulation was observed in case of R2-IR, here employed as a negative control nanobody. A very weak fluorescent signal was obtained in mice xenografted with MCKOS tumors imaged upon 11B12-IR or 15C4-IR injection, which is in agreement with low B_{max} of employed nanobodies-IR obtained in binding study to MCKOS cells. Subsequently, ROIs were drawn in cancer and healthy areas and the *ex vivo* T/B ratio were calculated. For the P114 cells, a clear difference was observed between the R2-IR control group and 11B12-IR+15CR-IR group (Fig.4B).

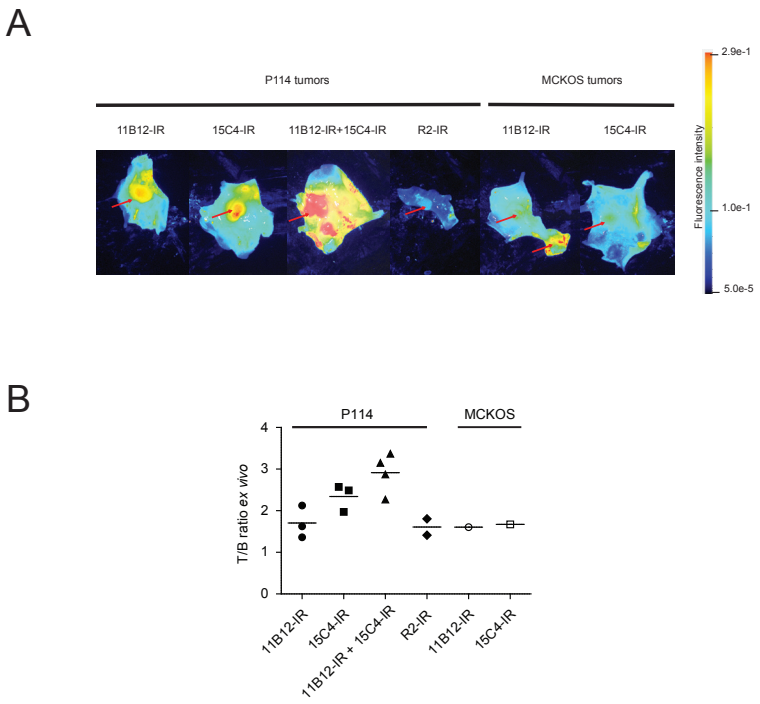

Fig.4. *Ex vivo* optical molecular imaging. A. Representative images of canine tumors surrounded by healthy tissue imaged *ex vivo* 24 hrs p.i. of 11B12-IR, 15C4-IR, a combination of both nanobodies-IR and R2-IR. B. Mean ± SEM of tumor/background (T/B) ratio of P114 tumors imaged *ex vivo* 24 hrs p.i. of 11B12-IR (n=3), 15C4-IR (n=3) and a combination of both nanobodies-IR (n=4) and R2-IR (n=2).

Discussion

Due to the fact that almost half of CMT has the potential to metastasize, the development of CMT-specific or cross-reactive nanobodies is of great importance in order to improve the detection of companion animals' cancer already at its early stages.

In this study we present the attempt to develop canine specific nanobodies for optical imaging. It was particularly challenging as several essential tools commonly used to select and evaluate obtained nanobodies were lacking. At the start of these studies, an ectodomain of canine HER2 was not available and PCR from a canine cDNA library was not successful. Moreover, several commercially available antibodies against HER2 were tested for their cross-reactivity by Western Blotting and none were cross-reactive. Therefore to develop nanobodies that recognize canine cancer biomarkers, such as HER2, we started with generation of phage display library by immunizing llamas with canine osteosarcoma HMPOS cells. The osteosarcoma is a commonly occurring highly malignant bone tumor, both in canine and human, shown to overexpress HER2 receptor [20]. A high excess of trastuzumab was used for specific elution of phages that are binding to canine HER2 expressing cells. As a result of this strategy, canine HER2 specific nanobodies recognizing the same or overlapping epitope as trastuzumab were expected to be eluted. Several nanobodies specifically binding to canine cells that are expressing different levels of HER2 were obtained. However, in the competition assay, trastuzumab could not compete off the binding of the best nanobodies. This indicates that the selected nanobodies do not recognize the same or overlapping epitope as trastuzumab. The maximal binding of the selected nanobodies was evaluated using a panel of canine cell lines, but the highest binding levels were obtained on P114 and Sh1b cells. Analogous studies were performed using trastuzumab and similar results were obtained, which suggests that selected here nanobodies may still be HER2-specific, but not trastuzumab competitors [7]. Further experiments are, however, required to determine the specificity of these nanobodies, which can be done by immunoprecipitation in combination with mass spectrometry analysis or using the, now available, canine HER2 ectodomain.

Different factors affect the intensity of the optical signal in the tumor. These include the number of fluorophores present on the nanobody. Conjugation of more than one fluorophore to the nanobody does not necessarily contribute to a higher intensity. First of all, conjugation of a fluorophore might affect the binding capacity of the nanobody, either by blocking nanobody binding to its antigen or by denaturation of a nanobody. Secondly, due to the small size, fluorophores in close proximity may quench the fluorescent signal. The signal also depends on the expression level of the targeted protein, which is demonstrated in this study by differences between P114 and MCKOS xenografts. Finally, the affinity of targeting moiety (i.e. nanobody) is of great importance. Due to their size, nanobodies are rapidly cleared from the body and the k_{on} should be sufficiently high to

allow for rapid binding to the tumor cells.

The binding affinities of both 11B12 and 15C4 were determined in a cell-based assay and for both nanobodies the apparent K_D was in low nanomolar range. Upon random dye conjugation only slight decrease of affinity was observed as could be expected due to lack of lysines in CDR regions of these nanobodies. Both 11B12-IR and 15C4-IR displayed a high degree of dye conjugation. The apparent affinity of both probes are in the nanomolar range upon random dye conjugation, but these values were higher than the apparent affinity of other nanobodies-IR reported to accumulate in human xenograft models [12,13].

The potential of the selected nanobodies as optical imaging probes was evaluated in a small-sized pilot *in vivo* experiment. For this experiment we used the P114 cells with a high HER2 expression level and MCKOS cells with low HER2 expression levels. No clear fluorescence was observed at the tumor site, when mice were imaged *in vivo*. However, after removal of the skin, a clear fluorescent signal was seen in the P114 xenografts, when the 15C4-IR or nanobody-IR combination was used. No fluorescence was observed in mice xenografted with the MCKOS cells, which is in agreement with the data showing low maximal binding of selected nanobodies to MCKOS cells *in vitro*. Tumor accumulation of the single nanobody observed for 15C4-IR, could be partially explained by its 2 fold higher apparent affinity than that of 11B12-IR. This specific accumulation of the probe revealed by *ex vivo* analysis of tumors, suggests that perhaps expression of the targeted antigen is too low to enable *in vivo* imaging.

Nanobodies have been shown to be feasible for both diagnosis and for use in an intraoperative setting [12,13]. Optical molecular imaging does not allow performing whole body scans, necessary to detect tumors located deep in the body, however, positron emission tomography (PET) could be applicable. The development of nanobody conjugated to a radionuclide for PET or SPECT imaging of human breast cancer have been shown by Xavier et al and Vaneycken et al. [10,21]. Testing of here presented nanobodies for their potential as PET/SPECT imaging probes would be of great importance broadening veterinary diagnostic options.

In conclusion, we have selected nanobodies binding to HER2 expressing canine cells. Pilot experiments show promising results with respect to optical imaging of HER2 expressing tumor cells in an invasive, surgical setting. Further experiments are required to confirm specificity for HER2 receptor and to improve the optical signaling obtained in the xenografts.

This development of canine-specific or cross-reactive nanobodies can greatly improve the diagnosis, management and therapy of companion dogs broadening currently available options in veterinary oncology. In addition, the developed canine-specific nanobodies could be used to target the delivery of toxic compounds to the tumor site. Such approaches have successfully been preclinically assessed for human cancer targeting, employing various nanocarries such as liposomes, micelles or albumin nanoparticles [14-17]. Alternatively, nanobody-drug conjugates could also be a

relevant approach to develop new therapies for canine tumors.

Supplementary information

Results

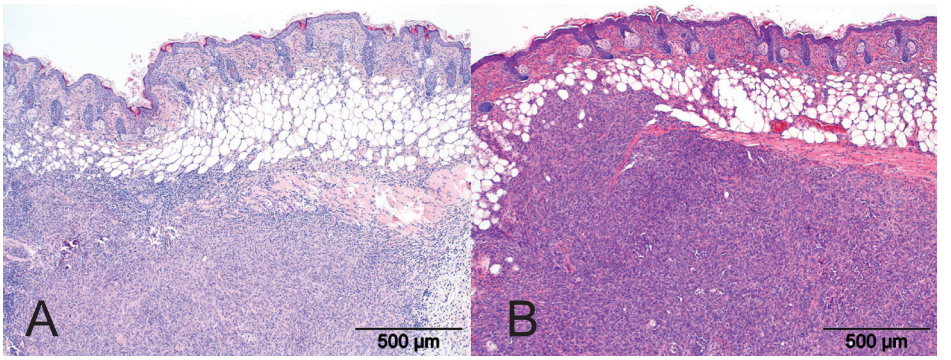

Fig.1S. Hematoxylin and eosin staining of tumor sections. A. P114, B. MCKOS.

References

1. Shafiee R, Javanbakht J, Atyabi N *et al.*: Diagnosis, classification and grading of canine mammary tumours as a model to study human breast cancer: an Clinico-Cytohistopathological study with environmental factors influencing public health and medicine. *Cancer. Cell. Int.* 13(1), 79 (2013).

2. Pinho SS, Carvalho S, Cabral J, Reis CA, Gartner F: Canine tumors: a spontaneous animal model of human carcinogenesis. *Transl. Res.* 159(3), 165-172 (2012).

3. Rivera P, von Euler H: Molecular biological aspects on canine and human mammary tumors. *Vet. Pathol.* 48(1), 132-146 (2011).

4. Martin de las Mulas J, Ordas J, Millan Y, Fernandez-Soria V, Ramon y Cajal S: Oncogene HER-2 in canine mammary gland carcinomas: an immunohistochemical and chromogenic in situ hybridization study. *Breast Cancer Res. Treat.* 80(3), 363-367 (2003).

5. Dutra AP, Granja NV, Schmitt FC, Cassali GD: c-erbB-2 expression and nuclear pleomorphism in canine mammary tumors. *Braz. J. Med. Biol. Res.* 37(11), 1673-1681 (2004).

6. Rungsipipat A, Tateyama S, Yamaguchi R, Uchida K, Miyoshi N, Hayashi T: Immunohistochemical analysis of c-yes and c-erbB-2 oncogene products and p53 tumor suppressor protein in canine mammary tumors. *J. Vet. Med. Sci.* 61(1), 27-32 (1999).

7. Singer J, Weichselbaumer M, Stockner T *et al.*: Comparative oncology: ErbB-1 and ErbB-2 homologues in canine cancer are susceptible to cetuximab and trastuzumab targeting. *Mol. Immunol.* 50(4), 200-209 (2012).

8. Hassanzadeh-Ghassabeh G, Devoogdt N, De Pauw P, Vincke C, Muyldermans S: Nanobodies and their potential applications. *Nanomedicine (Lond)* 8(6), 1013-1026 (2013).

9. Muyldermans S: Nanobodies: natural single-domain antibodies. *Annu. Rev. Biochem.* 82, 775-797 (2013).

10. Xavier C, Vaneycken I, D'huyvetter M *et al.*: Synthesis, preclinical validation, dosimetry, and toxicity of 68Ga-NOTA-anti-HER2 Nanobodies for iPET imaging of HER2 receptor expression in cancer. *J. Nucl. Med.* 54(5), 776-784 (2013).

11. Vaneycken I, Devoogdt N, Van Gassen N *et al.*: Preclinical screening of anti-HER2 nanobodies for molecular imaging of breast cancer. *FASEB J.* 25(7), 2433-2446 (2011).

12. Kijanka M, Warnders FJ, El Khattabi M *et al.*: Rapid optical imaging of human breast tumour xenografts using anti-HER2 VHHs site-directly conjugated to IRDye 800CW for image-guided surgery. *Eur. J. Nucl. Med. Mol. Imaging* 40(11), 1718-1729 (2013).

13. Oliveira S, van Dongen GA, Stigter-van Walsum M *et al.*: Rapid visualization of human tumor xenografts through optical imaging with a near-infrared fluorescent anti-epidermal growth factor receptor nanobody. *Mol. Imaging* 11(1), 33-46 (2012).

14. Heukers R, van Bergen En Henegouwen PM, Oliveira S: Nanobody-photosensitizer conjugates for targeted photodynamic therapy. *Nanomedicine* (2014).

15. Talelli M, Rijcken CJ, Oliveira S *et al.*:

Nanobody-shell functionalized thermosensitive core-crosslinked polymeric micelles for active drug targeting. *J. Control. Release* 151(2), 183-192 (2011).
16. Altintas I, Heukers R, van der Meel R *et al.*: Nanobody-albumin nanoparticles (NANAPs) for the delivery of a multikinase inhibitor 17864 to EGFR overexpressing tumor cells. *J. Control. Release* 165(2), 110-118 (2013).
17. Oliveira S, Schiffelers RM, van der Veeken J *et al.*: Downregulation of EGFR by a novel multivalent nanobody-liposome platform. *J. Control. Release* 145(2), 165-175 (2010).
18. Roovers RC, Laeremans T, Huang L *et al.*: Efficient inhibition of EGFR signaling and of tumour growth by antagonistic anti-EFGR Nanobodies. *Cancer Immunol. Immunother.* 56(3), 303-317 (2007).
19. Vermeulen JF, van Brussel AS, van der Groep P *et al.*: Immunophenotyping invasive breast cancer: paving the road for molecular imaging. *BMC Cancer* 12, 240-2407-12-240 (2012).
20. Flint AF, U'Ren L, Legare ME, Withrow SJ, Dernell W, Hanneman WH: Overexpression of the erbB-2 proto-oncogene in canine osteosarcoma cell lines and tumors. *Vet. Pathol.* 41(3), 291-296 (2004).
21. Vaneycken I, Govaert J, Vincke C *et al.*: In vitro analysis and in vivo tumor targeting of a humanized, grafted nanobody in mice using pinhole SPECT/micro-CT. *J. Nucl. Med.* 51(7), 1099-1106 (2010).

Chapter 5

Optimizing immuno-gold labeling protocols for nanobody-based detection of HER2 in breast cancer cells using immuno-electron microscopy

Marta M. Kijanka [*]
Elly G. van Donselaar [*]
Wally Müller
Mohamed el Khattabi
Theo C. Verrips
Paul M.P. van Bergen en Henegouwen
Jan A. Post

[*] *equal contribution*

Manuscript in preparation

Abstract

Introduction: Immuno-electron microscopy is commonly performed with the use of monoclonal antibodies. However, it is essential to further downsize the gold targeting moieties in order to improve the gold labeling accuracy, especially in case of indirect gold labeling. Here we evaluate the feasibility of antibody fragments indicated as nanobodies for immuno-electron microscopy.

Methods: We previously described the nanobody 11A4 which binds with high affinity and specificity to HER2 expressed in breast cancer cells. To obtain optimal immuno-gold labelling we tested the influence of fixation and several blocking solutions, such as bovine serum albumin, skimmed milk, acetylated bovine serum albumin, cold water fish gelatine, and a combination of cold water fish gelatine with acetylated bovine serum albumin. This optimized protocol was applied for post-embedment, Tokuyasu cryosections labeling as well as for pre-embedment labeling of HER2 in SKBR3 cells for both transmission and scanning electron microscopy as well as light microscopy.

Results: We show that formaldehyde fixation after incubation with the anti-HER2 nanobody or monoclonal antibody, trastuzumab does not affect their binding to the antigen. Among all tested blocking agents the best results were obtained with a mixture of cold water fish gelatine and acetylated bovine serum albumin, which allowed minimizing a-specific interactions (preventing the background labelling) with preservation of specific interactions at the same time.

Conclusion: We developed an optimized nanobody-based protocol for HER2 detection in Tokuyasu cryosections as well as for pre-embedment labeling of HER2 expressing cells for both transmission and scanning electron microscopy.

Introduction

Immuno-electron microscopy combines the localization of a defined protein at high resolution with fine structural details of the cell. Gold particles are the most often used electron dense markers, which can be prepared in different sizes and bound to specific antibodies enabling direct labeling of the protein of interest [1,2]. For indirect labeling, gold particles are bound to either protein A or an anti-IgG immunoglobulin resulting in general markers for immuno-electron microscopy. As IgGs have a molecular size of 14.2 nm by 8.5 nm, gold labeling occurs within a distance of approximately 10 nm from the target. In order to improve the accuracy of gold labeling, especially in case of an indirect gold labeling, further downsizing of the targeted gold particles is essential.

Here we investigated the possible application of a novel type of antibody fragments indicated as nanobody in immuno-electron microscopy. Nanobodies are defined as the variable domains of the heavy chain of heavy chain-only antibodies that are found in the members of the *Camelidae* family [3,4]. They are also referred to as VHHs or as single domain antibodies. Nanobodies contain three complementarity determining regions (CDRs) or hypervariable loops that are located between conserved framework regions [5]. In contrast to the six CDRs of the conventional antibodies, nanobodies have only three CDRs to participate in antigen recognition. Despite the smaller surface area of the paratope, nanobodies can bind with high affinity and high specificity to their target molecule. In the nanobody, the CDR3 is usually extended, which partially compensates for the reduced number of CDRs. The long CDR3 enables nanobodies to enter cavities present on the surface of the antigen causing nanobodies to bind predominantly conformation dependent epitopes [3,5]. Finally, nanobodies can be easily selected from immune libraries using phage display [5].

We have recently selected several HER2 targeted nanobodies from an immune MCF7 library [6]. In the current study we tested the feasibility of the recently described HER2 targeted nanobody, 11A4, for immuno-EM applications on HER2 positive human breast cancer cells. HER2 belongs to the ErbB family of receptor tyrosine kinases and is known to play an important role in breast cancer [7]. Parameters known to affect specificity of gold labeling were tested in order to obtain an optimized protocol for HER2 gold labeling using nanobodies. This protocol was used for post-embedment, on-section labeling of Tokuyasu cryosections. Furthermore, we show the feasibility of this nanobody to detect HER2 by its pre-embedment labeling in SKBR3 cells for both transmission (TEM) and scanning electron microscopy (SEM).

Materials and Methods

Cell lines and culture conditions

Human HER2-positive breast cancer cells, SKBR3, and HER2-negative breast cancer cells, MDA-MB-231, were purchased from the American Type Culture Collection (ATCC, Manassas, VA) and cultured in DMEM (Gibco) supplemented with 7.5% (v/v) FBS, 100 IU/ml penicillin, 100 mg/ml streptomycin and 2 mM L-glutamine at 37°C in a humidified atmosphere containing 5% CO_2.

Nanobody production

HER2 targeted nanobody, 11A4, was produced as described before [6]. Briefly, gene encoding the nanobody were re-cloned into pQVQ72 expression vector (kindly provided by QVQ B.V.). Production of nanobodies was induced by addition of 1 mM IPTG when bacteria reached log-phase. HER2-specific nanobody was purified from the periplasmic fraction by protein A affinity chromatography using a HiTrap protein A HP column (GE Healthcare, Zeist, The Netherlands) on the ÄKTAxpress system (GE Healthcare, Zeist, The Netherlands).

Binding study on SKBR3 and MDA-MB-231

SKBR3 or MDA-MB-231 cells were seeded at the density of 20.000 cells/well two days before the assay. Cells were fixed with 4% formaldehyde (FA) in PHEM (composed of 60 mM PIPES [Merck], 25 mM HEPES [Merck], 10 mM EGTA [Sigma-Aldrich], and 2 mM MgCl2 [Merck], pH adjusted to 6.9) buffer for 30 min at RT either before or after 1.5 hr incubation with a serial two-fold dilution of 11A4 nanobody (200 nM – 0.19 nM range) or monoclonal antibody (mAb), trastuzumab (10 nM – 0.009 nM) at 4^0C. Fixation was stopped by a 10 min incubation with 100 mM glycine. Cells were blocked with 2% milk powder in PBS (MPBS) for 30 min at RT, followed by 1 hr incubation at RT with rabbit anti VHH protein G purified serum 976 (home-made) in 2% MPBS and 1 hr incubation at RT with goat-anti-rabbit-IR800. Upon 2 consecutive washing steps with PBS, the fluorescent signal was detected with an Odyssey scanner.

Preparation of Tokuyasu samples

SKBR3 cells and MDA-MB-231 cells were grown in culture dishes to 80-90% confluency and then fixed with FA (final concentration 2% (w/v)). After 15 minutes the fixative was replaced by fresh 4% (w/v) FA in PHEM buffer (60 mM Pipes; 25 mM Hepes; 10 mM EGTA; 2 mM $MgCl_2$, pH 6.9,

[8]). Fixation was continued overnight at 4°C. After washing the cells with PHEM buffer, the cells were scraped in PHEM containing 1% (w/v) gelatin (Gelatine 250 LP30; I.P.D., Nijmegen, The Netherlands), transferred to 1.5 ml microcentrifuge tubes (Bioplastics) and spun down at 37°C for 3 minutes, 1200 rpm. After removing the supernatant the pellet was resuspended in warm 12% gelatin in PHEM buffer and left for 5 minutes in an incubator (type B15, Hereaus) at 37°C, while gently mixing two times on a vortex during this incubation. Next the cells were centrifuged for 3 minutes, 3000 rpm at 37°C after which the supernatant was removed. The remaining 12% gelatin in PHEM buffer was then almost completely removed. After 15 minutes warm (37°C) fresh 12% gelatin in PHEM was added and allowed to solidify. After gelation blocks of ~1 mm^3 were prepared on an ice-cooled metal plate under a stereo-microscope. The blocks were transferred to 2.3 M sucrose (Merck) in PHEM buffer and placed on a rotator at 4°C. After overnight infiltration the blocks were mounted on specimen holders and plunge frozen in liquid nitrogen.

Sectioning of Tokuyasu samples for immuno-fluorescence labeling

Following trimming of the samples on a glass knife at -100°C with a cryo-ultramicrotome (UC6/FC6;Leica Microsystems) to a suitable block shape, 500 nm cryosections were cut on a glass knife at the same temperature. Flat, glossy-looking sections were shifted from the knife edge with a guinee pig hair mounted on a wooden stick and picked up with a wire loop and a drop of a 1:1 mixture of 2% (w/v) methylcellulose (Sigma) and 2.3 M sucrose in 0.1 M phosphate buffer pH 7.4. Upon thawing, the sections were mounted in a wax-marked area on a silane-coated slides, covered with 2.3 M sucrose in 0.1 M phosphate buffer and stored at 4°C until immuno-fluorescence labeling.

Sectioning of Tokuyasu samples for immuno-gold labeling

Following trimming of the samples on a glass knife at -100°C with a cryo-ultramicrotome (UC6/FC6;Leica Microsystems) to a suitable block shape, 80 nm cryosections were cut on a dry diamond knife (Element Six B.V.) at the same temperature and under control of an ionizer (Static line; Leica Microsystems). Flat ribbons of glossy-looking sections were shifted from the knife edge with a guinee pig hair mounted on a wooden stick and picked up with a wire loop and a drop of a 1:1 mixture of 2% (w/v) methylcellulose (Sigma) and 2.3 M sucrose in 0.1 M phosphate buffer pH 7.4. Upon thawing, the sections were mounted on formvar (Fluka)-coated, carbon-stabilized copper grids (100 mesh hexagonal copper grids, Stork-Veco B.V.) and stored at 4°C until immuno-gold labeling.

Immuno-gold (IG) labeling of Tokuyasu cryosections

Grids containing sections of SKBR3 cells or MDA-MB-231 cells were placed on PBS at 37°C for 60 min to let the pick-up droplet diffuse away and melt the solidified gelatin present between the cells. The following steps were carried out at RT. Grids with sections were washed five times on drops of PBS containing 20 mM glycine (Merck) and blocked for 15 min on drops of PBS containing 1% BSA (Bovine Serum Albumin Fraction V, Sigma-Aldrich) or 0.225% (v/v) CFG + 0.1% (v/v) BSA-c (CFG: gelatin from cold water fish skin 45% in water (Sigma-Aldrich); BSA-c: acetylated Bovine Serum Albumin 10% in water (Aurion)) to prevent a-specific labeling. After blocking the grids with sections, they were incubated for 60 min on drops of 5 µl of 1, 3 or 10 µg/ml 11A4 nanobody in blocking solution followed by 5 washes on drops of 10x diluted blocking solution. Next the grids were incubated for 60 min on drops of 5 µl Rabbit anti-Llama antibody (RαVHH, 1 mg/ml, Rabbit 1219, QVQ, Utrecht, The Netherlands) diluted in blocking solution. After six washes on drops of 10x diluted blocking solution the grids with sections were incubated for 20 min on drops of 7 µl of Proteïn A coupled to 15 nm Gold (PAG15; CMC, Utrecht, The Netherlands), 1:60 diluted in blocking solution, washed on drops of PBS and fixed for 5 minutes with 1% glutaraldehyde (Taab) in PBS. The sections were then poststained for 5 minutes with 2% Uranyl Acetate (EMS) in 0.15 M Oxalic Acid (Merck) pH 7.4. Subsequently, after a quick wash, the grids with sections were transferred to drops of embedding solution containing 1.8% methyl cellulose (Sigma) and 0.4% uranyl acetate (EMS) in distilled water on parafilm on an ice-cooled metal plate. After 5-10 minutes incubation the grids with sections were picked up in a wire loop. Most of the excess of the viscous embedding solution was drained away on filterpaper after which the grids with sections were air-dried in a thin layer of embedding solution. The sections were viewed in a JEM 1010 (Jeol) at 80kV.

Immuno-fluorescence labeling on Tokuyasu cryosections

Upon preparation cryo-sections of SKBR3 and MDA-MB-231 cells (500 nm thick) were covered with a layer of 2% methylcellulose and 2.3 M sucrose and stored at 4°C until further use. Before labeling, sucrose was removed in subsequent washing steps and sections were incubated for 5 min at RT with sodium borhydride (1 mg/ml) in PBS followed by a wash with glycine in PBS and blocked twice for 5 min at RT with blocking solution (either 0.225% CFG + 0.1% BSA-c or 10% BSA in PBS). Sections were incubated with 1, 3 or 10 µg/ml of 11A4 nanobody in blocking solution for 1 hr at RT, followed incubation with first rabbit anti-VHH purified serum (R1219, 1:50, 1 h, RT) and then goat anti-rabbit-Alexa488 (1:100, 1 h, RT), both diluted in blocking solution. Sections were fixed with 4% FA+ 0.2% GA in 0.1 M phosphate buffer pH 7.4 and stained with DAPI (1:500, 5 min) before embedment in ProLong Gold.

Transmission electron microscopy of pre-embedment immuno-gold labeled SKBR3 cells

Labeling. SKBR3 cells cultured for three days on carbon-coated aclar (Aclar Embedding Film 2 mm thickness, EMS) were fixed by adding a volume of 4% FA in 0.1 M PHEM buffer pH 6.9 to the dish with cells (final concentration in the dish is 2% FA). After 15 min of fixation at RT the fixative/ medium mixture was replaced by fresh 4% FA in 0.1 M PHEM buffer pH 6.9. The cells were fixed for 2 hrs at RT followed by 16 hrs at 4°C. After washing six times 5 min with 0.15 M PBS pH 7.4 (137 mM NaCl; 2.7 mM KCl; 8.1 mM Na_2HPO_4 x 2 H_20; 1,7 mM NaH_2PO_4 x H_20), free aldehyde groups were quenched with 100 mM NH_4Cl in PBS for 10 min, after which the SKBR3 cells were washed twice in PBS for 5 minutes and exposed for 15 min to 0.225% (v/v) gelatin from cold water fish skin 45% in water (CFG) + 0.1% (v/v) acetylated Bovine Serum Albumin (BSA-c, 10% in water, Aurion) to prevent a-specific labeling. To immuno-gold label the HER2 receptors on the surface of the SKBR3 cells, the cells were incubated with the HER2 targeted nanobody 11A4 (VHH-11A4, 340 μg/ml, QVQ, Utrecht, The Netherlands) at 3 and 10 μg/ml diluted in 0.225 % (v/v) CGF + 0.1% (v/v) BSA-c/PBS) for 1 hr at RT. After three times 10 min washing with 0.0225% (v/v) CFG + 0.01% (v/v) BSA-c/PBS, Rabbit anti-Llama antibody (RαVHH, 1mg/ml, Rabbit 1216, QVQ, Utrecht, the Netherlands) 1:50 in 0.225 % (v/v) CGF + 0.1% (v/v) BSA-c/PBS was used as bridging antibody for 1 hr at RT. Thereafter the cells were washed three times 10 min with 0.0225% (v/v) CFG + 0.01% (v/v) BSA-c/PBS, and subsequently incubated with protein-A gold 15nm (PAG15, CMC, Utrecht, the Netherlands) 1:60 diluted in 0.225% (v/v) CFG + 0.1% (v/v) BSA-c/PBS for 20 min at RT to mark the antigen-antibody complex. Thereafter the cells were thoroughly washed for three times 10 min with PBS and three times 5 min with PBS.

Positive control. As a positive control SKBR3 cells were blocked with 1% (w/v) BSA (Albumin, Bovine fraction V) in PBS, then HER2 receptors present on the surface of SKBR3 cells were labeled with 10 μg/ml Herceptin (Roche) in 1% BSA/ PBS, after washing, as bridging antibody polyclonal Rabbit anti-Human IgG (code-Nr. A 0424, Dako) 1:2500 diluted in 1% (w/v) BSA/ PBS was used. After the next washing to mark the location of the HER2 receptors protein-A gold 15 nm was used (PAG15, CMC, Utrecht, The Netherlands) 1:60 diluted in 1% BSA/PBS. All washing steps were done with 0.1% (w/v) BSA in PBS.

Post-fixation. After labeling, the SKBR3 cells were fixed for 1 hr at RT or overnight, or over-weekend at 4 °C in a modified Karnovsky fixative [9],which was concocted as follows: 5 ml 4% FA; 2 ml 0.4 M sodium cacodylate buffer pH 7.2, 1 ml 25% glutaraldehyde, 0.5 ml 5 mM $CaCl_2$, 0.5 ml 10mM $MgCl_2$ and 1 ml distilled water for 10 ml fixative pH 7.2. After washing with 0.1 M sodium cacodylate buffer pH 7.2, SKBR3 cells were post fixed for 1 hr on ice in 1% OsO_4 (w/v) + 1.5% K_4FeCN_6 (w/v) in 0.08 M sodium cacodylate buffer pH 7.2.

Dehydration. After rinsing 8 times with distilled water the samples were dehydrated in an increasing

series of Ethanol, i.e. 30%, 50%, 70%, 80%, 90%, 96% with each step two times 5 minutes, thereafter 100%, six times 5 minutes at RT. Anhydrous ethanol was made by 100 ml 96% Ethanol and 2 ml acidified 2,2-dimethoxypropane (DMP). Acidified DMP was made by adding 50 µl 37% HCl to 50 ml DMP [10].

Embedment. Samples were infiltrated with a mixture of anhydrous ethanol-epon 1:1 for 18 hrs; 1:2 for 8 hrs; 1:3 for 18 hrs, and subsequently infiltrated with pure epon for 8, 18 and 6 hrs, each step with fresh pure epon (Epoxy embedding medium, Araldite hardener 964, hardener MNA and accelerator DMP-30). The SKBR3 cells with supporting aclar were placed in the cavities of an embedding mould (Agar Scientific) with the cells facing up. The cavities were filled to the top with epon, and polymerized for 72 hrs at 60^0C. Thereafter the specimen blocks were taken out of the mould, and the contour of the supporting aclar from each block was first scratched with the sharp corner of a single edged GEM razor blade, after which the aclar could be lifted up with the tip of a fine forceps and peeled off from the epon block. Subsequently, all the blocks without the supporting aclar were put back into the mould with sample side up, and on each block a droplet of epon was placed on the area, where the aclar was removed. Then the blocks were further polymerized for 24 hrs at 60^0C.

Ultra-microtomy. Epon sections of 50-55 nm were cut on a diamond knife (Diatome, Hatfield, PA, USA) with an Ultracut E ultramicrotome (Leica Microsystems, Vienna, Austria). Sections were picked up with a loop and transferred to formvar-coated, carbon-stabilized copper grids (100 mesh hexagonal copper grids, Stork Veco B.V., The Netherlands) and post-stained with 7% (w/v) uranyl acetate (EMS) in 70% methanol (Merck) for 6 min, and with Reynolds' lead citrate (Lead nitrate, Merck; tri-Sodium citrate dehydrate, [11]) for 2 min. The thin sectioned and stained samples were viewed with a transmission electron microscope JEM 1010 (Jeol Electron Microscope 1010, JEOL (Europe) B.V., The Netherlands) at an acceleration voltage of 80 kV.

Scanning electron microscopy of immuno-gold labeled SKBR3 cells

Once the SKBR3 cells were immuno-gold labeled and post-fixated for 1 hr on ice in 2% OsO_4 (w/v) in 0.1 M sodium cacodylate buffer pH 7.2, the samples were transferred into specimen baskets after washing 8 times with distilled water and subsequently dehydrated in an increasing series of ethanol as described in the section pre-embedment labeling above, and further processed for scanning electron microscopy. Samples were transported in the specimen baskets (Plastic capsules D 13 x H 18 mm fine mesh base, Leica) to a CPD-300 Leica critical point drying apparatus (Leica Microsystems, Vienna, Austria) with a CPD-chamber that was half filled with anhydrous ethanol and a 1/2-height-teflon holder. The specimen baskets with samples were rapidly put into the CPD-chamber in a way that they were still submerged in anhydrous ethanol. Once this holder was filled with the samples, a 1/3-height-teflon holder was put in the CPD-chamber and was filled with the remaining specimen baskets with

samples. On top of this 1/3-height-teflon holder, a 1/6-height-filler was placed. After closing the CPD-chamber the samples were critical point dried according to the CPD-300 Leica manual with liquid CO_2 as the transitional fluid. We used the following program settings: Automatic On, Stirrer On and 100% CO_2 in, with speed slow and a delay of 120 seconds; exchange with speed 5 and cycles 12; CO_2 out, heat slow and gas out with speed 40%. The total CPD processing time was about 2 hrs and 10 min. The dried specimens were mounted on Aluminum stubs (agar) containing a carbon adhesive (agar), and were subsequently coated with 1 nm Pt by the use of a Leica ACE600 sputter coater according to the Leica ACE600 manual (Leica Microsystems, Vienna, Austria). Thereafter the samples were viewed in an XL30 scanning electron microscopy equipped with a field emission gun (FEI Europe, Eindhoven, The Netherlands) at an acceleration voltage of 5 kV and a WD of 2.8 mm.

Results

Effect of formaldehyde fixation on binding of HER2-targeted nanobody

To evaluate the application of nanobodies in electron microscopy we used nanobody 11A4, which binds to cell surface-located HER2 with an affinity of 400 pM [6]. In resting cells, HER2 is expressed predominantly at the plasma membrane as internalization of this receptor tyrosine kinase is blocked [14]. As a result, plasmamembrane staining is considered as specific while cytoplasmic staining can be considered as aspecific. During the course of these experiments we used trastuzumab, a humanized mAb binding to human HER2, as a positive control. Essential for the preservation of the cellular structure for EM is the fixation, which is usually done with aldehydes. We first evaluated the effect of formaldehyde fixation on the binding of both the HER2-targeted nanobody and the mAb to the HER2 expressed by SKBR3 cells. Cells were incubated with different concentrations of the nanobody or mAb either before or after fixation, and their binding was detected by indirect fluorescence at 800 nm (Fig. 1). A good binding to SKBR3 cells was observed for both nanobody and mAb with an apparent affinity in the low nanomolar range. No differences were found between samples fixed prior to or after nanobody/mAb incubation, indicating that no significant effect of fixation of the cells with formaldehyde was observed. In control experiments with HER2 negative cells, MDA-MB-231, no binding of either nanobody or mAb was found irrespective of fixation time (data not shown).

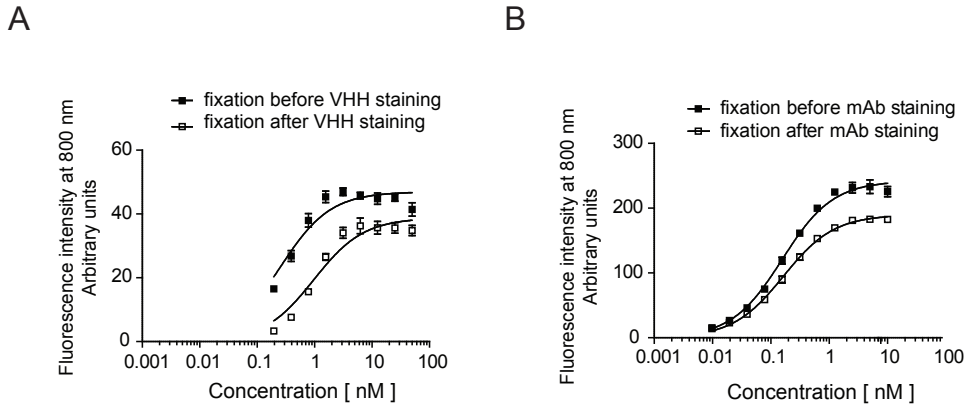

Fig.1. Effect of formaldehyde fixation on binding of 11A4 nanobody or trastuzumab. SKBR3 cells were either fixed with 4% formaldehyde prior to or after immune incubations with VHH (A) or mAb (B). Immune complexes were detected by secondary and tertiary antibodies conjugated to fluorophore IRDye800CW.

5

Optimization of blocking solution for on-section immuno-gold labeling

The on-section labeling method using Tokuyasu cryosections is ideal to label both intra- and extracellular proteins. However, this method is also challenging with respect to the occurrence of a-specific labeling. To obtain optimal immuno-gold labeling of cryosections, the background labeling should be minimized without hampering specific interactions at the same time. We have evaluated several blocking solutions commonly used for post-embedment labeling of antigens for TEM. SKBR3 cells were fixed using formaldehyde and processed for cryosectioning according to the Tokuyasu method [12,13]. Thick (500 nm) cryosections were incubated with different concentrations of HER2-targeted nanobody and the level of background staining was evaluated in wide field fluorescence microscopy. Two different blocking solutions were tested, bovine serum albumin (BSA) and the combination of cold water fish gelatin and acetylated bovine serum albumin (CFG/BSA-c) in PBS. No fluorescence was observed on sections which were blocked with either of the two solutions when the primary incubation was omitted. This indicates that the fluorescent secondary antibodies do not cause aspecific binding under these conditions (Fig. 2). In the presence of different concentrations of nanobody, BSA alone could not prevent a-specific binding, which was found both on sections from HER2 positive (SKBR3) and negative (MDA-MB-231) cells. Even the lowest concentration of nanobody (1 μg/ml) resulted in considerable background staining of sections from MDA-MB-231 cells (Fig. 2A). However, a blocking solution composed of a mixture of both CFG and BSA-c could reduce the a-specific interactions on these two cell types, even at high nanobody concentrations (Fig. 2B). Much less background was present on SKBR3 cryosections, whereas the specific signal was retained, and hardly any background could be detected on the HER2 negative cells, especially when

the lowest nanobody concentration was used. We also found that in order to preserve the fluorescent signal for a longer time during storage at 4°C an additional post-fixation could prevent dissociation of the immune complexes. For this reason sections were post-fixed upon incubation with secondary antibody (goat anti-rabbit-Alexa488) before DAPI staining and embedment in ProLong Gold.

In the next step we evaluated the suitability of these blocking agents for nanobody-based

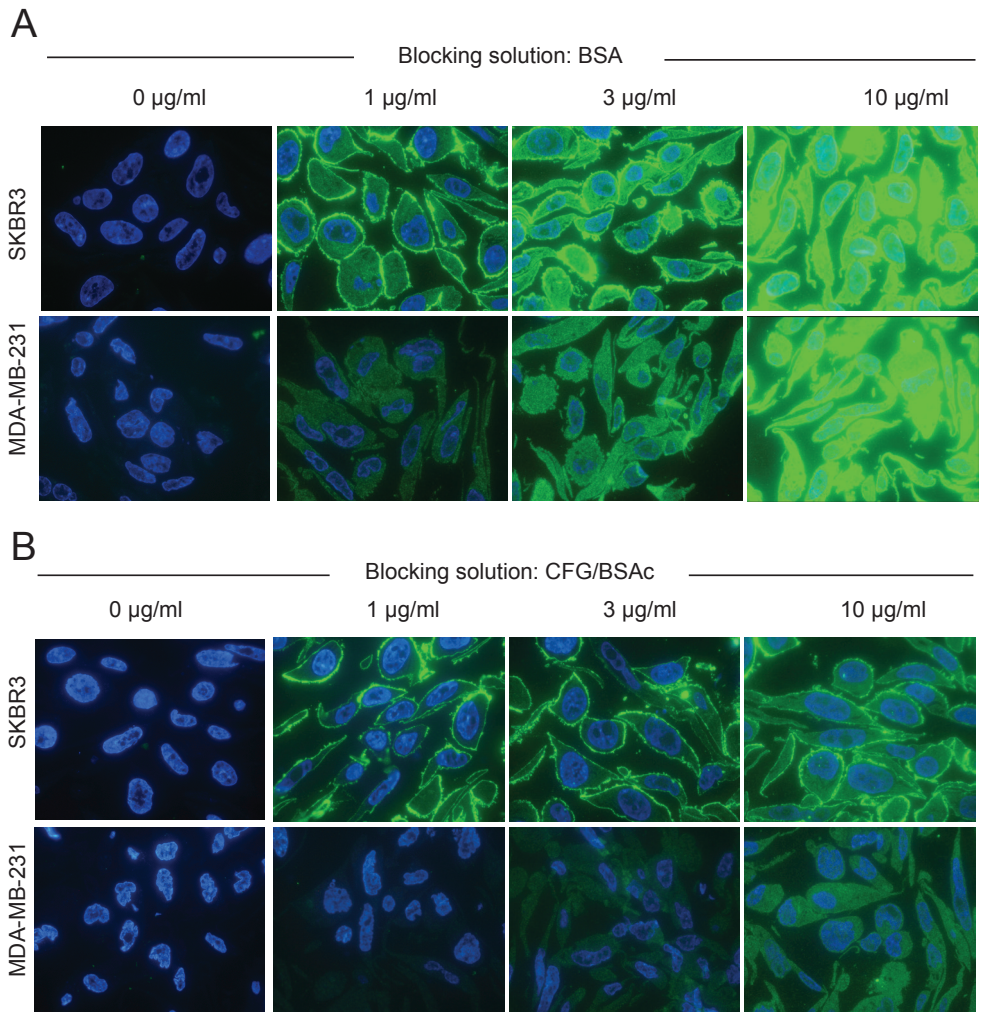

Fig. 2. Comparison of different blocking solutions by light microscopy. Thick cryosections of 500 nm of HER2-positive SKBR3 cells and HER2-negative MDA-MB-231 were incubated with different concentrations of nanobody (1 µg/ml, 3 µg/ml, 10 µg/ml) in the presence of either (A) bovine serum albumin (BSA) or (B) a mixture of cold water fish gelatin and acetylated bovine serum albumin (CFG/BSA-c). Immune complexes were stained with secondary and tertiary antibodies conjugated to Alexa 488 and nuclei were stained with DAPI. Sections were examined by wide field fluorescence microscopy.

immuno-gold labeling of cryosections. To enable binding of gold particles to the nanobody we used indirect labeling. The nanobody was first bound to rabbit anti-VHH serum followed by protein A-gold particles of 15 nm. Next to 0.225% CFG / 0.1% BSA-c and 1% BSA we also included skimmed milk (FREMA) in PBS (1% and 2%), 1% CFG, and 1% BSA-c. Again employment of 1% BSA as blocking solution resulted in high levels of gold labeling in the cytoplasm, which is considered as background labeling. This background staining was not diminished upon decrease of nanobody concentration used (from 10 μg/ml to 3 μg/ml) (Fig. 3). Application of 1% acetylated BSA resulted in the absence of background staining, but unfortunately also of specific HER2 labeling. Similar results were obtained with 1% and 2% FREMA (data not shown). Optimal labeling of the membrane-located HER2 was obtained when we applied a mixture of 0.225% CFG and 0.1% BSA-c. With 10 μg/ml of HER2-targeted nanobody still some background staining was present, however, after reduction of nanobody concentration to 3 μg/ml the background staining was almost completely prevented, while the specific label was preserved (Fig.3).

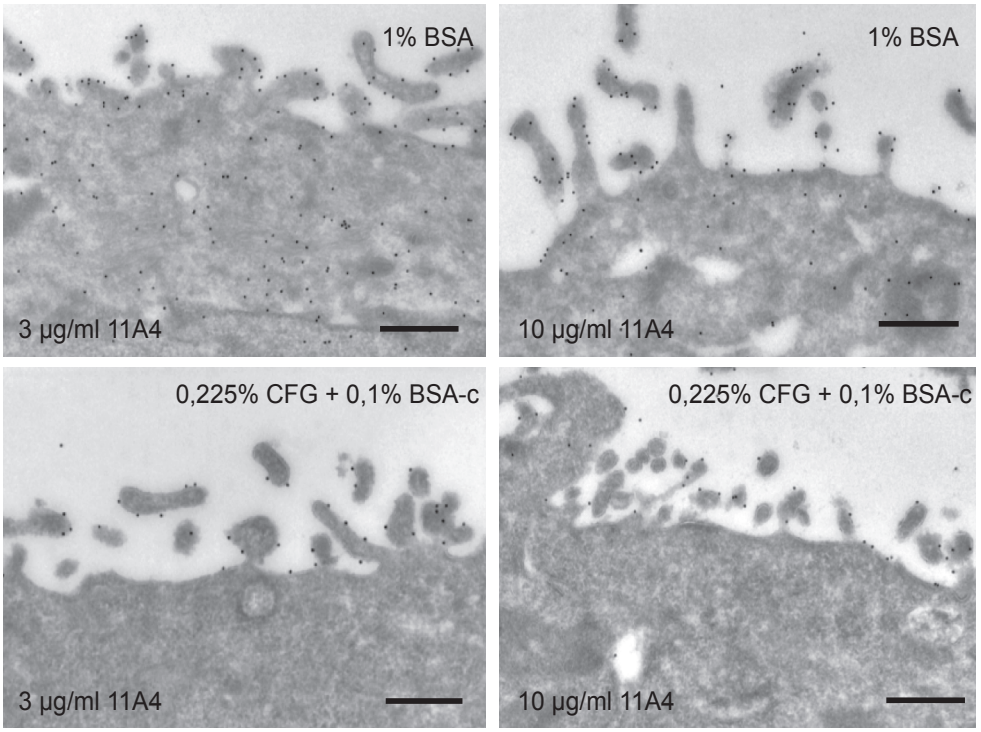

Fig. 3. Comparison of different blocking solutions used for Tokuyasu cryosections. SKBR3 cells were fixed with 4% formaldehyde and processed for cryosectioning. Sections were labeled for HER2 on SKBR3 cells with 11A4 nanobody (3 μg/ml and 10 μg/ml) after blocking with either bovine serum albumin or a mixture of cold fish gelatin and acetylated bovine serum albumin. Immune complexes were labeled with protein-A 15 nm gold particles. After post-fixation the samples were stained and examined with a transmission electron microscope. Scale = 500 nm.

The specific HER2 gold labeling was predominantly present at the plasma membrane, particularly in membrane ruffles. No gold particles were observed in the coated pits confirming previous data [14].

Nanobody-based pre-embedment immuno-gold labeling for TEM

The optimized labeling procedure was subsequently tested for pre-embedment labeling and examination using TEM. SKBR3 cells were incubated with either the 11A4 nanobody or the monoclonal anti-HER2 antibody trastuzumab. In both cases protein A-gold was used to detect either the nanobody or the trastuzumab. After the different incubations, cells were post-fixed and further processed for electron microscopy.

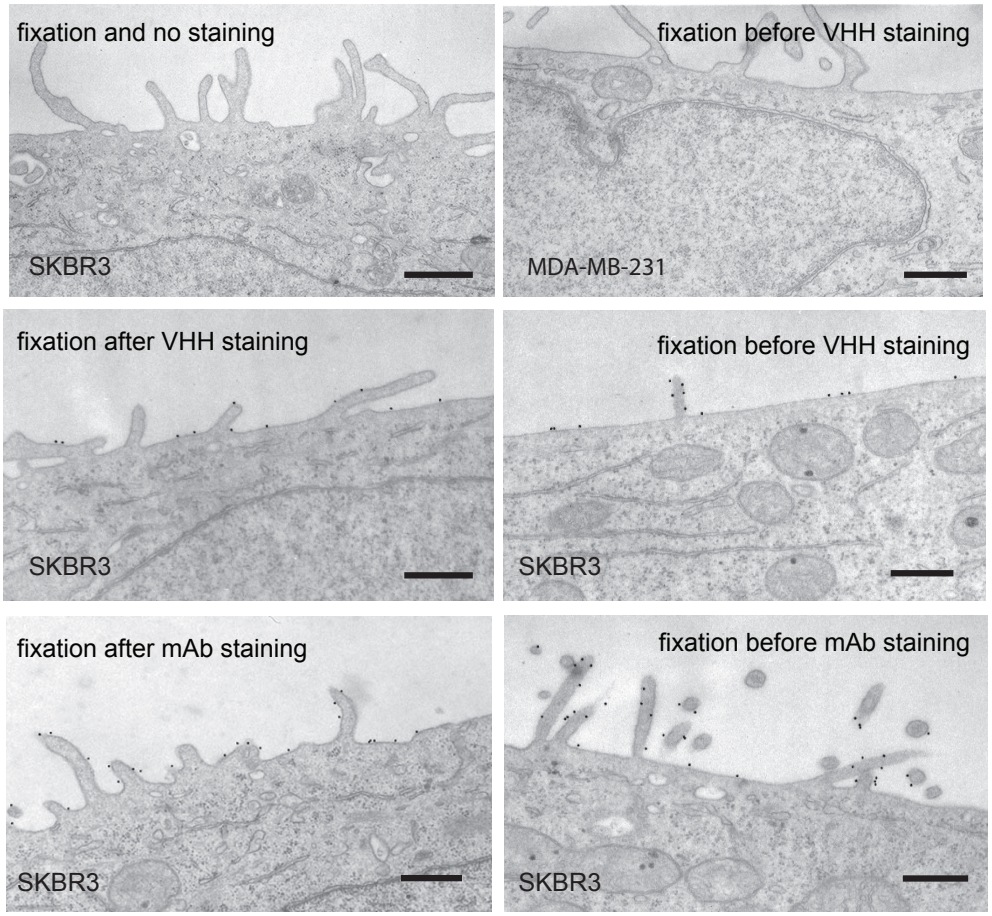

Fig. 4. Transmission electron microscopy of pre-embedment nanobody-based immuno-gold labeling of HER2. SKBR3 cells were either incubated with VHH or mAb after or before formaldehyde fixation. As negative controls, primary antibody was omitted or cells lacking HER2 expression (MDA-MB-231 cells) were used. Scale = 500 nm.

A similar immuno-gold labeling efficiency of nanobody and mAb treated samples was observed for cells labeled before and after fixation. (Fig.4) This result confirms that formaldehyde fixation does not affect the binding of either the HER2-targeted nanobody (11A4) or the mAb (trastuzumab). A higher labeling efficiency was observed for cells incubated with trastuzumab. Gold labeling was particularly seen at the membrane ruffles, which is in agreement with the cryosection labeling data.

Nanobody-based pre-embedment immuno-gold labeling for SEM

We finally tested the feasibility of HER2-targeted nanobodies for SEM applications using SKBR3 cells. In this experiment we again used the HER2-targeted mAb, trastuzumab, as a positive control. As a negative control the incubation with the nanobody was omitted. SKBR3 cells were fixed and immuno-gold labeling was performed using the optimal blocking mixture as described above, namely 0.225% CFG/0.1% BSA-c, to minimize a-specific interactions leading to background staining. The cells were dried at the critical point, Pt coated and examined with a XL30 scanning electron microscopy equipped with a field emission gun. No gold-labeling was seen in the SEM pictures of cells that were not incubated with the nanobody, but incubated with anti-VHH serum followed by protein A-gold (Fig. 5A). Immuno-gold labeling is clearly visible in case of cells labeled either with nanobody or trastuzumab (Fig. 5B and C). Again, a twofold higher amount of gold particles per μm^2 was obtained with cells labeled with trastuzumab in comparison to cells with HER2 targeted nanobody. Interestingly, filipodia that are appearing at the side of the SKBR3 cells were heavily labeled with the nanobody-gold conjugates (Fig. 5D).

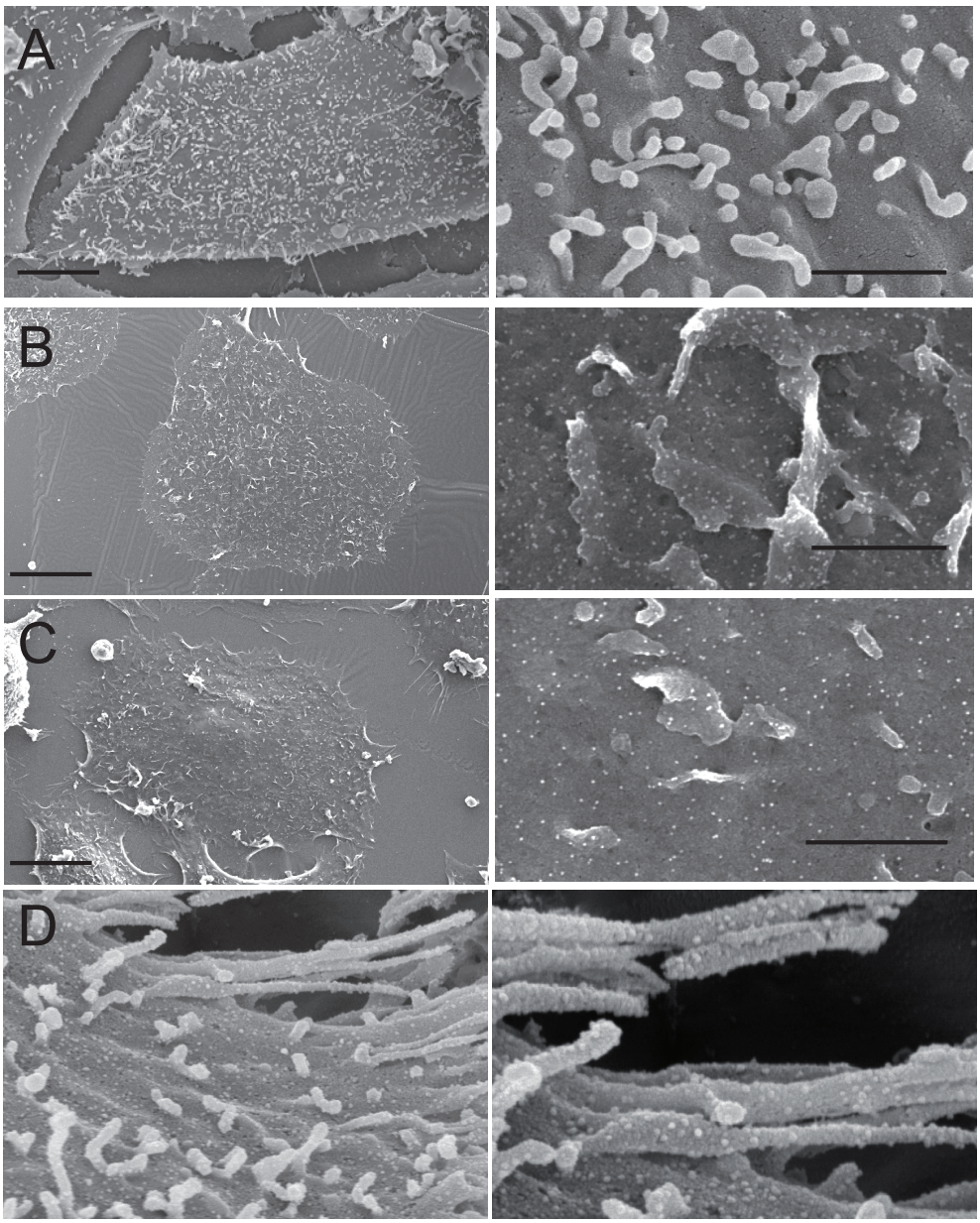

Fig. 5. Scanning electron microscopy of pre-embedment, nanobody-based immunogold labeling of SKBR3 cells. SKBR3 cells were fixed, incubated with (B) 11A4 nanobody or (C), as a positive control, trastuzumab, in the presence of a mixture of cold fish gelatin and acetylated bovine serum albumin. As negative control, the primary antibody incubation step was omitted (A). Interestingly, HER2 present at filopodia of SKBR3 cells was heavily labeled with 11A4 nanobody (D). Protein-A 15 nm gold was used to mark the location of HER2. Scale = 10 μm (right panel), 1 μm (left panel).

Discussion

In the present study we describe for the first time the use of nanobodies for immuno-EM applications. We used the recently developed HER2 targeted nanobody, 11A4, which binds specifically and with high affinity to the HER2 receptor present on the surface of breast cancer cells [6].

Essential for preservation of the ultrastructure of these cells is their fixation, which may affect both antibody and nanobody binding. The aldehydes that are used in most fixatives bind covalently to primary amines (in lysines) or thiols (in cysteins) within the HER2 molecule, which might render the antigen structure unrecognizable for mAb/nanobody. Formaldehyde is a commonly used fixative in EM applications that does not lead to much tissue shrinkage or distortion of cellular structure [14]. Fixation with formaldehyde performed before nanobody incubation did not affect the binding of either trastuzumab or of 11A4 to HER2 suggesting that both epitopes do not contain lysine or cystein residues.

To optimize the nanobody-based immuno-labeling, several blocking solutions were investigated among which are BSA, cold water fish gelatin and milk. BSA is a globular protein that adsorbs a-specifically onto the specimen surface. During this process the BSA unwinds and more contact-spots with the specimen are made. However, some spots on specimen surface are too small for globular BSA to bind and remain uncovered. This may explain the higher background staining obtained with BSA alone as a blocking agent. We therefore combined both CFG and BSA-c into the same blocking solution. The lysine and arginine residues of BSA-c have been acetylated to increase negative charge to facilitate molecule linearization and increase its hydrophobic character. Such linearized BSA-c is able to cover the specimen surface more uniformly, decreasing the non-specific background [15]. CFG has also been described to prevent a-specific binding. Best results, in terms of the lowest background labeling and highest specific staining, were obtained when the combination of CFG and BSA-c was employed.

A surprising result of our studies is the higher labeling efficiency of trastuzumab as compared to the nanobody immuno-gold labeling. The primary incubation with nanobody or mAb was done at saturating conditions, in principle covering all available HER2 binding sites. The difference in labeling intensities may therefore be explained by a lower dissociation of the bivalent trastuzumab during the secondary binding incubations. A post-fixation step at the end of the labeling procedure could indeed improve nanobody labeling intensity. This suggests that bivalent nanobodies, with reduced dissociation kinetics might improve labeling density of nanobody-based immunogold labeling.

Both immunofluorescence data as well as our TEM and SEM data show that HER2 is preferentially located at the membrane protrusions. The membrane protrusions on top of the cells, also indicated as top ruffles did not reveal HER2 staining in all cases. However, the filipodia at the side

of the cells show intense staining of HER2. Similar data were previously reported by Hommelgaard et al.[16] who furthermore demonstrated the absence of HER2 from coated pits and coated vesicles. In this paper we demonstrated the application of nanobodies both in pre-embedment labeling (TEM and SEM) and with post-embedment labeling using Tokuyasu cryosections. The feasibility of the nanobody used for both pre- and post-embedment EM applications opens up a possibility to further improve the resolution of gold labeling in EM applications. So far the smallest targeting domain tested for EM applications has been the recombinant single chain variable fragment antibodies (scFv). Their small molecular mass (26 kDa) resulted in increased labelling efficiency in comparison to mAb [17]. Although, we have here presented indirect nanobody labelling, direct and site specific gold conjugation to the nanobody will be the next step in introducing nanobodies to the daily EM routine. Direct labeling with nanobody-gold complexes will, as a result of their small size (2.5 nm x 4 nm and 15 kDa molecular mass), considerably improve the labeling resolution of EM as compared to antibodies (with a size of 14.2 nm x 8.5 nm).

References

1. Faulk WP, Taylor GM: An immunocolloid method for the electron microscope. *Immunochemistry* 8(11), 1081-1083 (1971).

2. Baschong W, Stierhof YD: Preparation, use, and enlargement of ultrasmall gold particles in immunoelectron microscopy. *Microsc. Res. Tech.* 42(1), 66-79 (1998).

3. Hassanzadeh-Ghassabeh G, Devoogdt N, De Pauw P, Vincke C, Muyldermans S: Nanobodies and their potential applications. *Nanomedicine (Lond)* 8(6), 1013-1026 (2013).

4. Muyldermans S, Baral TN, Retamozzo VC *et al.*: Camelid immunoglobulins and nanobody technology. *Vet. Immunol. Immunopathol.* 128(1-3), 178-183 (2009).

5. Muyldermans S: Nanobodies: natural single-domain antibodies. *Annu. Rev. Biochem.* 82, 775-797 (2013).

6. Kijanka M, Warnders FJ, El Khattabi M *et al.*: Rapid optical imaging of human breast tumour xenografts using anti-HER2 VHHs site-directly conjugated to IRDye 800CW for image-guided surgery. *Eur. J. Nucl. Med. Mol. Imaging* 40(11), 1718-1729 (2013).

7. Yarden Y: Biology of HER2 and its importance in breast cancer. *Oncology* 61 Suppl 2, 1-13 (2001).

8. Sobue K, Fujio Y, Kanda K: Tumor promoter induces reorganization of actin filaments and calspectin (fodrin or nonerythroid spectrin) in 3T3 cells. *Proc. Natl. Acad. Sci. U. S. A.* 85(2), 482-486 (1988).

9. Karnovsky MJ: A formaldehyde-glutaraldehyde fixative of high osmolality for use in electron microscopy. . *J. Cell Biol.* 27, 137A-138A (1965).

10. Muller LL, Jacks TJ: Rapid chemical dehydration of samples for electron microscopic examinations. *J. Histochem. Cytochem.* 23(2), 107-110 (1975).

11. Reynolds ES: The use of lead citrate at high pH as an electron-opaque stain in electron microscopy. *J. Cell Biol.* 17, 208-212 (1963).

12. Slot JW, Geuze HJ: Cryosectioning and immunolabeling. *Nat. Protoc.* 2(10), 2480-2491 (2007).

13. Tokuyasu KT: A technique for ultracryotomy of cell suspensions and tissues. *J. Cell Biol.* 57(2), 551-565 (1973).

14. Thavarajah R, Mudimbaimannar VK, Elizabeth J, Rao UK, Ranganathan K: Chemical and physical basics of routine formaldehyde fixation. *J. Oral Maxillofac. Pathol.* 16(3), 400-405 (2012).

15. Leunissen JLM, de Plas PFEM: Optimised Immuno Labelling using AURION Blocking Solutions and AURION BSA-c™ Newsletter 1 (2006).

16. Hommelgaard AM, Lerdrup M, van Deurs B: Association with membrane protrusions makes ErbB2 an internalization-resistant receptor. *Mol. Biol. Cell* 15(4), 1557-1567 (2004).

17. Malecki M, Hsu A, Truong L, Sanchez S: Molecular immunolabeling with recombinant single-chain variable fragment (scFv) antibodies designed with metal-binding domains. *Proc. Natl. Acad. Sci. U. S. A.* 99(1), 213-218 (2002).

Part 2

Chapter 6

Nanobody-based cancer therapy of solid tumors

Marta M. Kijanka
Bram Dorresteijn
Sabrina Oliveira
Paul M.P. van Bergen en Henegouwen

Submitted

Abstract

The development of tumor-targeted therapies using monoclonal antibodies has been very successful during the last 30 years. Nevertheless, the efficacy of the antibody-based therapy is still limited and further improvements are eagerly awaited. One of the promising novel developments that may overcome drawbacks of monoclonal antibody-based therapies is the employment of nanobodies. Current nanobody-based therapeutics can be divided into three different platforms with nanobodies functioning as: (A) receptor antagonists that interfere with signaling; (B) targeting moieties of effector domains, such as toxic peptides or drugs; and (C) targeting molecules on the surface of nanoparticles. In this review we describe factors that affect their performance at three different stages, which are essential for their feasibility for cancer therapy: (1) their systemic circulation upon intravenous injection and renal, hepatic or splenic filtration, (2) their extravasation and tumor penetration, and finally (3) their interaction with target molecules on the tumor tissue.

Introduction

Cancer therapy using monoclonal antibodies (mAbs) is a rapidly developing field. It has been more than 30 years since the first patient was subjected to a monoclonal antibody therapy [1]. The introduction of mAbs for cancer treatment has been without a doubt a remarkable success bringing us closer towards personalized medicine. Until now, 23 monoclonal antibodies have been approved by the US Food and Drug Administration (FDA) and are available on the market [2]. Most of them act by binding to transmembrane receptors or soluble ligands, thereby interfering with their signal transduction pathways, resulting in inhibition of tumor cell proliferation or angiogenesis. Due to the presence of an intact Fc domain, mAbs can evoke an antibody-dependent cell-mediated cytotoxicity (ADCC) by attracting complement or effector cells of the human immune system to the cancer site. mAbs have also been used as targeting moieties for the delivery of nanomedicines or nanoparticles containing a cytotoxic payload. In another approach, mAbs have been directly conjugated to cytotoxic drugs (such as e.g. auristatin, maytansine, calicheamicin or doxorubicin). Several of these mAb-drug conjugates have already reached the clinical trial phase [3]. Nevertheless, the large size of mAb alone (150 kDa, dimensions: 14.2 nm × 8.5 nm ×3.8 nm, [4]), further increased by the conjugation to a nanoparticle, is a considerable drawback as it leads to limited tumor penetration and slow distribution [5-7]. To overcome the limitations of full-length mAbs, smaller formats have been generated such as the naturally derived or synthetic antigen-binding fragment (Fab; ~ 50 kDa), variable fragment (Fv; ~ 15 kDa) or single-chain variable fragment (scFv; ~30 kDa). The advantage of the smaller size is in most cases counterbalanced by decreased stability resulting in aggregation (especially in case of scFv), lower affinity and/or difficulties in large scale production [8].

In the early 1990s, a new type of antibodies, the heavy chain antibodies (HcAbs, ~95 kDa) were discovered by serendipity by Hamers-Casterman and co-workers [9]. In contrast to the well-conserved structure of immunoglobulin-γ (IgG) in mammals, which consists of two identical heavy chains and two identical light chains [10], members of the Camelidae family have an additional IgG comprised of a homodimer of heavy chains only [9]. These fully functional antibody structures retain high binding capacities, similar to those obtained with conventional mAb, even though they lack the light chain. Due to the ease of immunization, HcAbs are mostly obtained from *Camelidae* (bactrian camels, dromedaries, alpacas, and llamas), even though HcAbs have also been found in cartilaginous fish (such as sharks, rays, and skates). Interestingly, the variable domain of the heavy chain from HcAbs alone (i.e. VHH, also referred to as nanobody or single domain antibody (sdAb)) is fully functional and currently the smallest naturally derived antigen-binding fragment (Fig.1).

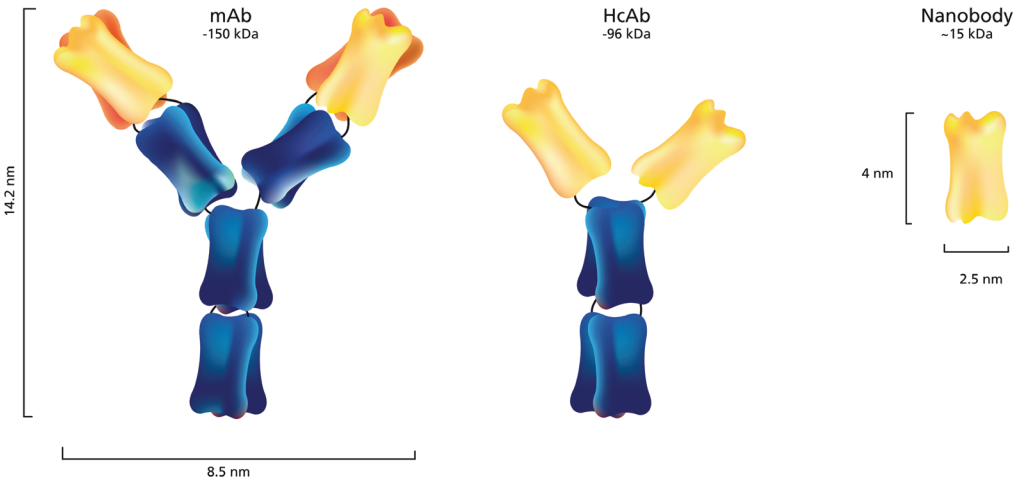

Fig. 1. Schematic overview of different antibody formats: conventional monoclonal antibody (mAb), heavy-chain only antibody (HcAb) and its derivative, i.e. nanobody, also referred as the variable domain of the heavy chain of a HcAb (VHH). Their molecular weight and size are depicted as well.

In this review we will describe the unique features of nanobodies relevant in the context of cancer therapy, which have attracted a considerable interest and opened a wide range of applications. After specifying the different therapeutic approaches in which nanobodies have been involved, the following sections will describe factors that affect the performance of nanobody-based therapeutics at the three major phases that are essential for cancer therapy: (1) during their systemic circulation upon intravenous injection and renal, hepatic or splenic filtration, (2) their extravasation and tumor penetration, and finally (3) their interaction with cancer targets.

Nanobodies: characteristics and therapeutic strategies

The molecular biology of nanobodies has recently been explained in detail in an excellent review by Muyldermans [11]. Clear advantages of nanobodies over conventional antibodies include size [12], stability [13,14] and solubility [15]. Because of these characteristics, nanobodies can be formulated as a long shelf-life, ready-to-use solution (www.Ablynx.com). Furthermore, nanobodies are relatively easy to produce in bacteria, yeast or mammalian cells, allowing large scale production at reasonable costs. The VHH is very similar to the human VH framework of family III, so most likely nanobodies have very low immunogenic potential, which was confirmed by recent studies from Ablynx [16]. In addition, when it becomes necessary, additional procedures can be taken to humanize nanobodies [17].

The single domain property of the nanobody allows for selections based on phage display, which, in principle, enables selection of nanobodies that specifically recognize any protein of

interest. This aspect makes the nanobody technology very versatile. Particularly in the context of cancer therapy, nanobodies can be used to target cancer cells and/or tumor vasculature that either solely express certain proteins or overexpress these proteins as compared to normal cells. In order to develop nanobodies that specifically bind and/or interfere with the activity of a target protein, three essential tools are needed: firstly, the phage display library, obtained from immunized animals. The immunization of animals from the *Camelidae* family can be done with the protein of interest, with cells or even purified cell compartments expressing this protein. From the peripheral blood lymphocytes of these animals, a library can be constructed following standard protocols [18,19]. The phage display technology allows for different selection protocols aimed at obtaining nanobodies with high affinity or for targets that are differentially expressed, like subtractive panning. Secondly, the purified protein of interest (in most cases available through purchase) and/or cell lines expressing this protein, while having a non-expressing cell line as negative control, are essential for panning. Thirdly, tools to detect the selected nanobodies during the screening procedures are required.

Nanobodies binding to receptors

Thus far, nanobodies have been selected to bind to receptors that are involved in cancer biology, thereby preventing ligand binding or conformational changes that lead to activation of signaling cascades. Such receptors are: the epidermal growth factor receptor 1 and 2 (EGFR or HER1 and HER2, respectively); EGFR variant III (EGFRvIII); the vascular endothelial growth factor receptor 2 (VEGFR2); the hepatocyte growth factor receptor (c-Met), and the oncogenic chemokine receptor CXCR7. EGFR, EGFRvIII, HER2 and c-Met belong to the family of receptor tyrosine kinases (RTKs). Nanobodies targeted to EGFR have been developed by Roovers et al. through phage display selection, combined with competitive elution with EGF or cetuximab, to select antagonistic anti-EGFR nanobodies [18]. Nanobody targeting EGFRvIII was selected by Omidfar et al. in five consecutive rounds of affinity phage display selection on successively decreasing amounts of synthetic peptide immobilized on magnetic beads [20]. Several nanobodies targeting HER2 were selected through phage display on immobilized HER2 [21,22] or on cells possessing high HER2 expression [22] and one HER2 targeted nanobody has been investigated as a targeting moiety for therapeutic application *in vitro* [23]. VEGFR2 belongs to the family of human VEGFR receptors 1-3 [24] and has an important role in embryogenesis and angiogenesis. This receptor has been described to be overexpressed in many types of cancers, among those in lung and colon cancers [25]. The nanobody targeting VEGFR2, which inhibits capillary tube formation *in vitro*, has been obtained through phage display selection on immobilized recombinant extracellular domain of this receptor [26]. The c-Met receptor is activated upon HGF binding and is involved in regulation of cell proliferation, motility and morphogenesis [27]. This receptor has been implicated in a variety

of human malignancies, such as colon, breast, ovarian, and hematological malignancies [28]. The anti-c-Met nanobody was shown to compete with HGF thereby inhibiting c-Met activation, cell proliferation and migration in vitro [29,30]. Different c-Met targeted nanobodies, also HGF competitors, were obtained through selections on immobilized c-Met, and the final selection was based on the maintenance of the binding affinity upon modification for conjugation to nanoparticles [30]. The chemokine receptor CXCR7 has recently been described as the receptor for chemokine CXCL11 and CXCL12, which upon activation stimulates other downstream signaling pathways [31]. Several tumors have been associated with CXCR7 overexpression, among which are breast and lung tumors [32]. The nanobodies targeting CXCR7 were selected on CXCR7 virus-like lipoparticles, followed by confirmation of their binding specificity on CXCR7-expressing cells. Further refinement was obtained by a selection based on competition with CXCL12.

Nanobodies binding to ligands

An alternative approach includes nanobodies that bind directly to the ligand, thereby preventing its binding to the receptor. This approach is only successful, when just one ligand is responsible for activation of the corresponding receptor. In this context, nanobodies have been developed for HGF and diverse chemokines. Anti-HGF nanobodies were obtained after selection of binders to immobilized HGF and the assessment of HGF/c-Met interaction inhibition. Chemokines generally play a role in immune responses and inflammatory processes, which may also be involved in cancer development [32]. Neutralizing nanobodies targeting diverse chemokines were obtained from a library constructed after llamas had been immunized with a mixture of recombinant chemokines, followed by phage display selections on immobilized chemokines and further selection for receptor antagonists and inhibition of cellular migration [33]. These neutralizing anti-chemokine nanobodies have not yet been evaluated *in vivo*.

Nanobodies and cancer therapy

In this context of cancer therapy, nanobodies described above have first been tested as antagonists (Table 1). Examples are nanobodies against EGFR and c-Met [18,29,34-36]. Both types of nanobodies were acting as effective antagonists for either the EGF or HGF signaling *in vitro*. Inhibition of tumor growth *in vivo* was obtained with the anti-EGFR nanobodies. In this latter study, the ultrafast clearance of nanobodies was circumvented by fusion of the anti-EGFR nanobodies with a nanobody targeting albumin that could prolong half-life from 1-2 hrs to 2-3 days [35]. Eradication of the tumors was not observed, despite the fact that different combinations of anti-EGFR nanobodies were used, either bi-valent or bi-paratopic. In this case, the absence of the Fc-domain, which is necessary to trigger

antibody-dependent cellular toxicity (ADCC) and complement-dependent cytotoxicity (CDC) upon antigen binding, was certainly one of the reasons for the limited antitumor effect [8,35]. On the contrary, in the study by Vosjan et al. nanobodies targeting HGF fused to an albumin binding domain were capable of inhibiting U87 MG tumor outgrowth and even curative responses were observed [34]. These studies show that the therapeutic effect of nanobodies is certainly dependent on the target and tumor model employed.

These results stimulated further investigations on different applications of the nanobodies in cancer therapy. On the basis of these developments we have categorized the anti-cancer nanobodies into three platforms: the antagonistic (or naked) nanobodies (platform A), nanobodies fused to effector domains like the Fc-domain, soluble Trail (sTrail), the Pseudomonas exotoxin A (variant PE38), or conjugated to photosensitizers (platform B), and nanobodies decorating the surface of nanoparticles, such as liposomes, micelles or albumin nanoparticles, which on their turn encapsulate drugs (platform C) (Fig.2). The conjugation of the nanobody to the nanoparticles is obtained via N-succinimidyl-S-acetyl-thioacetate (referred to as SATA) modification of the nanobodies that after de-protection react with maleimide or sulfhydryl groups available on the nanoparticles [37-39]. *In vitro* experiments employing nanobodies as targeting moieties of nanoparticles have shown improved binding to the target cells [33, 39-41].

Target	Platform(s)	*In vivo*	References
1. Receptors			
Epidermal growth factor receptor (EGFR)	A, B, C	Yes/No	[18,35][36][38,39,41,44-47]
Human epidermal growth factor receptor 2 (HER2)	B	No	[23]
Vascular endothelial growth factor receptor-2 (VEGFR2)	A, B	No	[26,48]
Hepatocyte growth factor receptor or c-Met	A, C	No	[29,30]
CXCR7	A	Yes	[49]
2. Ligands			
Hepatocyte growth factor (HGF)	A	Yes	[34]
Diverse chemokines	A	No	[33]

Table 1. Nanobodies in cancer therapy: the targets nanobodies bind to, the therapeutic platforms they have been used in (A. naked nanobodies acting as antagonists, B. targeting moieties of effector domains, C. targeting moieties of drug delivery systems), evaluated in preclinical *in vivo* studies, and corresponding references.

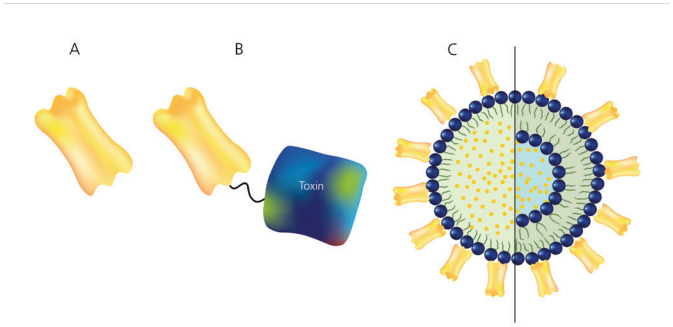

Fig. 2. Schematic representation of nanobody-based therapeutic platforms: receptor antagonists that interfere with receptor activation and signaling (A); targeting moieties of effector domains, such as toxic peptides or drugs (B); and targeting molecules on the surface of nanoparticles such as e.g. liposomes or micelles (C).

An important prerequisite for these latter two platforms is the restriction of drug toxicity to the tumor. An example of a platform B nanobody construct is the nanobody fused with an effector domain like an Fc-fragment, which would provide the nanobody with the typical ADCC activity restricted to the target cell [42]. The nanobody-drug conjugates can be designed with cleavable linkers to be cut by proteases within the tumor stroma or inside the tumor cell. Of interest in this respect is the recent development of biparatopic nanobodies that stimulate internalization via the clathrin-dependent pathway [43]. In the constructs of platform C, the protection of drugs is done by the attachment or encapsulation of the drugs onto or inside the nanoparticles. Release of these drugs from the particles can be achieved by leakage, or by mechanical destruction by ultrasound or intracellular degradation. The first liposomes that were decorated with anti-EGFR nanobodies were indeed shown to become internalized into the target cell [39]. Moreover, nanobody-targeted polymeric micelles containing doxorubicin were significantly more effective in inhibiting tumor growth and prolonging the survival of animals, compared to the untargeted formulation [44].

Three steps leading to therapy

For each of these platforms the distribution through the body and the delivery into the tumor tissue is different and the efficiency of this process contributes strongly to the efficacy of the treatment. A therapeutic formulation that is very effective in a 2D cell culture set-up, is not necessarily effective in an *in vivo* preclinical model. In this part of the review we will discuss the steps that the nanobody-based therapeutic molecules go through before reaching their therapeutic target *in vivo*.

Delivery of therapeutic agents can be done in different ways: oral, intravenous, intraperitoneal, or intra-tumoral. Nanobody technology is applicable to all above mentioned administration routes. However, each pathway has different demands for the nanobody-based

formulation. For instance, with oral application or intraperitoneal injection, the nanobody requires resistance to extreme conditions i.e. proteases and/or acidic pH. Nanobodies can be made resistant to proteases by adaptation of the sequence or by introduction of an additional disulfide bond to improve resistance to pepsin and chymotrypsin [50]. For intravenous injection, stability in serum is essential. Although most nanobodies have been described as very stable, when combined with effector domains or nanoparticles, the stability of these systems might be different. Instability of nanobody-based formulations may give rise to an early release of the drug before reaching the cancerous mass, which could result in severe side-effects and decreased therapeutic benefits. As nanobodies are usually sufficiently stable for intravenous injection, this way of administration is currently the most frequently used method for *in vivo* nanobody-based cancer therapy studies.

Systemic circulation upon intravenous injection

Intravenous administration of therapeutics is not always performed in close proximity to the tumor mass [51]. Consequently, the injected material needs to travel a sufficient period of time along the circulatory system in order to reach the tumor. Sufficient tumor accumulation requires therefore sufficient residence time of the nanobody in the blood stream, which differs for the type of nanobody platform. Naked nanobodies are rapidly cleared from the bloodstream, which reduces the time interval to bind to their target molecule. On the other hand, efficient clearance also decreases the risk of unwanted toxic side effects. Therefore, an appropriate balance between these factors might be essential for successful therapy. In case of larger nanobody drug formats, opsonization and subsequent recognition and uptake by reticuloendothelial system (RES) may occur leading to hepatic clearance of these therapeutic compounds.

Renal clearance

Renal clearance is a multifaceted process involving glomerular filtration, which depends on the size of the molecule [52]. Molecules with an *in vivo* hydrodynamic diameter (HD) smaller than 6 nm in size are filtered by fenestrations in the endothelial cell layer, in contrast to molecules with an HD > 8 nm. In general, the average weight cutoff for renal clearance is approximately 60 kDa [53,54]. For intermediate sized molecules, the filtration is further dependent on their charge. Positively charged molecules are more likely to be filtered due to the negative charge of the globular membrane [52,55]. Besides this, the charge of a molecule may provide interaction with plasma proteins, increasing the HD and preventing renal clearance [56]. However, in case of nanobodies there is no general rule for the net charge *in vivo*. Due to the small size of these molecules, their isoelectric point (pI) is mainly determined by the different amino acid composition of the CDR regions. It is important to note that

an extremely high or low pI will render some of the nanobodies not suitable for *in vivo* use [57]. The size (2.5 nm diameter and 4 nm height) and prolate shape of nanobodies predict rapid renal clearance [58]. This prediction has already been confirmed by several *in vivo* studies [22,59]. Importantly, the renal clearance and/or retention of the nanobody-toxin conjugates in the kidney may lead to renal toxicity. Whether these compounds are retained at the kidneys depends on the added size, change in charge and/or overall HD due to the coupled effector domain. For instance, a photosensitizer (PS) such as IRDye700DX results in addition of only 2 kDa [45], which in this case will result in clearance of the nanobody-PS construct through the kidneys. Nevertheless, in this particular context, nephrotoxicity is minimized due to the fact that the PS is only leading to toxicity when it is activated through specific illumination.

Although, no nanobody-effector domain platform for cancer therapy has been characterized *in vivo* so far, pharmacokinetic toxicology studies of other immunotoxins, such as B43-pokweed antiviral immunotoxin, already showed dose-dependent kidney toxicity due to renal retention [60,61]. To avoid toxicity, renal retention of nanobody-drug conjugates should be minimized. As the renal retention relies on the endocytic pathway, the co-infusion of gelofusine and/or lysine to compete with megalin may lower the retention [62]. Next to that, substitution of negative or positive residues of the nanobodies could affect renal retention [63]. Since the nanobody scaffold can be engineered to a certain extent, it can be designed to ensure lower renal retention [17,53]. A different method to reduce renal accumulation and retention is to lower the renal filtration rate [54], resulting in an increase of half-life and the chance of improved tumor uptake [64]. Increasing the size by for instance glycosylation [65], PEGylation [66] or non-covalently binding to circulating serum proteins (albumin), such as the fusion with an albumin-binding nanobody [34], can prolong half-life and thus lower renal retention [64].

In contrast to the described kidney clearance for antagonistic nanobodies and targeting nanobodies with effector domains, nanoparticles decorated with nanobodies are, due to their size, not eliminated through the kidneys. These larger types of the nanobody platforms (nanoparticles) are cleared by the liver.

Hepatic clearance

The hepatobiliary system is the primary route of excretion for drugs that are too large for renal filtration [52]. Compounds and particles that undergo hepatic clearance are catabolized by hepatocytes [67]. Kupffer cells and hepatocytes are parts of the biliary system and particles endocytosed by these cells are excreted into the bile. Kupffer cells have a much higher phagocytotic capacity than hepatocytes and form the RES or mononuclear phagocyte system. Particles taken up by Kupffer cells rely exclusively on intracellular degradation, however, particles that are not broken down, will

be retained inside the cells. Hepatic clearance has a preference for removal of particles with a HD of 10-20 nm as their primary task is filtration of, for instance, viruses [56]. Next to the liver, phagocytic cells of the RES reside also in the spleen, making this organ another target of clearance of non-glomerular cleared compounds.

Nanobody-based drug delivery systems such as albumin nanoparticles, liposomes or micelles are spherical with a large HD [52]. A biodistribution study of untargeted liposomes indeed showed an accumulation in liver and spleen [68]. Of interest is that saturation of the liver accumulation results in a shift of the liposome distribution to the spleen [69], appointing the liver as the main clearance organ of liposomes. Moreover, accumulation of liposomes into the tumor might also occur after saturation of the liver. Modifications of liposomes can be done in order to avoid "first-pass" hepatic clearance, at least to a certain extent. For instance, PEGylation of liposomes lowers opsonization by plasma proteins and increases circulation time by avoiding phagocytosis by the RES components [70]. Although accumulation at the tumor depends on the circulation time of liposomes, an increase in circulation time does not directly translate into increased tumor uptake [71].

Nanobody extravasation and tumor penetration

The second phase of drug delivery into a solid tumor, once the drug has reached the tumor blood circulation or the nearby blood supply, is the extravasation from the bloodstream and retention at the tumor site to allow interaction with cancer cells resulting in accumulation in the tumor. Transport of nanobody-based therapeutics across the vessel wall is mediated by diffusion and fluid transport. In normal tissue, a net negative pressure between blood vessel and interstitial space exists resulting in fluid movement towards interstitial space and further to lymphatic ducts. In tumors, the interstitial fluid pressure (IFP) is higher than that of surrounding tissue. This elevated IFP limits the transport of large molecules (such as mAb) and particles into the interstitial matrix and it becomes more dependent upon diffusion [72]. Targeted therapeutics are aimed at binding to receptors present on tumor cells. However, the binding site barrier effect, first suggested by Fujimori et al. [73], was described as a limiting factor of high affinity binding mAbs that, due to their large size, hamper the diffusion of other mAb molecules into the tumor tissue [72]. Importantly, this effect was not observed with small molecules such as affibodies and nanobodies that are able to distribute throughout tumors in a more homogenous manner [12,64]. In the study by Oliveira and co-workers, tumor distribution of 15 kDa nanobodies was compared with a 150 kDa mAb after conjugation to the fluorophore IRDye800CW (IR). The EGFR-specific 7D12-IR nanobody showed a homogeneous distribution of the probe in A431 human tumor xenografts already 30 min to 2 hrs post injection, which lead to a relatively high tumor uptake, whereas the negative control R2-IR did not accumulate at the tumors. An irregular distribution of the cetuximab-IR in the tumor stroma was observed, possibly due to the

binding site barrier effect [74]. Similar results were obtained for the anti-EGFR affibody conjugated to IR, in contrast to cetuximab-IR, which was confined to the center of the tumor [75]. Homogenous distribution of the drug throughout the tumor mass is essential for successful treatment. If only part of the tumor mass will be exposed to the drug, complete tumor eradication will not be achieved leading to eventual tumor re-growth [69]. In this respect, nanobodies are expected to outperform monoclonal antibodies.

As the molecular size is an important factor for diffusion, the diffusion capacity of nanobody-targeted nanoparticles (platform C) is dependent on their size, where the smallest will have a better chance to diffuse into the tumor (Fig. 3).

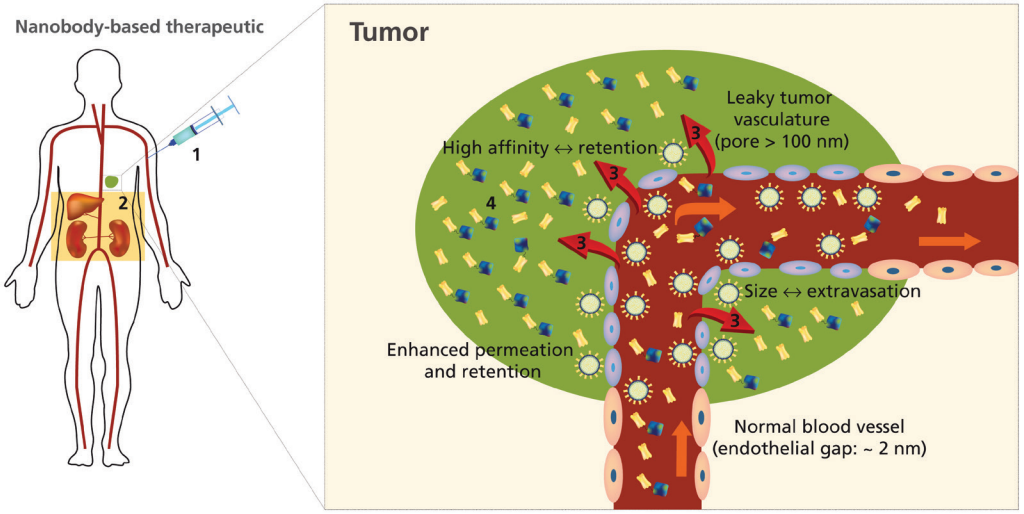

Fig. 3. Schematic representation depicting the journey of nanobody-based therapeutics upon administration. Upon intravenous injection (1) the nanobody-based therapeutic circulates in the blood stream for different time, which strongly depends on the size of the employed platform. With the blood flow, it reaches the main clearance organs, i.e. kidney and liver (2), but also the tumor site. To exert its cytotoxic activity, nanobody-based therapeutics need to extravasate from the circulation into the tumor mass (3). This extravasation is enabled due to leaky vasculature of the tumor. Nanobodies belonging to platform (C) accumulate at the tumor due to the EPR effect (enhanced permeation and retention) and are not capable of homogenous tumor penetration, therefore they localize in close proximity to the blood vessels. On the other hand, nanobodies of platform (A) and (B) may homogenously diffuse throughout the tumor mass due to their small size, and their high binding affinity is essential to associate with their targets. The specificity of interaction of each of the platforms with target cells depends strongly on the nanobody employed (4).

Importantly, blood and lymphatic vasculature differ substantially in tumors and normal tissues. Blood vessels of healthy tissues are normally well sealed and continuous, which prevents extravasation of therapeutic compounds. In contrast, immature, dilated tumor vessels are leaky due to the presence of much larger pores in post capillary venules, often exceeding 100 nm in size [71]. This hyperpermeability of tumor vasculature allows leakage of macromolecules and nanoparticles into the tumor. This phenomenon is referred to as the enhanced permeability and retention effect (EPR

effect), and was first described by Matsumura and Maeda in 1986 [74]. Due to the EPR effect, high levels of doxorubicin were delivered to the tumor site with cross-linked polymeric micelles with a diameter of ~70 nm, decorated with EGFR-targeting nanobodies [40]. On the other hand, no significant effect on tumor growth inhibition of a 14C tumor xenograft model was observed with liposomes encapsulating the small tyrosine kinase inhibitor AG538 and decorated with anti-EGFR nanobody [46], despite the fact that a clear inhibitory effect on cell proliferation was observed *in vitro*. This lack of toxic effect can be attributed to the electrostatic interactions between this cationic liposome formulation with serum proteins, thereby affecting the circulation time and subsequent accumulation at the tumor site. On the other hand, active targeting by the surface-bound nanobodies does not contribute to significant accumulation of nanoparticles in solid tumors, but has a vital contribution to the subsequent step.

Nanobody interaction with targets

For all mentioned nanobody platforms, the final step before the therapeutic mechanism of action, is the actual binding to the target molecule, which is mediated by the nanobody. The specificity of this last stage is essential for the therapy to occur with minimal side effects. For antagonistic nanobodies, high binding affinity is essential as these nanobodies are expected to compete off the natural ligands, which normally bind with high affinity themselves to their receptor. Phage display selections can specifically be aimed at retrieval of high affinity binders. In addition, improvement of binding affinity can be obtained by preparing a family library, based upon the CDR3 sequence of an already selected nanobody. A disadvantage of the nanobody technology is that the conjugation to an effector domain might have a severe effect on the binding properties of the nanobody. Crystal structures of nanobodies have shown that the N-terminus is positioned close to the site of the CDR sequences and conjugation to this site of the protein might affect antigen binding.

Although not in all cases, random conjugation to the primary amines (lysines and N-terminus of protein) was found to affect binding properties of the nanobody [22]. In this study, the conjugation of the fluorophore IRDye800CW was shown to completely prevent the binding of a HER2-tdirected nanobody to its target *in vivo*. Importantly, affinity was retained after conjugation of this fluorophore to a C-terminal cystein [22]. Thus, the best solution for the conjugation of effector domains to the nanobody appears to be via the C-terminus. Two nanobodies fused to effector domains have been described and both have been fused to the C-terminus: the anti-VEGFR2 has been fused to PE38 [48], and an anti-EGFR nanobody to sTRAIL [26]. In the latter case, a drop in affinity was observed, but in this particular set-up it did not hamper the efficacy in killing cancer cells. Alternatively, click chemistry, intein- and sortase-based conjugation systems are in development and may contribute to further functionalization of the nanobodies [76-80].

Recently, for theranostic purposes, we have randomly conjugated EGFR targeted nanobodies to a traceable photosensitizer (PS) for photodynamic therapy (PDT) [45]. Binding affinity of these EGFR-targeted nanobody-PS conjugates remained in the low nanomolar range and these conjugates are expected to behave *in vivo* very similarly to what has been observed in molecular imaging studies [12]. After the preclinical testing, more will be known on the feasibility of the approach where the fluorescent nanobody-PS conjugate can be detected through optical imaging, enabling guidance of the actual treatment (i.e. PDT). After binding of the nanobody to their target receptor, e.g. EGFR, they undergo a very slow internalization (one round of internalization is completed after 24 hrs). For a more rapid internalization of the cargo, the use of biparatopic nanobodies was recently introduced [43]. These biparatopic nanobodies consist of two different nanobodies binding to the same target protein (EGFR), but on different, non-overlapping sites. As a result these nanobodies stimulate receptor clustering, which induces receptor internalization and subsequently degradation in lysosomes. Similar results were shown for antibody constructs [81]. This method allows specific binding to the target cells, followed by internalization, enabling the reversible conjugation of drugs that are sensitive to intracellular proteases, such as e.g. cathepsin B, to be then released for their action.

When nanobodies are employed as targeting moieties of long circulating nanoparticles, such as PEGylated-liposomes or branched gold nanoparticles, affinity becomes less critical. This is mainly because the affinity will be sufficient as a result of avidity as several nanobodies are present on the same particle. Mamot et al. have shown that the targeting moiety has a function in cellular uptake of the particles [71,82,83]. This has been demonstrated with nanobodies binding to cell membrane proteins as for instance anti-EGFR nanobodies conjugated to liposomes [39,41,46], polymeric micelles [38,44], or to albumin nanoparticles [47]. Another example is the binding of the anti-c-Met nanobody conjugated to albumin nanoparticles to the human ovarian carcinoma cell line TOV, stably expressing c-Met [30]. Also in this case, multiple nanobodies on the surface of those particles result in clustering of their target receptor at the membrane causing their internalization. The c-Met targeted albumin nanoparticles clearly entered the route of early endosomes, late endosomes and lysosomes, where degradation of both nanoparticle and c-Met took place [30]. Although these nanoparticles were able to induce activation of c-Met, the degradation of this receptor (i.e. down-regulation) seemed to be the most prominent effect. On the contrary, EGFR targeted liposomes were able to inhibit EGF-induced activation and also induced EGFR receptor down-regulation [39]. Interestingly, scFv-liposomes also targeting EGFR were unable to induce the same EGFR down-regulation effect, which is believed to be related to the fact that nanobodies dissociate from their targets only at very acidic pH (below pH of late endosomes) [39]. Thus, by remaining attached to the nanobody, EGFR is unable to recycle to the cell membrane and therefore the EGFR-nanobody-liposome is directed to lysosomes for degradation.

Lysosomal routing and subsequent degradation is very valuable as it leads to the down-regulation of receptors that play an active role in tumor proliferation. This routing also opens the possibility to incorporate sensitive linkers (pH, protease) enabling release of the cargos from the nanoparticle in the endolysosomal system. For instance, the EGFR targeted nanobody liposomes containing IGF-1R targeted kinase inhibitor were clearly able to release the kinase inhibitor, which then reached the target site of action (i.e. cytoplasm) [41,46]. Similarly, the EGFR targeted nanobody albumin nanoparticles that trafficked to the lysosomes were also able to release the multikinase inhibitor from its linker, as this one could perform its mechanism of action (*in vitro* study) [47]. In case of the EGFR targeted nanobody-micelles containing doxorubicin as payload [38,44], doxorubicin was coupled to the polymer with a hydrolytically degradable linker (at pH 5), allowing the release of doxorubicin from the polymer upon trafficking of the nanoparticles to the late endosomes/lysosomes [84]. In these examples, cargos were very low molecular weight drugs, which could diffuse out of the late endosomes/lysosomes compartments. More complex will be the situation where the cargo cannot cross the cell membrane, unless binding of the nanobody to the target protein is sufficient for the mechanism of action. That seems to be the case for the HER2 targeted branched gold nanoparticles for photothermal therapy [23] and also to EGFR targeted nanobodies conjugated to photosensitizers for PDT [45]. Nevertheless, in the latter case, enhanced toxicities were documented upon increased internalization of the conjugates.

Conclusion and future perspectives

Research on application of nanobodies in cancer therapy has resulted in the development of three distinct nanobody-based therapeutic platforms: (A) naked nanobodies, (B) nanobodies as targeting moieties transporting effector domains and (C) nanobodies as targeting molecules on the surface of nanoparticles encapsulating a drug. The reviewed studies demonstrate that nanobody-based platforms may, due to their unique characteristics, overcome some of the obstacles that hamper successful therapy at different stages upon intravenous injection of monoclonal antibodies. To date, although some exception exists depending on the target and tumor, nanobodies as receptor antagonists do not seem sufficiently effective as they lack an effector function (i.e. Fc tail). Currently introduced nanobody-effector domains are promising and further developments may contribute to a higher efficacy with respect to full tumor eradication. Of interest are activatable systems, in which drugs only become toxic upon change in pH or after enzymatic cleavage, specifically within tumor cells [85]. In this context, nanobody-drug conjugates may benefit from internalization mediated by biparatopic nanobodies. In this platform B, like in the other platforms, specificity is governed by the nanobody targeting to the tumor marker. Although a few tumor markers have been described, the future challenge will be the further development of tumor specific markers. Also future *in vivo*

studies concentrating on immunogenicity of nanobody-based formulations are eagerly awaited as most cancer therapies require repeated drug administrations. Once these issues are clarified, clinical trials may be initiated to further establish the most effective treatment platform.

Most of the reviewed literature focuses on intravenous delivery of nanobody-based platforms, however, it is known that heterogeneous vascularization and limited diffusion due to increased IFP hamper uniform drug distribution especially in large tumors. Although the existing nanobody platforms offer possibilities to circumvent this, future studies should investigate alternative ways of therapeutic nanobody delivery. One of the directions for further research could be the potential of engineered stem cell based therapeutics as initiated by van de Water et al. [86]. Constructs encoding bivalent anti-EGFR nanobodies were packaged into lentiviral virions and used to create neural stem cells secreting nanobodies. These cells were then implanted in mice bearing tumors in a dorsal skinfold window chamber. The authors reported that nanobodies secreted by stem cells efficiently localized to brain tumors, that a continuous release of nanobodies inhibited EGFR signaling and reduced brain tumor growth [86].

The tumor targeting of nanobodies (platform A) and nanobody-conjugates (platform B) are very promising as their relatively small size allows for better distribution through solid tumors. Nevertheless, future research should be aimed at preventing rapid clearance of these small therapeutic molecules, through increase of their half-life in patients, though still with minimal side-effects. Targeting of nanoparticles by nanobodies (platform C) remains a very potent strategy as a large payload can be encapsulated in a nanoparticle, protecting normal tissues, although their distribution through the tumor may be less effective due to their size. The design of smaller (< 100 nm) and biodegradable nanoparticles, still able to encapsulate a sufficient amount of drugs, that are released upon a particular stimulus at the tumor site, might improve distribution and thus the efficacy of these systems. Tumor heterogeneity in terms of receptor expression is one of many challenges to be overcome in order to provide successful therapy. In this respect, novel tumor targets are necessary. Personalized medicine will require the initial analysis of the expression levels of tumor markers. This can be done by analysis of a biopsy using a cocktail of nanobodies with different specificities, and detection either by microscopy or by FRET-based detection system we recently developed [87]. Subsequently, the appropriate nanobody-based therapy could be selected. This approach will greatly improve the attempts of personalized medicine in the coming future.

Executive summary

Nanobodies as solid cancer therapeutics:

- Nanobodies, even though ten times smaller than conventional monoclonal antibodies, retain high target specificity and affinity.
- Due to the ease of nanobody engineering they can be employed into three nanobody-based therapeutic platforms, such as: (A) receptor antagonist to interfere with or block the activation of a certain signaling pathway, (B) targeting moiety that transports effector domains, such as toxic peptides or drugs, or (C) targeting molecules on the surface of nanoparticles.
- So far nanobodies targeting receptors such as EGFR, HER2, VEGFR2, c-Met, CXCR7 or ligands (HGF, chemokines) have been developed.

Systemic circulation upon injection:

- Residence time in the blood stream upon iv injection is an important factor, which depends on the type of nanobody platform, and affects nanobody-based therapeutic accumulation at the tumor.
- Size and shape of the molecule are the main determinants of the secretion route. In general, an average weight cutoff for renal clearance is approximately 60 kDa and preference for particles with a hydrodynamic diameter < 8nm.
- Therapeutics that did not undergo renal clearance are removed by hepatic clearance, which preferentially removes particles with a hydrodynamic diameter of 10-20 nm.
- Several strategies can be employed to prolong residence time in the circulation such as coupling to anti-albumin nanobody in case of platform A or PEGylation in case of platform C.

Nanobody extravasation and tumor penetration:

- Due to elevated interstitial pressure, penetration of therapeutics into the tumor is mediated by diffusion. As this depends on size, nanobodies in platforms A and B penetrate tumors much better than mAb.
- The hyperpermeability of chaotically organized tumor blood vessels and lack of lymphatic drainage lead to passive accumulation of platform C therapeutics at the tumor site.
- Nanobody interaction with targets:
- Specific interaction with target cells in case of all platforms is mediated by the nanobody,
- High affinity of the nanobody allows it to remain at the tumor and escape renal clearance in case of platform A and B.
- High affinity of nanobody does not play a major role when nanobodies are employed as targeting moieties of liposomes, micelles or nanoparticles (platform C), which accumulate at the tumor as

a consequence of the enhanced permeability and retention effect.

References

1. Oldham RK, Dillman RO: Monoclonal antibodies in cancer therapy: 25 years of progress. *J. Clin. Oncol.* 26(11), 1774-1777 (2008).

2. Oliveira S, Heukers R, Sornkom J, Kok RJ, van Bergen En Henegouwen PM: Targeting tumors with nanobodies for cancer imaging and therapy. *J. Control. Release* 172(3), 607-617 (2013).

3. Senter PD: Potent antibody drug conjugates for cancer therapy. *Curr. Opin. Chem. Biol.* 13(3), 235-244 (2009).

4. Sarma VR, Silverton EW, Davies DR, Terry WD: The three-dimensional structure at 6 A resolution of a human gamma Gl immunoglobulin molecule. *J. Biol. Chem.* 246(11), 3753-3759 (1971).

5. Siontorou CG: Nanobodies as novel agents for disease diagnosis and therapy. *Int. J. Nanomedicine* 8, 4215-4227 (2013).

6. Baker JH, Lindquist KE, Huxham LA, Kyle AH, Sy JT, Minchinton AI: Direct visualization of heterogeneous extravascular distribution of trastuzumab in human epidermal growth factor receptor type 2 overexpressing xenografts. *Clin. Cancer Res.* 14(7), 2171-2179 (2008).

7. Rudnick SI, Adams GP: Affinity and avidity in antibody-based tumor targeting. *Cancer Biother. Radiopharm.* 24(2), 155-161 (2009).

8. Bell A, Wang ZJ, Arbabi-Ghahroudi M *et al.*: Differential tumor-targeting abilities of three single-domain antibody formats. *Cancer Lett.* 289(1), 81-90 (2010).

9. Hamers-Casterman C, Atarhouch T, Muyldermans S *et al.*: Naturally occurring antibodies devoid of light chains. *Nature* 363(6428), 446-448 (1993).

10. Padlan EA: Anatomy of the antibody molecule. *Mol. Immunol.* 31(3), 169-217 (1994).

11. Muyldermans S: Nanobodies: natural single-domain antibodies. *Annu. Rev. Biochem.* 82, 775-797 (2013).

12. Oliveira S, van Dongen GA, Stigter-van Walsum M *et al.*: Rapid visualization of human tumor xenografts through optical imaging with a near-infrared fluorescent anti-epidermal growth factor receptor nanobody. *Mol. Imaging* 11(1), 33-46 (2012).

13. Dumoulin M, Conrath K, Van Meirhaeghe A *et al.*: Single-domain antibody fragments with high conformational stability. *Protein Sci.* 11(3), 500-515 (2002).

14. van der Linden RH, Frenken LG, de Geus B *et al.*: Comparison of physical chemical properties of llama VHH antibody fragments and mouse monoclonal antibodies. *Biochim. Biophys. Acta* 1431(1), 37-46 (1999).

15. Muyldermans S, Atarhouch T, Saldanha J, Barbosa JA, Hamers R: Sequence and structure of VH domain from naturally occurring camel heavy chain immunoglobulins lacking light chains. *Protein Eng.* 7(9), 1129-1135 (1994).

16. Bartunek J, Barbato E, Heyndrickx G, Vanderheyden M, Wijns W, Holz JB: Novel antiplatelet agents: ALX-0081, a Nanobody directed towards von Willebrand factor. *J. Cardiovasc. Transl. Res.* 6(3), 355-363 (2013).

17. Vincke C, Loris R, Saerens D, Martinez-Rodriguez S, Muyldermans S, Conrath K: General strategy to humanize a camelid single-domain antibody and identification of a universal humanized nanobody scaffold. *J. Biol.*

Chem. 284(5), 3273-3284 (2009).

18. Roovers RC, Laeremans T, Huang L *et al.*: Efficient inhibition of EGFR signaling and of tumour growth by antagonistic anti-EFGR Nanobodies. *Cancer Immunol. Immunother.* 56(3), 303-317 (2007).

19. Pardon E, Laeremans T, Triest S *et al.*: A general protocol for the generation of Nanobodies for structural biology. *Nat. Protoc.* 9(3), 674-693 (2014).

20. Omidfar K, Rasaee MJ, Modjtahedi H, Forouzandeh M, Taghikhani M, Golmakani N: Production of a novel camel single-domain antibody specific for the type III mutant EGFR. *Tumour Biol.* 25(5-6), 296-305 (2004).

21. Vaneycken I, Devoogdt N, Van Gassen N *et al.*: Preclinical screening of anti-HER2 nanobodies for molecular imaging of breast cancer. *FASEB J.* 25(7), 2433-2446 (2011).

22. Kijanka M, Warnders FJ, El Khattabi M *et al.*: Rapid optical imaging of human breast tumour xenografts using anti-HER2 VHHs site-directly conjugated to IRDye 800CW for image-guided surgery. *Eur. J. Nucl. Med. Mol. Imaging* 40(11), 1718-1729 (2013).

23. Van de Broek B, Devoogdt N, D'Hollander A *et al.*: Specific cell targeting with nanobody conjugated branched gold nanoparticles for photothermal therapy. *ACS Nano* 5(6), 4319-4328 (2011).

24. Holmes K, Roberts OL, Thomas AM, Cross MJ: Vascular endothelial growth factor receptor-2: structure, function, intracellular signalling and therapeutic inhibition. *Cell. Signal.* 19(10), 2003-2012 (2007).

25. Olsson AK, Dimberg A, Kreuger J, Claesson-Welsh L: VEGF receptor signalling - in control of vascular function. *Nat. Rev. Mol. Cell Biol.* 7(5), 359-371 (2006).

26. Behdani M, Zeinali S, Khanahmad H *et al.*: Generation and characterization of a functional Nanobody against the vascular endothelial growth factor receptor-2; angiogenesis cell receptor. *Mol. Immunol.* 50(1-2), 35-41 (2012).

27. Bottaro DP, Rubin JS, Faletto DL *et al.*: Identification of the hepatocyte growth factor receptor as the c-met proto-oncogene product. *Science* 251(4995), 802-804 (1991).

28. Gherardi E, Birchmeier W, Birchmeier C, Vande Woude G: Targeting MET in cancer: rationale and progress. *Nat. Rev. Cancer.* 12(2), 89-103 (2012).

29. Schmidt Slordahl T, Denayer T, Helen Moen S *et al.*: Anti-c-MET Nanobody((R)) - a new potential drug in multiple myeloma treatment. *Eur. J. Haematol.* 91(5), 399-410 (2013).

30. Heukers R, Altintas I, Raghoenath S *et al.*: Targeting hepatocyte growth factor receptor (Met) positive tumor cells using internalizing nanobody-decorated albumin nanoparticles. *Biomaterials* 35(1), 601-610 (2014).

31. Rajagopal S, Kim J, Ahn S *et al.*: Beta-arrestin- but not G protein-mediated signaling by the "decoy" receptor CXCR7. *Proc. Natl. Acad. Sci. U. S. A.* 107(2), 628-632 (2010).

32. Miao Z, Luker KE, Summers BC *et al.*: CXCR7 (RDC1) promotes breast and lung tumor growth in vivo and is expressed on tumor-associated vasculature. *Proc. Natl. Acad. Sci. U. S. A.* 104(40), 15735-15740 (2007).

33. Blanchetot C, Verzijl D, Mujic-Delic A *et al.*: Neutralizing nanobodies targeting diverse

chemokines effectively inhibit chemokine function. *J. Biol. Chem.* 288(35), 25173-25182 (2013).

34. Vosjan MJ, Vercammen J, Kolkman JA, Stigter-van Walsum M, Revets H, van Dongen GA: Nanobodies targeting the hepatocyte growth factor: potential new drugs for molecular cancer therapy. *Mol. Cancer. Ther.* 11(4), 1017-1025 (2012).

35. Roovers RC, Vosjan MJ, Laeremans T *et al.*: A biparatopic anti-EGFR nanobody efficiently inhibits solid tumour growth. *Int. J. Cancer* 129(8), 2013-2024 (2011).

36. Omidfar K, Amjad Zanjani FS, Hagh AG, Azizi MD, Rasouli SJ, Kashanian S: Efficient growth inhibition of EGFR over-expressing tumor cells by an anti-EGFR nanobody. *Mol. Biol. Rep.* 40(12), 6737-6745 (2013).

37. Altintas I, Heukers R, van der Meel R *et al.*: Nanobody-albumin nanoparticles (NANAPs) for the delivery of a multikinase inhibitor 17864 to EGFR overexpressing tumor cells. *J. Control. Release* 165(2), 110-118 (2013).

38. Talelli M, Rijcken CJ, Oliveira S *et al.*: Nanobody-shell functionalized thermosensitive core-crosslinked polymeric micelles for active drug targeting. *J. Control. Release* 151(2), 183-192 (2011).

39. Oliveira S, Schiffelers RM, van der Veeken J *et al.*: Downregulation of EGFR by a novel multivalent nanobody-liposome platform. *J. Control. Release* 145(2), 165-175 (2010).

40. Talelli M, Rijcken CJ, Oliveira S *et al.*: Nanobody-shell functionalized thermosensitive core-crosslinked polymeric micelles for active drug targeting. *J. Control. Release* 151(2), 183-192 (2011).

41. van der Meel R, Oliveira S, Altintas I *et al.*: Tumor-targeted Nanobullets: Anti-EGFR nanobody-liposomes loaded with anti-IGF-1R kinase inhibitor for cancer treatment. *J. Control. Release* 159(2), 281-289 (2012).

42. Bannas P, Well L, Lenz A *et al.*: In vivo near-infrared fluorescence targeting of T cells: comparison of nanobodies and conventional monoclonal antibodies. *Contrast Media Mol. Imaging* 9(2), 135-142 (2014).

43. Heukers R, Vermeulen JF, Fereidouni F *et al.*: Endocytosis of EGFR requires its kinase activity and N-terminal transmembrane dimerization motif. *J. Cell. Sci.* 126(Pt 21), 4900-4912 (2013).

44. Talelli M, Oliveira S, Rijcken CJ *et al.*: Intrinsically active nanobody-modified polymeric micelles for tumor-targeted combination therapy. *Biomaterials* 34(4), 1255-1260 (2013).

45. Heukers R, van Bergen En Henegouwen PM, Oliveira S: Nanobody-photosensitizer conjugates for targeted photodynamic therapy. *Nanomedicine* (2014).

46. van der Meel R, Oliveira S, Altintas I *et al.*: Inhibition of tumor growth by targeted anti-EGFR/IGF-1R nanobullets depends on efficient blocking of cell survival pathways. *Mol. Pharm.* 10(10), 3717-3727 (2013).

47. Altintas I, Heukers R, van der Meel R *et al.*: Nanobody-albumin nanoparticles (NANAPs) for the delivery of a multikinase inhibitor 17864 to EGFR overexpressing tumor cells. *J. Control. Release* 165(2), 110-118 (2013).

48. Behdani M, Zeinali S, Karimipour M *et al.*: Development of VEGFR2-specific Nanobody Pseudomonas exotoxin A conjugated to provide

efficient inhibition of tumor cell growth. *N. Biotechnol.* 30(2), 205-209 (2013).

49. Maussang D, Mujic-Delic A, Descamps FJ *et al.*: Llama-derived single variable domains (nanobodies) directed against chemokine receptor CXCR7 reduce head and neck cancer cell growth in vivo. *J. Biol. Chem.* 288(41), 29562-29572 (2013).

50. Hussack G, Hirama T, Ding W, Mackenzie R, Tanha J: Engineered single-domain antibodies with high protease resistance and thermal stability. *PLoS One* 6(11), e28218 (2011).

51. Nichols JW, Bae YH: Odyssey of a cancer nanoparticle: from injection site to site of action. *Nano Today* 7(6), 606-618 (2012).

52. Longmire M, Choyke PL, Kobayashi H: Clearance properties of nano-sized particles and molecules as imaging agents: considerations and caveats. *Nanomedicine (Lond)* 3(5), 703-717 (2008).

53. Vaneycken I, Govaert J, Vincke C *et al.*: In vitro analysis and in vivo tumor targeting of a humanized, grafted nanobody in mice using pinhole SPECT/micro-CT. *J. Nucl. Med.* 51(7), 1099-1106 (2010).

54. Vegt E, Melis M, Eek A *et al.*: Renal uptake of different radiolabelled peptides is mediated by megalin: SPECT and biodistribution studies in megalin-deficient mice. *Eur. J. Nucl. Med. Mol. Imaging* 38(4), 623-632 (2011).

55. Kobayashi H, Le N, Kim IS *et al.*: The pharmacokinetic characteristics of glycolated humanized anti-Tac Fabs are determined by their isoelectric points. *Cancer Res.* 59(2), 422-430 (1999).

56. Choi HS, Liu W, Misra P *et al.*: Renal clearance of quantum dots. *Nat. Biotechnol.* 25(10), 1165-1170 (2007).

57. Li T, Bourgeois JP, Celli S *et al.*: Cell-penetrating anti-GFAP VHH and corresponding fluorescent fusion protein VHH-GFP spontaneously cross the blood-brain barrier and specifically recognize astrocytes: application to brain imaging. *FASEB J.* 26(10), 3969-3979 (2012).

58. Muyldermans S, Baral TN, Retamozzo VC *et al.*: Camelid immunoglobulins and nanobody technology. *Vet. Immunol. Immunopathol.* 128(1-3), 178-183 (2009).

59. Cortez-Retamozo V, Lauwereys M, Hassanzadeh Gh G *et al.*: Efficient tumor targeting by single-domain antibody fragments of camels. *Int. J. Cancer* 98(3), 456-462 (2002).

60. Gunther R, Chelstrom LM, Wendorf HR *et al.*: Toxicity profile of the investigational new biotherapeutic agent, B43 (anti-CD19)-pokeweed antiviral protein immunotoxin. *Leuk. Lymphoma* 22(1-2), 61-70, follow.186, color plate II-V (1996).

61. Uckun FM, Yanishevski Y, Tumer N *et al.*: Pharmacokinetic features, immunogenicity, and toxicity of B43(anti-CD19)-pokeweed antiviral protein immunotoxin in cynomolgus monkeys. *Clin. Cancer Res.* 3(3), 325-337 (1997).

62. Gainkam LO, Caveliers V, Devoogdt N *et al.*: Localization, mechanism and reduction of renal retention of technetium-99m labeled epidermal growth factor receptor-specific nanobody in mice. *Contrast Media Mol. Imaging* 6(2), 85-92 (2011).

63. Ekblad T, Tran T, Orlova A *et al.*: Development and preclinical characterisation of 99mTc-labelled Affibody molecules with reduced renal uptake. *Eur. J. Nucl. Med. Mol.*

Imaging 35(12), 2245-2255 (2008).

64. Tijink BM, Laeremans T, Budde M *et al.*: Improved tumor targeting of anti-epidermal growth factor receptor Nanobodies through albumin binding: taking advantage of modular Nanobody technology. *Mol. Cancer. Ther.* 7(8), 2288-2297 (2008).

65. Newkirk MM, Novick J, Stevenson MM, Fournier MJ, Apostolakos P: Differential clearance of glycoforms of IgG in normal and autoimmune-prone mice. *Clin. Exp. Immunol.* 106(2), 259-264 (1996).

66. Chapman AP, Antoniw P, Spitali M, West S, Stephens S, King DJ: Therapeutic antibody fragments with prolonged in vivo half-lives. *Nat. Biotechnol.* 17(8), 780-783 (1999).

67. Kuntz E: Hepatology : principles and practice; history, morphology, biochemistry,diagnostics, clinic, therapy. Springer, Heidelberg (2006).

68. Xie H, Svenmarker P, Axelsson J *et al.*: Pharmacokinetic and biodistribution study following systemic administration of Fospeg(R) - a Pegylated liposomal mTHPC formulation in a murine model. *J. Biophotonics* (2013).

69. Gabizon A, Horowitz AT, Goren D, Tzemach D, Shmeeda H, Zalipsky S: In vivo fate of folate-targeted polyethylene-glycol liposomes in tumor-bearing mice. *Clin. Cancer Res.* 9(17), 6551-6559 (2003).

70. Lewanski CR, Stewart S: Pegylated liposomal adriamycin: a review of current and future applications. *Pharm. Sci. Technolo Today* 2(12), 473-477 (1999).

71. Mamot C, Drummond DC, Noble CO *et al.*: Epidermal growth factor receptor-targeted immunoliposomes significantly enhance the efficacy of multiple anticancer drugs in vivo. *Cancer Res.* 65(24), 11631-11638 (2005).

72. Jain RK, Stylianopoulos T: Delivering nanomedicine to solid tumors. *Nat. Rev. Clin. Oncol.* 7(11), 653-664 (2010).

73. Fujimori K, Covell DG, Fletcher JE, Weinstein JN: A modeling analysis of monoclonal antibody percolation through tumors: a binding-site barrier. *J. Nucl. Med.* 31(7), 1191-1198 (1990).

74. Li Y, Wang J, Wientjes MG, Au JL: Delivery of nanomedicines to extracellular and intracellular compartments of a solid tumor. *Adv. Drug Deliv. Rev.* 64(1), 29-39 (2012).

75. Sexton K, Tichauer K, Samkoe KS, Gunn J, Hoopes PJ, Pogue BW: Fluorescent affibody peptide penetration in glioma margin is superior to full antibody. *PLoS One* 8(4), e60390 (2013).

76. Wood DW, Camarero JA: Intein Applications: From Protein Purification and Labeling to Metabolic Control Methods. *J. Biol. Chem.* (2014).

77. Popp MW, Antos JM, Ploegh HL: Site-specific protein labeling via sortase-mediated transpeptidation. *Curr. Protoc. Protein Sci.* Chapter 15, Unit 15.3 (2009).

78. Mao H, Hart SA, Schink A, Pollok BA: Sortase-mediated protein ligation: a new method for protein engineering. *J. Am. Chem. Soc.* 126(9), 2670-2671 (2004).

79. Proft T: Sortase-mediated protein ligation: an emerging biotechnology tool for protein modification and immobilisation. *Biotechnol. Lett.* 32(1), 1-10 (2010).

80. Moses JE, Moorhouse AD: The growing applications of click chemistry. *Chem. Soc. Rev.* 36(8), 1249-1262 (2007).

81. Spangler JB, Neil JR, Abramovitch S *et al.*:

Combination antibody treatment down-regulates epidermal growth factor receptor by inhibiting endosomal recycling. *Proc. Natl. Acad. Sci. U. S. A.* 107(30), 13252-13257 (2010).
82. Mamot C, Drummond DC, Greiser U *et al.*: Epidermal growth factor receptor (EGFR)-targeted immunoliposomes mediate specific and efficient drug delivery to EGFR- and EGFRvIII-overexpressing tumor cells. *Cancer Res.* 63(12), 3154-3161 (2003).
83. Mamot C, Ritschard R, Kung W, Park JW, Herrmann R, Rochlitz CF: EGFR-targeted immunoliposomes derived from the monoclonal antibody EMD72000 mediate specific and efficient drug delivery to a variety of colorectal cancer cells. *J. Drug Target.* 14(4), 215-223 (2006).
84. Talelli M, Iman M, Varkouhi AK *et al.*: Core-crosslinked polymeric micelles with controlled release of covalently entrapped doxorubicin. *Biomaterials* 31(30), 7797-7804 (2010).
85. Lim EK, Jang E, Lee K, Haam S, Huh YM: Delivery of cancer therapeutics using nanotechnology. *Pharmaceutics* 5(2), 294-317 (2013).
86. van de Water JA, Bagci-Onder T, Agarwal AS *et al.*: Therapeutic stem cells expressing variants of EGFR-specific nanobodies have antitumor effects. *Proc. Natl. Acad. Sci. U. S. A.* 109(41), 16642-16647 (2012).
87. Hofman EG, Ruonala MO, Bader AN *et al.*: EGF induces coalescence of different lipid rafts. *J. Cell. Sci.* 121(Pt 15), 2519-2528 (2008).

Chapter 7

A potential treatment for trastuzumab resistant breast cancer: nanobody-targeted photodynamic therapy

Marta M. Kijanka
Małgorzata Krawczyk-Durka
Elly G. van Donselaar
Jan A. Post
Paul M.P. van Bergen en Henegouwen
Sabrina Oliveira

Manuscript in preparation

Abstract

Introduction: Breast cancer treatment has been revolutionized by approval of a monoclonal antibody (mAb), trastuzumab. This mAb targets the extracellular part of HER2 receptor, which is a predictive and prognostic breast cancer marker. Despite its unquestionable success the problem of primary resistance affects 65% of patients. Moreover, more than 70% of patients, who initially respond to the trastuzumab treatment acquire resistance over time. This highlights the need for development of new therapies that would allow treatment of trastuzumab resistant cancers.

Methods: In this study we present the development of potent, traceable nanobody-photosensitizer conjugates for the use in photodynamic therapy (PDT). Nanobodies targeting HER2 receptor expressed by trastuzumab sensitive and resistant cells were obtained in phage display selections. Monovalent nanobodies were engineered into a biparatopic construct stimulating HER2 receptor internalization. The specificity of selected nanobodies was tested in an immunofluorescence assay in a panel of breast cancer cells, whereas their affinity was evaluated in a binding study. Two of the selected nanobodies were further evaluated as PDT nanomedicines. For this purpose they were conjugated randomly to a traceable photosensitizer (PS, IRDye700DX) and tested in a PDT *in vitro* assay.

Results: Results show that three selected nanobodies displayed affinities in low nanomolar range and bound specifically to HER2 receptor. Two nanobodies with highest affinities, 1D5 and 1D5-18A12, were conjugated to PS and an approximately 2 fold drop in affinity was observed on SKBR3 and HCC-1954 cells. Both nanobody-PS conjugates potently induced cell death of HER2 overexpressing cells (SKBR3, HCC-1954 and HCC-1419 cells) with IC_{50} values in low nanomolar range, whereas this was not the case for nanobodies alone, PS alone or nanobody-PS without light illumination.

Conclusion: The developed nanobody-photosensitizer conjugates are potent nanomedicines, capable of inducing cell death of both trastuzumab resistant and sensitive HER2-overexpressing cells. Furthermore, due to fluorescent properties of employed PS they enable the combination of molecular imaging with breast cancer therapy.

Introduction

Breast cancer is one of the most common cancers in women worldwide. Despite increased understanding of its development and progression, as well as advance in development of novel therapeutic strategies, breast cancer remains a clinical challenge. Nowadays, operable breast cancer is treated primarily with surgery followed by radiation therapy to prevent local disease reoccurrence (adjuvant radiation therapy) [1-3]. The primary tumor, depending on its size and location, may be managed by lumpectomy or mastectomy [2]. In some cases, surgical intervention is preceded by neoadjuvant therapy, which by downsizing large tumors facilitates breast-conserving surgery in patients, who would otherwise require a mastectomy [2,4,5]. Systemic management of breast cancer is obtained by three types of therapies, which are administered in order to prevent development of distant metastases. These adjuvant therapies include endocrine therapy (suitable for patients, whose tumors express estrogen and/or progesterone receptors), chemotherapy (employing taxanes or anthracyclines) and, more recently, biological therapy (employing biological agents directed against molecular targets on the surface or in proximity of cancer cells) [2,6,7].

The development of targeted therapy utilizing monoclonal antibodies (mAb) was a major breakthrough in breast cancer treatment. Due to the selective character of these anti-proliferative agents, less severe side-effects have been associated with these therapies. In 1998, trastuzumab (Herceptin®) was approved by Food and Drug Administration (FDA) for use in women with metastatic breast cancer, whose tumors overexpress the HER2 protein [8]. Trastuzumab is a recombinant, humanized mAb, which recognizes an epitope on subdomain 4 of HER2 extracellular domain [9,10]. In 2012, mAb Pertuzumab (Omnitarg®) which inhibits HER2 dimerization by binding to subdomain 2, was approved by the FDA.

HER2, a validated predictive and prognostic marker, is a member of the human epidermal growth factor receptors family (ErbB family). Similarly to other members of this family, it consists of an extracellular domain, a hydrophobic transmembrane part and intra-cellular domain possessing tyrosine kinase activity followed by a substrate domain. A unique feature of this receptor is the absence of a known ligand and the presence at the membrane in an open conformation, which makes it a preferred dimerization partner for other ErbB receptors. Upon cross-phosphorylation by ligand-bound dimerization partners, intracellular signal transduction pathways are activated leading to increased cell proliferation and motility, neo-angiogenesis and decreased apoptosis. This receptor is overexpressed in 20-25% of breast cancer patients, resulting in a more aggressive disease with a greater likelihood of its recurrence and poor prognosis [11].

The exact mode of the inhibitory action of trastuzumab still remains unclear, although several mechanisms have been proposed. Binding to HER2 results in (i) inhibition of signal transduction leading to inhibition of cell cycle progression [9,12,13] and (ii) inhibition of angiogenesis [12]. Secondly, binding of trastuzumab and pertuzumab may stimulate antibody depended cellular

cytotoxicity (ADCC) [12-14]. At the moment, treatment combinations that include trastuzumab are considered a standard of care for HER2 overexpressing breast cancer patients. Clinical trials evaluated administration of trastuzumab both concurrent with chemotherapy and sequential, in neo- and adjuvant setting, as well as in early and locally advanced breast cancer [11]. Unfortunately, less than 35% of patients with HER2 overexpressing tumors respond to the trastuzumab treatment [9]. This is a result of a *de novo* or 'primary' resistance. Moreover, 70% of patients, who initially responded to the therapy, will acquire resistance and progress to a metastatic disease within 24 to 36 months [9]. Several mechanisms responsible for this resistance have been proposed so far, such as: (i) aberrant activation of downstream signaling pathways, (ii) compensatory activation of parallel signaling pathways, (iii) steric hindrance of receptor-monoclonal antibody interaction, (iv) truncation of the extracellular domain bearing the epitope recognized by the monoclonal antibody [9,12]. At the moment HER2 receptor status remains the only available biomarker for selecting breast cancer patients suitable for trastuzumab-based treatment, even though there are no clinical markers for trastuzumab resistance. The development of novel imaging and therapeutic approaches (also designated theranostics) for HER2 overexpressing breast cancer patients is therefore of great importance, as it would simultaneously allow the diagnosis, the subsequent treatment of HER2-positive lesions, and the detection of HER2 for following treatment monitoring.

Photodynamic therapy (PDT) is a therapy approved for clinical treatment of several types of cancer (e.g. skin, lung, bladder, head and neck) and non-oncological disorders (e.g. actinic keratosis, age-related macular degeneration) [15]. PDT relies on photosensitizing properties of a chemical compound (photosensitizer, PS), combined with a specific wavelength of light and oxygen present in close proximity to the PS. The PS exposure to light leads to a transition from ground to the excited state and during its return to ground state singlet oxygen is formed [16,17]. Singlet oxygen and/or ROS toxicity induces direct cellular damage, impairment of tumor-associated vasculature and immune response against cancer cells, resulting in cancer cell death via apoptosis or necrosis [16]. Even though the activation of the PS occurs locally, where light is applied, the fact that conventional PS are small, hydrophobic, and non-selective molecules, makes PDT often associated with unwanted phototoxicity. The conjugation of PS to conventional monoclonal antibodies, referred to as photo-immunotherapy, reduces this unwanted reaction, by specifically targeting the PS to cancer cells [18,19].

Recently we have introduced a novel format of targeted PDT by conjugating the traceable photosensitizer IRDye700DX to nanobodies [20]. Nanobodies (also referred to as VHHs or single domain antibodies) are the smallest naturally occurring, functional antigen binding fragments of only 15 kDa, derived from heavy-chain only antibodies present in *Camelidae*. Although nanobodies have been employed for therapy on their own (naked nanobodies [21]), in this context nanobodies are employed as targeting moieties, that carry the therapeutic entity, here a PS. The expected advantage over conventional antibodies, which is based on molecular imaging studies [22,23], is the faster accumulation

at the tumor site and the faster removal of unbound fraction from the blood circulation, as well as a more homogenous distribution within the tumor due to their size [23]. Thus far, we have shown in vitro that EGFR-targeted nanobody-PS conjugates are very potent PDT agents and that bi-paratopic nanobody-PS conjugates lead to an improved efficacy of PDT due to the internalization of the conjugate [20].

In this study we focused on the selection and *in vitro* evaluation of two monovalent and one biparatopic nanobody specifically targeting HER2. The two most promising nanobodies were then conjugated to the traceable photosensitizer IRDye700DX, characterized *in vitro* and evaluated as potential nanomedicines for treatment of both trastuzumab-sensitive and resistant breast cancer cells. These new conjugates are promising novel nanomedicines that, besides combining imaging with therapy, may successfully overcome trastuzumab resistance of human breast cancer cells.

Materials and methods

Phage display selection and production of anti-HER2 nanobodies

To select nanobodies specifically binding to human HER2 two different, previously described phage display libraries were panned (MCF7L1 and BT474L1) [22]. Briefly, anti-HER2 phages were selected on recombinant purified HER2-ECD captured on a Maxisorp plate (Nunc, Rochester, MN, USA) via rabbit-anti-human IgG antibody (DakoCytomation, Glostrup, Denmark). Coated wells were blocked with 4% milk powder in PBS for 1 h at RT. Phages pre-blocked with 4% milk-powder for 30 min at RT were panned for binding to immobilized HER2-ECD. After extensive washing with PBS/0.05% Tween-20, phages were eluted with trypsin (Sigma-Aldrich Chemie B.V. Zwijndrecht, Netherlands). The coding sequences of the obtained nanobodies binding to the HER2 ectodomain were identified by performing sequence analysis (Macrogen Inc., Amsterdam, The Netherlands). From these selections, two distinct nanobodies targeting HER2, namely 1D5 and 18A12 were identified and employed in this study. From these two nanobodies, a bivalent nanobody, i.e. 1D5-18A12, was constructed as nanobody-encoding genes were PCR amplified using the Expand High Fidelity PCR System (Roche, Mannheim, Germany) with an appropriate primer set, purified, cut with restriction enzymes and cloned into Sfi1-BstEII cut pET28A vector. Linker sequence (composed of two Gly4-Ser (G4S) repeats) was encoded in the primers. Constructs were sequenced to verify that no mutations were introduced by PCR. These nanobodies were produced in E.coli and TALON affinity purified as described before [23].

Cell lines and culture conditions

Several human breast cancer cell lines were employed, which differ in HER2 expression level and

are either responsive or resistant to trastuzumab treatment. HER2-positive breast cancer cell lines SKBR3, BT474, and MCF7, which are sensitive to trastuzumab treatment, and the HCC-1419, HCC-1954, and JIMT1 cell lines, which are resistant to trastuzumab treatment were employed. As HER2-negative breast cancer cell line, MDA-MB-231 was employed. All these cell lines, except the JIMT1 cell line, were purchased from the American Type Culture Collection (ATCC, Manassas, VA, USA). JIMT1 cells were purchased from DMSZ (DSMZ GmbH, Braunschweig, Germany). HCC-1419 cells, due to difficulty in handling, were not included in all assays. All cells, except from HCC-1419 and HCC-1954 cells, were cultured in DMEM (Gibco) supplemented with 7.5% (v/v) FBS, 100 IU/ml penicillin, 100 mg/ml streptomycin, and 2 mM L-glutamine. HCC-1419 and HCC-1954 cells were maintained in RPMI medium supplemented as described above.

Western blot

Half a million cells were resuspended in reducing sample buffer (50mM Tris-HCl pH 6.8, 10% glycerol, 100mM DTT, 2% SDS and 0.01% bromophenol blue) and PBS with a ratio 1:4 and boiled for 5 min at 100°C. Western blot analysis was performed using the following primary antibodies: rabbit anti-HER2 (2242, Cell Signaling Technology, Danvers, MA, USA), mouse anti-EGFR (c74B9, Cell signaling Technology), mouse anti α-tubulin (DM1A, Millipore, Billerica, MA, USA) and as secondary antibodies: goat anti-rabbit IRDye800CW (Li-COR Biosciences, Lincoln, Nebraska) and goat anti-mouse IRDye680RD (Li-COR Biosciences, Lincoln, Nebraska, USA). Membranes were scanned with an Odyssey Scanner (Li-COR Biosciences, Lincoln, Nebraska, USA) and the images analyzed with the Odyssey software.

Proliferation assay

Five thousand cells per well were seeded, next day cells were washed with DMEM without phenol red supplemented with 7.5 % (v/v) fetal bovine serum (FBS), 100 IU/ml penicillin, 100 mg/ml streptomycin and 2 mM L-glutamine and treated with 20 μg/ml trastuzumab for 96 hours without refreshing the medium. To determine the percentage of viable cells, the Alamar Blue assay was performed according to manufacturer's protocol (AbD Serotec, Oxford, United Kingdom) .

Competition assay

Competition assay was performed on recombinant purified HER2-ECD captured on a Maxisorp plate (Nunc, Rochester, MN, USA) via rabbit-anti-human IgG antibody (DakoCytomation, Glostrup, Denmark). Coated wells were blocked with 4% milk powder in PBS (mPBS)

for 1h at RT. Phages expressing 1D5 or 18A12 on their surface were preblocked with 4% milkpowder for 30 min at RT and added to immobilized HER2-ECD together with bacterial periplasms containing 1D5 or 18A12. After 2 hrs incubation at RT the plate was washed with PBS/0.05% Tween-20. The remaining, HER2-bound phages were detected with mouse-anti-M13-PO antibody (incubation for 1 h at RT in 2% mPBS). The color reaction was initiated by addition of OPD and stopped by 1M H_2SO_4. The absorbance was read out at 490 nm.

Internalization assay

Nanobodies were labeled according to the IODO-GEN method as described by Salacinski et al. [24]. Internalization assays using ^{125}I-labeled proteins were performed on SKBR3 cells following a protocol described before [25]. Radioactivity of both surface bound fraction and internalized fraction were determined using the gamma counter and the ratio of internalized to bound was plotted against time to determine specific internalization rate constants. Experiments were performed in triplicate. Data represent the mean ± SEM.

Visualization of nanobody internalization in electron microscopy

SKBR3 cells were grown to 70% confluency in culture dishes and incubated for 24 hrs at 37°C with the selected HER2-targeted nanobodies or without nanobody, as a control. Next day, after short wash with warm culture medium, cells were fixed with 4% (w/v) formaldehyde (FA, Sigma-Aldrich Chemie B.V. Zwijndrecht, Netherlands) in PHEM buffer (60 mM PIPES, 25 mM HEPES, 10 mM EGTA, 2 mM $MgCl_2$, pH 6.9) first for 2 hrs at room temperature (RT) and continued overnight at 4°C. Next, cells were scraped from the plate and solidified in 12% gelatin. Gelatin blocks of ~1mm^3 were prepared on an ice-cooled metal plate under a stereo-microscope. After an overnight infiltration with 2.3 M sucrose, the blocks were plunge frozen in liquid nitrogen. Ultra-thin sections (80-90 nm) were cut under control of an ionizer (Diatome AG) with a cryo-ultramicrotome (UC6/FC6; Leica Microsytems, Rijswijk, The Netherlands). Upon removal of residual gelatin and blocking in PBS containing 0.225% (v/v) CFG + 0.1% (v/v) BSA-c (CFG: Gelatin from cold water fish skin 45% in water (Sigma-Aldrich Chemie B.V. Zwijndrecht, Netherlands), BSA-c: acetylated Bovine Serum Albumin 10% in water (Aurion, Wageningen, The Netherlands) to prevent non-specific labeling, sections were immunogold labeled. Incubation with rabbit anti-VHH serum (RαVHH, 1mg/ml, 1:50, Rabbit 1219, QVQ, Utrecht, The Netherlands) in the blocking buffer was carried out for 1 h, followed by 20 minutes incubation with protein A coupled to 15 nm Gold (PAG15; CMC, Utrecht, The Netherlands) in blocking buffer. Sections were further fixed with 1% Glutaraldehyde (Taab, Berks, England) in PBS, post-stained with 2% Uranyl

Acetate (EMS) in 0.15 M Oxalic Acid (Merck, Haarlem, The Netherlands) pH 7.4 and embedded in 1.8% Methyl Cellulose (Sigma-Aldrich Chemie B.V. Zwijndrecht, Netherlands) and 0.4% Uranyl Acetate (EMS) in distilled water. The grids with sections were air-dried in a thin layer of embedding solution and viewed in a JEM 1010 transmission electron microscope (Jeol Ltd., Tokyo, Japan).

Determination of apparent affinity of nanobodies on HER2-positive cells

For apparent affinity determination on HER2-positive cells, 20.000 cells/well were seeded 2 days in advance. Cells were incubated at 4^0C for 1.5 h with a dilution series of nanobodies in DMEM without phenol red, supplemented with 25 mM HEPES and 1% BSA, pH 7.2 (binding buffer). Nanobodies were added in a concentration range from 500 nM to 0.48 nM. After several washes cells were fixed with 4% formaldehyde (FA) for 30 min at RT and the fixative was blocked by 10 min incubation with 100 mM glycine in PBS. The detection of bound nanobodies was performed with the use of rabbit anti-VHH protein G purified serum (1:1000 for 1h at RT), followed by a goat anti rabbit – IRDye800 (1:1000 for 1h at RT). The fluorescence signal was detected using the 800 nm channel of the Odyssey scanner (LI-COR).

Immunofluorescence

Two hundred thousand HER2 positive or HER2 negative cells were grown on coverslips for 2 days. On the day of the assay, cells were washed with CO_2-independent medium and incubated for 1.5 h at 4°C with a 50 nM solution of a nanobody (namely 1D5, 18A12, 1D5-18A12). Unbound nanobodies were removed and cells were fixed with 4% FA. Bound nanobody was detected with rabbit anti-VHH protein G purified serum (1:1000 for 1 h at RT), followed by goat anti-rabbit Alexa 488 (1:1000 for 1 h at RT; Invitrogen, Breda, The Netherlands), and cell nuclei was stained with DAPI (Roche, Almere, The Netherlands). Images were acquired using Zeiss confocal microscope.

Conjugation of PS IRDye700DX to the nanobodies and their binding affinities

The photosensitizer IRDye700DX (PS) was purchased from LI-COR (LICOR Biosciences, Lincoln, Nebraska) as an N-hydroxysuccinimidine (NHS) ester. Conjugation of the PS was performed with a fourfold molar excess of PS for monovalent nanobodies and twofold molar excess for the bivalent nanobody for 2 hrs at RT. After conjugation, the unconjugated PS was removed using sequentially two (in case of 1D5-18A12) or three (in case of 1D5) Pierce Zeba™ Desalting Spin Columns. The degree of conjugation (D.O.C.) was determined according to the instructions given by the provider of the PS.

For determination of apparent binding affinity of these conjugates to HER2

expressing cells, the assay was performed as described for the nanobodies except that the cell bound nanobody-PS conjugates were detected directly, through the PS fluorescence, after the washing steps using the 700 nm channel of the Odyssey scanner.

In vitro PDT

One day after seeding 20.000 cells per well in 96-well plate (Greiner Bio-One, Alphen a/d Rijn, The Netherlands), cells were washed with DMEM without phenol red supplemented with 7.5 % (v/v) fetal bovine serum (FBS), 100 IU/ml penicillin, 100 mg/ml streptomycin and 2 mM L-glutamine (PDT medium). Then cells were incubated with a dilution series of nanobody-PS conjugates for 30 min at 37^0C. After the incubation (also referred to as pulse) cells were washed twice with the PDT medium and the detection of total fluorescence (i.e. bound and internalized fluorescence of the nanobody-PS conjugates) was performed immediately afterwards using the Odyssey scanner. Then the cells were illuminated for 42 min with 4 mW/cm^2 fluence rate for a total light dose of 10 J/cm2, using a custom made device consisting of 96 LED lamps (670 +/- 10nm, 1 LED per well), connected to a water bath thermostated at 37°C. An Orion Laser power/energy monitor (Ophir Optronics LTD, Jerusalem, Israel) was used to measure and adjust the light intensity. After illumination, cells were placed back in an incubator. In all experiments, an internal negative control was included (those cells were not subjected to illumination). Experiments were repeated at least twice.

Cell viability assay

After an overnight post-treatment incubation, cells were incubated with Alamar Blue Reagent, according to the manufacturer's protocol (AbD Serotec, Oxford, United Kingdom). The fluorescence was detected with a Fluorostar 2h after addition of the reagent. Results are expressed as cell viability in percentage (%), relatively to the untreated cells. Half of the maximal inhibitory concentration (IC50) was determined using the GraphPad Prism 5.02 software (San Diego, CA, USA). Data is plotted in triplicate ± SEM.

Imaging of live and dead cells

HER2 positive and negative cells were seeded in 96-wells plates one day before pulse with 25 nM nanobody-PS followed by illumination (10 J/cm^2 of light dose). Live cells were detected with calcein AM (Invitrogen), whereas dead cells with propidium iodide (Invitrogen) staining right after light illumination and 3 hrs or 24 hrs after light illumination, unless stated otherwise. Fluorescence images were taken using the bright field, GFP and RFP and Cy5 channels on the EVOS Microscope (Advanced Microscopy Group, AMG, Thermo Fischer Scientific, Bleiswijk, The Netherlands) equipped with 10x

objective (Plan Fluor, 10x, NA 0.3, Air and working distance 8.3 mm, AMG) as described before [20].

Apoptosis assay

Cells were treated with PDT (as described above) and the possibility of cell death through apoptosis was assessed immediately after illumination. For this the following stains were employed: acridine orange, which stains condensed chromatin in green, typical for apoptotic cells, and ethidium homodimer, which only stains cells in red when their membrane is damaged, occurring during necrosis (procedure similar to what is described in [26]). For the positive control, 5 μM campthotecin was employed to induce apoptosis after 16 hrs incubation with cells. Fluorescence images were taken the EVOS Microscope (Advanced Microscopy Group, AMG, Thermo Fischer Scientific, Bleiswijk, The Netherlands) equipped with 20x objective (Plan Fluor, 10x, NA 0.3, Air and working distance 8.3 mm, AMG). From a total of 100 cells counted, in triplicates for each sample, the early apoptotic cells and dead cells were distinguished from the living cells and data is plotted in percentages ± SD.

Statistical analysis

Data was analyzed using the GraphPad Prism 5.02 software for Windows. Analysis of significance was performed by Student's t-test and differences with p-values ≤ 0.05 were considered significant.

Results

Affinity selection and characterization of HER2 targeted nanobodies

To obtain nanobodies that bind to the human HER2 receptor with high affinity, two phage display libraries were panned on captured HER2 extracellular domain (ECD). This resulted in the selection of two nanobodies, which bind specifically and with high affinity to HER2: 1D5 from the MCF7L1 library and 18A12 from the BT474L1 immune library. These two nanobodies were further engineered into a bivalent nanobody (Fig.1S A). To study the binding of these nanobodies to HER2, we used a panel of different cell lines, both sensitive and resistant to trastuzumab: SKBR3, BT474, HCC-1954 and HCC-1419, which are highly HER2 expressing cells, JIMT1, which has a moderate HER2 expression level and MDA-MB-231, which are considered negative for HER2 expression (Fig.1S B and C) [27,28]. The binding specificity of the three nanobodies was confirmed by immunofluorescence. A clear fluorescent signal was observed for all three nanobody formats at the cell membrane of HER2 positive cells (SKBR3, BT474, HCC-1954, and HCC-1419), whereas no fluorescence was observed at the negative cell line (MDA-MB-231) (Fig.1 and Fig 1S B). For JIMT1 cells a very faint fluorescence signal was detected, only in case of the bivalent nanobody.

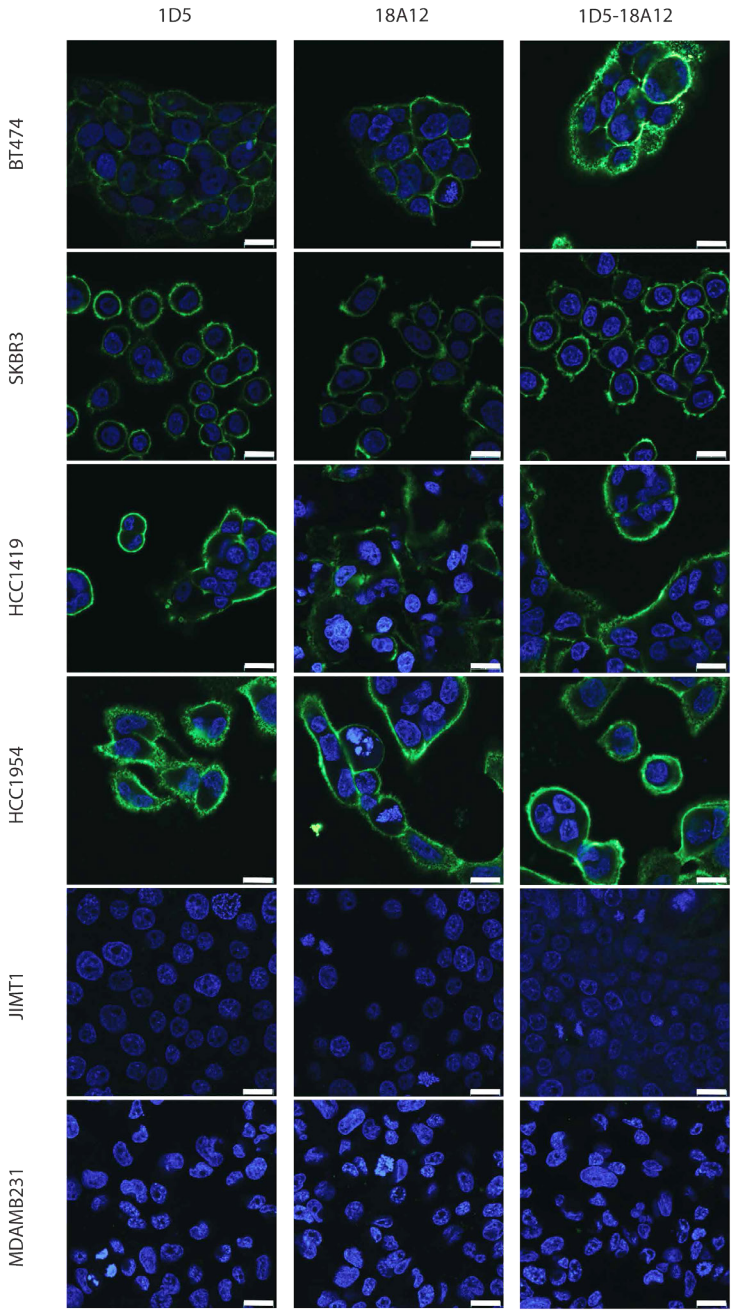

Fig. 1. Selected nanobodies are HER2 specific. The HER2 overexpressing cell lines: SKBR3, BT474, HCC-1419 and HCC-1954 , the low HER2 expressing cell line JIMT1 , and the HER2 negative cell line MDA-MB-231 were incubated with the nanobodies, monovalent (1D5 and 18A12) or bivalent (1D5-18A12) at 50 nM concentration, and imaged using confocal microscopy (scale bar = 20 μm).

We have previously shown that internalizing nanobodies are more effective in PDT than the nanobodies that remain at the cell surface [20]. In that study, internalization of PS was obtained by employing a biparatopic nanobody, which is known to promote receptor-mediated internalization [29].

To assess whether the bivalent nanobody 1D5-18A12 is in fact a biparatopic nanobody, a competition set-up was employed to evaluate whether the nanobodies 1D5 and 18A12 bind to different epitopes of HER2 ECD. Results clearly showed that the two nanobodies recognize non-overlapping epitopes, as the excess of one of them did not affect the binding of the phage expressing the other one on its surface (Fig. 2 A). Furthermore, the displacement by the same nanobody highlights the specificity in binding HER2 ECD and rules out the a-specific association. Internalization of these HER2-targeting nanobodies was analyzed using radio-labeled nanobodies. The 18A12 nanobody showed a slight increase in the internalization rate constant as compared to 1D5. The biparatopic nanobody 1D5-18A12 showed a ten-fold increase in internalization confirming previous results [29] (Fig.2 B). The EM data further confirmed internalization of both nanobody constructs (Fig.4S). Moreover, the engineered biparatopic nanobody did not compete for the binding epitope with trastuzumab (data not shown).

To determine the apparent binding affinities of the selected HER2 targeted nanobodies we performed binding studies on a panel of HER2 expressing cells: SKBR3, HCC1954 and JIMT1 cells. The HER2 negative cell line MDA-MB-231 was also employed, to determine whether the nanobodies could bind non-specifically at high concentrations. Very high affinities were observed for all three nanobodies binding to HER2 positive cells (Fig.2 C-E and Table 1).

Cell line	Affinity of the nanobody [nM]		
	1D5	18A12	1D5-18A12
SKBR3	4.1 ± 1.7	11.5 ± 4.0	3.1 ± 0.6
HCC-1954	2.1 ± 0.4	16.7 ± 4.9	4.6 ± 0.6

Table 1. Affinities of HER2-targeted nanobodies determined using SKBR3 and HCC-1954 cells.

Importantly, no binding was observed to the MDA-MB-231 cells, not even at the highest concentrations. On JIMT1 cells, only very low binding was observed with the biparatopic nanobody, which correlates with the moderate/low HER2 expression level (Fig 1S B). The differences in the extent of maximum binding (B_{max}) between HCC-1954 and SKBR3 most likely reflect differences in epitope availability, as the HER2 expression determined by western blotting is only slightly higher in HCC-1954 cells (Fig. S1).

In conclusion, the employed selection strategy resulted in two new nanobodies that bind specifically and with high affinity to the HER2 receptor in its natural surroundings. Combining these two nanobodies resulted in a biparatopic nanobody that preserves the HER2-specificity and induces HER2 internalization.

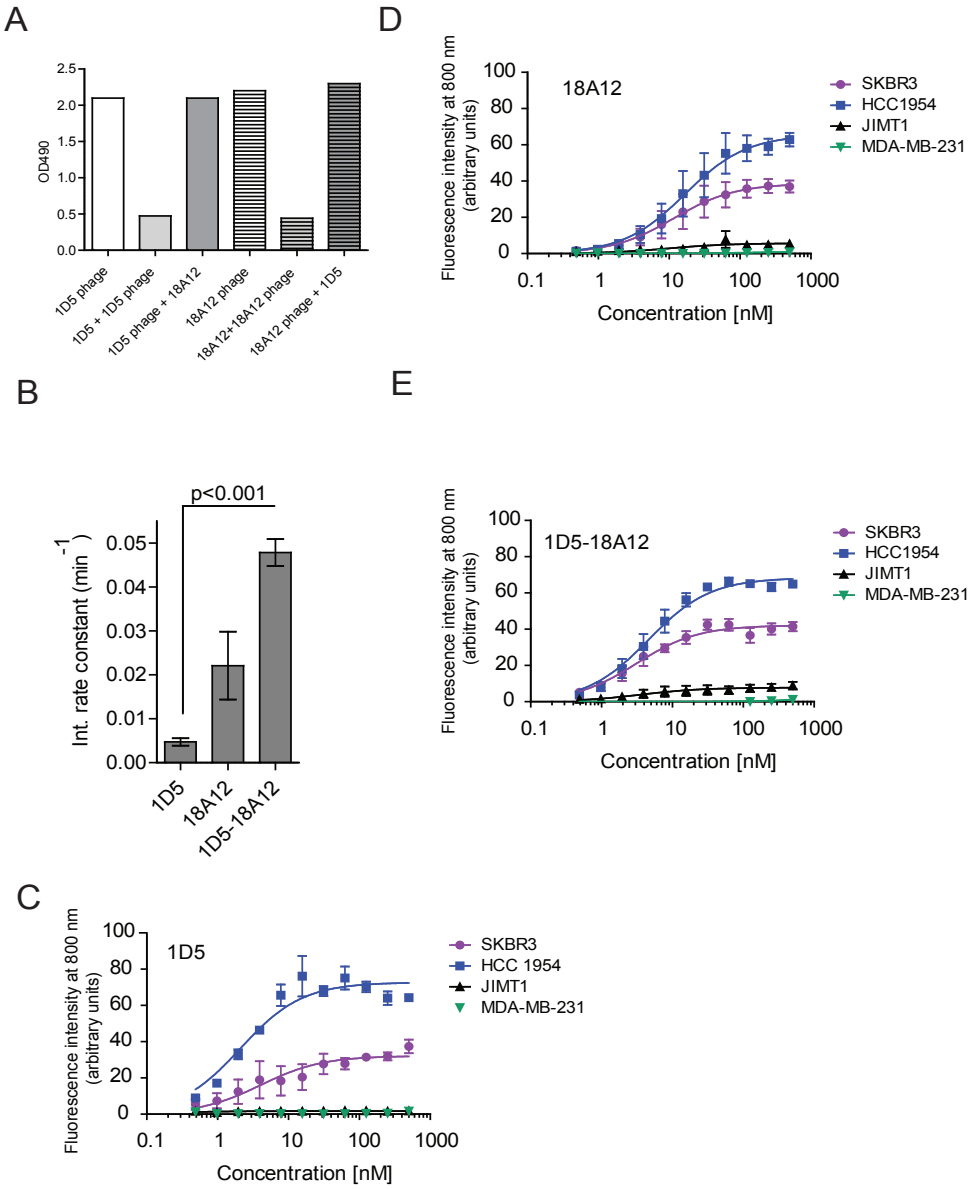

Fig. 2. Development of HER2 specific, internalizing biparatopic nanobody. The selected HER2 targeted nanobodies, 1D5 and 18A12, recognize non-overlapping epitopes. A. Phages expressing one of the nanobodies were incubated with periplasmic extract containing the other nanobody on captured HER2-ECD. The HER2-bound phages were detected using mouse-anti-M13-PO antibody and the graph shows absorbance at 490 nm. B. The biparatopic nanobody internalizes 10 times faster than its monovalent counterpart 1D5, as determined in internalization study on SKBR3 cells. Graph shows mean ± SEM (n=9). C-E. All selected nanobodies bind to cell lines according to their HER2 expression level: HCC-1954 > SKBR3 > JIMT1 and not to MDA-MB-231 cells. Detection of bound nanobodies was performed through primary and secondary antibodies (Materials and Methods).

Production and characterization of nanobody-PS conjugates

The two HER2 targeted nanobodies displaying the highest affinity were considered the most promising (i.e. 1D5 and 1D5-18A12) and therefore these were further evaluated for their therapeutic potential in targeted photodynamic therapy (PDT) of breast cancer. For this, the nanobodies were randomly conjugated to the IRDye700DX (PS) through NHS ester by coupling to the primary amines of the nanobodies (i.e. N-terminal amino acid and lysine residues) as described before [20], and subsequently purified. The obtained PS conjugated nanobodies are referred to as nanobody-PS (1D5-PS and 1D5-18A12-PS). The success of the conjugation was examined by SDS-PAGE, which also showed the remaining free PS. All nanobody-PS preparations contained less than 10% of free PS (Fig.2S A). The D.O.C. (PS to protein ratio) was close to one for all nanobody-PS conjugates and this process was reproducible.

Nanobody-PS conjugates bind specifically to HER2 on trastuzumab-sensitive and resistant cells

It is known that random conjugation may have a detrimental effect on the binding properties of nanobodies [20,22], therefore apparent affinities of 1D5-PS and 1D5-18A12-PS were tested in a binding study on SKBR3, BT474, HCC-1954, and MDA-MB-231 cells. These studies were performed under non-internalizing conditions at 4°C. The fact that the PS here employed is also a good fluorophore, allowed for direct detection of the nanobody-PS conjugates bound to cells (Fig. 3 A and B). The apparent affinity of both 1D5-PS and 1D5-18A12-PS were affected (Table 2).

Cell line	Affinity of the nanobody-PS [nM]	
	1D5-PS	1D5-18A12-PS
SKBR3	8.2 ± 0.9	7.8 ± 0.9
BT474	7.5 ± 1.6	16.7 ± 2.5
HCC-1954	5.4 ± 0.9	10.1 ± 1.1

Table 2. Affinity of 1D5-PS and 1D5-18A12-PS determined using SKBR3, BT474 and HCC-1954 cells.

An approximately 2 fold drop in affinity was observed for both mono- and bivalent nanobody when binding to SKBR3 or to HCC1954 cells. Importantly, both nanobody-conjugates remained able to bind with low nanomolar affinities and specifically to HER2 receptor present on trastuzumab-sensitive cells (SKBR3 and BT474 cells), and on trastuzumab resistant cells (HCC-1954), and did not bind to HER2 negative cells (MDA-MB-231), which correlates with expression levels of HER2 receptor.

Nanobody-PS conjugates are potent and specific PDT agents

The selectivity and therapeutic potential of nanobody-PS induced PDT was assessed with *in vitro* PDT

assays on different HER2-expressing cell lines. For these, the nanobody-PS conjugates were incubated with the cells for 30 min at 37°C. This short time incubation was sufficient to reach a plateau of fluorescence intensity (from approx. 12.5 nM concentrations), which suggests saturation (Fig. 3C and D).

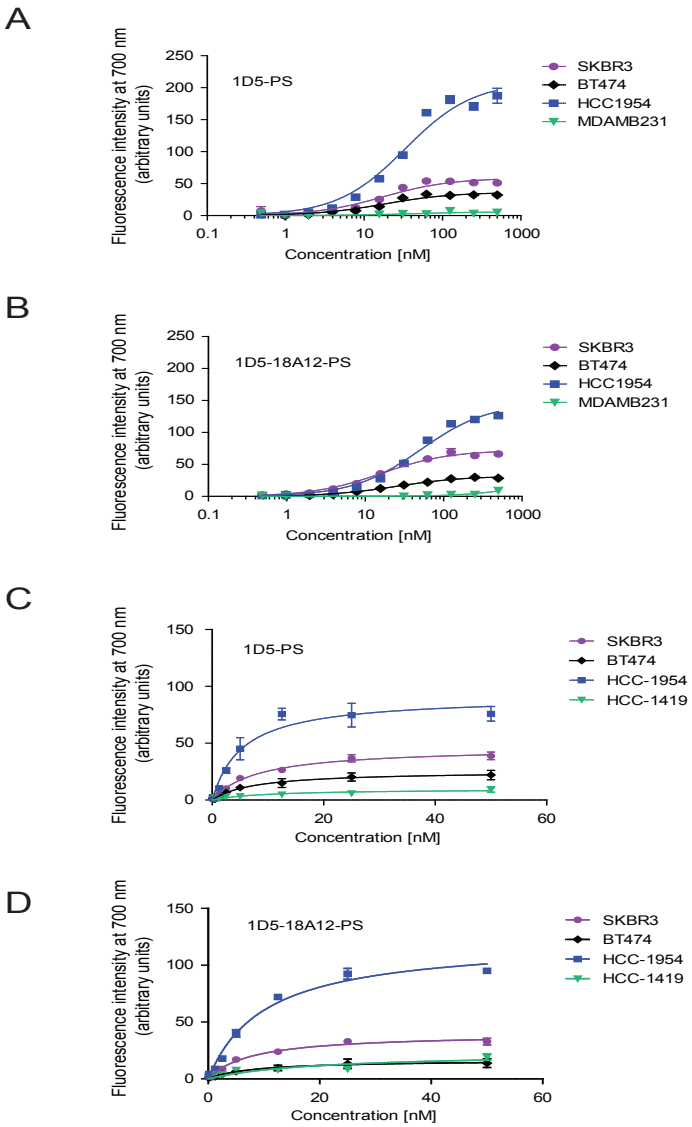

Fig. 3. Nanobody-PS conjugates bind to cell lines according to their HER2 expression levels. Dilution series of 1D5-PS (A) and 1D5-18A12-PS (B) were incubated with cells for 1 h 30 min at 4°C to determine apparent affinity. Bound nanobodies are directly detected through fluorescence of the PS. Total fluorescence intensity associated with cells after 30 min pulse at 37°C with a concentration range of 1D5-PS (C) or 1D5-18A12-PS (D).

The fluorescence of the PS was used to detect cell-associated nanobody-PS conjugates. After illumination for PS activation, both nanobody-PS showed to be very potent and capable of inducing cell death. The determined nanomolar IC_{50} values are summarized in Table 3.

Cell line	IC_{50} of nanobody-PS [nM]	
	1D5-PS	1D5-18A12-PS
SKBR3	7.2 ± 3.4	3.1 ± 1.7
BT474	5.7 ± 3.1	5.5 ± 1.6
HCC-1954	5.5 ± 1.9	1.8 ± 1.5
HCC-1419	4.7 ± 0.9	1.7 ± 0.5

Table 3. IC_{50} values of 1D5-PS and 1D5-18A12-PS determined using SKBR3, BT474, HCC-1954 and HCC-1419 cells.

No toxicity was observed on trastuzumab-resistant JIMT1 cells, whereas high toxicity was observed for trastuzumab-resistant HCC-1954 and HCC1419 cells (Fig.4).

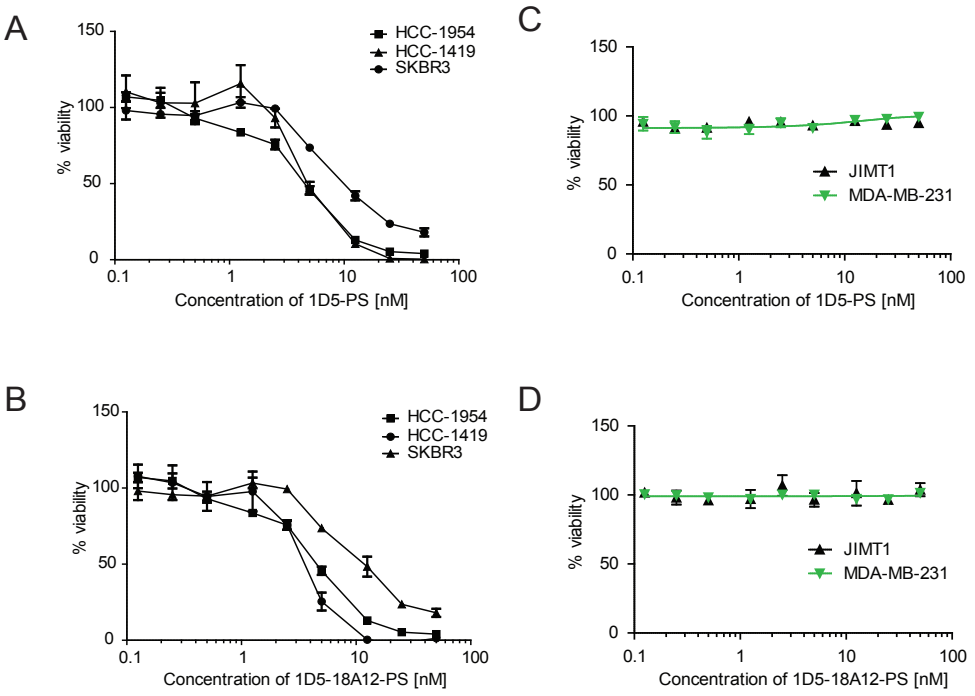

Fig.4. Nanobody-PS are potent, HER2-specific PDT agents. Cell viability determined 24 hrs after illumination with 10 J/cm^2. PDT with HER2 overexpressing cells and 1D5-PS (A) or 1D5-18A12-PS (B). Attempt on low or negative HER2 expressing cells with 1D5-PS (C) or 1D5-18A12-PS (D).

The lack of toxic effect on JIMT1 cells is most likely a result of low receptor levels on the cell surface. The IC_{50} determined for the 1D5-PS were approximately 2 fold lower than IC_{50} of 1D5-

18A12-PS as determined on SKBR3 cells and approximately 3 fold lower when determined on HCC-1954 or HCC-1419 cells (Table 3).

Both nanobody-PS caused no toxicity on HER2 negative, MDA-MB-231 cells, which proved their HER2 specificity (Fig. 4 C and D). Lack of toxicity on both JIMT1 and MDA-MB-31 cells is in agreement with binding assays (Fig.2) and pulse data (data not shown). Importantly, nanobodies alone, PS alone or nanobody-PS without light illumination were also tested using SKBR3 and HCC-1954 cells and did not affect their viability (Fig. 3S B and C).

To assess the effect of PDT at different time points post illumination, dead cells were distinguished from live cells with propidium iodide, which permeates only into dead cells, and calcein AM, which enables visualization of live cells exclusively. For both 1D5-PS and 1D5-18A12-PS, already as early as immediately after the illumination, some cell damage was observed due to propidium iodide staining of a small fraction of both SKBR3 and BT474 cells. This effect increased with time as shown by the increase of propidium iodide staining and the decrease of calcein staining (Fig. 5).

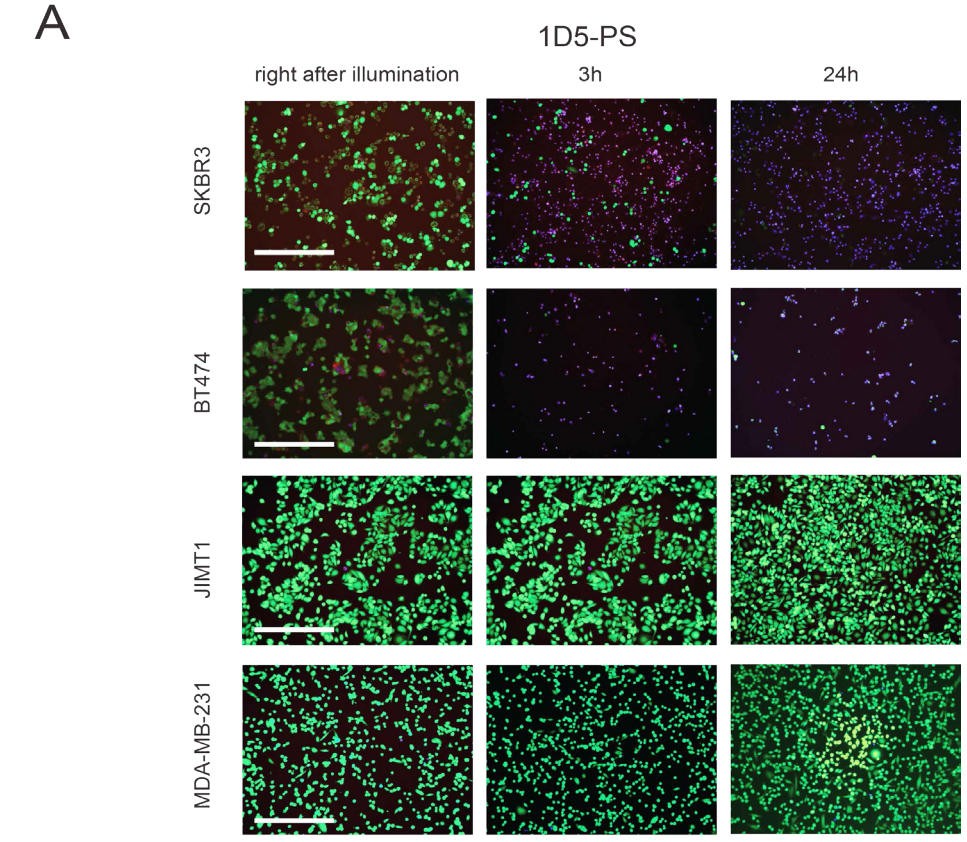

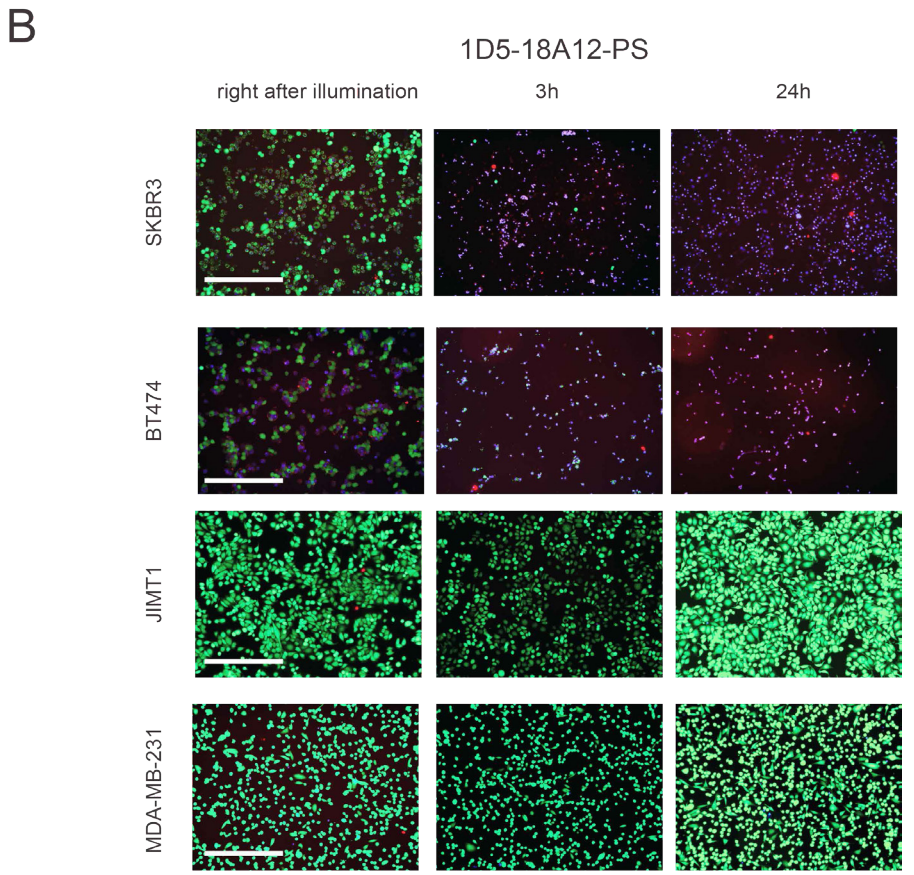

Fig.5. Imaging of live and dead cells. HER2 positive - SKBR3, BT474, JIMT1 - and negative -MDA-MB-231 cells were pulsed with 25 nM nanobody-PS, 1D5-PS (A) and 1D5-18A12-PS (B) followed by light illumination (10 J/cm^2 of light dose). Live cells were detected with calcein AM (green), whereas dead cells with propidium iodide (purple) staining right after light illumination and 3 hrs or 24 hrs after light illumination. Pictures were obtained with an EVOS Microscope equipped with 10x objective. Scale = 400 μm

The trastuzumab resistant cells, HCC-1954 were also clearly susceptible to the treatment with nanobody-PS. Dead cells were visualized with propidium iodide shortly after light illumination. Twenty four hours later this toxic effect was even more pronounced with the majority of HER2 expressing cells being positive for the marker of dead cells (Fig. 6).

The mechanism of PDT toxicity was investigated by staining cancer cells subjected to photodynamic treatment with acridine orange (which stains condensed chromatin, typical for apoptotic cells), and ethidium homodimer (which only stains cells, when their membrane is damaged, occurring during necrosis). Shortly after light illumination ethidium homodimer staining was detected, suggesting necrosis due to cell membrane damage (Fig. 7).

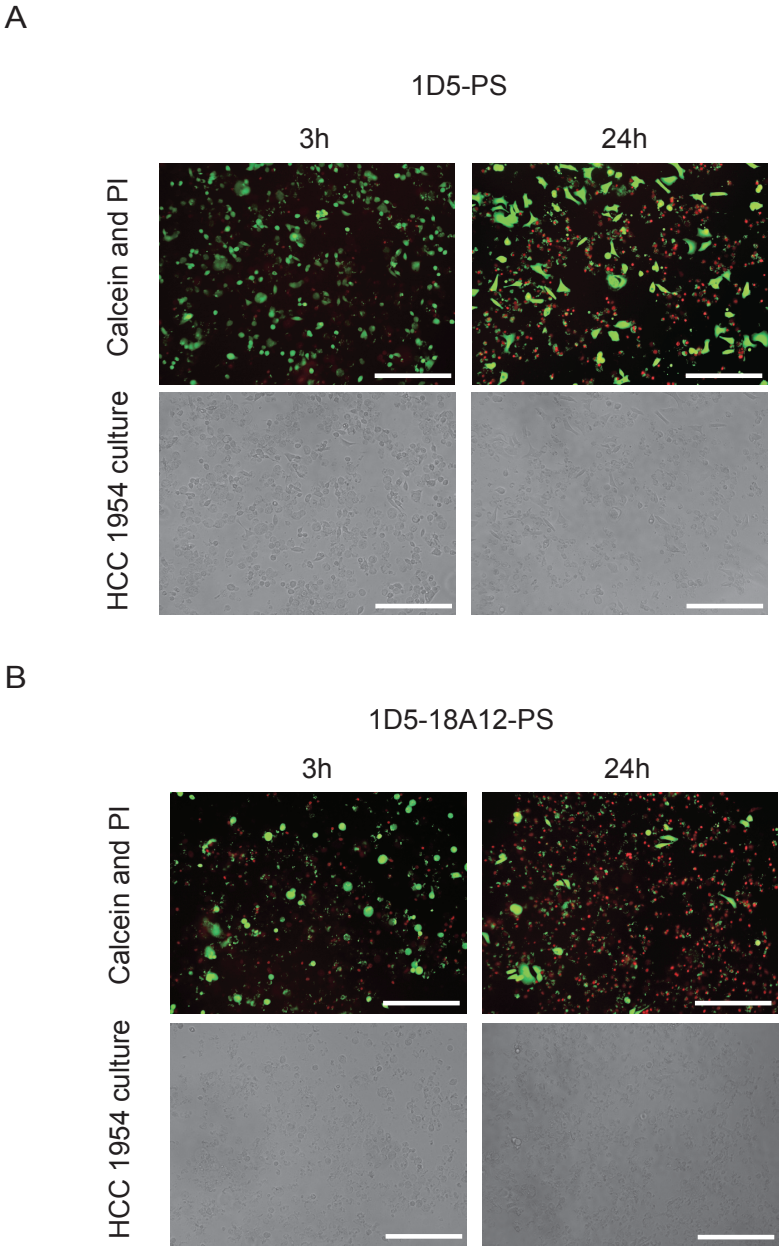

Fig.6. Imaging of live and dead trastuzumab resistant cells. HER2 positive HCC-1954 cells, resistant to trastuzumab treatment, were pulsed with 25 nM nanobody-PS, 1D5-PS (A) and 1D5-18A12-PS (B) followed by light illumination (10 J/cm^2 of light dose). Live cells were detected with calcein AM (green), whereas dead cells with propidium iodide (purple/red) staining 3 hrs and 24 hrs after light illumination. Pictures were obtained with the EVOS Microscope equipped with 10x objective. Scale = 400 μm.

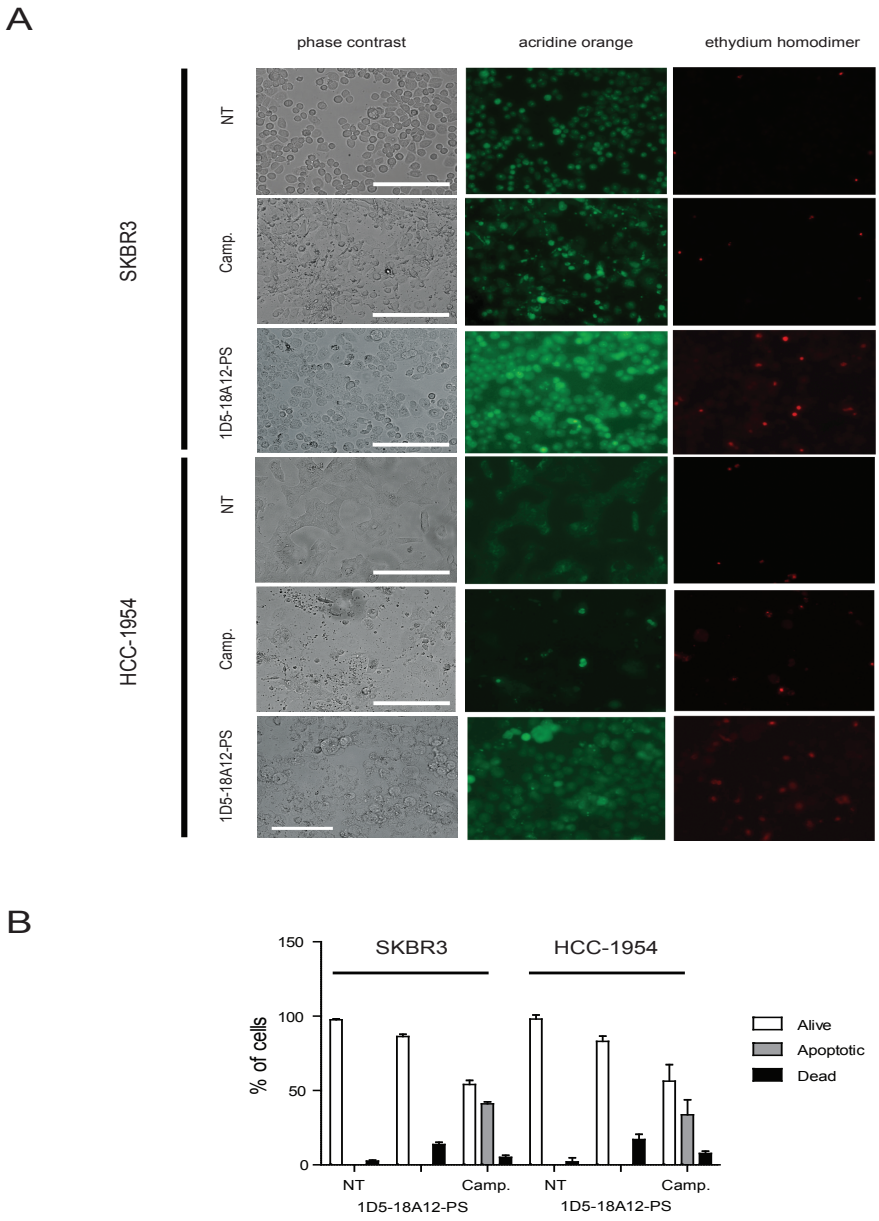

Fig.7. Biparatopic nanobody-PS induce necrosis right after light illumination. A. SKBR3 and HCC-1954 cells were pulsed with 1D5-18A12-PS and immediately after illumination two stains were employed to assess the mechanism of cell death: acridine orange, which either stains the entire nucleus (live cells) or stains condensed chromatin (apoptosis) in green, and ethidium homodimer, which only stains cells in red when their membrane is damaged, occurring during necrosis. As a positive control, campthotecin (Camp.) was employed to induce apoptosis after 16h incubation with cells. Pictures were obtained with an EVOS Microscope equipped with 20x objective. Scale = 200 μm. B. Quantification of apoptotic, necrotic and alive cells expressed as percentage of 100 cells counted. Data is plotted in percentages ± SD.

Discussion

At this moment, breast cancer treatment is limited to surgery often followed by radio-, hormonal and chemotherapy. There are only four HER2 specific drugs that have been approved by the FDA for the treatment of HER2 positive breast cancer patients, namely the humanized monoclonal antibodies trastuzumab and pertuzumab, small molecule tyrosine kinase inhibitor – lapatinib and a monoclonal antibody - drug conjugate ado-trastuzumab-emtansine (Kadcyla). Even though these treatments have proven to be effective, the problem of *de novo* and acquired resistance affecting 70% of HER2 positive breast cancer patients has a detrimental effect on their efficacy. There is therefore a great need for development of new treatments for HER2 positive breast cancers, in particular to treat the trastuzumab-resistance cancers, for which there are currently no predictive and validated biomarkers.

To our knowledge, this is the first study in which the potential of HER2 targeted nanobodies conjugated to a PS is evaluated as potential nanomedicines in targeted PDT for treatment of both trastuzumab-sensitive and trastuzumab-resistant cells. Here we show that the developed nanobody-PS conjugates specifically targeting HER2 receptor were capable of binding specifically to this receptor, present on both trastuzumab-sensitive and resistant cell lines with high affinities (Fig. 3). Furthermore, already shortly upon light illumination, after 30 min pulse at 37^0C, the cell association of the nanobodies-PS and their subsequent internalization resulted in cell death of HER2 overexpressing cells, an effect which became more pronounced 3 hrs and 24 hrs post illumination (Fig. 4-6). This photodynamic treatment was highly specific as the HER2 negative cells remained unaffected, as shown by the PDT *in vitro* assays.

So far, efforts towards targeted PDT have employed monoclonal antibodies and, only recently, the potential of nanobodies has been addressed as targeting moieties for PS. The unquestionable advantage of nanobodies is the combination of their small size (only 15 kDa), which leads to shorter blood-circulation and better tumor penetration, with high binding affinity for their targets, resulting in their high accumulation at the tumor site, which has been shown in breast cancer imaging studies [22,23]. For these reasons PDT employing nanobodies will most likely lead to decreased phototoxicity and will allow light application more rapidly after PS administration.

One of the major disadvantages of currently approved PS is their spectral properties, compelling the PS excitation with light below 700 nm, which results in light penetration of only a couple of millimeters [30,31]. In this study a recently described fluorescent near-infrared IRDye700DX is used, which allows deeper tissue penetration. Fluorescent properties of this PS make it a very interesting molecule as it could be employed both for diagnosis and treatment. In a clinical setting such nanobody-PS conjugates could be employed firstly to image the tumor and assist the surgeon in its resection and secondly, upon light administration to the resected area, to intoxicate the remaining cancer cells.

The bivalent construct turned out to be biparatopic and, as previously described for

other biparatopics [29], led to a faster internalization of the HER2 receptor in comparison to a monovalent counterpart. The internalization of the biparatopic nanobody was also confirmed by the EM images. The aim of developing the biparatopic nanobody was to ensure high accumulation of the fluorophore not only on the outside of the cell membrane, but also inside the cell itself. Heukers et al. showed an added value of the EGFR targeted biparatopic nanobody in PS delivery, resulting in an increased cell toxicity [20]. Here, the difference in IC_{50} values obtained for mono- and biparatopic nanobodies are not as pronounced as in Heukers et al. study, which may be explained by the increased conjugation of PS to the monovalent nanobody. Here we report the D.O.C. of approximately 1 for both nanobody formats employed, whereas Heukers et al. obtained a D.O.C. of 0.5 and 1.5 for the monovalent and biparatopic nanobodies targeting EGFR, respectively.

As shown by our results, the efficiency of targeted PDT depends strongly on receptor expression levels. The concept of the threshold dose was introduced already in early 1980s. According to it, a certain minimal concentration of toxic product, such as singlet oxygen, needs to be exceeded for the tissue damage to occur [32]. In targeted PDT, the amount of PS present at the tumor depends on the expression level of antigen against which the targeting moiety (nanobody) is raised. We have not observed any effect of nanobody-PS on trastuzumab-resistant JIMT1 cells, which are characterized by low HER2 expression, whereas a clear effect was visible with HER2-overexpressing trastuzumab resistant HCC-1954 and HCC-1419 and trastuzumab sensitive SKBR3 and BT474 cells. This may most likely be explained by too low HER2 expression levels, as PDT on MCF7 cells (HER2 positive cells expressing comparable HER2 levels to JIMT1 cells) also did not result in cell death. Abundant cell-surface expression of cancer-related markers is therefore essential for successful targeted PDT. JIMT1 cells express EGFR, therefore we have also tested our nanobody-based PDT approach with recently described EGFR targeted nanobody-PS conjugates, 7D12-9G8-PS [20], which led to 20% decrease in JIMT1 cell viability (data not shown). These observations suggest that targeting a protein overexpressed on JIMT1 cell surface would likely lead to a much more pronounced toxicity.

Triple-negative breast cancers remain a clinical challenge [33]. They do, however, often show EGFR overexpression. There is no EGFR-targeted treatment approved by the U.S. FDA except for lapatinib. Current EGFR-targeted treatment encompasses use of monoclonal antibodies and small molecule tyrosine inhibitors, nevertheless cases reporting acquiring resistance to this available medication have been described [34]. The current study brings in the new possibility of treating tumors resistant to available therapy options with nanobody-PS conjugates.

In this study we present a nanobody-based strategy to overcome trastuzumab resistance in breast cancer. Other therapeutics currently under development include a small molecule tyrosine inhibitor – neratinib, mTOR inhibitors – everolimus and temsirolimus, and a monoclonal antibody – bevacizumab. Nevertheless, the biggest disadvantage of these therapies in comparison to here presented nanobody-based PDT approach is their poor HER2 specificity [35].

In conclusion, we demonstrated development of HER2 targeting nanobody-PS conjugates potently and specifically killing cells that are known to be HER2 positive/trastuzumab-sensitive as well as HER2 positive/trastuzumab resistant cells. The next step is to evaluate performance of these conjugates as image-guided therapy agents (or theranostics), combining tumor molecular imaging with therapy *in vivo*.

Supplementary information

Results

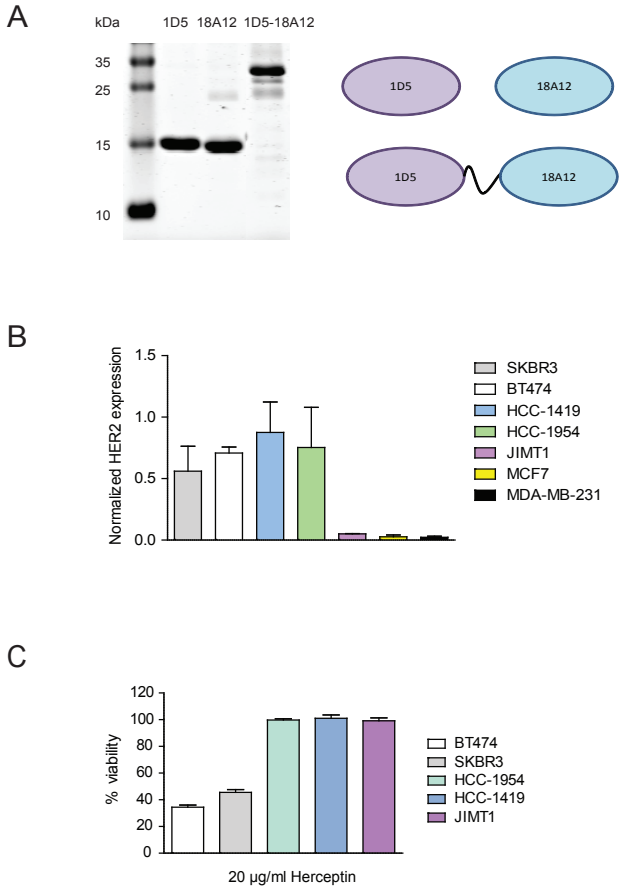

Fig.1S. A. SDS-PAGE gel of produced and purified nanobodies, and their schematic representation. B. Quantification of HER2 expression determined by Western Blot, normalized against α-tubulin staining. Bars represent mean ± SD (n=2). C. Determination of trastuzumab-sensitivity status of employed HER2 expressing cell lines. Graph shows percentage of cell viability upon continuous incubation with 20 µg/ml of trastuzumab for 96 hours. Bars represent mean ± SD (n=4).

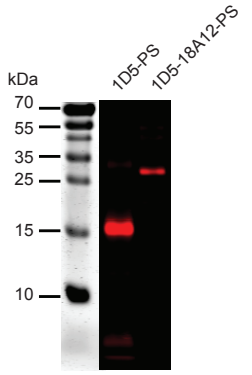

Fig.2S. Fluorescent nanobody-PS conjugated separated by SDS-PAGE. Conjugates are identified as 1D5-PS and 1D5-18A12-PS.

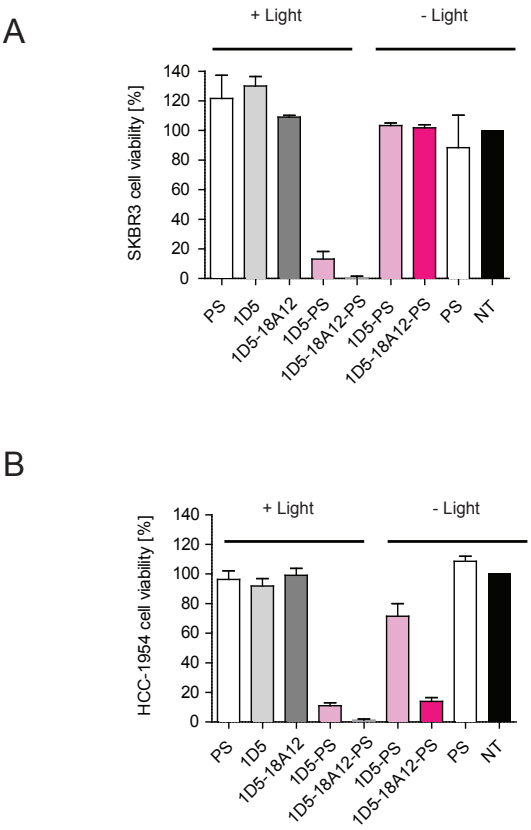

Fig.3S. Viability of A. SKBR33 and B. HCC1954 cells upon incubation with PS alone, nanobody or nanobody-PS upon illumination with 10 J/cm^2 light dose or not subjected to illumination. Data is expressed as percentage of cell viability in relation to non-treated cells, mean ± SD.

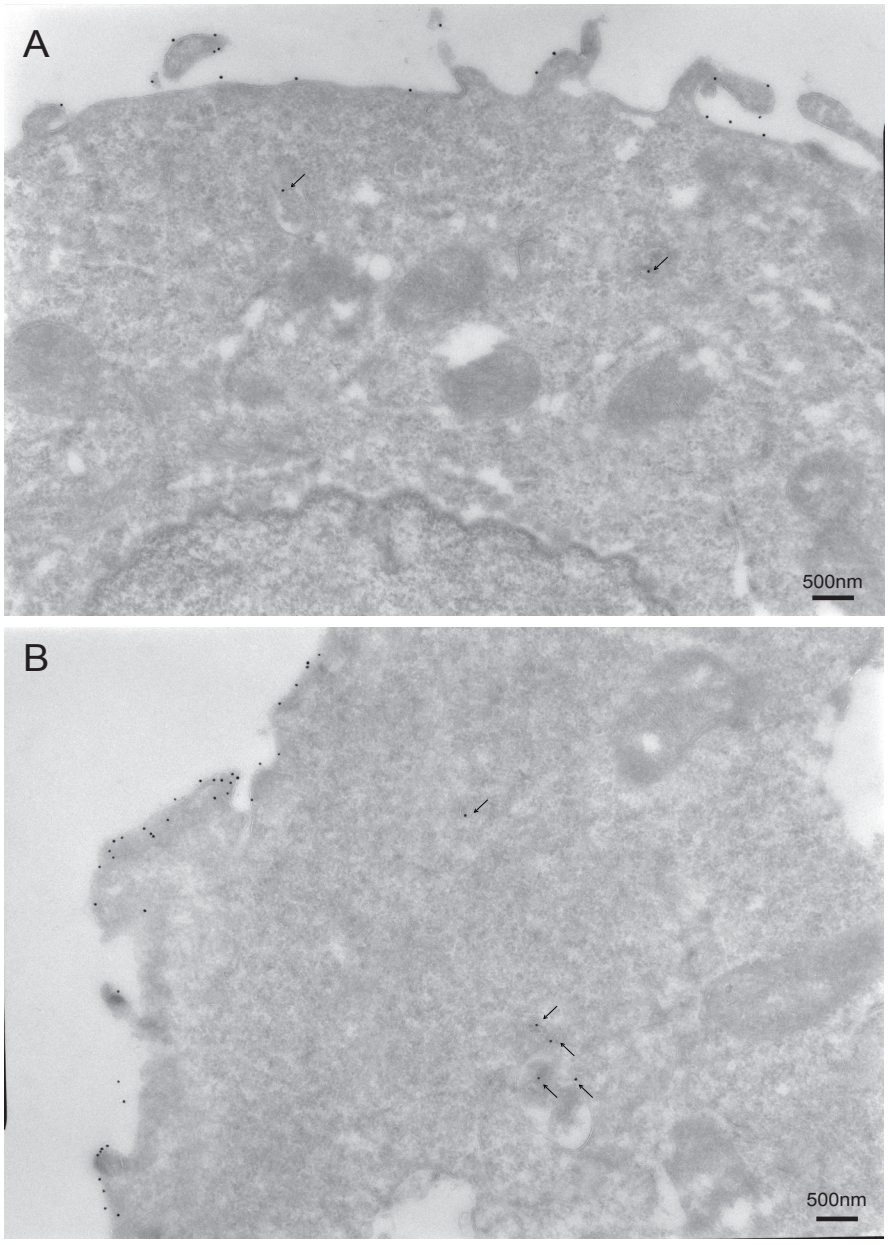

Fig.4S. Electron microscopy pictures of internalized and membrane-bound immunogold labeled nanobodies upon 24 hrs incubation with SKBR3 cells. A. 1D5, B. 1D5-18A12. Arrows point to internalized nanobodies. Scale bar = 500 nm.

References

1. Hartmann S, Reimer T, Gerber B: Management of early invasive breast cancer in very young women (<35 years). *Clin. Breast Cancer.* 11(4), 196-203 (2011).

2. Akram M, Siddiqui SA: Breast cancer management: past, present and evolving. *Indian J. Cancer* 49(3), 277-282 (2012).

3. Cardoso F, Loibl S, Pagani O *et al.*: The European Society of Breast Cancer Specialists recommendations for the management of young women with breast cancer. *Eur. J. Cancer* 48(18), 3355-3377 (2012).

4. Sulpher J, Dent R, Dent S: Neoadjuvant chemotherapy in breast cancer: what questions remain? *Curr. Opin. Support. Palliat. Care.* 8(1), 59-63 (2014).

5. Gampenrieder SP, Rinnerthaler G, Greil R: Neoadjuvant chemotherapy and targeted therapy in breast cancer: past, present, and future. *J. Oncol.* 2013, 732047 (2013).

6. Goble S, Bear HD: Emerging role of taxanes in adjuvant and neoadjuvant therapy for breast cancer: the potential and the questions. *Surg. Clin. North Am.* 83(4), 943-971 (2003).

7. Ellis P: Current and future directions for adjuvant chemotherapy in early-stage breast cancer. . *Eur. J. Cancer Suppl* 4, 14-20 (2006).

8. Figueroa-Magalhaes MC, Jelovac D, Connolly RM, Wolff AC: Treatment of HER2-positive breast cancer. *Breast* 23(2), 128-136 (2014).

9. Vu T, Claret FX: Trastuzumab: updated mechanisms of action and resistance in breast cancer. *Front. Oncol.* 2, 62 (2012).

10. Cho HS, Mason K, Ramyar KX *et al.*: Structure of the extracellular region of HER2 alone and in complex with the Herceptin Fab. *Nature* 421(6924), 756-760 (2003).

11. Moja L, Tagliabue L, Balduzzi S *et al.*: Trastuzumab containing regimens for early breast cancer. *Cochrane Database Syst. Rev.* 4, CD006243 (2012).

12. Wong AL, Lee SC: Mechanisms of Resistance to Trastuzumab and Novel Therapeutic Strategies in HER2-Positive Breast Cancer. *Int. J. Breast Cancer.* 2012, 415170 (2012).

13. Gajria D, Chandarlapaty S: HER2-amplified breast cancer: mechanisms of trastuzumab resistance and novel targeted therapies. *Expert Rev. Anticancer Ther.* 11(2), 263-275 (2011).

14. Arnould L, Gelly M, Penault-Llorca F *et al.*: Trastuzumab-based treatment of HER2-positive breast cancer: an antibody-dependent cellular cytotoxicity mechanism? *Br. J. Cancer* 94(2), 259-267 (2006).

15. Shishkova N, Kuznetsova O, Berezov T: Photodynamic therapy for gynecological diseases and breast cancer. *Cancer. Biol. Med.* 9(1), 9-17 (2012).

16. Oleinick NL, Morris RL, Belichenko I: The role of apoptosis in response to photodynamic therapy: what, where, why, and how. *Photochem. Photobiol. Sci.* 1(1), 1-21 (2002).

17. Celli JP, Spring BQ, Rizvi I *et al.*: Imaging and photodynamic therapy: mechanisms, monitoring, and optimization. *Chem. Rev.* 110(5), 2795-2838 (2010).

18. Mitsunaga M, Ogawa M, Kosaka N, Rosenblum LT, Choyke PL, Kobayashi H: Cancer cell-selective in vivo near infrared photoimmunotherapy targeting specific

membrane molecules. *Nat. Med.* 17(12), 1685-1691 (2011).

19. Solban N, Rizvi I, Hasan T: Targeted photodynamic therapy. *Lasers Surg. Med.* 38(5), 522-531 (2006).

20. Heukers R, van Bergen En Henegouwen PM, Oliveira S: Nanobody-photosensitizer conjugates for targeted photodynamic therapy. *Nanomedicine* (2014).

21. Oliveira S, Heukers R, Sornkom J, Kok RJ, van Bergen En Henegouwen PM: Targeting tumors with nanobodies for cancer imaging and therapy. *J. Control. Release* 172(3), 607-617 (2013).

22. Kijanka M, Warnders FJ, El Khattabi M *et al.*: Rapid optical imaging of human breast tumour xenografts using anti-HER2 VHHs site-directly conjugated to IRDye 800CW for image-guided surgery. *Eur. J. Nucl. Med. Mol. Imaging* 40(11), 1718-1729 (2013).

23. Oliveira S, van Dongen GA, Stigter-van Walsum M *et al.*: Rapid visualization of human tumor xenografts through optical imaging with a near-infrared fluorescent anti-epidermal growth factor receptor nanobody. *Mol. Imaging* 11(1), 33-46 (2012).

24. Salacinski PR, McLean C, Sykes JE, Clement-Jones VV, Lowry PJ: Iodination of proteins, glycoproteins, and peptides using a solid-phase oxidizing agent, 1,3,4,6-tetrachloro-3 alpha,6 alpha-diphenyl glycoluril (Iodogen). *Anal. Biochem.* 117(1), 136-146 (1981).

25. Wiley HS, Cunningham DD: The endocytotic rate constant. A cellular parameter for quantitating receptor-mediated endocytosis. *J. Biol. Chem.* 257(8), 4222-4229 (1982).

26. Ribble D, Goldstein NB, Norris DA, Shellman YG: A simple technique for quantifying apoptosis in 96-well plates. *BMC Biotechnol.* 5, 12 (2005).

27. O'Brien NA, Browne BC, Chow L *et al.*: Activated phosphoinositide 3-kinase/AKT signaling confers resistance to trastuzumab but not lapatinib. *Mol. Cancer. Ther.* 9(6), 1489-1502 (2010).

28. Sahin O, Frohlich H, Lobke C *et al.*: Modeling ERBB receptor-regulated G1/S transition to find novel targets for de novo trastuzumab resistance. *BMC Syst. Biol.* 3, 1-0509-3-1 (2009).

29. Heukers R, Vermeulen JF, Fereidouni F *et al.*: Endocytosis of EGFR requires its kinase activity and N-terminal transmembrane dimerization motif. *J. Cell. Sci.* 126(Pt 21), 4900-4912 (2013).

30. Ron R Allison, Gordon H Downie, Rosa Cuenca, Xin-Hua Hu, Carter JH Childs, Claudio H Sibata: Photosensitizers in clinical PDT. . *Photodiagnosis and Photodynamic Therapy* 1, 27-42 (2004).

31. Cui S, Yin D, Chen Y *et al.*: In vivo targeted deep-tissue photodynamic therapy based on near-infrared light triggered upconversion nanoconstruct. *ACS Nano* 7(1), 676-688 (2013).

32. Farrell TJ, Wilson BC, Patterson MS, Olivo MC: Comparison of the in vivo photodynamic threshold dose for photofrin, mono- and tetrasulfonated aluminum phthalocyanine using a rat liver model. *Photochem. Photobiol.* 68(3), 394-399 (1998).

33. Hudis CA, Gianni L: Triple-negative breast cancer: an unmet medical need. *Oncologist* 16 Suppl 1, 1-11 (2011).

34. Brand TM, Iida M, Wheeler DL: Molecular mechanisms of resistance to the EGFR

monoclonal antibody cetuximab. *Cancer. Biol. Ther.* 11(9), 777-792 (2011).
35. Chung A, Cui X, Audeh W, Giuliano A: Current status of anti-human epidermal growth factor receptor 2 therapies: predicting and overcoming herceptin resistance. *Clin. Breast Cancer.* 13(4), 223-232 (2013).

Chapter 8

Nanobody-targeted and RNase-loaded nanoparticles based on a hydrophilic polyester aimed for cancer therapy

Marta M. Kijanka [*]
Neda Samadi [*]
Sabrina Oliveira
Tina Vermonden
Joep B. van den Dikkenberg
Cornelus F. van Nostrum
Maryam Amidi
Paul M.P. van Bergen en Henegouwen
Wim E. Hennink

[*] *equal contribution*

Manuscript in preparation

Abstract

Introduction: Ribonucleases (RNases), small enzymes degrading RNA, have recently attracted a lot of attention as potential anti-cancer drugs. However, due to their small size, which results in their fast renal clearance, and insufficient internalization, new strategies to improve cytotoxicity of these enzymes are needed. Development of targeted therapeutic nanoparticles offers an attractive possibility of an improved efficacy of encapsulated therapeutics, combined with a reduction of unwanted side-effects to which healthy tissues in proximity of cancer cells are subjected.

Methods: In this study we present the development of biodegradable PLGHMGA nanoparticles (NPs) loaded with RNase as a therapeutic protein. To efficiently target HER2 overexpressing cells, a nanobody specific for the HER2 receptor was coupled via a terminal cysteine to maleimide groups present at the distal end of the PEG chains and exposed at the surface of the NPs.

Results: PLGHMGA NPs loaded with RNase were obtained using a double emulsion solvent evaporation technique. They showed 80% release of the loaded protein in 12 days. A fully preserved catalytic activity of the released RNase was confirmed by an enzymatic activity assay. Nanobody-decorated NPs showed greater binding and uptake by HER2 over-expressing cells compared to NPs devoid of nanobody. Free RNase exhibited no cytotoxicity demonstrating inefficient uptake of this enzyme. Dose-dependent cytotoxicity was observed for RNase-loaded NPs and was further improved upon conjugation of HER2-specific nanobody to the NP surface.

Conclusion: The developed PLGHMGA nanoparticles are promising candidates to exploit therapeutic potential of RNases.

Introduction

Ribonucleases (RNases) are small (10–28 kDa) basic proteins with a net positive charge under physiological conditions. They can bind to negatively charged cell membranes, enter cells by endocytosis and translocate into the cytosol, where they degrade RNA, when evading the ribonuclease inhibitor protein (RI) [1]. Therefore, these proteins have raised attention for use as anti-cancer therapeutics [2,3]. However, due to rapid renal filtration of these enzymes (half-life: < 5 minutes [4]) repetitive administration of high doses is required, leading to renal toxicity [5-7]. Local administration in (the vicinity of) tumors decreases the side effects of these proteins, but the efficacy remains relatively poor due to insufficient cellular internalization.

Importantly, it has been shown that when these proteins were introduced into the cytosol of cells using different strategies they become thousands of times more effective [8,9]. Successful evasion from the RNase inhibitor (RI), a 50 kD protein present in the cytosol of mammalian cells, has also been suggested to be essential for the accomplishment of the cell killing activity of RNase. The interaction between RI and RNases is among the strongest of known protein-protein complexes [10-12].

Ranpirnase (Onconase®, ONC) is the only ribonuclease that has been evaluated in phase III clinical trials for malignant mesothelioma in the U.S.A. and Europe [13,14]. This enzyme can exert its cytotoxic effect to cancer cells at much lower concentrations as compared with other RNases [6,14]. Although still debatable, different mechanisms have been proposed for the high potency of Onconase®, such as a greater cell association due to existence of specific receptors for Onconase® on mammalian cell surfaces, evasion from neutralization by RI, and/or cleavage of dsRNAs into small interfering RNAs (RNAi), which in turn can cause cell death [1,5,13,15,16].

Importantly, different studies have shown that if RNase A (RI sensitive) and Onconase® are conjugated to targeting ligands such as antibodies, and actively delivered into the cytosol of specific cancer cells, both enzymes exert similar cytotoxic efficacy [17,18]. Several studies have shown that conjugation of RNases to tumor targeting antibodies or antibody fragments resulted in enhanced intracellular delivery and hence a substantial therapeutic potency [19-21]. Alternatively other strategies to enhance the cytotoxic efficacy of RNases have been employed, such as combination therapy [18] or encapsulation of RNase into nanogels [22].

In recent years, nanoparticle (NP) based systems [23,24] and particularly those based on biodegradable polyesters (e.g. PLGA and PLLA) have been investigated for (intracellular) delivery of therapeutic peptides and proteins [25-30]. The high drug loading capacity, high stability, and also physical protection of the loaded protein against degradation in the lysosomes, make them attractive candidates for intracellular delivery of proteins in general and thus also for RNases. Moreover, long circulating targeted NPs can be obtained by surface modification of NPs with PEG, and targeting molecules such as antibodies, antibody fragments, peptides and nanobodies

that can render them cell specific [31]. Nanobodies are the variable domains of heavy chain only antibodies present in *Camelidae* and some sharks. They are promising targeting molecules, because of their higher affinity than other antibody fragments derived from conventional antibodies [32-34]. The HER2 (human epidermal growth factor receptor 2) receptor is overexpressed in aggressive types of breast cancer and has become an important target for breast cancer therapy [35,36]. Recently, we have developed a HER2 targeted nanobody (11A4) and demonstrated its specific binding to HER2 receptor *in vitro* and *in vivo*, in molecular optical imaging studies [37].

We have also reported on new particles of nano- and micrometer size based on a hydrophilic polyester, (poly(D,L-lactic-co-glycolic-co-hydroxymethyl glycolic acid) (PLGHMGA)), which showed tailorable release patterns for model proteins and peptides [38-41] and relatively fast degradation and better protein compatibility due to lack of acidification during degradation [39-42]. We also investigated the protein release characteristics of PEGylated nanoparticles prepared from blends of PEG-PLGHMGA and PLGHMGA [43]. In the present study, we evaluated the potential of these PEGylated PLGHMGA nanoparticles for the intracellular delivery of RNase A. To actively target these to HER2 positive cells, we developed a method to conjugate the functional nanobody 11A4 mentioned above.

Materials and Methods

Materials

Ribonuclease A (RNase A) and ribonucleic acid from baker's yeast (*S. cerevisiae*) were purchased from Sigma-Aldrich (USA). D,L-lactide was obtained from Purac (The Netherlands). Peptide grade dichloromethane (DCM), chloroform, methanol, ethyl acetate, acetonitrile, diethyl-ether, tetrahydrofuran (THF), glacial acetic acid and toluene were purchased from Biosolve (The Netherlands). Disodium hydrogen phosphate (Na_2HPO_4), sodium dihydrogen phosphate (NaH_2PO_4), sodium azide (NaN_3, 99%), aldrithiol, poly(ethylene glycol) methyl ether (MePEG) with molecular weight of 2000, poly(vinyl alcohol) (PVA; MW 30,000–70,000; 88% hydrolyzed) and tin (II) 2-ethylhexanoate ($SnOct_2$) were products of Sigma-Aldrich (USA). BCA reagent was from Interchim (USA), and Pd/C (palladium, 10 wt% on activated carbon, Degussa type E101 NE/W) was purchased from Aldrich (The Netherlands). Alexa Fluor 532 (Alexa 532) was purchased from LI-COR Biosciences (USA). SH-PEG2000-NH_2 was from CreativePEGworks (USA). Maleimide-PEG5000-PLGA (lactide/glycolide molar ratio 50:50, MW PLGA-PEG: 25 kDa) was purchased from PolySciTech (USA). 4',6-Diamidino-2-phenylindole (DAPI) and PBS were purchased from Roche (The Netherlands) and Lonza Verviers (Belgium), respectively. The 11A4 nanobody was produced as described before [37]. Unless otherwise stated, all chemicals were used as received.

Synthesis of the 2-pyridyldithio-PEG-amine macroinitiator from aldrithiol-2 and thiol-PEG2000-amine

The macroinitiator pyridyldithio-PEG-NH_2 was synthesized in a single step reaction from aldrithiol-2 and thiol-PEG2000-amine. In detail, a solution of thiol-PEG-amine (500 mg, 0.5 mmol) in methanol (10 ml) was added drop-wise to a solution of aldrithiol-2 (88 mg, 1 mmol) in methanol (10 ml) to which a catalytic amount (10 µl) of glacial acetic was added. The resulting reaction mixture was stirred at room temperature under an N_2 atmosphere for 5 hrs. Subsequently, methanol was evaporated under reduced pressure and the resulting crude product (yellow oil), was dissolved in chloroform and precipitated in diethyl ether two times. Finally, the obtained product, 2-pyridyldithio-PEG-amine, was obtained as white/greenish solid. The structure of the obtained product was confirmed by ^{1}H NMR analysis and the percentage of converted thiol end groups was calculated by dividing the peak area of one proton of pyridine to one proton of PEG2000.

Synthesis of (methoxy or thiol)-PEG-PLGHMGA and PLGHMGA (co)polymers

Random and diblock co-polymers of benzyl protected hydroxymethylglycolide (BMG) and D,L-lactide were synthesized by ring opening polymerization in melt using benzyl alcohol (BnOH), MePEG2000 or 2-pyridyldithio-PEG-amine as initiators and stannous octoate as catalyst, as described previously [38,43,44]. The molar ratio of initiator/monomer was 1/300. The protecting benzyl and the pyridinethiol groups of the resulting 2-pyridyldithio-PEG-PLGBMGA were removed in a hydrogenation reaction using Pd/C as catalyst [44]. The synthesized polymers are denoted as PLGHMGA for the co-polymer of D,L-lactic acid, hydroxymethyl glycolic acid (HMG) and glycolic acid, and PEG-PLGHMGA and thiol-PEG-PLGHMGA for the block co-polymers of MePEG and thiol-PEG-amine with PLGHMGA, respectively. ^{1}H-NMR (DMSO, d^6): 1.3-1.5 (m, 3H, -CH_3), 2.5 (s, CH_3, DMSO), 3.3 (s, H_2O), 3.5 (PEG methylene units), 3.7-3.9 (m, 2H, CH-$\underline{CH_2}$-OH), 4.7-5 (m, 2H, O-$\underline{CH_2}$-C(O)O), 5.2-5.4 (m, 2H, -$\underline{CH}$-CH_3 of lactic + 1H, $\underline{CH}$-CH_2-OH of HMG)

Synthesis of Alexa 532-PEG-PLGHMGA

The synthesis of PLGHMGA labeled with Alexa 532 was performed as follows. Three mg (20 µM) dithiothreitol (DTT) was added to a solution of 50 mg thiol-PEG-PLGHMGA in 1 ml DCM while stirring at room temperature to reduce possible disulfide bonds. After 15 minutes, the polymer was precipitated in dry methanol, collected by filtration and dried under N_2 atmosphere overnight. Next, the polymer was dissolved in 1 ml ACN and added to a solution of maleimide-functional Alexa 532 in PBS pH 7.4 (1 mg/ml, approximately 1 µmol polymer (-SH)/1 µmol Alexa 532 (maleimide)),

also containing 25 mM EDTA under N_2 atmosphere and vigorous stirring. The reaction was continued for 3 hrs at room temperature. ACN was then evaporated under reduced pressure and the precipitated polymer in the remaining aqueous phase (PBS) was recovered after centrifugation. To remove unreacted Alexa 532, the polymer was dissolved in chloroform and precipitated in methanol.

Polymer characterization

The compositions of the co-polymers were determined by ^{1}H NMR in DMSO using a Gemini-300 MHz spectrometer at 298 K. To investigate the removal of the 2-pyridinethiol group after hydrogenation of 2-pyridyldithio-PEG-PLGBMGA, the polymers before and after hydrogenation were treated with DTT in chloroform and precipitated in diethyl-ether (DEE). The absorbance of the resulting supernatant was measured at 343 nm using UV spectrophotometry to detect the release of 2-pyridinethiol. The molar composition (lactic acid (L), glycolic acid (G) and hydroxymethyl glycolic acid (HMG)) was determined as described before [38]. The molecular weights of the obtained polymers were determined using GPC (Waters Alliance system), with a Waters 2695 separating module and a Waters 2414 refractive index detector. Two PL-gel 5 µm Mixed-D columns fitted with a guard column (Polymer Labs, MW range 0.2–400 kDa) were used and calibration was done using polystyrene standards with narrow molecular weight distributions. THF was used as the mobile phase (1 ml/min). The Alexa 532 conjugated polymer was characterized using GPC with dual RI and fluorescence detection (excitation wave length 531 nm, emission wave length 554 nm).

NPs preparation

NPs were prepared by a double emulsion solvent evaporation technique as described in the literature [45-47]. PLGHMGA and the different di-block co-polymers were dissolved in DCM to a final concentration of 5% w/v (150 mg/3 ml). For example, to prepare nanobody conjugated and Alexa 532 labelled NPs loaded with RNase, 1.5 mg of labelled di-block copolymer, 15 mg maleimide-PEG5000-PLGA, 15 mg PEG2000-PLGHMGA and 119 mg PLGHMGA were dissolved in 3 ml DCM (for the preparation of NPs without maleimide, 15 mg maleimide-PEG5000-PLGA was replaced by PEG2000-PLGHMGA). A solution of RNase in reverse osmosis water (300 µl, 150 mg/ml) was then emulsified in solution of 3 ml of polymer in DCM in an ice-bath using an ultrasonic homogenizer (LABSONIC P, B.Braun Biotech) for 1 min at 40% amplitude. Subsequently, the w/o emulsion was emulsified into an external aqueous phase (30 ml) containing poly(vinyl alcohol) 5% (w/v) in NaCl 0.9% (w/v), filtered through 0.2 µm Millipore filter, in an ice-bath using the same ultrasonic homogenizer for 2 min at 60% amplitude to form a water-in-oil-in-water (w/o/w) emulsion. DCM was subsequently evaporated at room temperature under reduced pressure for 1 hour. NPs were recovered by ultracentrifugation

(20'000 g for 20 min, J-26XP, Beckman Colter, Avanti®) and washed twice with 45 ml 0.9% NaCl.

Characterization of the NPs

NPs were suspended in distilled water and their average size and size distribution were measured using Dynamic Light Scattering (DLS; Zetasizer 4000, Malvern Instruments, Malvern, UK) at 25°C at an angle of 90° (Z-average). The zeta-potential of the NPs, suspended in 10 mM sodium phosphate buffer (NaCl 0.4 mM, Na_2HPO_4 6.6 mM, NaH_2PO_4 3 mM, pH 7.4), was determined by laser Doppler electrophoresis using a Zetasizer Nano-Z (Malvern Instruments Ltd.). The morphology of the NPs was studied using Transmission Electron Microscopy (TEM, Tecnai 10, Philips, 100kV) according to the following procedure. Twenty five µl of nanoparticle suspension was placed onto parafilm, and formvar/carbon-coated copper grids were placed on top of the sample droplets for 2 minutes. Excess liquid was removed by filter paper and, subsequently, the grids were negatively stained by placing them on top of 20 µl droplets of 2% uranyl acetate in demineralized water on parafilm for 2 minutes. Excess liquid was removed by filter paper and the grids were dried for 5 minutes at room temperature before the measurement.

Conjugation of the nanobody to the NPs' surface

Prior to conjugation of the nanobody to maleimide functionalized NPs, the nanobody dissolved in PBS buffer (1 mg/ml) was reduced in 50 mM Tris-HCl pH 8.5 also containing 20 mM TCEP. The reduction step was done at room temperature for 15 min, after which TCEP was removed from the nanobody sample by buffer exchange with 0.4 mM EDTA-PBS pH 7 using Zeba Spin Desalting Columns (ThermoScientific). Maleimide functionalized NPs were mixed with a solution of nanobody (molar ratio of 2 nanobodies to 1 maleimide) and incubated overnight at 4°C while rotating head-over-head (15 rpm/min). Subsequently, the NPs were centrifuged for 15 min at 15.000 g at 4°C and washed with PBS buffer twice to remove unconjugated nanobody. The obtained pellet of maleimide functionalized NPs conjugated to 11A4 nanobody was then resuspended in PBS. Conjugation of 11A4 nanobody to the nanoparticle surface was confirmed by dot blot using rabbit anti VHH protein G purified serum and goat anti rabbit IR800 antibody for detection. The amount of unconjugated 11A4 present in the supernatant obtained after centrifugation was analyzed by gel electrophoresis and compared to standard nanobody solutions with known concentrations.

Determination of RNAse loading into NPs

To determine the remaining RNase loading after nanobody conjugation, we exposed non-

conjugated RNase-loaded nanoparticles to the same conditions as we used for the nanobody-conjugation, but in the absence of nanobody (i.e. incubation overnight in PBS/EDTA buffer at 4^0C, centrifugation and washing). Particles were freeze dried at -50^0C and at 0.5 mbar in a Chris Alpha 1-2 freeze-drier (Osterode am Harz, Germany) for 12 hrs. Protein loading was determined by dissolving approximately 10 mg of freeze-dried NPs in 1 ml DMSO. Next, 5 ml of a 0.05 M NaOH solution containing 0.5% (w/v) SDS (sodium dodecyl sulfate) was added, essentially as described earlier [48]. The resulting solution was then analyzed for protein content by a BCA protein assay. The protein loading percentage (L%) is expressed as the encapsulated amount of protein divided by the dry weight of the loaded particles and multiplied by 100%.

In vitro release of RNase from NPs

For release, non-conjugated particles were suspended in a certain volume of sodium phosphate buffer (6 mM NaCl, 99 mM Na_2HPO_4, 49 mM NaH_2PO_4, 4 mM NaN_3, pH 7.4) to obtain a dispersion of ~2 mg particles/ml. Samples of 300 µl of the homogeneous particle suspension were aliquoted into 500 µl eppendorf tubes. Also, 2 ml of the particle suspension was taken and washed twice with reverse osmosis water (centrifuged for 20 minutes at 20.000 g; Hermle Z233MK-2 centrifuge) and the obtained pellets were freeze-dried and used to determine the exact particle concentration as well as protein loading. The particle suspensions in Eppendorf tubes were incubated at 37^0C under mild agitation. At different time points, a tube was taken and the particles were centrifuged at 20.000 g for 20 min. The amount of RNase released in the supernatant was measured by UPLC (Acquity UPLC®) equipped with a BEH300 C18 1.7 µm column. A gradient was run from the starting composition, ACN/H_2O, (5/95%) / 0.1% TFA, to ACN/H2O, (60/40%) / 0.1% TFA in 6 min. The mobile phase was delivered to the column at a flow rate of 0.250 ml/min, the injection volume was 7.5 µl, and detection was by measuring the UV absorbance at 280 nm. RNase standard solutions (10-400 µg/ml) were used for calibration.

RNase bioactivity assay

The bioactivity of released RNase was determined by a method described by Kalnitskey et al. [49] based upon the release of acid-soluble oligonucleotides following the digestion of yeast RNA. In short, solutions with different concentrations of RNase (0-12 µg/ml) in 0.1 M sodium acetate buffer pH 5 were freshly prepared and incubated at 37^0C for 5-8 minutes. RNA was dissolved in the same buffer (concentration 10 mg/ml) and also incubated at 37^0C. Next 500 µl of the enzyme solution was added to 500 µl of the RNA solution and the tubes were incubated for 4 minutes at 37^0C. The enzymatic reaction was stopped by the addition of 500 µl of solution

of uranyl acetate (0.75%)/perchloric acid (25%) in water and the tubes were transferred into an ice bath and cooled for 5 minutes. After centrifugation for 10 min at 15.000 g the supernatant was taken and diluted 30 times with reverse osmosis water and the absorbance at 260 nm was measured. Specific enzyme activity was calculated as follows: units/µg= A260 x 30/µg enzyme.

Cell line and cell culture condition

Two human breast cancer cell lines SKBR3 (ATCC® HTB-30™, HER2 overexpressing) and MDA-MB-231 (ATCC® CRM-HTB-26™, HER2 negative) were obtained from American Type Culture Collection (ATCC, LGC Standards GmbH, Wesel, Germany) and maintained in Dulbecco's Modified Eagle's Medium (DMEM, Gibco) with 7.5% (v/v) FBS, 100 IU/ml penicillin, 100 mg/ml streptomycin, and 2 mM L-glutamine at 37^0Cin a humidified atmosphere containing 5% CO_2.

Binding of NPs to cells

Five hundred thousand SKBR3 cells (HER2 positive cells) or MDA-MB-231 cells (HER2 negative cells) were seeded on glass cover slips and cultured in DMEM overnight. The next day, the medium was removed and the cells were incubated with Alexa 532 labelled NPs (with or without nanobody conjugated) for only 1 h at 4^0C in CO_2-independent medium (Gibco) to avoid internalization. After incubation, the cells were washed once with CO_2-independent medium, fixed with 4% paraformaldehyde (PFA) and the cell nuclei were stained with DAPI. Cell-bound NPs were visualized by fluorescence microscopy. Images were acquired using wide-field fluorescence (Olympus AX70) and confocal microscopy (Confocal Laser Scanning microscope Zeiss LSM5 Pascal).

Uptake and cytotoxicity of NPs

Five thousand SKBR3 cells (HER2 positive cells) or MDA-MB-231 cells (HER2 negative cells) were seeded into a 96 well plate in DMEM. After overnight culture, the medium was exchanged by medium containing the nanoparticle formulations (particle concentration: 0.375-12 mg/ml), free nanobody (1-1000 nM) or RNase (3 to 100 µM RNase). The cells were subsequently incubated for 72 hrs without medium refreshment. Cells incubated with Alexa 532 labelled NPs were visualized with fluorescence microscopy using an EVOS microscope (Advanced Microscopy Group, AMG, Thermo Fischer Scientific) equipped with 20x objective (Plan Fluor, 10x, NA 0.3, air and working distance 8.3 mm) and a LED-based fluorescence light cube (Cat. no. 12-563-471, Westover Scientific Inc., AMG). Phase contrast images were also obtained to assess cell morphology. ImageJ software was used for quantification of the mean fluorescence intensity. Regions of interest

(ROI) were drawn around 8 cells per picture as well as in an area without cells (background). After background subtraction, the average fluorescence intensity of each ROI was calculated. Cell viability was assessed after 72 hrs using the Alamar Blue reagent, which is an indicator for living-cells' reducing environment, according to the manufacturer's instructions. The mean values of two independent experiments with triplicates are shown ± SD.

Results

Synthesis and characterization of PLGHMGA, MePEG-PLGHMGA and thio-PEG-PLGHMGA

2-Pyridinethiol was coupled to thiol-PEG2000-NH_2 in methanol and the aimed product, 2-pyridyldithio-PEG2000-NH_2, was obtained in a yield of ~60% (Fig.1 A). Thiopyridine is used to protect functional thiol end groups during the ring opening polymerization [50]. In the NMR spectrum of the pyridyldithio-PEG2000-NH_2 (Fig. 1 B and C) it appeared that the signals of methylene protons (at 2.3 and 2.6 ppm) next to functional thiol end group of the starting compound disappeared and shifted to 3.0-3.2 ppm corresponding to methylene protons next to pyridyldithio group. This indicates (almost) quantitative end group conversion. Random co-polymers of benzyl protected hydroxymethyl glycolide (BMG) and D,L-lactide (L) (BMG/D,L-lactide: 35/65 mol%), using BnOH, MePEG or 2-pyridyldithio-PEG2000-NH_2 as initiators, were synthesized by ring opening polymerization in melt at 130 °C (Fig. 1 D). After removal of the protective groups, the co-polymers were obtained in high yields (>70%). The copolymer compositions as well as number average molecular weights for the di-block copolymers were determined by ^{1}H NMR spectroscopic analysis.

Polymer	Composition x:y [a]		Molecular weight (kg/mol)			
	Feed ratio	Polymer ratio (NMR)	GPC M_n	GPC M_w	NMR	Theoretical M_n [b]
$MePEG_{2000}$-PLGBMGA	35:65	37:63	19	30	38	56
$MePEG_{2000}$-PLGHMGA		31:69	16	26	45	45
2-pyridyldithio-PEG-PLGBMGA		35:65	16	23	43	56
SH-PEG_{2000}- PLGHMGA		32:68	15	23	49	45
PLGBMGA		36:64	27	57	--	54
PLGHMGA		36:64	24	44	--	43

Table 1. Characteristics of the polymers; [a] x:y denotes the molar ratio of BMG/D,L-Lactide or HMG/D,L-Lactide; [b] based on the initiator/monomer molar ratio of 1/300.

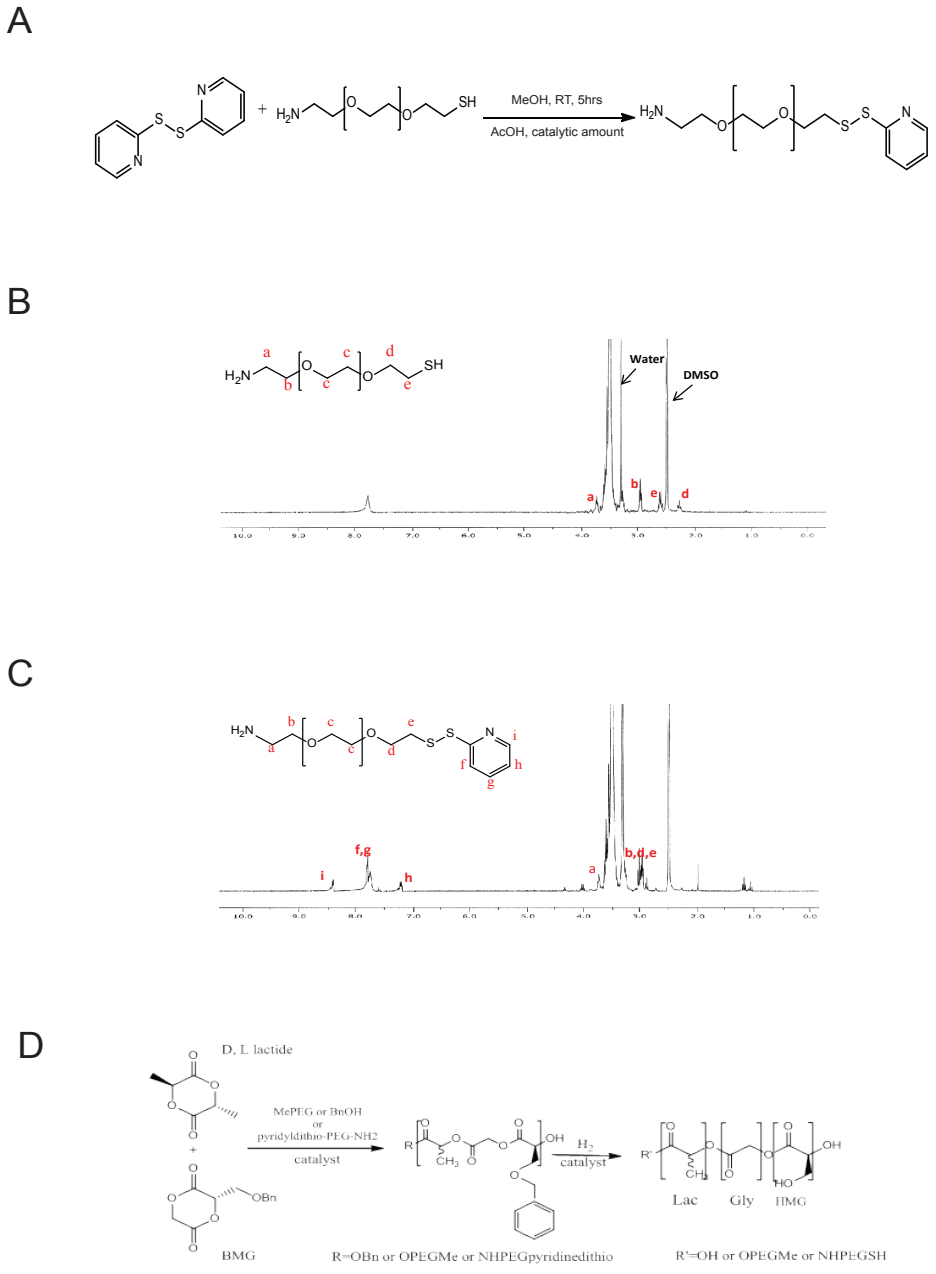

Fig. 1. Steps leading to synthesis of PLGHMGA (co)polymers. A. Synthesis of the 2-pyridyldithio-PEG-NH2 macroinitiator. ^{1}H NMR spectrum in deuterated DMSO of 2-pyridyldithio-PEG-amine (used as macroinitiator for the synthesis of 2-pyridyldithio-PEG-PLGBMGA). ^{1}H δ :
B. 2.5 (s, CH_3, DMSO), 2.9-3.1 (m, 6H, O-$\underline{CH_2}$-$\underline{CH_2}$-S and $\underline{CH_2}$-CH_2-NH_2), 3.3 (s, H_2O), 3.5 (PEG methylene units), 3.7 (m, 2H, O-CH_2-$\underline{CH_2}$-NH_2), 7.1-8.5 (m, 4H, pyridine ring), 7.8-8.0 (s, 2H, NH_2).

C. 2.3 (m, 2H, O-$\underline{CH_2}$-CH_2-SH), 2.5 (s, CH_3, DMSO), 2.6 (m, O-CH_2-$\underline{CH_2}$-SH), 3.0 (m, 2H, $\underline{CH_2}$-CH_2-NH_2), 3.3 (s, H_2O), 3.5 (PEG methylene units), 3.7 (m, 2H, O-CH_2-$\underline{CH_2}$-NH_2), 7.8-8.0 (s, 2H, NH_2).
D. Synthesis of hydrophilic aliphatic polyesters with pendant hydroxyl groups based on lactic acid, glycolic acid and hydroxymethylglycolic acid; poly(lactic-co-glycolic-co-hydroxymethylglycolic acid).

The results presented in Table 1 demonstrate that the copolymer compositions were close to the monomer feed ratios. ^{1}H NMR analysis also demonstrates that complete removal of the protecting benzyl groups of BMG units occurred after catalytic hydrogenation. Due to relative minor proportion of the number of pyridine protons to the number of polymer chain protons, the 2-pyridinethiol groups were not visible in the NMR spectra of the di-block 2-pyridyldithio-PEG-PLGBMGA. Therefore, successful removal of the 2-pyridinethiol group during the hydrogenation of this polymer was proven by releasing any covalently bound 2-pyridinethiol using DTT in chloroform before and after hydrogenation, and subsequent precipitation of the polymer in diethyl-ether. The obtained supernatant from 2-pyridyldithio-PEG-PLGBMGA (i.e. before hydrogenation) revealed a significant absorbance at 343 nm after treatment with DTT, confirming the presence of 2-pyridinethiol. However, the supernatant from the hydrogenated polymer showed no UV absorbance at 343 nm, indicating that the 2-pyridinethiol group was indeed removed from the polymer during hydrogenation. The conjugation of Alexa 532 to the obtained sulfhydryl reactive end group of PEG-PLGHMGA co-polymer was conducted via a simple click chemistry reaction by mixing the dye and co-polymer. The obtained polymer was characterized using GPC with dual RI and fluorescence detection. Appearance of the Alexa 532 fluorescence peak with the same retention time of the polymer in the RI signal indicates successful conjugation of the fluorophore to the thiol end group of PEG-PLGHMGA.

Preparation and characterization of RNase-loaded NPs

RNase-loaded NPs were prepared by a double emulsion solvent evaporation method [46,47]. To enable the subsequent functionalization of the NPs, maleimide-PEG5000-PLGA was added to the formulation. It has been previously shown that surface-functionalizable PLGA NPs were prepared by the addition of PEG-PLGA/PLA with a reactive group (e.g. maleimide) at the PEG terminal [51-53] using the same method as used in the present study. It should be noted that *in vivo* studies done by Gref et al. demonstrated that for optimal stealth behavior, the threshold w% content of PEG in NPs made of blends of different PEG di-block co-polymers (e.g. PEG-PLGA and PEG-PLA) was 2-5% [54]. Since we used 10 w% of maleimide-PEG5000-PLGA, we also added 10% of MePEG2000-PLGHMGA to obtain particles with a total of ~2 w% PEG for optimal stealth behavior. We choose to use PEG2000 for the latter component (versus PEG5000 for the maleimide functional block co-polymer) to favor the accessibility of the maleimide units on the surface of the NPs for subsequent reaction with the nanobody [55]. It appeared that

particles of around 280 nm and with a relatively low PDI (around 0.1) were obtained. RNase loading % (L%) after exposure of the NPs to the conditions of nanobody conjugation was around 3.5%. TEM analysis shows that spherical and non-porous NPs were formed (Fig. 2).

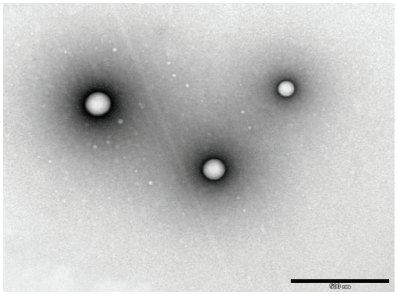

Fig. 2. TEM picture of non-conjugated NPs. Scale bar = 500 nm.

Release of RNase from NPs

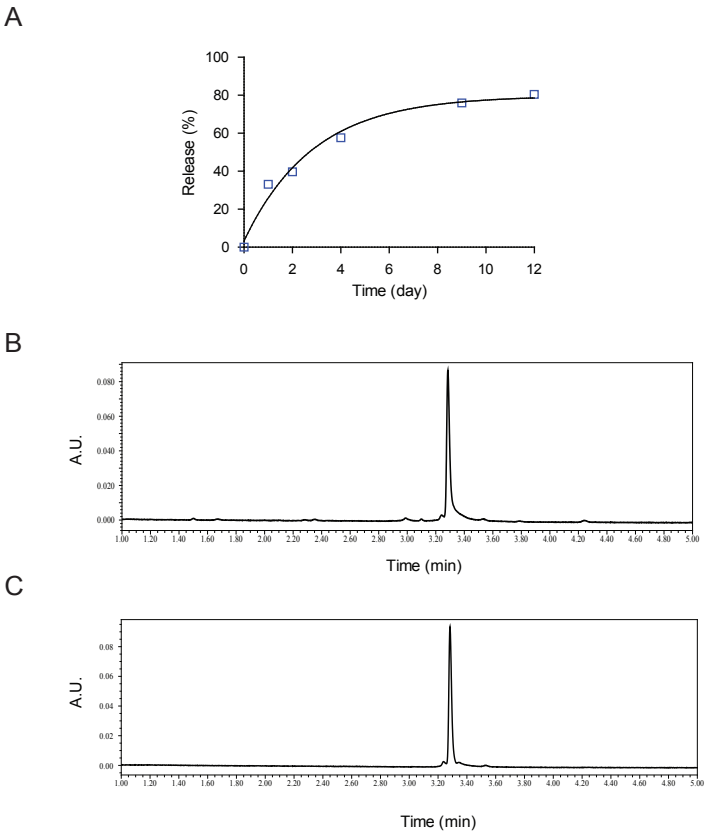

Fig. 3. A. Release of RNase from non-conjugated NPs (n=1). The percentage of the released protein is relative to the amount of protein encapsulated in the nanoparticles. UPLC chromatogram of (B) RNase released from NPs and (C) native RNase.

RNase-loaded NPs showed no initial burst and a sustained release of RNase reaching 80% at day 10 (Fig. 3 A). UPLC analysis of released RNase showed a single peak with the same retention time of native RNase, indicating that the primary structure of the released protein was retained [56,57] (Fig. 3 B and C). Importantly, a digestion bioactivity assay showed that the enzymatic activity of released RNase was fully preserved, demonstrating that the structural integrity of the released protein was retained (data not shown).

Conjugation of 11A4 nanobody to the surface of NPs

The 11A4 nanobody was reduced using TCEP to make the C-terminal cysteine available for conjugation with the maleimide groups present at the terminal end of the PEG-chains exposed at the surface of the NPs. After incubation of the reduced nanobody with the nanoparticles, non-conjugated nanobody was retrieved by centrifugation. The percentage of nanobody-maleimide conjugation was estimated through gel electrophoresis analysis of the unconjugated nanobody: 65% of the total maleimide available is suggested to be conjugated to nanobody. Dot blot analysis of the pelleted nanoparticles clearly showed the presence of conjugated nanobody, when these resulted from the mixture of maleimide-NPs with 11A4 possessing the C-terminal cysteine, in case of empty and RNase loaded NPs (Fig. 4).

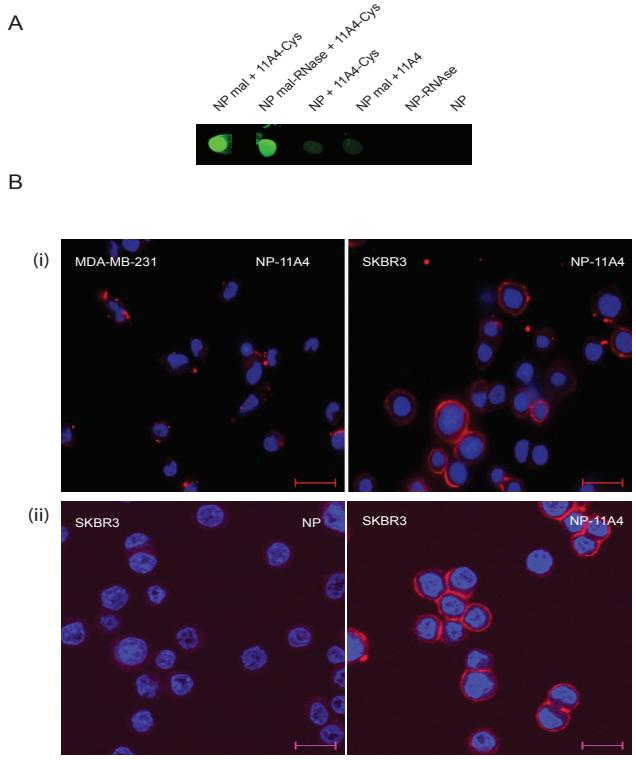

Fig. 4. A. Dot blot analysis of NP with maleimide (NP mal) or without (NP) incubated with 11A4 nanobody with an additional C-terminal cystein (11A4-Cys) or without (11A4). B. (i) Wide-field fluorescence microscopy pictures of Alexa 532 conjugated nanobody-decorated NPs incubated with MDA-MB-231 (HER2 negative) cells and SKBR3 (HER2 overexpressing) cells. (ii) Confocal microscopy pictures of SKBR3 cells incubated with non-targeted Alexa 532 conjugated NPs or nanobody-decorated Alexa 532 conjugated NPs. Incubations were performed at 4°C for 1 h, scale bar = 20 µm.

Dot blot analysis of nanoparticles lacking maleimide groups (NP no maleimide) that were incubated with the nanobody containing available C-terminal cystein showed hardly any presence of nanobody after centrifugation, demonstrating that the nanobody was not physically adsorbed on the surface of the NPs. The same result was obtained when nanoparticles containing maleimide groups were incubated with nanobody devoid of additional C-terminal cystein. The zeta potentials of NPs before and after nanobody conjugation were -1.3 and -0.7 mV, respectively. This small change can be explained by the slight positive charge of the nanobody at pH 7.4 (theoretical pI: 8.48, http://web.expasy.org/protparam/).

Cell binding of NPs

The ability of nanobody-conjugated NPs to bind to HER2 overexpressing cells was investigated using Alexa 532-labelled NPs. Incubation of these NPs with HER2 positive SKBR3 cells at 4^0C resulted in a clear membrane staining, whereas very low fluorescence was detected after incubation of the same nanoparticles with HER2 negative MDA-MB-231 cells (Fig. 4 B, (i)). This proves that the nanobody coupled to the surface of the NPs preserved its binding specificity for the receptor. The binding of non-targeted NPs to HER2 positive cells was also tested, and hardly any binding of these NPs was detected compared to binding of nanobody-conjugated NPs (Fig. 4 B, (ii)). This low unspecific binding of the nanobody decorated NPs to cells lacking HER2 receptors and of the non-targeted NPs to HER2 positive cells can likely be explained by the almost neutral zeta-potential of the NPs. Overall, these results clearly indicate that specific targeting of nanobody-decorated nanoparticles to HER2 positive cells occurs.

Uptake and cytotoxic activity of NPs

HER2 positive SKBR3 cells were incubated with empty nanobody targeted and non-targeted nanoparticles for 24 hrs. In cells incubated with targeted NP many vesicles were present, whereas in case of cells incubated with non-targeted NP hardly any vesicles were found (Fig.5 A). Fluorescently labelled NPs, both targeted as well as non-targeted, were incubated with SKBR3 cell for 3 days without medium refreshment. Images taken at the end of incubation time revealed that both types of NP were taken up by the cells (Fig.5 B). Importantly, NPs decorated with HER2 specific nanobody showed substantially higher uptake (about a factor 5). Untreated cells were regularly shaped, with perfectly delineated borders, while cells treated with RNase loaded NPs had irregular shapes and were smaller. These results indicate that cell viability was compromised upon incubation with RNase-loaded NPs.

The cytotoxic effect of RNase-loaded and nanobody conjugated NPs were compared to that of free RNase, non-targeted RNase-loaded NPs, and empty NPs (Fig. 6). The results show that both empty NPs (up to 12 mg/ml particle concentration, which is equivalent to the highest

concentration of RNase loaded NPs tested) and free RNase (up to a concentration of 100 μM) did not affect cell viability of SKBR3 cells, whereas non-conjugated NPs showed toxicity, which led to 80 % cell death at the highest concentration of RNase tested (28 μM RNase; IC_{50}: 14 μM, Fig.6).

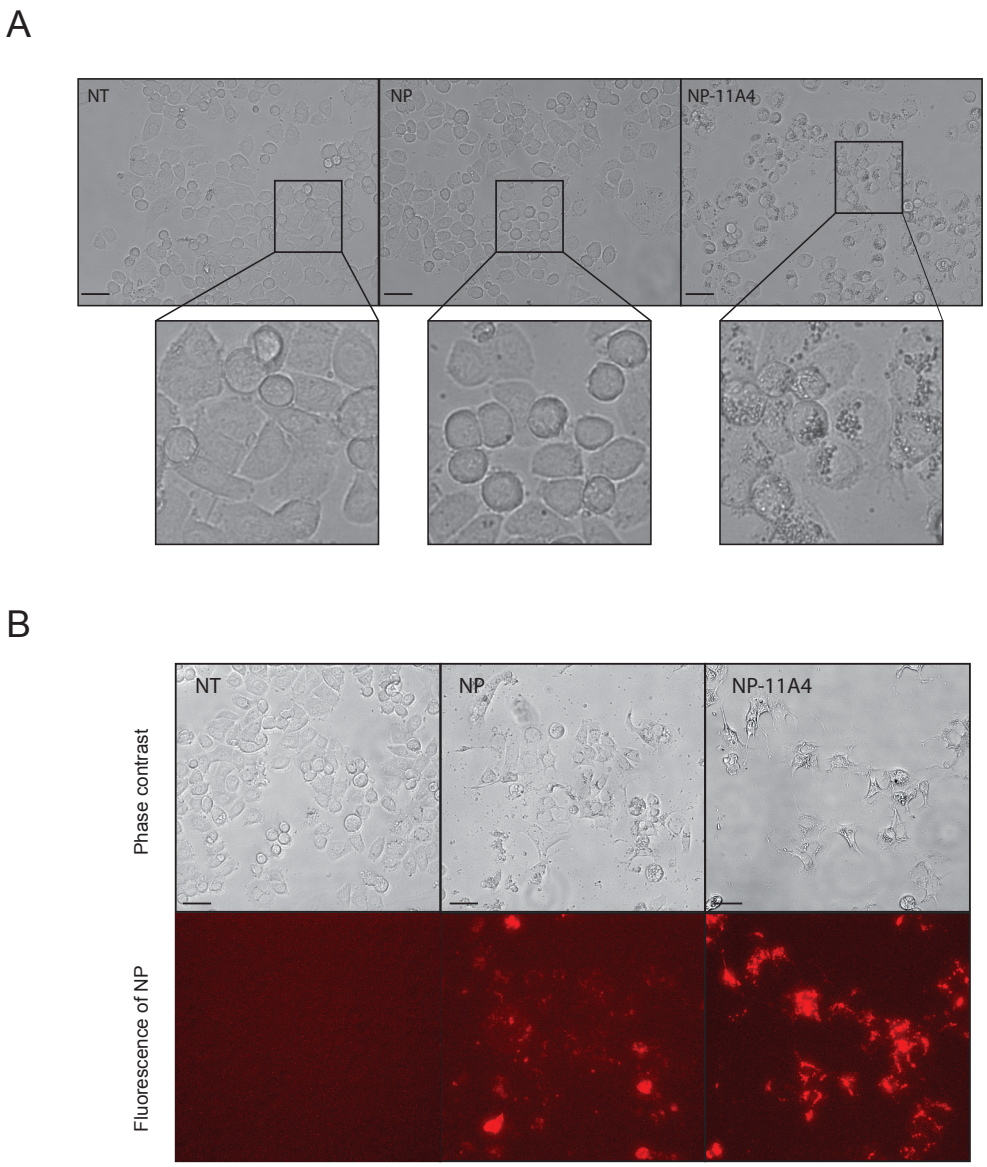

Fig. 5. Images obtained with an EVOS inverted microscope. A. Phase contrast images of non-treated SKBR3 cells (NT) and of SKBR3 cells treated with non-targeted nanoparticles (NP) or with nanobody-targeted nanoparticles (NP-11A4) for 24 hrs. Scale = 50μm. B. Phase contrast images (top) and fluorescent images (bottom) of non-treated SKBR3 cells (NT), cells treated with non-targeted RNase-loaded and fluorescently labelled nanoparticles (NP) and cells treated with nanobody-targeted RNase-loaded and fluorescently labelled nanoparticles (NP-11A4) for 3 days. Scale = 50μm.

The cell viability was further decreased upon incubation with RNase-loaded nanobody decorated NPs, which led to 95% cell death (28 μM RNase; IC_{50}: 4 μM, Fig.6). To rule out the possibility of an effect of the 11A4 nanobody on cell viability, the free nanobody, at a much higher dose than that was present in the NP formulation, was incubated with the HER2 overexpressing as well as the HER2 negative cell lines. Our results demonstrated no reduction in cell viability.

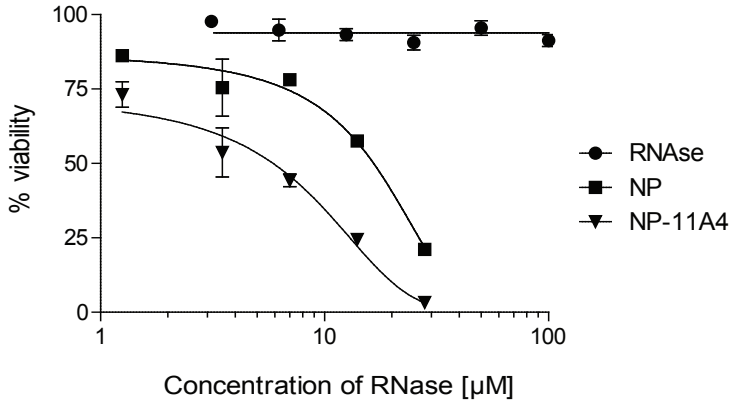

Fig. 6. Viability of SKBR3 cells upon 72 hrs incubation with RNase-loaded conjugated and non-conjugated NPs or free RNase (non-treated cells set to 100%). Empty NPs up to concentration of 12 mg/ml did not affect the cell viability. This is the same concentration of nanoparticles at highest μM concentration of RNase. Graph presents mean ± SD.

Discussion

The development of targeted therapeutic nanoparticles attracts much attention as it allows to improve the efficacy of encapsulated therapeutics and at the same time reduce the unwanted side-effects.

Early studies have demonstrated that most RNases do not exert considerable cytotoxic activities unless they are internalized [9,58]. Our data supports these observations as free RNase did not show cytotoxic activity, likely because of its insufficient uptake. The observed cytotoxic effect of RNase loaded NP was further improved upon HER2 specific nanobody conjugation. The addition of nanobody on the surface of NPs improves their specific binding and most likely stimulates internalization due to receptor clustering. It has to be highlighted that RNase should be present in the cytoplasm to induce apoptotic cell death, as a result of RNase-catalyzed degradation of cytosolic RNAs. Thus, the cytotoxic effect of the RNase-loaded NPs is due to either the release of RNase in the endosome, which subsequently destabilizes these cellular compartments resulting in release of the enzyme into the cytosol, or due to destabilization of the endosomes by particles followed by release of the entrapped enzyme in the cytosol (or due to a combination of both).

Enhanced and selective uptake of PLGA and other polymer-based NPs decorated

with HER2 targeted mAb (e.g. trastuzumab) into different cell lines, including SKBR3, has been reported previously by others [59-61]. It has been shown that actively internalized RNases are able to escape endosomal compartments and evade degradation [17,18]. Here we employed nanobodies as targeting units. This approach allows to reduce the cost of targeted nanoparticle formulation as generation of nanobodies is a fast and relatively cheap process. Furthermore, nanobodies are considered to have a low immunogenic potential.

Secondly, endosomes and lysosomes are predominantly acidic (pH 4 to 5). At this pH, RNase (pI 9.6) has a strong positive charge and hence likely interacts with negatively charged membranes, leading to membrane destabilization and their subsequent release into the cytoplasm. Previous studies on the cellular processing of (non-conjugated) PLGA nanoparticles have shown that after uptake a main fraction of the nanoparticles recycles back to the outside of the cell, while a small fraction enters secondary endosomes and lysosomes and finally translocates into the cytoplasm via an essentially unknown mechanism [62]. Given the structural resemblance with PLGA, the same cellular fate can be also expected for PLGHMGA NPs. Furthermore, it has been shown that the cellular uptake of PLGA NPs depends on their size and surface properties, but also on cell type, incubation time and particle concentration. However, it is important to emphasize that ligand-conjugated NPs have different intracellular trafficking pathways than non-conjugated NPs [63].

It should be mentioned that in our previous study almost complete removal of PEG (shedding) of PLGHMGA NPs occurred in five days due to preferential hydrolysis of the ester bond between the PEG and PLGHMGA block. The cellular binding of our NPs and their subsequent internalization occurs in 1-2 days at most (Fig. 5), which suggests that the shedding of the PEG layer does not occur to a great extent outside the cell. During further incubation, however, it is possible that the gradual PEG shedding results in enhanced endosomal/lysosomal escape of NPs.

Our data show that by decorating RNase loaded NP with a HER2-specific nanobody the toxicity is improved, however toxicity of non-targeted RNase loaded NP is already high. We anticipate that the added value of nanobody conjugation and therefore targeting to HER2 overexpressing cells will be more pronounced in *in vitro* toxicity assays with shorter incubation period than the one presented here (e.g. 1-2 hrs). Furthermore, targeted delivery of RNase loaded NP may result in decrease of unwanted side toxicity in an *in vivo* situation.

In conclusion, we developed a nanobody targeted biodegradable nanoparticle based system that allows for specific delivery of RNase to HER2 overexpressing cells resulting in an improved cytotoxicity.

References

1. Youle RJ, Newton D, Wu YN, Gadina M, Rybak SM: Cytotoxic ribonucleases and chimeras in cancer therapy. *Crit. Rev. Ther. Drug Carrier Syst.* 10(1), 1-28 (1993).

2. De Lorenzo C, D'Alessio G: From immunotoxins to immunoRNases. *Curr. Pharm. Biotechnol.* 9(3), 210-214 (2008).

3. Krauss J, Arndt MA, Dubel S, Rybak SM: Antibody-targeted RNase fusion proteins (immunoRNases) for cancer therapy. *Curr. Pharm. Biotechnol.* 9(3), 231-234 (2008).

4. Baynes JW, Wold F: Effect of glycosylation on the in vivo circulating half-life of ribonuclease. *J. Biol. Chem.* 251(19), 6016-6024 (1976).

5. Aleksandrowicz J, Urbanczyk J, Ostrowska A, Sierko J: Further research on the activity of ribonucleases in the blood and urine of patients suffering from proliferative hemocytopathia. *Blood* 13(7), 652-664 (1958).

6. Ardelt W, Ardelt B, Darzynkiewicz Z: Ribonucleases as potential modalities in anticancer therapy. *Eur. J. Pharmacol.* 625(1-3), 181-189 (2009).

7. Telford IR, Kemp JF, Taylor EF, Yeaman MW: Effect of ribonuclease on survival of ascites tumor bearing mice. *Proc. Soc. Exp. Biol. Med.* 100(4), 829-831 (1959).

8. Newton DL, Ilercil O, Laske DW, Oldfield E, Rybak SM, Youle RJ: Cytotoxic ribonuclease chimeras. Targeted tumoricidal activity in vitro and in vivo. *J. Biol. Chem.* 267(27), 19572-19578 (1992).

9. Saxena SK, Rybak SM, Winkler G *et al.*: Comparison of RNases and toxins upon injection into Xenopus oocytes. *J. Biol. Chem.* 266(31), 21208-21214 (1991).

10. Shapiro R: Cytoplasmic ribonuclease inhibitor. *Methods Enzymol.* 341, 611-628 (2001).

11. Lee FS, Vallee BL: Structure and action of mammalian ribonuclease (angiogenin) inhibitor. *Prog. Nucleic Acid Res. Mol. Biol.* 44, 1-30 (1993).

12. Dickson KA, Haigis MC, Raines RT: Ribonuclease inhibitor: structure and function. *Prog. Nucleic Acid Res. Mol. Biol.* 80, 349-374 (2005).

13. Turcotte RF, Lavis LD, Raines RT: Onconase cytotoxicity relies on the distribution of its positive charge. *FEBS J.* 276(14), 3846-3857 (2009).

14. Zwolinska M, Smolewski P: Onconase: a ribonuclease with antitumor activity. *Postepy Hig. Med. Dosw. (Online)* 64, 58-66 (2010).

15. Altomare DA, Rybak SM, Pei J *et al.*: Onconase responsive genes in human mesothelioma cells: implications for an RNA damaging therapeutic agent. *BMC Cancer* 10, 34-2407-10-34 (2010).

16. Ardelt B, Ardelt W, Darzynkiewicz Z: Cytotoxic ribonucleases and RNA interference (RNAi). *Cell. Cycle* 2(1), 22-24 (2003).

17. Rybak SM: Antibody-onconase conjugates: cytotoxicity and intracellular routing. *Curr. Pharm. Biotechnol.* 9(3), 226-230 (2008).

18. Wu Y, Saxena SK, Ardelt W *et al.*: A study of the intracellular routing of cytotoxic ribonucleases. *J. Biol. Chem.* 270(29), 17476-17481 (1995).

19. Chang CH, Gupta P, Michel R *et al.*: Ranpirnase (frog RNase) targeted with a humanized, internalizing, anti-Trop-2 antibody has potent cytotoxicity against diverse epithelial cancer cells. *Mol. Cancer. Ther.* 9(8), 2276-2286

(2010).
20. Chang CH, Sapra P, Vanama SS, Hansen HJ, Horak ID, Goldenberg DM: Effective therapy of human lymphoma xenografts with a novel recombinant ribonuclease/anti-CD74 humanized IgG4 antibody immunotoxin. *Blood* 106(13), 4308-4314 (2005).
21. Newton DL, Hansen HJ, Mikulski SM, Goldenberg DM, Rybak SM: Potent and specific antitumor effects of an anti-CD22-targeted cytotoxic ribonuclease: potential for the treatment of non-Hodgkin lymphoma. *Blood* 97(2), 528-535 (2001).
22. Choi JH, Jang JY, Joung YK, Kwon MH, Park KD: Intracellular delivery and anti-cancer effect of self-assembled heparin-Pluronic nanogels with RNase A. *J. Control. Release* 147(3), 420-427 (2010).
23. Chen W, Zheng M, Meng F *et al.*: In situ forming reduction-sensitive degradable nanogels for facile loading and triggered intracellular release of proteins. *Biomacromolecules* 14(4), 1214-1222 (2013).
24. Maier K, Martin I, Wagner E: Sequence defined disulfide-linked shuttle for strongly enhanced intracellular protein delivery. *Mol. Pharm.* 9(12), 3560-3568 (2012).
25. Choi SH, Park TG: G-CSF loaded biodegradable PLGA nanoparticles prepared by a single oil-in-water emulsion method. *Int. J. Pharm.* 311(1-2), 223-228 (2006).
26. Rajapaksa TE, Stover-Hamer M, Fernandez X, Eckelhoefer HA, Lo DD: Claudin 4-targeted protein incorporated into PLGA nanoparticles can mediate M cell targeted delivery. *J. Control. Release* 142(2), 196-205 (2010).
27. Taha MA, Singh SR, Dennis VA: Biodegradable PLGA85/15 nanoparticles as a delivery vehicle for Chlamydia trachomatis recombinant MOMP-187 peptide. *Nanotechnology* 23(32), 325101-4484/23/32/325101. Epub 2012 Jul 23 (2012).
28. Diwan M, Elamanchili P, Lane H, Gainer A, Samuel J: Biodegradable nanoparticle mediated antigen delivery to human cord blood derived dendritic cells for induction of primary T cell responses. *J. Drug Target.* 11(8-10), 495-507 (2003).
29. Ye M, Kim S, Park K: Issues in long-term protein delivery using biodegradable microparticles. *J. Control. Release* 146(2), 241-260 (2010).
30. Danhier F, Ansorena E, Silva JM, Coco R, Le Breton A, Preat V: PLGA-based nanoparticles: an overview of biomedical applications. *J. Control. Release* 161(2), 505-522 (2012).
31. Betancourt T, Byrne JD, Sunaryo N *et al.*: PEGylation strategies for active targeting of PLA/PLGA nanoparticles. *J. Biomed. Mater. Res. A.* 91(1), 263-276 (2009).
32. Hassanzadeh-Ghassabeh G, Devoogdt N, De Pauw P, Vincke C, Muyldermans S: Nanobodies and their potential applications. *Nanomedicine (Lond)* 8(6), 1013-1026 (2013).
33. Muyldermans S: Nanobodies: natural single-domain antibodies. *Annu. Rev. Biochem.* 82, 775-797 (2013).
34. Oliveira S, Heukers R, Sornkom J, Kok RJ, van Bergen En Henegouwen PM: Targeting tumors with nanobodies for cancer imaging and therapy. *J. Control. Release* 172(3), 607-617 (2013).
35. Wang Y, Liu P, Du J, Sun Y, Li F, Duan

Y: Targeted siRNA delivery by anti-HER2 antibody-modified nanoparticles of mPEG-chitosan diblock copolymer. *J. Biomater. Sci. Polym. Ed.* 24(10), 1219-1232 (2013).

36. Ruan J, Song H, Qian Q *et al.*: HER2 monoclonal antibody conjugated RNase-A-associated CdTe quantum dots for targeted imaging and therapy of gastric cancer. *Biomaterials* 33(29), 7093-7102 (2012).

37. Kijanka M, Warnders FJ, El Khattabi M *et al.*: Rapid optical imaging of human breast tumour xenografts using anti-HER2 VHHs site-directly conjugated to IRDye 800CW for image-guided surgery. *Eur. J. Nucl. Med. Mol. Imaging* 40(11), 1718-1729 (2013).

38. Samadi N, van Nostrum CF, Vermonden T, Amidi M, Hennink WE: Mechanistic studies on the degradation and protein release characteristics of poly(lactic-co-glycolic-co-hydroxymethylglycolic acid) nanospheres. *Biomacromolecules* 14(4), 1044-1053 (2013).

39. Ghassemi AH, van Steenbergen MJ, Barendregt A *et al.*: Controlled release of octreotide and assessment of peptide acylation from poly(D,L-lactide-co-hydroxymethyl glycolide) compared to PLGA microspheres. *Pharm. Res.* 29(1), 110-120 (2012).

40. Ghassemi AH, van Steenbergen MJ, Talsma H, van Nostrum CF, Crommelin DJ, Hennink WE: Hydrophilic polyester microspheres: effect of molecular weight and copolymer composition on release of BSA. *Pharm. Res.* 27(9), 2008-2017 (2010).

41. Ghassemi AH, van Steenbergen MJ, Talsma H *et al.*: Preparation and characterization of protein loaded microspheres based on a hydroxylated aliphatic polyester, poly(lactic-co-hydroxymethyl glycolic acid). *J. Control. Release* 138(1), 57-63 (2009).

42. Liu Y, Ghassemi AH, Hennink WE, Schwendeman SP: The microclimate pH in poly(D,L-lactide-co-hydroxymethyl glycolide) microspheres during biodegradation. *Biomaterials* 33(30), 7584-7593 (2012).

43. Samadi N, van Steenbergen MJ, van den Dikkenberg JB *et al.*: Nanoparticles Based on a Hydrophilic Polyester with a Sheddable PEG Coating for Protein Delivery. *Pharm. Res.* (2014).

44. Leemhuis M, van Nostrum CF, Kruijtzer JAW *et al.*: Functionalized poly(α-hydroxyacid) s via ring-opening polymerization: toward hydrophilic polyesters with pendant hydroxyl groups.. *Macromolecules* 39, 3500-3508 (2006).

45. Zambaux MF, Bonneaux F, Gref R, Dellacherie E, Vigneron C: Preparation and characterization of protein C-loaded PLA nanoparticles. *J. Control. Release* 60(2-3), 179-188 (1999).

46. Dunne M, Corrigan I, Ramtoola Z: Influence of particle size and dissolution conditions on the degradation properties of polylactide-co-glycolide particles. *Biomaterials* 21(16), 1659-1668 (2000).

47. Panyam J, Dali MM, Sahoo SK *et al.*: Polymer degradation and in vitro release of a model protein from poly(D,L-lactide-co-glycolide) nano- and microparticles. *J. Control. Release* 92(1-2), 173-187 (2003).

48. Sah H: A new strategy to determine the actual protein content of poly(lactide-co-glycolide) microspheres. *J. Pharm. Sci.* 86(11), 1315-1318 (1997).

49. Kalnitskey et al.: Worthington Biochemical Coprporation (Ribonuleic Acid Assay). (1959).
50. Molla MR, Ghosh S: Exploring versatile Sulfhydryl Chemistry in the Chain End of a Synthetic Polylactide. . *Macromolecules* 45(21), 8561-8570 (2012).
51. Toti US, Guru BR, Grill AE, Panyam J: Interfacial activity assisted surface functionalization: a novel approach to incorporate maleimide functional groups and cRGD peptide on polymeric nanoparticles for targeted drug delivery. *Mol. Pharm.* 7(4), 1108-1117 (2010).
52. Zhang L, Han L, Qin J, Lu W, Wang J: The use of borneol as an enhancer for targeting aprotinin-conjugated PEG-PLGA nanoparticles to the brain. *Pharm. Res.* 30(10), 2560-2572 (2013).
53. Patil YB, Toti US, Khdair A, Ma L, Panyam J: Single-step surface functionalization of polymeric nanoparticles for targeted drug delivery. *Biomaterials* 30(5), 859-866 (2009).
54. Gref R, Luck M, Quellec P *et al.*: 'Stealth' corona-core nanoparticles surface modified by polyethylene glycol (PEG): influences of the corona (PEG chain length and surface density) and of the core composition on phagocytic uptake and plasma protein adsorption. *Colloids Surf. B Biointerfaces* 18(3-4), 301-313 (2000).
55. Wang M, Thanou M: Targeting nanoparticles to cancer. *Pharmacol. Res.* 62(2), 90-99 (2010).
56. van de Weert M, Hennink WE, Jiskoot W: Protein instability in poly(lactic-co-glycolic acid) microparticles. *Pharm. Res.* 17(10), 1159-1167 (2000).
57. Frokjaer S, Otzen DE: Protein drug stability: a formulation challenge. *Nat. Rev. Drug Discov.* 4(4), 298-306 (2005).
58. Erickson HA, Jund MD, Pennell CA: Cytotoxicity of human RNase-based immunotoxins requires cytosolic access and resistance to ribonuclease inhibition. *Protein Eng. Des. Sel.* 19(1), 37-45 (2006).
59. Koopaei MN, Dinarvand R, Amini M *et al.*: Docetaxel immunonanocarriers as targeted delivery systems for HER 2-positive tumor cells: preparation, characterization, and cytotoxicity studies. *Int. J. Nanomedicine* 6, 1903-1912 (2011).
60. Sun B, Ranganathan B, Feng SS: Multifunctional poly(D,L-lactide-co-glycolide)/montmorillonite (PLGA/MMT) nanoparticles decorated by Trastuzumab for targeted chemotherapy of breast cancer. *Biomaterials* 29(4), 475-486 (2008).
61. Yousefpour P, Atyabi F, Vasheghani-Farahani E, Movahedi AA, Dinarvand R: Targeted delivery of doxorubicin-utilizing chitosan nanoparticles surface-functionalized with anti-Her2 trastuzumab. *Int. J. Nanomedicine* 6, 1977-1990 (2011).
62. Panyam J, Labhasetwar V: Dynamics of endocytosis and exocytosis of poly(D,L-lactide-co-glycolide) nanoparticles in vascular smooth muscle cells. *Pharm. Res.* 20(2), 212-220 (2003).
63. Furumoto K, Ogawara K, Yoshida M *et al.*: Biliary excretion of polystyrene microspheres depends on the type of receptor-mediated uptake in rat liver. *Biochim. Biophys. Acta* 1526(2), 221-226 (2001).

Chapter 9

Summary and Future Perspectives

1. Summary

The first part of the thesis focuses on detection of HER2 receptor expressed by human breast cancer cells using molecular optical imaging approach, but also immuno-electron microscopy.

Since most breast cancer related deaths are a result of metastatic disease, an early detection of the disease (at its pre-invasive or invasive stage) followed by complete resection of the lesion could potentially result in a decreased mortality rate [1]. To enable lesion detection and its subsequent removal, sensitive imaging techniques are needed. Optical molecular imaging, when implemented into clinical practice, has the potential to enable non-invasive detection of cancer, monitoring of therapy response, and to allow image guided surgery for radical tumor resections and of their neighboring precursors with minimal removal of surrounding normal tissue. Moreover, optical molecular imaging would likely be highly suitable for *ex vivo* analysis of biopsies.

In **Chapter 2**, the development of targeted tracers for molecular optical imaging is presented. Nanobodies, functional antigen binding fragments of only 15 kDa, are the variable domains of the heavy chain of heavy-chain only antibodies that are found in animals from the *Camelidae* family. Due to their small size (ten times smaller molecular weight than conventional antibodies, which is below glomerular filtration threshold) they are able to rapidly distribute and accumulate in the tumor, combined with a fast clearance from non-targeted tissues, resulting in high tumor-to-background ratios (T/B ratio) shortly after the administration, thereby enabling a clear visualization and delineation of the tumor. HER2-targeting nanobodies described in this chapter were obtained from phage display selections directed towards high affinity binders and displayed affinities below 10 nM. We show that random conjugation of a 1 kDa IRDye800CW-NHS had a detrimental effect on the binding properties of all tested nanobodies-IR, however it was most pronounced in case of 11A4 nanobody, which possesses a lysine in the CDR3 region (1000 fold drop in affinity). Preservation of high affinity of the nanobody upon conjugation is essential for nanobody efficient accumulation and retention at the tumor, as indicated by Wittrup et al [2]. Indeed, no tumor accumulation of randomly conjugated 11A4 was observed in the SKBR3 xenograft model. The problem of affinity loss was solved by introduction of an additional cystein in the C-terminal region of the nanobody enabling a site-specific conjugation of the maleimide-functionalized fluorophore. Upon such conjugation the affinities of all tested nanobodies-IR remained in low nanomolar range. After initial evaluation of nanobodies as optical imaging probes in a HER2-positive SKBR3 xenograft model, 11A4 was chosen as the lead candidate. Its performance as targeted imaging agent was further compared with that of a monoclonal antibody, trastuzumab-IR. We showed that imaging with 11A4-IR resulted in obtaining comparable T/B ratios as with mAb-IR already much shorter after injection (4 hrs vs 72 hrs, respectively). Importantly, 11A4-IR accumulated only in HER2 positive tumors, whereas trastuzumab-IR was also found in HER2 negative ones

(probably due to the enhanced permeability and retention effect (EPR) [3]). Furthermore, the feasibility of nanobody-IR use for image-guided surgery in an intraoperative setting was confirmed.

Recently, it has been demonstrated that to obtain a high breast cancer detection rate, a panel of several membrane markers is required [4]. One of prerequisites for a successful optical imaging is high tumor specificity, which can be obtained by employing fluorescent probes targeting tumor-specific biomarkers. Biomarkers, the (over)expression of which is associated with cancer development, have been identified. They include the human epidermal growth factor receptor 2 (HER2) and the hypoxia marker carbonic anhydrase IX (CAIX) [4-6]. **In Chapter 3** we show that a combination of two nanobody-based optical probes that specifically recognize two independent cancer biomarkers, conjugated to the same near-infrared (NIR) fluorophore, resulted in higher T/B ratios, thereby improving tumor detection. In this part of the thesis an orthotopic tumor model mimicking ductal carcinoma *in situ* of the breast (DCIS) was used, as it resembles human tumor morphology much better than an ectotopic (e.g. subcutaneous) model [7]. Currently the assessment of biomarkers' expression relies exclusively on *ex vivo* methods such as immunohistochemistry (IHC), *in situ* hybridization (using fluorescence (FISH) or silver (SISH) or DAB chromogen (CISH)), or PCR based techniques such as multiplex ligation-dependent probe amplification [8]. To obtain material for these assessments, a biopsy is required. Here, we show that nanobodies conjugated to two distinct NIR fluorophores can be used in a dual-spectral imaging setting, allowing for non-invasive determination of tumor molecular status (in this case, HER2 and CAIX expression). Breast cancer is known to metastasize into lung, bone and liver [1,9]. Here, we show that the dual-spectral nanobody combination targeting HER2 and CAIX is able to detect lung metastasis in an invasive setting. Furthermore, direct immunofluorescence of the NIR fluorophores coupled to nanobodies already present in the tumor tissue, allows for assessment of the expression of cancer targets in excised material without requiring further costly lab processing.

In **Chapter 4** we present the development of canine tumor specific nanobodies. Dogs are known to spontaneously develop tumors, which in many aspects resemble human malignancies (such as tumor growth over long periods of time in the presence of fully functional immune system, inter- and intratumoral heterogeneity, development of metastases) [10,11]. As a result, besides developing new possibilities for veterinary interventions, more interest is now expressed in using dogs as models for novel drug evaluation. Here we aimed at the development of canine HER2 specific nanobodies for canine tumor imaging and targeted therapy. We immunized llamas with canine osteosarcoma cells, HMPOS, and constructed phage display libraries. Their subsequent panning on canine cells expressing HER2 receptor combined with specific elution with HER2-targeted mAb, trastuzumab, resulted in selection of several binders. Two of these nanobodies, namely 11B12 and 15C4, displayed high affinity on a panel of canine cancer cells, both prior to as well as upon random conjugation of IRDye800CW-NHS ester. They were further evaluated as

optical imaging probes in a pilot *in vivo* study employing two xenograft models (P114 and MCKOS) differing in target protein expression. We show that imaging using single nanobody-IR does not result in clear tumor delineation, most likely due to too low level of target protein expression, whereas imaging employing both nanobodies-IR simultaneously leads to clear tumor visualization *ex vivo*. We show nanobody-IR accumulation at the tumor in an intraoperative setting in case of single nanobody-IR injection and simultaneous injection of the two nanobody-IR, in contrast to no accumulation of negative control nanobody, R2-IR. However, the exact target of the selected nanobodies remains to be determined, since results of mass spectrometry have been inconclusive.

As presented in the first three experimental chapters of this thesis, nanobodies prove to be a valuable tool for *in vivo* cancer imaging. Furthermore, in **Chapter 5** the feasibility of HER2 targeted nanobody, 11A4, for immuno-EM applications is evaluated. We present an optimized protocol for HER2 receptor pre-embedment gold labeling for scanning and transmission microscopy as well as for post-embedment labeling of Tokuyasu, cryo-immuno-EM sections using HER2 targeted nanobody.

The second part of this thesis focuses on development of nanobody-therapy for breast cancer. Nanobodies can be employed into three distinct therapeutic platforms, such as (A) naked nanobodies being receptor antagonists interfering with signaling cascades, (B) targeting moieties of effector domains, such as toxic peptides, photosensitizers, or drugs, and (C) targeting molecules decorating the surface of nanoparticles, which encapsulate toxic cargo. The second part of the thesis focuses on evaluation of HER2 targeted nanobody-based therapeutics representing platforms (B) and (C).

In **Chapter 6** we describe characteristics of nanobody-based therapeutics that influence their fate upon intravenous injection for cancer therapy. We discuss factors affecting their systemic circulation and renal, hepatic or splenic filtration, their extravasation and tumor penetration, and finally their interaction with target molecules on the tumor tissue.

Nanobody-photosensitizer conjugates (nanobody-PS) are a potent example of platform (B), in which the nanobody moiety is used to target a PS that produces toxic species upon light illumination of the PS at its site of action. In **Chapter 7** we present the development and characterization of nanobody-PS conjugates specific for HER2 receptor to be used in photodynamic therapy (PDT). The employed selection strategy resulted in two new nanobodies that bind specifically and with high affinity to the HER2 receptor in its natural surroundings. High affinity of these nanobodies is of crucial importance for their successful performance *in vivo* as explained in Chapter 6. Combining these two nanobodies resulted in a biparatopic nanobody that preserves the HER2-specificity and induces HER2 internalization, which is in agreement with the results of Heukers et al [12]. After random conjugation of the fluorescent PS, the binding affinities remained in the low nanomolar range. Both binding studies and pulse data show that the interaction of nanobody-PS conjugates with the breast cancer cells correlates well with HER2 expression levels. Since less than 35% of patients respond to initial trastuzumab treatment due to primary resistance and the fact that 70%

of them will progress to a metastatic disease within 24 to 36 months as a result of an acquired resistance [13], there is a great need for development of novel therapies. Here we show that obtained nanobody-PS conjugates are specific and potent PDT agents (IC_{50} values < 10 nM), which upon illumination with light lead to necrosis of both trastuzumab sensitive and resistant cells. Nanobodies employed in this strategy as targeting moieties are responsible for rapid association with HER2 positive cells to enable the delivery of toxic species, only produced upon light illumination of PS, to its site of action, and thereby most likely decreasing unwanted phototoxicity when tested *in vivo*.

Recently, more interest has been expressed in nanobody-targeted delivery of nanomedicines encapsulating a toxic payload. These systems, due to their size, accumulate in the tumors in a passive manner, strongly depending on the EPR effect as explained in Chapter 6. To improve their therapeutic potential, but mostly to decrease their unwanted toxicity by specific targeting to their site of action, these systems have been decorated with nanobodies [14-17]. In **Chapter 8** we evaluate the suitability of PEG-PLGHMGA nanoparticles (NP) for nanobody-targeted intracellular delivery of therapeutic protein – ribonuclease A (RNase A) able to catalyze the degradation of cytosolic RNAs. The obtained data show that RNase A was released from NP during 12 days and that the protein retained its bioactivity (as shown by the enzymatic assays). The cytotoxic potential of nanobody-targeted RNase A loaded NPs was compared to that of free RNase, non-targeted RNase A loaded NPs and empty NPs. We show that neither empty NPs nor free RNase A resulted in SKBR3 cell toxicity (up to a concentration of 100 μM), whereas non-targeted RNase loaded NPs led to a 75% of cell death at the highest concentration of RNase (28 μM; IC_{50}: 14 μM). Importantly, RNase A loaded NPs conjugated to the HER2 specific nanobody 11A4 led to a more pronounced cytotoxicity, resulting in 90% cell death at the highest concentration of RNase (28 μM; IC_{50}: 4 μM). Our results indicate that RNase A was released intracellularly, where it could exert its activity by catalyzing the degradation of cytosolic RNAs.

2. Future perspectives

Molecular imaging performed with the use of optical tracers is recently gaining more and more attention, however, due to limited light penetration depth this modality is perfectly suitable for detection of superficial (or endoscopically reachable) tumors or use in an intraoperative setting, but not for performing whole body scans. Over recent years, an increasing amount of data has been obtained supporting the concept of image-guided surgery as a valuable tool for cancer therapy. Nevertheless, before image-guided surgery is translated into routine clinical practice several challenges need to be overcome.

The prerequisite for successful image-guided surgery is obtaining high contrast between tumor and healthy tissue. This can be obtained by the use of targeted tumor-specific probes, which bind exclusively to cells expressing the tumor-related biomarker. Increasing knowledge on potentially valuable tumor biomarkers may accelerate development of novel, tumor-targeted probes.

More interest is now expressed in development of novel probe formats smaller than mAbs to facilitate rapid optical imaging. Nanobodies, which are ten times smaller in terms of molecular weight than conventional mAbs, possess several characteristics essential for an optical imaging probe designed for rapid imaging. These characteristics include high affinity and specificity towards targets against which they are raised, combined with small size enabling fast distribution and homogenous tumor penetration resulting in high accumulation at the tumor site shortly upon injection. Furthermore, ease and speed of nanobody generation in the phage display process as well as ease of their engineering make them an attractive probe platform. Nanobodies are known to have a low immunogenic potential, but due to the fact that both naked nanobodies as well as conjugated to fluorophores are cleared by the kidneys, additional studies focusing on nephrotoxicity should be performed.

To improve the contrast between healthy and cancer tissue, besides using tumor-specific nanobodies targeting receptors ideally (over)expressed only in cancer cells, one may envision use of a single nanobody conjugated to multiple fluorophores at the same time. We showed that random dye conjugation may have a detrimental effect on nanobody binding capacity, therefore development of site-directed conjugation strategies is highly advised. Nevertheless, such probes would have to be first optimized to ensure that the quenching of the fluorophores is minimized. Furthermore, site-directed conjugation would be the preferred strategy for clinical translation as it is very important to be able to obtain a uniform product consisting of predominantly labeled nanobody. In case of random conjugation, some nanobodies may contain more than 1 fluorophore while at the same time some may not contain any.

Another way to improve the contrast between healthy and cancer tissue is targeting multiple tumor biomarkers at the same time. This would allow to overcome intratumoral heterogeneity. Such cocktails of nanobodies could be conjugated to the same fluorophore in order to increase the T/B ratio or each of the nanobodies could be conjugated to a different NIR fluorophore ('nanobody cocktail'). The use of 'nanobody cocktail' opens up a possibility to determine the tumor molecular status noninvasively, without the need for taking a biopsy and prior to surgery. This would allow evaluation and adjustment of adjuvant or neo-adjuvant therapy, especially in case of metastatic patients. Due to the small size of nanobodies, 'cocktails' containing nanobodies conjugated to the same fluorophore and targeting several non-overlapping epitopes on the surface of the one biomarker could enable overcoming low T/B ratios due to low expression levels of biomarker.

Interestingly, HER2-targeting nanobodies characterized in this thesis do not compete with trastuzumab for the binding epitope. This opens up a possibility of employing them for monitoring of response to trastuzumab treatment. Low immunogenic potential of nanobodies would most likely enable repetitive imaging to follow the response to the treatment in time.

To ensure introduction of optical imaging modality into a routine clinical practice, developments of tumor specific fluorescent agents need to be accompanied by improvements in dedicated detection systems. Furthermore, such systems should be easily available to a large group of

surgeons in order to stimulate adoption of the technique [18]. At the moment the commercially available systems are capable of detection of a single wavelength, whereas if 'cocktails' of nanobodies are to be used to determine the tumor molecular status *in vivo* detection of more than one wavelength is necessary.

In Chapter 4 we present development of canine specific nanobodies for rapid optical imaging. So far we were not able to determine the exact target of selected nanobodies. Future studies should focus on this challenge by employing an immunoprecipitation protocol combined with mass spectrometry analysis. In parallel, additional phage display selections may be performed in order to develop canine HER2 specific nanobodies. The phage outputs of past selections performed on canine cell lines may be used as input for further panning on e.g. human breast cancer cells expressing HER2 receptor. Furthermore, efforts may be taken to produce canine HER2 extracellular domain in bacterial or mammalian expression systems. Possession of this valuable tool would greatly simplify the future nanobody characterization.

We showed that HER2 specific nanobody may be successfully employed for electron microscopy imaging. In these primary feasibility studies we demonstrate an optimized protocol for indirect nanobody detection via rabbit anti- VHH serum as primary antibody source. Next step is to directly conjugate gold particles to this nanobody in order to further increase the resolution of EM technique. Studies employing 11A4 nanobody should rather focus on site-specific gold conjugation as we showed that random conjugation of a fluorophore to this particular nanobody results in complete loss of its affinity.

An attractive option for combining cancer imaging with therapy is the use of nanobody-based theranostics. One can envision the employment of nanobodies conjugated to fluorescent photosensitizers firstly to guide the surgeon in the radical tumor resection in the intraoperative setting, and secondly for photodynamic therapy (PDT) upon light illumination of the area of the excised tumor. Such approach would likely minimize the risk of disease re-occurrence and increase the chance for obtaining clean surgical margins. Before implementing of nanobody-PS conjugates in the clinic, these should be evaluated in appropriate *in vivo* models. Nanobody-PS conjugates presented in this thesis are potent PDT agents not only in trastuzumab-sensitive cells, but also in resistant ones. The issue of acquired or intrinsic trastuzumab resistance is a great hurdle for treatment of HER2 positive breast cancer patients. The presented PDT approach used in an invasive setting could solve this problem.

Furthermore, this PDT approach may be translated into designing new therapeutic option for triple-negative breast cancer. Triple-negative breast cancers do not express hormone receptor or HER2, but are often associated with EGFR overexpression. In contrast to HER2, EGFR is present not only on the surface of cancer tissue, but is also expressed in a variety of healthy tissues. Due to the fact that nanobody-PS are toxic only upon light illumination, EGFR-targeted nanobody-PS in an intraoperative setting could be the basis for an interesting PDT alternative for this particular group of cancer patients.

Finally, in Chapter 8 we report on HER2 targeted PEGylated PLGHMGA nanoparticles (NP) encapsulating a therapeutic protein (RNAse A). Future studies should focus on evaluation

of this improved therapeutic effect *in vivo* in a suitable model. It would be of interest to determine the toxicity of presented HER2 targeted nanoparticles in trastuzumab-resistant models both *in vitro* and *in vivo*. The exact mechanism by which the RNAse is released inside the target cells remains unknown. Studies focusing on unraveling whether cytotoxic result is obtained by either (i) the release of therapeutic protein from NP in the endosomes, leading to destabilization of these cellular compartments and further resulting in its translocation into the cytosol, or (ii) destabilization of the endosomes by NP followed by release of the trapped enzyme in the cytosol, or (iii) a combination of both, should be performed. Furthermore, optimization of the PEGylated PLGHMGA nanoparticles may be required to avoid their uptake by reticuloendothelial system (RES). This optimization must include modulating the size of the NP.

3. Summarizing conclusions

Taken together, the work presented in this thesis has led to the following conclusions:

- Nanobody-fluorophore conjugates are promising tools for rapid optical imaging of breast cancer in non-invasive and intraoperative setting, both in mono- and dual-spectral set-up.
- Nanobodies can be used for immuno-EM applications.
- Nanobody-photosensitizer conjugates are promising, potent therapeutic agents leading to cell death of both trastuzumab-sensitive and resistant human breast cancer cells.
- The biodegradable nanoparticles encapsulating RNase A and surface decorated by HER2-specific nanobody, can potentially be used for intracellular targeted delivery of therapeutic proteins to human breast cancer cells.

References

1. Weigelt B, Peterse JL, van 't Veer LJ: Breast cancer metastasis: markers and models. *Nat. Rev. Cancer.* 5(8), 591-602 (2005).

2. Wittrup KD, Thurber GM, Schmidt MM, Rhoden JJ: Practical theoretic guidance for the design of tumor-targeting agents. *Methods Enzymol.* 503, 255-268 (2012).

3. Fang J, Nakamura H, Maeda H: The EPR effect: Unique features of tumor blood vessels for drug delivery, factors involved, and limitations and augmentation of the effect. *Adv. Drug Deliv. Rev.* 63(3), 136-151 (2011).

4. Vermeulen JF, van Brussel AS, van der Groep P *et al.*: Immunophenotyping invasive breast cancer: paving the road for molecular imaging. *BMC Cancer* 12, 240-2407-12-240 (2012).

5. Ward C, Langdon SP, Mullen P *et al.*: New strategies for targeting the hypoxic tumour microenvironment in breast cancer. *Cancer Treat. Rev.* 39(2), 171-179 (2013).

6. Pinheiro C, Sousa B, Albergaria A *et al.*: GLUT1 and CAIX expression profiles in breast cancer correlate with adverse prognostic factors and MCT1 overexpression. *Histol. Histopathol.* 26(10), 1279-1286 (2011).

7. Behbod F, Kittrell FS, LaMarca H *et al.*: An intraductal human-in-mouse transplantation model mimics the subtypes of ductal carcinoma in situ. *Breast Cancer Res.* 11(5), R66 (2009).

8. Moelans CB, de Weger RA, van Blokland MT *et al.*: HER-2/neu amplification testing in breast cancer by multiplex ligation-dependent probe amplification in comparison with immunohistochemistry and in situ hybridization. *Cell. Oncol.* 31(1), 1-10 (2009).

9. Minn AJ, Gupta GP, Siegel PM *et al.*: Genes that mediate breast cancer metastasis to lung. *Nature* 436(7050), 518-524 (2005).

10. Khanna C, Lindblad-Toh K, Vail D *et al.*: The dog as a cancer model. *Nat. Biotechnol.* 24(9), 1065-1066 (2006).

11. Paoloni M, Khanna C: Translation of new cancer treatments from pet dogs to humans. *Nat. Rev. Cancer.* 8(2), 147-156 (2008).

12. Heukers R, Vermeulen JF, Fereidouni F *et al.*: Endocytosis of EGFR requires its kinase activity and N-terminal transmembrane dimerization motif. *J. Cell. Sci.* 126(Pt 21), 4900-4912 (2013).

13. Vu T, Claret FX: Trastuzumab: updated mechanisms of action and resistance in breast cancer. *Front. Oncol.* 2, 62 (2012).

14. Altintas I, Heukers R, van der Meel R *et al.*: Nanobody-albumin nanoparticles (NANAPs) for the delivery of a multikinase inhibitor 17864 to EGFR overexpressing tumor cells. *J. Control. Release* 165(2), 110-118 (2013).

15. Talelli M, Rijcken CJ, Oliveira S *et al.*: Nanobody-shell functionalized thermosensitive core-crosslinked polymeric micelles for active drug targeting. *J. Control. Release* 151(2), 183-192 (2011).

16. Talelli M, Oliveira S, Rijcken CJ *et al.*: Intrinsically active nanobody-modified polymeric micelles for tumor-targeted combination therapy. *Biomaterials* 34(4), 1255-1260 (2013).

17. van der Meel R, Oliveira S, Altintas I *et al.*: Inhibition of tumor growth by targeted anti-EGFR/IGF-1R nanobullets depends on efficient blocking of cell survival pathways. *Mol. Pharm.* 10(10), 3717-3727 (2013).

18. Keereweer S, Van Driel PB, Snoeks TJ *et al.*: Optical image-guided cancer surgery: challenges and limitations. *Clin. Cancer Res.* 19(14), 3745-3754 (2013).

Part 3

Appendix

Nederlandse samenvatting

1. **Samenvatting**

Het eerste deel van de scriptie gaat over de detectie van HER2 receptoren die tot expressie zijn gebracht op een humane borstkankercellijn gebruik makende van optische moleculaire imaging en immuno electronen microscopie.

Aangezien de meeste borstkanker gerelateerde sterfgevallen komen door metastase, zou een vroege detectie van de ziekte (in de pre-invasieve of invasieve fase) gevolgd door complete resectie van de lesie kunnen leiden tot een verlaagde mortaliteit [1]. Om lesies vroeg te detecteren en weg te halen, zijn er gevoelige imaging technieken nodig. Wanneer optische moleculaire imaging is geïmplementeerd in de kliniek, heeft het de potentie om non-invasief kanker te detecteren, om de respons op een therapie te volgen en om *image guided surgery* te gebruiken om radicale tumoren weg te snijden tezamen met hun aangrenzende precursors met minimale verwijdering van gezond weefsel. Te meer, optische moleculaire imaging zal waarschijnlijk hoogst geschikt zijn voor *ex vivo* analyse van biopsies.

In **Hoofdstuk 2** worden de resultaten met betrekking tot de ontwikkeling van de tracers uiteengezet. Nanobodies, het functionele antigen bindende fragment van slechts 15kDa, zijn het variabele domein van de zware keten van enkel-zware keten antilichamen die worden gevonden in dieren van de *Camelidae* familie. Door hun kleine formaat (tien keer kleiner in moleculair gewicht vergeleken met een conventioneel antilichaam, wat kleiner is dan de glomerulaire filtratie drempel) zijn ze in staat om snel te distribueren en te accumuleren in de tumor. Gepaard met een snelle efflux van niet-target-bevattend weefsel, kunnen ze hoge tumor/achtergrond ratios (T/A ratio) behalen kort na administratie en daarmee de tumor goed visualiseren en afbakenen. De HER2 bindende nanobodies die beschreven zijn in dit hoofdstuk waren gevonden door *phage-display* selecties uit te oefenen met als doel om hoge affine binders te isoleren. De nanobodies vertoonden affiniteiten onder de 10nM. Wij laten zien dat willekeurig geconjugeerd 1kDa IRDye800CW-NHS aan de nanobodies de bindings capaciteiten van alle geteste probes aantastte en dat dit voornamelijk het geval was voor nanobody 11A4, die een lysine in de CDR3 regio bevat (1000x vermindering in affiniteit). Behoud van de hoge affiniteit van de nanobodies na conjugatie is essentieel voor efficiënte accumulatie en retentie in de tumor, zoals getoond door Wittrup et al. [2]. Inderdaad, wij konden geen tumor accumulatie zien van willekeurig geconjugeerd 11A4 in een SKBR3 xenograft model. Het probleem van het affiniteit verlies was opgelost door de introductie van een additionele cysteïne in het C-terminale domein van het nanobody, wat toeliet om een locus specifieke conjugatie uit te oefenen met een maleimide gefunctionaliseerde fluorofoor. Na deze conjugaties lieten alle geteste IR-nanobodies affiniteiten zien in het lage nanomolaire gebied. Na een initiële evaluatie van alle nanobodies als optische imaging probe tegen het HER2-positieve SKBR3 xenograft model, was 11A4 gekozen als primaire kandidaat. De resultaten van 11A4 als een optische probe waren ook vergeleken

met een conventioneel monoclonaal antilichaam, trastuzumab-IR. We laten zien dat met 11A4-IR dezelfde T/A ratio verkregen kon worden als MAb-IR, maar al op veel eerdere tijdspunten (4h vs 72h, respectievelijk). 11A4-IR accumuleerde alleen in HER2-positieve tumoren, waar trastuzumab-IR ook werd gevonden in HER2-negatieve tumoren (waarschijnlijk door het *enhanced permeability and retention* effect (EPR) [3]). Ook hebben we hiermee bevestigd dat het gebruik van nanobody-IR conjugaten voor *image-guided surgery* haalbaar is.

Onlangs is het bewezen dat om een hoge borstkanker detectie te krijgen er een panel van verschillende membraan markers nodig is [4]. Één van de vereisten voor een succesvolle optische imaging is een hoge tumor specificiteit, welke verkregen kan worden door gebruik van fluorescente probes die tumor specifieke biomarkers herkennen. Biomarkers die tot (over)expressie worden gebracht in de tumor ontwikkeling zijn inmiddels geïdentificeerd. Tot deze groep behoren de humane epidermale groeifactor receptor 2 (HER2) en de hypoxia marker carbonisch anhydrase IX (CAIX) [4-6]. In **Hoofdstuk 3** laten we zien dat een combinatie van twee nanobody gebaseerde optische probes die specifiek twee onafhankelijke tumor biomarkers kunnen herkennen, en geconjugeerd aan dezelfde nabij-infrarode (NIR) fluorofoor, resulteren in een hogere T/A ratio, wat tot een betere tumor detectie leidde. In dit deel van de scriptie is een orthotopisch tumor model gebruikt wat ductaal carcinoma *in situ* (DCIS) in de borst nabootst, omdat dit model de morfologie van een humane tumor veel beter weerspiegelt dan een ectopisch (e.g. subcutaan) model [7]. Op het moment wordt de evaluatie van de expressie van biomarkers voornamelijk gedaan op basis van *ex vivo* methodes zoals immunohistochemie (IHC), *in situ* hybridisatie (met fluorescentie (FISH), zilver (SISH) of het DAB chromogeen (CISH)) of PCR gebaseerde methodes zoals multiplex ligatie-afhankelijke probe amplificatie [8]. Een biopsie is nodig om dit soort testen uit te voeren. In dit hoofdstuk laten we zien dat nanobodies geconjugeerd aan twee verschillende fluoroforen gebruikt kunnen worden in een duospectrale imaging setup, wat de mogelijkheid creëert om non-invasieve typering uit te oefenen op de tumor voor moleculaire markers (in dit geval HER2 en CAIX). Borstkanker metastaseert veelal naar de longen, botten en de lever [1,9]. We laten zien dat de duospectrale nanobody combinatie die HER2 en CAIX herkennen metastasering naar de longen kan herkennen in een invasief model. Te meer, directe immunofluorescentie van de NIR-fluorofoor nanobody conjugaties die al aanwezig zijn in het geïsoleerde tumor materiaal kan gebruikt worden voor een evaluatie van de expressie van de markers in het tumor materiaal zonder dat daar kostbare processing technieken in het lab aan te pas komen.

In **Hoofdstuk 4** presenteren we de ontwikkeling van honden tumor specifieke nanobodies. Honden ontwikkelen soms spontaan tumoren, die in veel opzichten humane lesies nabootsen (zoals in tumor groei over lange periodes in de aanwezigheid van een functionerend immuun systeem, in inter- en intratumor heterogeniteit, en in de ontwikkeling van metastase) [10,11]. Door deze overeenkomsten, en de mogelijkheid op nieuwe veterinaire behandelingen, is er steeds meer interesse

om honden te gebruiken als model voor nieuwe medicijn evaluaties. In dit hoofdstuk laten we de ontwikkeling zien van hond specifieke HER2 herkennende nanobodies voor honden tumor imaging and therapie. Lama's waren geïmmuniseerd met een honden osteosarcoma cellijn, HMPOS, en *phage-display* libraries waren met geëxtraheerd weefsel gemaakt. Deze libraries waren gebruikt als input voor selectierondes op honden cellen die HER2 tot expressie brengen. Door middel van specifieke elutie met de anti-HER2 mAb trastuzumab, waren enkele specifieke binders geïsoleerd. Twee van deze nanobodies, 11B12 en 15C4 genaamd, lieten hoge affiniteit zien op een panel van honden kankercellen, zowel voor als na willekeurige conjugatie van IRDye800CW-NHS ester. Ze waren verder geëvalueerd als optische imaging probe in een pilot *in vivo* studie waar twee xenograft modellen (P114 en MCKOS) waren gebruikt die verschillende expressie patronen hebben. Wij laten zien dat imaging met alleen één nanobody-IR probe niet resulteert in een duidelijke tumor uitlijning, wat waarschijnlijk wordt veroorzaakt door lage expressie niveaus van het target eiwit. *Ex vivo* imaging aan de andere hand met beide nanobody-IR constructen leidde tot goede tumor visualisatie. In een intraoperatieve setting hebben wij laten zien dat zowel injectie van één nanobody-IR construct als mede twee nanobody-IR constructen leidt tot goede tumor accumulatie in tegenstelling tot de negatieve controle nanobody, R2-IR. De exacte target van de nanobodies moet nog worden vastgesteld omdat massa spectrometrie onderzoek hiernaar geen duidelijke resultaten gaf.

Uit de eerste drie experimentele hoofdstukken van deze scriptie is op te maken dat nanobodies waardevolle middelen zijn voor *in vivo* kanker imaging. In **Hoofdstuk 5** hebben we de haalbaarheid getoetst om HER2 herkennend nanobody 11A4 te gebruiken voor immuno electronen microscopie. Wij presenteren een geöptimaliseerd protocol voor HER2 receptor pre-embedment goud labeling for zowel scanning als mede transmissie electronen microscopie. Ook hebben wij een protocol gemaakt voor post-embedment labeling van Tokuyasu cryo-immuno electronen microscopie secties gebruik makend van een HER2 herkenned nanobody.

Het tweede deel van deze scriptie beschrijft de ontwikkeling van nanobody gebaseerde therapie voor borstkanker. Nanobodies kunnen op een aantal verschillende manieren worden gebruikt voor therapeutische doeleinden: (A) naakte nanobodies die antogonistisch werken op membraan receptor, (B) als een targeting onderdeel voor een effector domein, zoals een toxisch peptide, een photosensitizer of medicijnen, en (C) een targeting molecuul wat het oppervlak bedekt van een nanoparticle wat toxische stoffen bevat. Het tweede deel van deze scriptie gaat over de ontwikkeling van een HER2 herkennend nanobody gebaseerde therapie die valt in categorieën (B) en (C).

In **Hoofdstuk 6** beschrijven we de karakteristieken van een nanobody gebaseerde therapie wanneer deze worden ingespoten voor kankertherapie. We bediscussiëren de factoren die invloed uitoefenen op hun systemische circulatie, hun filtratie in de nieren, lever en milt, hun extravasatie en tumor penetratie, en ook hun interactie met de moleculen op het oppervlak van het tumor weefsel.

Nanobody-photosensitizer conjugaten (nanobody-PS) zijn een goed voorbeeld van

categorie (B), waar het nanobody onderdeel gebruikt wordt om de photosensitizer naar een bepaalde plek toe te sturen, alwaar het toxische radicalen los laat wanneer het locaal met licht wordt beschenen. In **Hoofdstuk 7** presenteren wij de ontwikkeling en karakterisatie van nanobody-PS conjugaties die de HER2 receptor herkennen en bedoeld zijn voor photodynamische therapie (PDT). Een nieuwe, specifieke selectie strategie resulteerde in twee nieuwe nanobodies die specifiek en met hoge affine binden aan HER2 in zijn natuurlijke omgeving. Hoge affine van deze nanobodies is van cruciaal belang voor een succesvol resultaat *in vivo* zoals is uitgelegd in hoofdstuk 6. Ligatie van deze twee nanobodies leidde tot een biparatopische nanobody waar de specificiteit voor HER2 was behouden en welke internalisatie van HER2 induceerde. Deze resultaten doen sterk denken aan het internalisatie mechanisme zoals beschreven door Heukers *et al* [12]. Na willekeurige conjugatie van de fluorescente PS bleven de affiniteiten van de constructen in het lage nanomolaire gebied. Zowel bindings studies als mede pulse studies hebben laten zien dat de interactie van nanobody-PS conjugaten met borstkanker cellen goed correleert met HER2 expressie niveaus. Aangezien er bij slechts 35% van de patiënten een respons is op de behandeling met trastuzumab door primaire resistentie en het feit dat 70% van hen binnen 24 tot 36 maanden metastasering zullen krijgen door verkregen resistentie [13], is er een grote vraag naar de ontwikkeling van nieuwe therapieën. In dit hoofdstuk laten we zien dat de ontwikkelde nanobody-PS conjugaten specifieke en krachtige PDT middelen zijn (IC_{50} waardes < 10nM), welke bij belichting leiden tot necrose van zowel trastuzumab sensitieve als resistente cellen. De nanobodies die in deze strategie worden gebruikt als targeting onderdeel zijn verantwoordelijk voor de snelle associatie met HER2 positieve cellen om de toxische substantie af te leveren die onder invloed van locaal licht zorgen voor cel dood. Aangezien het licht locaal beschenen wordt, wordt er verwacht dat er weinig phototoxiciteit plaats vindt in gezond weefsel.

Vanuit het veld wordt er steeds vaker gekeken om nanobodies te gebruiken voor nanobody gemedieerde afgifte van nanomedicine die een toxische cargo bevatten. Dit soort systemen accumuleren passief in tumoren door hun grootte, maar is onderhevig aan het EPR effect zoals beschreven in hoofdstuk 6. Om hun therapeutische potentie te vergroten, maar ook tegelijkertijd om niet specifieke toxiciteit te verlagen, worden deze nanomedicines met nanobodies gecoat om meer specifieke targeting te krijgen naar de lesie [14-17]. In **Hoofdstuk 8** hebben we geëvalueerd of PEG-PLGHMGA nanoparticles (NP) geschikt zijn voor nanobody gemedieerde intracellulaire afgifte van een therapeutische eiwit, ribonuclease A (RNase A) wat cytosolisch RNA kan afbreken. De verkregen data laten zien dat RNase A was afgegeven van de NP gedurende 12 dagen en dat het eiwit zijn bioactiviteit behield (op basis van enzymatische assays). De cytotoxische potentie van nanobody gemedieerde RNase A geladen NP afgifte was vergeleken met vrij RNase A, RNase A geladen NPs niet geconjugeerd met nanobodies en lege NPs. We laten zien dat noch lege NPs, noch vrij RNase A resulteerde in SKBR3 cel toxiciteit (tot concentraties van 100 μM). Aan de andere hand de NPs die niet waren gecoat met nanobodies leidde tot 75% cel dood op de hoogste geteste concentratie

(28 μM; IC_{50} = 15 μM). RNase A geladen NPs die wel waren geconjugeerd aan HER2 specifieke nanobody 11A4 lieten een hogere cytotoxiciteit zien, waar 90% cel dood werd gevonden op de hoogste concentratie (28 μM; IC_{50} = 5 μM). Onze resultaten laten zien dat RNase A intracellulair was afgegeven waar het cytosolisch RNA kon afbreken.

2. **Toekomst perspectieven**

Moleculaire imaging uitgevoerd met optische tracers krijgt recentelijk steeds meer aandacht, maar door de gelimiteerde licht penetratie van deze methode is deze techniek niet geschikt voor hele lichaam scans, maar wel ideaal geschikt voor oppervlakkige (of endoscopisch bereikbare) tumoren of voor gebruik in een intraoperatieve setting. De laatste jaren is er steeds meer data verzameld wat het concept van *image-guided surgery* ondersteund als een waardevolle methode voor kanker therapie. Desondanks zijn er nog een aantal hordes die genomen moeten worden voordat *image-guided surgery* als routine behandeling wordt opgenomen in de kliniek.

De vereiste voor succesvolle *image-guided surgery* is om hoge contrast te krijgen tussen tumor en gezond weefsel. Dit kan verkregen worden door gebruik te maken van tumor-specifieke probes die alleen binden aan cellen die de tumor gerelateerde marker tot expressie brengen. Meer kennis over potentieel waardevolle biomarkers kan de ontwikkeling van nieuwe, tumor herkennende probes versnellen.

Meer interesse wordt er nu gelegd op de ontwikkeling van nieuwe probes die kleiner zijn dan mAbs om snelle optische imaging te faciliteren. Nanobodies, die 10 keer kleiner zijn in moleculair gewicht dan conventionele mAbs, hebben een aantal karakteristieken die essentieel zijn voor een optische probe bedoeld voor snelle imaging. De karakteristieken die nanobodies zo geschikt maken zijn de hoge affiniteit en specificiteit voor de targets die ze herkennen, gecombineerd met hun kleine formaat wat voor een snelle en homogene distributie zorgt bij de tumor kort na injectie. Het gemak en de snelheid van zowel het *phage display* proces als de genetische constructies, maken dat het nanobody platform erg aantrekkelijk is. Studies hebben aangetoond dat nanobodies lage immunogenetische potentiaal hebben. Maar aangezien zowel naakte nanobodies als nanobodies die zijn geconjugeerd met een fluorofoor worden verwijderd door renale filtratie, moeten er meer studies gedaan worden om de nefrotoxiciteit van de probes in kaart te brengen.

Om het contrast tussen gezond en kankerweefsel te verbeteren, kan naast gebruik te maken van tumor specifieke probes die receptoren herkennen die tot (over)expressie komen op tumor weefsel ook gedacht worden aan het gebruik van een enkel nanobody wat geconjugeerd is aan een aantal fluoroforen. Wij laten zien dat willekeurig geconjugeerde fluoroforen soms een beschadigend effect hebben op de bindingscapaciteiten van de nanobody en gebaseerd daarop raden wij aan om locus specifieke conjugatie strategieën te ontwikkelen. De techniek achter het maken van de probes

met meerdere fluoroforen per molecuul en die allemaal locus specifiek geconjugeerd worden, moet nog wel verder geöptimaliseerd worden om het quenching effect te minimaliseren. Daarnaast denken wij dat de locus specifieke conjugatie methode ook belangrijk is voor de uiteindelijke commercialisatie, aangezien het de mogelijkheid biedt om een uniform product af te leveren. Met willekeurige conjugatie kunnen nanobodies soms meer dan 1 fluorofoor bevatten en soms ook helemaal geen fluorofoor.

Een andere methode om het contrast tussen gezond en kankerweefsel te vergroten is om meerdere tumor biomarkers tegelijkertijd te targeten. Dit zou het probleem van intratumorale heterogeniteit oplossen. Zulke cocktails van nanobodies kunnen alle geconjugeerd worden aan dezelfde fluorofoor om de T/A ratio te vergroten of elke nanobody zou aan een ander fluorofoor gekoppeld kunnen worden. Het gebruik van een nanobody cocktail opent de mogelijkheid om de moleculaire status van de tumor non-invasief te typeren zonder dat daar biopsies aan te pas hoeven komen. Dit kan helpen bij de evaluatie en aanpassing van adjuvant of neo-adjuvant therapie, vooral in het geval van metastatische patiënten. Door het kleine formaat van de nanobodies kan gedacht worden om een cocktail te maken met nanobodies die op één biomarker meerdere epitopen herkennen. Dit zou de T/A ratio kunnen verhogen voor biomarkers wiens expressie niveau laag is.

De HER2 herkennende nanobodies die zijn beschreven in deze scriptie competeren niet met het bindings epitoop van trastuzumab. Dit betekent dat de beschreven nanobodies gebruikt kunnen worden om de respons op trastuzumab therapie te volgen. De lage immunogenetische potentie van de nanobodies laat ook toe dat er meerdere keren een dosis kan worden geïnjecteerd om de therapie in tijd te volgen.

Om uiteindelijk optische imaging te introduceren in de kliniek moeten de ontwikkelingen van de tumor specifieke fluorescente probes hand in hand gaan met ontwikkelingen in toegewijde detectie systemen. Zulke systemen zouden in voldoende mate aanwezig moeten zijn voor gebruik door chirurgen om de adoptie van de techniek te stimuleren [18]. Op het moment kunnen de commerciële systemen alleen één golflengte meten. Als een cocktail van nanobodies met verschillende fluoroforen gebruikt wil worden om de moleculaire status van de tumor te bepalen, moeten er dus nog ontwikkelingen plaats vinden in deze apparaten.

In hoofdstuk 4 hebben we de ontwikkelingen gepresenteerd van de hond specifieke nanobodies die bedoeld zijn voor snelle optische imaging. Tot dus ver zijn we er niet in geslaagd om de target van de geselecteerde nanobodies vast te stellen. Toekomstige studies kunnen focussen op dit probleem door een immuunprecipitatie aanpak te gebruiken in combinatie met massa spectrometrie. In parallel kunnen meer *phage display* selecties plaats vinden om nieuwe binders te selecteren tegen honden HER2. De faag output van voorgaande selecties op honden cel lijnen kan gebruikt worden als een input voor meerdere rondes op bijvoorbeeld humane borstkankercellen die HER2 receptor tot expressie brengen. Ook zou er tijd gestoken moeten worden om honden HER2 receptor ectodomein

recombinant te produceren in een bacterieel of zoogdier expressie systeem. Dit zou een waardevolle tool zijn die toekomstige nanobody selecties zou moeten eenvoudigen.

Wij laten zien dat HER2 specifiek nanobody succesvol gebruikt kan worden in electronen microscopie studies. In deze beginnende haalbaarheids studies hebben we een geöptimaliseerd protocol gemaakt voor indirecte nanobody detectie met konijn-anti-VHH serum als primair antilichaam. De volgende stap in het ontwikkelingsproces zou zijn om de nanobody direct te koppelen met goud om zo de resolutie te vergroten van deze electronen microscopie techniek. Studies waar nanobody 11A4 wordt gebruikt moeten alleen locus specifieke conjugaties gebruiken aangezien we hebben aangetoond dat willekeurige conjugatie van een fluorofoor aan dit specifieke nanobody resulteert in verlies van affiniteit.

Een aantrekkelijke optie voor de combinatie van tumor imaging met tumor therapie is het gebruik van nanobody gebaseerde theranostiek. Nanobodies kunnen geconjugeerd worden aan photosensitizers die initieel de chirurg laten zien waar de tumor zit voor tumor resectie, maar daarna ook gebruikt kunnen worden voor photodynamische therapie (PDT) onder invloed van licht in het getroffen gebied. Zo'n aanpak is waarschijnlijk het beste om de terugkeer kans van de ziekte te minimaliseren. Voordat nanobody-PS conjugaten worden gebruikt in de kliniek moeten deze eerst gevalideerd worden in een gepast *in vivo* model. De nanobody-PS conjugaten die beschreven zijn in deze scriptie zijn potente PDT probes tegen niet alleen trastuzumab-sensitieve cellen, maar ook resistente cellen. Het probleem van verkregen of intrinsieke resistentie tegen trastuzumab is een grote horde in de therapie tegen HER2 positieve borstkanker patiënten. De beschreven PDT aanpak zou kunnen helpen om deze horde te overbruggen.

Deze PDT aanpak zou ook kunnen worden getransleerd naar de constructie van nieuwe therapeutische opties voor trippel-negatieve borstkanker. Deze soort borstkanker brengen geen hormoon receptor of HER2 tot expressie, maar hebben vaak EGFR overexpressie. In tegenstelling to HER2 is EGFR aanwezig niet alleen op het oppervlak van kanker weefsel, maar ook op geselecteerd gezond weefsel. Aangezien nanobody-PS alleen toxisch is wanneer het wordt belicht, zou dit een erg interessante oplossing kunnen bieden voor anti-EGFR therapie in een intraoperatieve setting.

In hoofdstuk 8 presenteren we data over HER2 herkennend, gePEGyleerd PLGHMGA nanoparticles die een therapeutisch eiwit bevatten (RNase A). Toekomstige studies moeten zich richten op de evaluatie of dit middel ook beter werkt *in vivo* in een geschikt model. Het zou interessant zijn om te weten wat de toxiciteit is van het nieuwe middel tegen trastuzumab-resistente modellen zowel *in vitro* als *in vivo*. Het exacte mechanisme waarmee de RNase wordt afgegeven binnenin de target cellen is onbekend. Studies die zich richten op het begrijpen of het cytotoxische resultaat komt door (i) de afgifte van het therapeutische eiwit van de NP in de endosomen, wat leidt tot destabilisatie van deze cellulaire compartimenten en daarmee toegang geeft tot het cytosol, of (ii) de destabilisatie van de endosomen door NP wat tot gevolg heeft dat het therapeutische eiwit kan

ontsnappen en transloceren naar het cytosol, of (iii) een combinatie van beide, moeten worden uitgevoerd. Ook moeten waarschijnlijk de nanoparticles zelf worden geoptimaliseerd om opname door het reticuloendotheliale systeem tegen te gaan. Bij deze optimalisatie ligt de modulatie van hun grootte waarschijnlijk voornamelijk ten grondslag.

3. Samenvattende conclusies

Bij elkaar gevoegd heeft het werk wat gepresenteerd is in deze scriptie geleid tot de volgende conclusies:

- Nanobody-fluorofoor conjugaten zijn veelbelovende probes voor snelle optische imaging van borstkanker in een non-invasieve en intraoperatieve setting, voor zowel een mono- als een duospectrale setup.
- Nanobodies kunnen gebruikt worden voor immuno electronen microscopische toepassingen.
- Nanobody-photosensitizer conjugaten zijn veelbelovende, potente therapeutische probes die kunnen leiden tot cel dood van zowel trastuzumab-sensitieve als trastuzumab-resistente humane borstkankercellen.
- De biologisch afbreekbare nanoparticles die RNase A bevatten en op hun oppervlak zijn geconjugeerd met HER2-specifieke nanobodies kunnen potentieel gebruikt worden voor intracellulaire afgifte van therapeutische eiwitten naar humane borstkankercellen.

Reference

1. Weigelt B, Peterse JL, van 't Veer LJ: Breast cancer metastasis: markers and models. *Nat. Rev. Cancer.* 5(8), 591-602 (2005).

2. Wittrup KD, Thurber GM, Schmidt MM, Rhoden JJ: Practical theoretic guidance for the design of tumor-targeting agents. *Methods Enzymol.* 503, 255-268 (2012).

3. Fang J, Nakamura H, Maeda H: The EPR effect: Unique features of tumor blood vessels for drug delivery, factors involved, and limitations and augmentation of the effect. *Adv. Drug Deliv. Rev.* 63(3), 136-151 (2011).

4. Vermeulen JF, van Brussel AS, van der Groep P *et al.*: Immunophenotyping invasive breast cancer: paving the road for molecular imaging. *BMC Cancer* 12, 240-2407-12-240 (2012).

5. Ward C, Langdon SP, Mullen P *et al.*: New strategies for targeting the hypoxic tumour microenvironment in breast cancer. *Cancer Treat. Rev.* 39(2), 171-179 (2013).

6. Pinheiro C, Sousa B, Albergaria A *et al.*: GLUT1 and CAIX expression profiles in breast cancer correlate with adverse prognostic factors and MCT1 overexpression. *Histol. Histopathol.* 26(10), 1279-1286 (2011).

7. Behbod F, Kittrell FS, LaMarca H *et al.*: An intraductal human-in-mouse transplantation model mimics the subtypes of ductal carcinoma in situ. *Breast Cancer Res.* 11(5), R66 (2009).

8. Moelans CB, de Weger RA, van Blokland MT *et al.*: HER-2/neu amplification testing in breast cancer by multiplex ligation-dependent probe amplification in comparison with immunohistochemistry and in situ hybridization. *Cell. Oncol.* 31(1), 1-10 (2009).

9. Minn AJ, Gupta GP, Siegel PM *et al.*: Genes that mediate breast cancer metastasis to lung. *Nature* 436(7050), 518-524 (2005).

10. Paoloni M, Khanna C: Translation of new cancer treatments from pet dogs to humans. *Nat. Rev. Cancer.* 8(2), 147-156 (2008).

11. Khanna C, Lindblad-Toh K, Vail D *et al.*: The dog as a cancer model. *Nat. Biotechnol.* 24(9), 1065-1066 (2006).

12. Heukers R, Vermeulen JF, Fereidouni F *et al.*: Endocytosis of EGFR requires its kinase activity and N-terminal transmembrane dimerization motif. *J. Cell. Sci.* 126(Pt 21), 4900-4912 (2013).

13. Vu T, Claret FX: Trastuzumab: updated mechanisms of action and resistance in breast cancer. *Front. Oncol.* 2, 62 (2012).

14. Altintas I, Heukers R, van der Meel R *et al.*: Nanobody-albumin nanoparticles (NANAPs) for the delivery of a multikinase inhibitor 17864 to EGFR overexpressing tumor cells. *J. Control. Release* 165(2), 110-118 (2013).

15. Talelli M, Oliveira S, Rijcken CJ *et al.*: Intrinsically active nanobody-modified polymeric micelles for tumor-targeted combination therapy. *Biomaterials* 34(4), 1255-1260 (2013).

16. Talelli M, Rijcken CJ, Oliveira S *et al.*: Nanobody-shell functionalized thermosensitive core-crosslinked polymeric micelles for active drug targeting. *J. Control. Release* 151(2), 183-192 (2011).

17. van der Meel R, Oliveira S, Altintas I *et al.*: Inhibition of tumor growth by targeted anti-EGFR/IGF-1R nanobullets depends on efficient blocking of cell survival pathways. *Mol.*

Pharm. 10(10), 3717-3727 (2013).
18. Keereweer S, Van Driel PB, Snoeks TJ *et al.*: Optical image-guided cancer surgery: challenges and limitations. *Clin. Cancer Res.* 19(14), 3745-3754 (2013).

Appendix

Curriculum Vitae

Curriculum Vitae

Marta Magdalena Kijanka was born on 3rd of November 1985 in Wrocław, Poland. In 2007 she obtained a Bachelor degree in biotechnology after successful defence of her bachelor dissertation written under the supervision of prof. Arkadiusz Kozubek. She continued her education on the Medical Biotechnology. Her master project was performed under the supervision of prof. Arkadiusz Kozubek. During her master studies she participated in the Socrates/Erasmus programme and she did a 5 months long internship at the Department of Pharmaceutics of Utrecht University. During this internship she worker with dr Niels Hagenaars on a project focusing on the visualization of influenza antigens from various vaccine formulations in frozen and paraffin-embedded sections of the nasal cavity at different time points after intranasal application. In 2009, selected from an international group of 660 applicants, she was chosen as one of 50 participants for the International Talent Programme for Life Sciences & Health held in the Netherlands. Shortly after defending her master thesis in July 2009, she started working as research assistant in the group of dr. Paul van Bergen en Henegouwen. In January 2010 she started her PhD project on development and pre-clinical characterization of anti-HER2 nanobodies for molecular optical imaging and therapy of breast cancer. The results of her project are presented in this dissertation.

Appendix

List of Publications

List of Publications

1. **Kijanka et al.** Rapid optical imaging of human breast tumour xenografts using anti-HER2 VHHs site-directly conjugated to IRDye 800CW for image-guided surgery. *Eur J Nucl Med Mol Imaging*. 2013 Oct; 40 (11): 1718-29

2. Hagenaars N., **Mania M**. et al. Role of trimethylated chitosan (TMC) in nasal residence time, local distribution and toxicity of an intranasal influenza vaccine. *J Control Release*. 2010 May; 21 (144): 17-24

3. **Kijanka M.** et al. Nanobody-based cancer therapy of solid tumors.
   Submitted

4. **Kijanka M.**[#], van Brussel A. S. A.[#] et al. Dual-probe optical imaging of breast cancer with a combination of VHHs targeting CAIX and HER2.
   Submitted

5. **Kijanka M.**[#], Samadi N.[#] et al. Nanobody-targeted and RNAse-loaded nanoparticles based on a hydrophilic polyester aimed for cancer therapy.
   Manuscript in preparation

6. **Kijanka M.** et al. A potential treatment for trastuzumab resistant breast cancer: nanobody-targeted photodynamic therapy.
   Manuscript in preparation

7. **Kijanka M.** et al. Development of canine HER2 targeted nanobodies for optical imaging.
   Manuscript in preparation

8. **Kijanka, M.**[#], van Donselaar, E.G.[#] et al. Optimizing immuno-labeling protocol for nanobody-based detection of HER2 in breast cancer cells using immuno-EM.
   Manuscript in preparation

[#]equal contribution

Appendix

Affiliations of collaborating authors

Affiliations of collaborating authors

Maryam Amidi,
Department of Pharmaceutics, Utrecht Institute for Pharmaceutical Sciences, Utrecht University, Utrecht, The Netherlands

Paul M.P. van Bergen en Henegouwen,
Division of Cell Biology, Department of Biology, Faculty of Science, Utrecht University, Utrecht, The Netherlands

Aram S.A. van Brussel,
Division of Cell Biology, Department of Biology, Science Faculty, Utrecht University, Utrecht, The Netherlands and Department of Pathology, University Medical Center Utrecht, Utrecht, The Netherlands

Gooitzen M. van Dam,
Department of Surgery, Division of Surgical Oncology, BioOptical Imaging Center, University of Groningen, Groningen, The Netherlands

Paul J. van Diest,
Department of Pathology, University Medical Center Utrecht, Utrecht, The Netherlands

Joep B. van den Dikkenberg,
Department of Pharmaceutics, Utrecht Institute for Pharmaceutical Sciences, Utrecht University, Utrecht, The Netherlands

Elly G. van Donselaar,
Biomolecular Imaging, Department of Biology, Faculty of Science, Utrecht University, Utrecht, The Netherlands

Bram Dorresteijn,
Division of Cell Biology, Department of Biology, Faculty of Science, Utrecht University, Utrecht, The Netherlands

Sofia Doulkeridou,
Division of Cell Biology, Department of Biology, Faculty of Science, Utrecht University, Utrecht,

The Netherlands

Mohamed El Khattabi,
QVQ BV, Utrecht The Netherlands

Wim E. Hennink,
Department of Pharmaceutics, Utrecht Institute for Pharmaceutical Sciences, Utrecht University, Utrecht, The Netherlands

Purvi Jain,
Division of Cell Biology, Department of Biology, Faculty of Science, Utrecht University, Utrecht, The Netherlands

Małgorzata Krawczyk-Durka,
Division of Cell Biology, Department of Biology, Faculty of Science, Utrecht University, Utrecht, The Netherlands

Marjolijn N. Lub-de Hooge,
Hospital and Clinical Pharmacy, University Medical Center of Groningen, Groningen, The Netherlands

Willem P.Th.M. Mali,
Department of Radiology, University Medical Center Utrecht, Utrecht, The Netherlands

Wally Müller,
Biomolecular Imaging, Department of Biology, Faculty of Science, Utrecht University, Utrecht, The Netherlands

Cornelus F. van Nostrum,
Department of Pharmaceutics, Utrecht Institute for Pharmaceutical Sciences, Utrecht University, Utrecht, The Netherlands

Vasilis Ntziachristos,
Biological Imaging & Institute for Medical and Biological Imaging, Technische Universität München and Helmholtz Zentrum München, Munich, Germany

Sabrina Oliveira,
Division of Cell Biology, Department of Biology, Faculty of Science, Utrecht University, Utrecht, The Netherlands

Jan A. Post,
Division of Cell Biology, Department of Biology, Faculty of Science, Utrecht University, Utrecht, The Netherlands

Peter J.M. Rottier,
Division of Virology, Department of Infectious Diseases & Immunology, Faculty of Veterinary Medicine, Utrecht University, Utrecht, The Netherlands

Neda Samadi,
Department of Pharmaceutics, Utrecht Institute for Pharmaceutical Sciences, Utrecht University, Utrecht, The Netherlands

Monique H. Verheije,
Division of Pathology, Department of Pathobiology, Faculty of Veterinary Medicine, Utrecht University, Utrecht, The Netherlands

Tina Vermonden,
Department of Pharmaceutics, Utrecht Institute for Pharmaceutical Sciences, Utrecht University, Utrecht, The Netherlands

Theo C. Verrips,
QVQ BV, Utrecht The Netherlands

Elisabeth G.E. de Vries,
Department of Medical Oncology, University Medical Center of Groningen, Groningen, The Netherlands

Elsken van der Wall,
Division of Internal Medicine and Dermatology, University Medical Center Utrecht, Utrecht, The Netherlands

Frank-Jan Warnders,
Hospital and Clinical Pharmacy, University Medical Center of Groningen, Groningen,
The Netherlands

Carlo Zimarino,
Division of Cell Biology, Department of Biology, Faculty of Science, Utrecht University, Utrecht,
The Netherlands

Appendix

Acknowledgements

From the bottom of my heart I would like to thank

EVERYONE

who for the last 4 years supported me in completing this thesis...

Dziękuję !

Thank you !

Dank U !